Charting the development of functional visuotopic maps in the larval zebrafish

Bard, Andrew Daniel

Awarding institution:
King's College London

Take down policy

If you believe that this document breaches copyright please contact librarypure@kcl.ac.uk providing details, and we will remove access to the work immediately and investigate your claim.

Charting the development of functional visuotopic maps in the larval zebrafish

A thesis presented for the degree of
Doctor of Philosophy
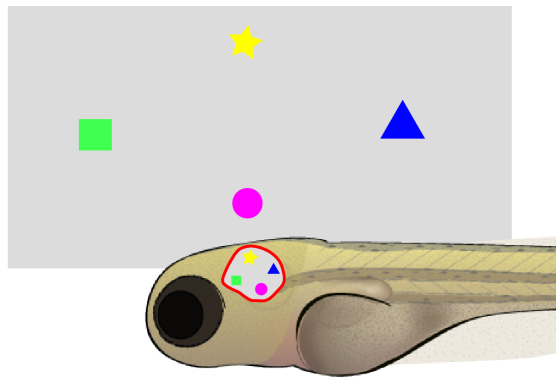
Andrew Bard

supervised by Dr Andrew Lowe,

Professor Gareth Barker & Professor Jon Clarke

Centre for Developmental Neurobiology
King's College London, UK
April 12, 2019

Word count: **45491**

Statement Of Authorship

All work within this thesis was performed by the author, except for contributions by Dr Andrew Lowe where specifically noted.

Abstract

Topographic maps, in which neighbour relations between neurons are conserved over a projection between brain areas, are a recurrent feature of visual systems. By examining the retinal ganglion cell (RGC) synapses to the zebrafish tectum at the population level, I have explored hitherto inaccessible questions regarding development, refinement and alignment of distinct maps within the same target field. Given that functional types of RGC stratify into laminae within the tectum, what are the developmental dynamics and parameters governing these maps and alignment between them? Do they encode visual space with the same precision?

The parameters governing axonal arbour refinement vary across species, likely related to differences in nurture and environmental pressures. In the zebrafish, the situation is complicated by mismatched growth of the tectum with respect to the retina, necessitating constant remodelling of retinotectal connectivity. Although topography is maintained during this process, it is not known how precise this topography is. How does map precision change in response to experience during development? This question is particularly interesting given recent theoretical results suggesting that perfect topography may not be optimal for decoding the visual world. These, and other salient issues, are explored in greater detail within my introduction (**Chapter 1**).

Quantifying the precision of topographic mappings is a non-trivial problem, so metrics require empirical validation. **Chapter 2** is a comparative study of various metrics for topographic precision using in-silico modelled data, and particularly focusing on quantification of maps derived from multiple experimental subjects. Metrics were compared on their ability to discriminate different levels of order, their resistance to global shape distortion, and the amount of data they required to perform optimally. Having selected one metric for further development, a statistical framework for testing differences in order between multiple-subject datasets was derived. Finally, a method for interpreting sources of topographic disorder in biologically relevant distance units was developed.

I constructed a novel visual presentation system, maximising visual coverage and resolution, the details of which are described in **Appendix A**. Using simultaneous visual presentation and confocal imaging of a calcium indicator in RGC axon terminals allowed characterisation of RGC functional selectivity. In **Chapter 3** I explored the development of two feature-selective topographic maps formed by retinal ganglion cells (RGCs) in the tectum. I focused on

orientation-selective (OS) and direction-selective (DS) RGCs, pooling data from fish of different ages (3, 7 and 10 days post fertilisation, dpf) into standardised anatomical spaces. Such experiments revealed nonuniform, nonmatching coverage of the tectum by OS and DS RGCs, suggestive of regional specialisation. DS and OS maps also exhibit differing levels of topographic order, with the DS map more ordered than the OS at all ages. For both functional types, order changes nonlinearly during development, with maps at 10dpf less ordered than those at 7dpf, providing empirical evidence to the notion that a topographic encoding of visual space may be non-optimal.

Finally, in **Chapter 4**, fish were reared in altered visual environments in order to specifically explore the role of visual experience in the development of topographic maps formed by DS and OS RGCs. Three different conditions were used: complete darkness, an enriched/naturalistic environment, and strobe lights. Functional imaging of topographic maps in 10dpf animals reared in these conditions suggests complex relationships between visual experience and map properties, including the representation of the cardinal axes of visual space, and overall map precision. Visual experience affects feature-selective maps differentially, with a far greater impact on OS maps than DS.

My thesis offers insight into how feature-selective topographic maps in the tectum develop. It suggests that, despite a globally uniform density of RGCs in the retina, regions could be specialised for the detection of specific features, although specialisation is dependent on the visual environment of the animal as it develops. This is of great interest to the community, raising questions about how animals might behaviourally maximise the matching of retinal biases with the statistics of their environment. Finding that topographic order does not necessarily increase with age adds evidence for the hypothesis that topographic maps are not directly used in decoding the visual scene.

Contents

11

List of Figures

14

15

List of Tables

Chapter 1

Introduction

Topographic maps, in which neighbour relations are conserved in a projection between two spaces are a recurrent feature of sensory systems, across species and brain areas. Specifically, if a projection between brain areas is topographically organised, then neurons which have adjacent dendrites in one brain area will also have adjacent axons in the other. Understanding the process of map formation and ultimately the purpose of neuronal maps such as these has been identified as one of the 23 most important problems in systems neuroscience [1].

When an image is formed on the retina, it is processed and transformed through several different cell types, arranged in laminae. It is then sent to the brain via retinal ganglion cells (RGCs), with different types of RGCs encoding different features of the visual environment. Retinotopy refers to the conservation of neighbour relations between RGC somata and their axons within the brain. Visuotopy, a related concept, refers to the conservation of neighbour relations between the positions of neurons (or axons) in the brain and the locations of their receptive fields in visual space. This thesis sets out to examine the development of topographic maps formed by different types of RGCs in the zebrafish visual system, using a functional approach to classify RGCs and a standardised anatomical space to pool data from multiple animals. This chapter will give an overview of how the zebrafish visual system is organised, with particular focus on the retinotectal projection and its topographic properties, and finally touching on the technical challenges associated with studying topographic maps.
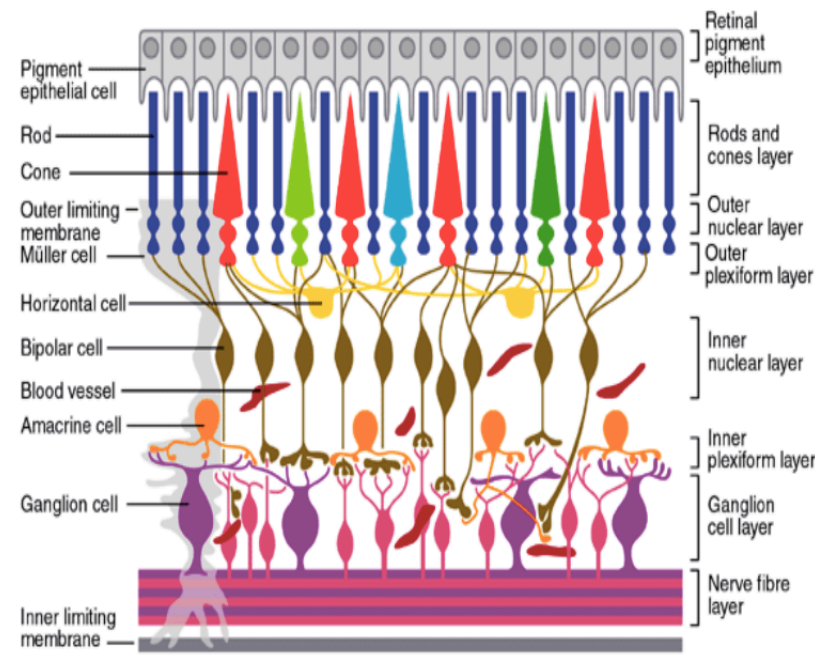
Figure 1.1: **Structure of the vertebrate retina**, showing the different laminae and their constituent types of neuron. Light falls on the retina from the bottom of this diagram. Image from Wilkinson-Berka, 2004 [3].

1.1   Structure and function of the retina

The schema for retinal organisation is well-conserved across vertebrates [2]. Light passes through the cornea and lens, forming an image on the retina. The retina is composed of three nuclear layers: the outer nuclear layer (ONL), inner layer (INL) and ganglion cell layer (GCL). Sandwiched between these are two synaptic layers: the outer plexiform layer (OPL) and inner plexiform layer (IPL). Within these, structures are the 5 classes of retinal neuron, illustrated in **fig. 1.1**.

Photoreceptors, lying in the ONL, transduce light into electrical signals via opsins. Opsins absorb photons of specific wavelengths of light, triggering hyperpolarisation via coupled intracellular G-proteins [4]. In the zebrafish, there are 5 different types of photoreceptors, specified by their expression of a specific opsin: rods, with broad spectral sensitivity and particularly useful at low light levels, and four kinds of cones, sensitive to UV, short, medium and long wavelengths. Zebrafish vision is blue-shifted and spectrally broader than humans [5–7].

Horizontal cells have their cell bodies in the INL, and are GABAergic interneurons which modulate photoreceptors, maintaining the firing rate of bipolar cells within their reasonable dynamic range [8], meaning that areas of contrast within especially bright, or dim, objects can still be distinguished. This gain control has been implicated in edge detection and the creation of classical centre-surround receptive fields [9]. Horizontal cells take inputs from photoreceptors, but typically integrate across a greater retinal area than bipolar cells: as they are connected to each other via gap junctions, their receptive fields extend beyond their dendrites [10]. Zebrafish have one morphological type connected to rods, and two connected to cones [11] - the cone-connected varieties can be subdivided according to their spectral sensitivity, determined by which photoreceptors they take inputs from [12].

Bipolar cells also have their cell bodies in the INL, and take synaptic inputs from the photoreceptors via their dendrites in the OPL. Broadly, they can be classified as ON or OFF, depending on whether they respond to light or dark stimuli. As photoreceptors hyperpolarise with light [13], ON bipolar cells are sign-inverting, while OFF are sign-conserving. When more finely classified according to morphology, 17 different types of bipolar cell have been identified in the zebrafish, however these types have not been explicitly linked to stereotyped functional identities [14]. They extend their axons into the IPL, wherein the ON and OFF axons segregate into different laminae. The laminar distributions of their axons determine which RGCs they synapse with.

Amacrine cells, interneurons with their cell bodies in the INL, have diverse structural and functional properties, with up to 28 different types so far identified in the zebrafish [15]. They have historically proved difficult to understand as their structure is not traditionally polar: they lack axons, and synapse onto bipolar cells, RGCs and each other, and are largely inhibitory. They refine the information flow from bipolar cells from RGCs and are vital for the emergence of correct functional selectivity in RGCs, such as direction selectivity [16] and orientation selectivity [17].

RGCs take their inputs from both bipolar cells and amacrine cells, via their dendrites in the IPL. RGC dendrites lie in defined IPL sublayers, defining their synaptic inputs and thus their functional selectivity. In mice, these laminar distributions arise via initially diffuse projections followed by pruning, although this refinement approaches completion prior to eye opening [18]. In contrast, no such pruning has been seen in zebrafish, in which most RGC dendrites grow directly to their final

lamina [19].

RGC cell bodies, unsurprisingly, lie in the GCL. As the final outputs of the retina, their axons extend through a "blind spot" known as the optic disc (where no photoreceptors are found) and project into retinorecipient brain areas. The retinal circuitry decomposes the image that falls onto the retina into a number of features. There are two ways to interpret the evolutionary optimisation process of selecting these features. One view is that the width of the optic nerve limits the number of axons (and therefore the amount of information) that can be sent to the brain, so it is advantageous for the retina to compress information prior to sending it on. An alternative view is that the features sent to the brain must be ethologically relevant for the animal, and appropriate compression of the information sent to the brain allows size of the optic disc to be minimised. Thus, much research has focused on precisely which features are encoded by which RGCs, discussed below.

1.1.1 Classification of Retinal Ganglion cells

The debate about how many types of RGC there are, and the precise features that they encode, is ongoing. Certain criteria have been suggested as necessary to specify a type of RGC, and are generally accepted within the field [20, 21]:

- Tiling within the retina

- Stereotyped and unique axo-dendritic morphology

- Stereotyped and unique transcriptional signature

- Stereotyped and unique functional selectivity

The above criteria all require a certain level of qualification: they are not necessarily as simple as they seem. Due to the limits of experimental techniques, it is impossible to assess all of these criteria simultaneously in a high-throughput manner - we must rely on one, or at maximum two, criteria to identify types in any single experiment. As a result, defining types of RGCs in a completely unambiguous way is technically difficult.

The criteria that neurons of a single type should be evenly-spaced [20] can be stated more precisely as that the positions of neurons within a type should be dependent

22

on each other, while different types should be independent. The distinction is illustrated in Bleckert et al., 2014 [22], a study which shows that for two types of mouse RGC (identified by genetic markers, see below) there are gradients of density across the retina. More specifically, each type of RGC is expected to tile the retina, meaning that its dendritic arbours cover the whole retina with a minimum of overlap between them [23], achieved by local homotypic avoidance rather than the imposition of top-down lattice-like structures [24]. This tiling ensures that each point in visual space is covered exactly once by each type of RGC. Given that there exist differences in density within types (for example, [22]) and that types are expected to tile the retina, this casts doubt on whether morphology is sufficient to unambiguously specify RGC types. In a region of low density for a specific type, a member of that type is expected to have a far larger dendritic arbour than in a region of high density [23, 25].

That RGCs of a particular type should be uniquely identifiable according to a molecular signature is widely believed. However, all cells express many genes and whether a single binarised expression level is sufficient to identify types of RGC is a hotly debated topic. It was hypothesised that binarised expression of combinations of ≤ 3 genes should uniquely specify each type of RGC [20]. However, a recent study performed single-cell RNA-Seq on many mouse RGCs and identified 40 clusters, of which some could not be uniquely specified even by combinations of 5 genes [26]. That said, many functionally-defined types (see below) are specifically marked by smaller combinations of genes [20, 22, 26–29].

Historically, much research into types of RGC has assumed that dendritic morphology defines their upstream connectivity, in turn suggesting that dendritic morphology predicts functional identity to a certain extent. This has not been directly validated. The recent findings that morphologically and genetically similar bipolar cells in different parts of the retina may be functionally distinct due to differing photoreceptor inputs [30] suggest a more complex view, as they imply that RGCs with identical dendritic morphology might have differing functional identity depending where they are located in the retina.

In the mouse, 22 types of RGC have been found based on dendritic arbourisations [31], while clustering according to functional criteria has revealed more than 30 types [32], and transcriptional profiling suggests 40 [26]. In the zebrafish, 11 types have been identified according to dendritic morphology [33], while

23

more than 50 types of RGC have been suggested based on combinations of axo-dendritic morphology [34]. However, as that study relied on expert observation of sparse-labelled neurons, and no functional or molecular validation, there could be extra functional diversity, or some redundancy within such a typeification schema. Currently, there are no studies providing genetic identification criteria for any zebrafish RGC types; thus, despite the difficulties involved, if we are interested in how the visual world is represented, functional characterisation must be the gold standard for identifying types of RGCs.

Classification according to functional criteria is normally performed using simplified stimulus sets, designed to represent simple visual features that can be easily parameterised: often monochrome gratings, bars or dots. Assessing and classifying neurons according to their functional selectivity is limited by the stimulus set used - for example, one study characterised zebrafish RGCs as responding to specific contrast changes (ON, OFF or ON-OFF) [35], but the stimuli chosen did not allow finer-scale categorisation. Broader stimulus sets, such as that used in Baden et al., 2016 (including a "chirp" stimulus, dense binary noise, moving bars and full-field coloured flashes) [32] allow clustering techniques to be used to identify functional types, but very quickly become unwieldy unless very large numbers of cells are recorded from due to the extra time needed to present more stimuli, and the complexity of the required analysis. Natural images (and movies) can provide more insight into the "real world" features being detected by particular types, but these are problematic. Analysis is complicated due to autocorrelation within natural images, and many more experimental epochs are required for full characterisation; one study required more than 8000 images for characterisation of receptive fields within primate V2 [36]. Such experiments are a practical challenge in many experimental systems, due to the length of time from which a preparation can be reliably recorded. Additionally, in retinal explant experiments, compensation of the presented image for the distortion introduced by the explant procedure would be extremely problematic for natural images.

Motion-sensitive RGCs, and contrast selectivity

From a functional perspective, the most-characterised functional types of RGCs in the zebrafish are those selective for oriented or directed motion. Direction-selective (DS) RGCs encode a specific direction of motion, but not its opposite, while

orientation-selective (OS) RGCs respond well to two opposite directions, but not their orthogonals [37, 38]. The selectivity angles for DS RGCs are roughly anterior, upwards with a posterior component, and downwards with a posterior component; these are equivalent to those found in the goldfish [39]. The OS RGCs can be broken down into 4 angular-specific variants, responding approximately to motion in the cardinal and diagonal axes of visual space [38].

RGCs that respond best to increments or decrements in light levels are described as being ON or OFF, while those that respond to both are described as ON-OFF. This aspect of their functional identity is determined by which layer of the IPL their dendrites sample, with the ON-OFF cells being bistratified. They can be further characterised into those which respond very quickly to the appropriate change in light level, but their response ends quickly (transient) and those whose response decays far slower (sustained). At 5-6 dpf, it appears that there are ON, OFF and ON-OFF RGCs in the zebrafish retina but ON-OFF cells predominate [35], although in this study responses were not characterised further than contrast selectivity. Studies in adult goldfish have revealed 3 populations of DS RGC, of similar angles to those of zebrafish, and composed only of ON and OFF [39]. However, it is not known how zebrafish OS and DS RGCs are broken down into contrast selective variants.

In contrast to the zebrafish, in the mouse cosegregation of responses to contrast and direction of motion is very well-studied, with precise knowledge about which contrast changes are represented in RGCs for each direction of motion. Mice possess four populations of ON-OFF DS RGCs, responsive to movement along the cardinal axes of visual space [28, 40, 41]. They can each be uniquely specified by coexpression of CART and one other molecular marker each [20, 29], and have bistratified dendritic arbours. Mice additionally have three populations of ON DS RGCs respond to angles roughly equivalent to those of the fish mentioned earlier [29]. However, these ON DS RGCs do not project to the superior colliculus (SC), but rather to the accessory optic system, where they are involved in the encoding and compensation of self-motion [42]. Finally, mice are known to possess a single class OFF DS RGC, selective for dorsal motion [27]: these are marked additionally by the expression of a single gene, JAM-B, and the presence of a highly anisotropic dendritic arbour (extending ventrally from the soma), in contrast to the ON-OFF DS RGCs. OS RGCs have been identified in the mouse [43, 44], as well as cats [45], rabbits [46] and primates [47] but genetic and morphological markers are currently

lacking.

1.2 The zebrafish retinotectal projection and tectal structure

Each class of RGC (corresponding to a specific extracted feature) sends its information to the brain as a parallel channel of information [48]. In zebrafish, all retinotectal projections are contralateral (**fig. 1.2**). Retinal neurons project to 10 different areas, termed arbourisation fields (AFs). The optic tectum (AF10) is the largest of these area, receiving input from 97% of RGCs, while the second largest (AF9, the pretectum) receives around 3%. All remaining AFs receive axon collaterals from these two largest areas [34, 49].
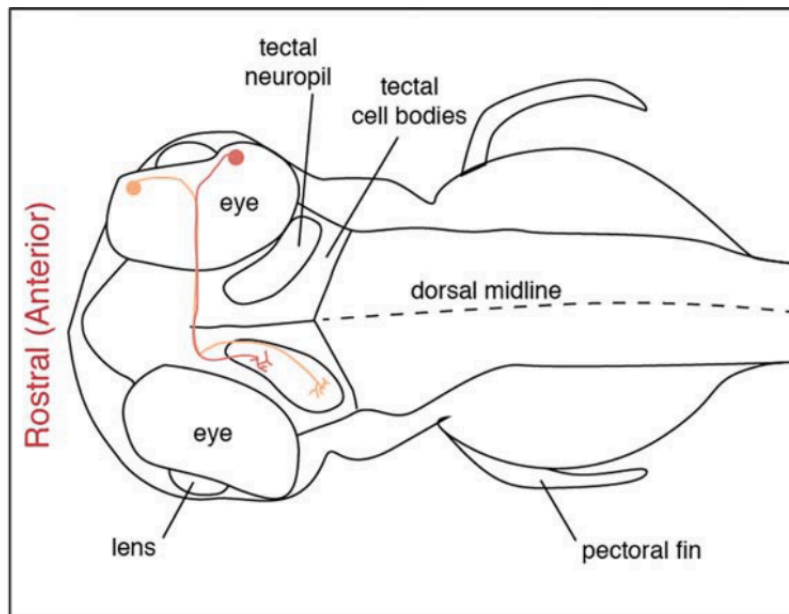
Figure 1.2: **The zebrafish retinotectal projection**, showing contralateral projections. Image adapted from Kita et al., 2014 [50].

1.2.1 Structure of the tectum

The zebrafish tectum, which is generally regarded as the homologue of the mammalian superior colliculus (SC), is a large bilateral structure within the midbrain.

It is a site of multisensory integration and motor control, and is thought to coordinate many different behaviours such as prey capture, and the avoidance of predators [51]. It can be coarsely divided into two areas: the stratum periventriculare (SPV), a deep layer in which most of the tectal cell bodies lie, and the neuropil areas, found more superficially and where RGC axons, and tectal dendrites, form their arbours. The neuropil area can be further divided into four zones: from superficial to deep, the stratum opticum (SO), stratum fibrosum et griseum superficiale (SFGS), statum griseum centrale (SGC) and the stratum album centrale (SAC). The largest of these is the SFGS, which receives around 80% of the retinotectal axons. It has previously been subdivided into sublaminae, although the precise number specified in the literature varies [33, 51].

Most, but not all, RGC axons form planar axonal arbours with respect to the topographic surface of the tectum [33]. As previously demonstrated, DS and OS neurons segregate into partially-overalpping laminae within the tectal neuropil [37, 38], each forming a visuotopic map [52]. Thus, the RGCs within the tectum form multiple laminae, each representing a different feature of visual space, and stacked on top of each other (see **fig. 1.3**), although with a certain degree of overlap between them.

visual field

retinal circuitry

visual features in types of RGC

to tectum via optic nerve

superimposed maps in tectum
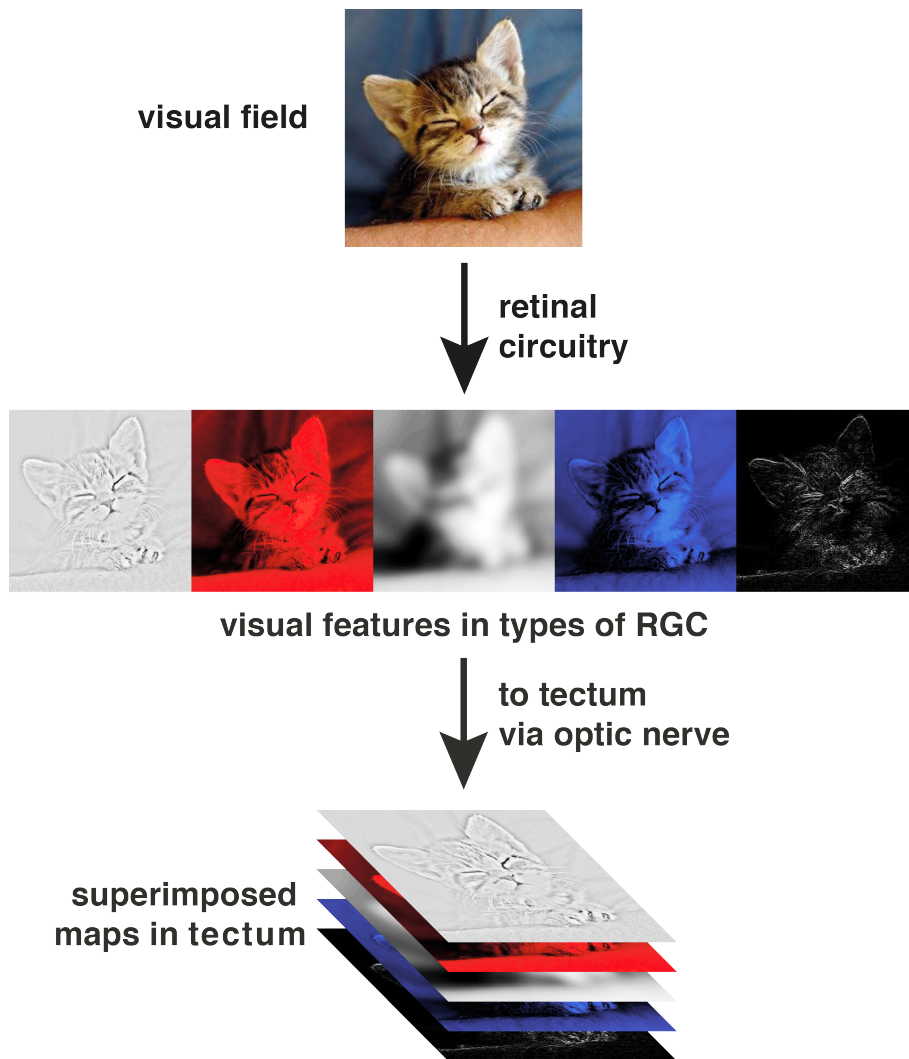
Figure 1.3: **Schematic representation of the retinotectal projection.** Retinal circuitry transforms the visual field such that different types of RGC encode different features of the visual field. They then project to the tectum in a topographically-ordered manner, meaning that tectal laminae represent matched maps of the visual field.

1.3 Formation of retinotopic maps
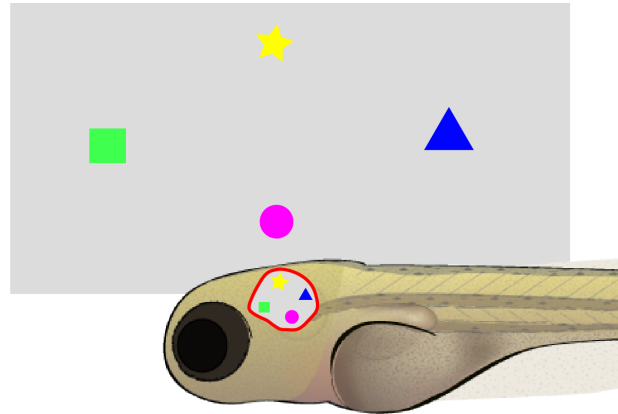
Figure 1.4: **Visuotopy in the zebrafish:** the visual field (grey rectangle) is reciprocated as topographic maps in the contralateral tectum (outlined in red). Following the inverted pattern of light on the retina, and inversions during contralateral projection, the tectal map very closely resembles the visual field.

In the zebrafish, the first RGCs reach the tectal neuropil and arbourise between 2-3 dpf [49, 53, 54]. Their axons enter from the anterior pole of the tectum, and find their termination zones via a biased branching and stabilisation model, in contrast to other species. Whereas mammals and birds overshoot and prune, and frog RGCs grow directly to their targets, zebrafish use a biased branching and stabilisation model for RGC axon growth [55, 56], whereby individual neurites frequently extend and retract, while maturing synapses nucleate the formation of new branches [57]. Image-forming brain areas, like the tectum, receive RGC axons as topographic maps. That is, RGCs representing adjacent areas of visual space and having neighbouring dendritic arbours project to adjacent locations in the tectum. As the image on the retina is inverted in both axes, and a further inversion occurs between the retina and tectum, the tectal map in the zebrafish appears approximately the same as the visual field, as seen in **fig. 1.4**.

Different classes of RGC segregate into laminae each encoding different features in parallel: a widely-applicable axiom for projection neurons is that their arbours should stay out of 3D, i.e. forming planar axonal arbours [58]. Thus, the location which any individual axon must target is defined in three dimensions: the two dimensions of a retinotopic lamina, representing the orthogonal axes of visual
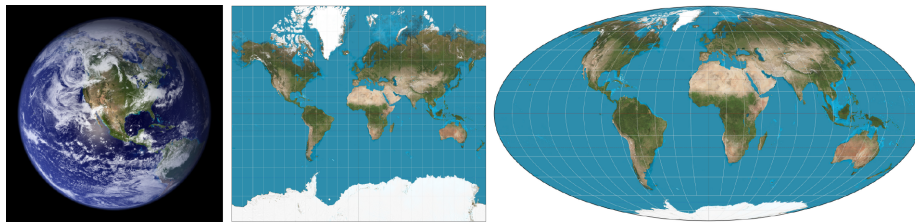
Figure 1.5: **Projections between surfaces with different curvature necessitate distortions.** In this example, 2 different 2D maps of the globe are shown. **Left:** The Earth, seen from space (source: NASA) **Centre:** Cylindrical projection which preserves both latitudinal and longitudinal coordinates, but distorts distances and relative areas. **Right:** The Mollweide projection, which retains correct areas and latitude coordinates but distorts the appearance of longitudinal coordinates. Many other projections are possible, each retaining some characteristics at the expense of others.

space, and additionally its laminar location, specified by its type; which visual feature it encodes, determined by its dendritic morphology. Because of the projection from a hemispherical retina to a roughly-flat surface in the tectum, the tectal map must be distorted to a certain extent, as exemplified in **fig. 1.5**, and such distortions have been observed in vivo [52].

Given that axons from RGCs of the same type occupy the same lamina, and compete for space within it (see **section 1.3.2**), it seems logical that they must tile in a similar way to their dendrites; if not, greater overlap between adjacent axonal arbours would produce an increased level of oversampling in the tectum relative to the retina. However, this effect has not been conclusively demonstrated other than in Drosophila, in which the visual system is rather differently organised [59, 60]. Demonstrating whether axons tile in retinorecipient laminae stems from the difficulty of labelling all of the axons from a single class of RGC, but still being able to differentiate individual neurons, in individual animals.

In general, the formation of multiple retinotopic maps is a two-stage process. Within each tectal lamina, axonal locations are determined by defined molecular cues, present in gradients across both RGCs and retinorecipient laminae. Later, maps are refined according to neuronal activity, either spontaneous or visual-evoked. This fits within a broader schema of how neural systems form, across species: connectivity is initially specified by molecular cues, with an increasing contribution of neuronal activity as animals mature [58].

1.3.1 Molecular guidance cues

Although not perfectly understood, the best-studied parts of the machinery required for development of retinotopy are molecular guidance cues: secreted and membrane-bound molecules which guide the growth and connectivity of both axons and dendrites, best-studied in the mouse and the chick. If one eye of a newt is rotated, gross behavioural deficits result, indicating that the central projections of RGCs maintain their positions [61]. This finding led to Sperry's chemoaffinity hypothesis: each RGC axon and tectal dendrite has its final position encoded in physico-chemical gradients [62]. The molecules expressed in the tectum are interpreted as attractive or repulsive by the RGC axonal growth cone, causing extension, retraction or turning [63]. The chemoaffinity hypothesis was originally confirmed using ex-vivo co-culture of chick RGCs with rearranged slices of tectal tissue, showing that RGC axons exhibited a preference for growing on the substrate they would have occupied in vivo [64]. Meanwhile, independent research demonstrated that the Eph receptors and ephrins exhibited patterns of expression consistent with Sperry's ideas [65].

How do such gradients specify the positions of individual axons within the whole retinotectal projection? Removal of a portion of the goldfish retina leads to initial correct target finding by retinal axons, but the map subsequently expands to cover the whole tectal surface [66]. Similarly, if a portion of the tectum is ablated, the remaining surface contains the whole topographic map, but compressed [66]. Similar results have been obtained in zebrafish [53]. Thus, the interpretation of chemical gradients by RGCs is ratiometric rather than absolute.

Ephrins are membrane-bound repulsive cues expressed in gradients along the axes of the tectum. Their cognate Eph receptor is expressed in a complementary gradient in the RGCs across the retina, leading to graded positioning of each axon. Mediolateral and anterioposterior axes are specified by different molecules (see **fig. 1.6**). However, the gradients presented have been cartoonised, and the neatness of those gradients has not been quantified. In zebrafish, they were identified by large-scale random mutagenesis, followed by screening for phenotypes in which the retinotectal connection was disrupted [67–69]. In mice, ephrin-As are required for topographic map formation but do not specify laminae within the SC: RGC axonal arbours of ephrin-A knockout mice still innervate the correct laminae, but produce disorganised topographic maps within them [70].

Tectal ephrin gradients come into being before any RGC axons arrive: rostrocaudal ephrin gradients are induced by the mid-hindbrain boundary (MHB). When the MHB is removed, RGC axons overgrow and occasionally bypass the tectum entirely [71]. Blocking downstream effectors of ephrin signalling, such as focal adhesion kinase, leads to similarly overgrown axons [72]. Thus, axons essentially continue growing until they reach a region where a high enough concentration of the appropriate ephrin causes them to halt.

Different molecules specify different axes of the retinotectal projection: for example, one of the molecules specifying the identity of dorsal retina is Radar (Gdf6a). Mutation of this gene in zebrafish produces a compressed map on the medial tectum, while the lateral half (normally recieving dorsal RGCs) remains completely empty [73]. The zebrafish mediolateral axis, in addition to being specified by certain ephrins/Ephs (see **fig. 1.6**), is specified by a gradient of Semaphorin 3D, a secreted protein which repels ventral RGC axons expressing the receptors neuropilin 1A/1D [74]. Not all of the genes involved in the creation of retinotopic maps have known mechanisms of action: for example Cyfip2, mutated in *nevermind*, has unknown binding partners [69].

Early work in the chick demonstrated that the laminar targeting of RGC axons is determined by molecular cues different from those guiding retinotopy [75]. In fact, the gross laminar distribution of zebrafish RGCs within the tectum is thought to be almost entirely hardwired via genetically encoded signals [76, 77]. Laminae are defined by a gradient of Slit1, secreted by tectal cells with high-superficial and low-deep concentration gradient, and Robo2 receptors on the RGC axons [78]: *Astray* mutants (lacking the Robo2 receptor) exhibit larger, more complex RGC axonal arbours [79]. Additionally Nel, an extracellular matrix protein expressed in the chick tectum, excludes RGC axons from specific laminae, although its axonal binding partner is currently unknown [80]. However, recent findings suggest that while laminar distribution of RGC axons in the zebrafish requires intact Slit/Robo signalling, tectal neurons can eventually acquire their correct functional identities even when the correct laminar targeting of RGCs is disrupted, albeit later during development [81].
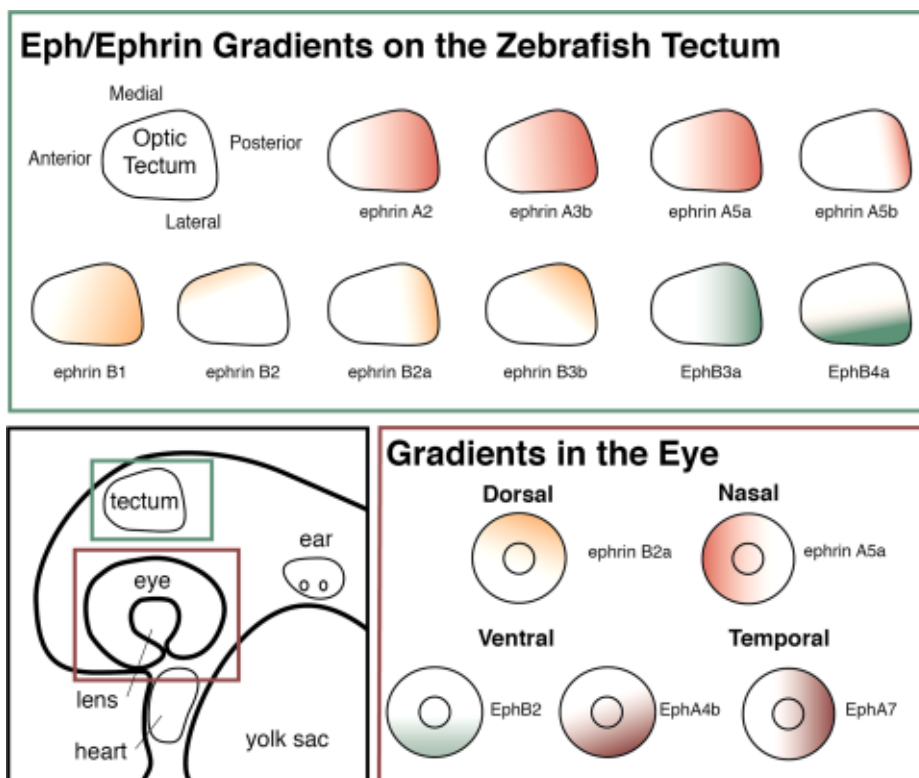
Figure 1.6: **Gradients of ephrin and Eph expression** in the zebrafish retina and tectum, showing molecules specifying both mediolateral and anterioposterior tectal axes. Image adapted from [50].

1.3.2 Activity-dependent refinement

When a third eye is transplanted into frogs, its RGC axons and those of the original eye interleave within the tectum, forming a striped pattern [82]. Removal of one tectum in goldfish, leading to aberrant ipsilateral RGC projections, produces analogous results [83]. These results indicate a role for neuronal activity in organisation of the map, as if molecular guidance cues were the only determinant of tectal axonal arbour location, the axons from the two eyes would intermingle fully.

In many species including mice [84], rats [85], ferrets [86], turtles [87] and chicks [88], retinal neurons exhibit spontaneous activity during development. It has been suggested that the function of such activity patterns is to provide patterns of activation that have similar statistics to visual-evoked activity, but prior to visual experience [89]. This spontaneous activity takes the form of spreading waves across the retina, and is important for the development of topographic maps. For example, when such retinal waves are disrupted by knockout of the $\beta2$ subunit of the nicotinic acetylcholine receptor in mice, RGCs exhibit disorganised retinotopic mapping in both the SC [90] and the lateral geniculate nucleus of the thalamus [91]. Dark-rearing of turtles leads to more spontaneously-active RGCs. This leads to an increase in RGC receptive field size. Silencing cholinergic activity using drugs led to smaller receptive field sizes in the dark-reared condition [87]. Taken together, these data imply that while molecular cues and spontaneous activity in early development gives a rough template for RGC dendrite growth, fine refinement requires real visual experience in these species.

However, in fish (which develop while exposed to external visual input) intrinsically-generated patterned activity is not thought to be necessary. Correlations naturally arise within natural visual scenes, giving rise to correlated activity patterns similar to retinal waves in frogs [92]. Although goldfish retinae exhibit spontaneous activity during development, this activity does not appear to be episodic or correlated like retinal waves [93]. In contrast, the zebrafish does exhibit retinal waves, although they largely cease around 3 dpf [94], and their functional importance for development of the retinotectal connection has not been established.

Neuronal activity has large effects on the axonal arbours of zebrafish RGCs in

the tectum. A live imaging study, which showed that RGC axons arbourise in a trial-and-error fashion, with more branches emerging from stable synapses, supports this idea indirectly [57]. Experiments directly manipulating activity levels have given contrasting results, resulting in an unclear picture of how axons compete for space within the tectum to produce tiling. In *macho* mutants, which misregulate expression of Na_V properly, or animals whose neurons have been silenced using TTX, nasodorsal axons have expanded arbours which are shifted rostrally (that is, they prematurely stop growing) [69, 95]. However, sparse overexpression of K^+ channels, reducing activity in individual RGCs, leads to a reduction in arbour size, while concurrent global silencing of neuronal activity with TTX in this context appeared to return arbour size to normal, implying a role for competition between active neurons in determining the domains of their axonal arbours [96]. Such divergent results have been explained differently, such as the varying strength and timing of silencing methods and the time at which arbours were observed [50] - there is clearly a complex interaction between many different factors.

NMDA receptors are particularly important in activity-dependent plasticity, matching the firing patterns of pre- and post-synaptic neurons via Hebbian mechanisms. Treatment of frog tecta with NMDA antagonists produces disordered retinotectal maps, and overgrown RGC arbours [97]. In zebrafish, NMDA antagonists increase arbour size [98], and NMDA retrograde signalling is thought to be largely responsible for the extensive pruning [57] observed in vivo. When pre- and post-synaptic cells fire in synchrony, retrograde signalling via arachidonic acid stabilises synapses: when this retrograde process is disrupted, axonal arbours are reduced in size and their branches turn over faster [99], interpreted as a reduction in branch stability. Other molecules, such as BDNF, have been similarly implicated in Xenopus [100] and zebrafish [99, 101]. However, most work to date has largely focussed on how these factors affect single (sparsely-labelled) neurons - how they affect macroscopic map organisation has been explored far less thoroughly.

Visual experience

One of the key tools for studying the role of visual experience in the development of neural systems is to rear animals in altered visual environments. In mammals, this has often been achieved using surgery such as suturing the eyes shut, massively reducing the amount of light that can reach the eyes [102]. A simpler solution, and

one particularly easy to implement in the study of zebrafish, is to rear them in the absence of light ("dark-rearing"). For example, one study found that dark-rearing did not disrupt the laminar structures of the retinal IPL, or the optic tectum, concluding that the laminar targeting of RGCs is in fact a hardwired process [76].

Additionally, dark-rearing of goldfish leads to larger multiunit receptive field sizes during optic nerve regeneration, which has been interpreted as being due to altered retinotectal connectivity [103], while rearing zebrafish in dim light leads to reduced survival of tectal neurons, and their integration into existing circuitry [101]. These findings imply that both the retinotopic map, and downstream tectal circuitry, are dependent on visual experience to develop properly.

Stroboscopic rearing has, in the past, been used to examine whether visual experience is instructive or permissive for the development of correct retinotectal projections. Examination of the RGC axonal arbours of goldfish, defined by morphology, are affected far more than others by rearing in strobe lights [104], although in this study, analysis did not differentiate between laminar and topographic axes. On a more global level, optic nerve regeneration after optic nerve crush with stroboscopic conditions prevents normal shrinking tectal multiunit receptive field sizes in the goldfish, to the same extent as dark-rearing [103], implying that not only the presence, but also the content of visual experience, is important for topographic precision.

Most work in zebrafish to date has focussed largely on molecular pathways and neuronal morphology at the level of single-neurons - how these factors macroscopically affect map organisation is largely unknown, and will be explored within this thesis. Furthermore, are different classes of RGC more or less susceptible to alterations in visual drive? Are different classes of RGC differentially sensitive to enrichment or absence of the features that they encode? Although the gross laminar targeting of RGCs does not appear to be affected by visual drive when all RGC types are pooled [76], when classified by function there is some evidence that OS RGCs are more affected by dark-rearing than the DS [38]. Could there be analogous differences in phenotype in the topographic plane?

1.3.3 Development and alignment of multiple maps

RGC inputs to the zebrafish tectal neuropil consists of multiple topographic maps arranged in laminae, each encoding different visual features, as illustrated in **fig. 1.3** - although, as discussed, these laminae are partially overlapping. These maps must become aligned with each other, such that a single tectal neuron can integrate the same point in visual space across different laminae. The only investigation of how maps align in the zebrafish was performed in the PhD thesis of Aenea Hendry [52], who found that DS and OS maps become misaligned at 7 dpf when animals are dark-reared.

One of the most widely-studied examples of map alignment is that of binocular vision, particularly in mammals. Mammals, unlike zebrafish, have both contralateral and ipsilateral projection patterns of RGC. RGCs from both eyes view similar regions of visual space; in order for binocular vision to be coherent, topographic maps formed by ipsilateral and contralateral RGCs must be matched across the eye-specific laminae of retinorecipient structures, such as the SC and the dLGN. Sperry predicted that in order for the same molecules to produce two maps of opposite polarity, there must be a radial gradient of the appropriate molecules in the retina [62], and this in fact turned out to be the case for EphA receptors in both ferrets [105] and humans [106].

Mice lacking teneurin-M3 have aberrant ipsilateral projections to the dLGN, but their contralateral connections are unaffected, resulting in severe visual deficits as a direct consequence of incoherent ipsilateral and contralateral maps [107]. Interestingly, the same molecule is necessary for the correct development of orientation selectivity, and correct axonal projections of OS RGCs in the larval zebrafish tectum [108], while DS RGCs are unaffected by its knockout. Given that the phenotype of teneurin-M3 knockout zebrafish is in large part due to a failure in the amacrine cells which underlie the functional identity of OS RGCs and not the RGCs themselves [17], these findings indicate that the functional identity of OS RGCs must be correctly specified in order for them to project their axons correctly - indicating the role of activity-dependent mechanisms in the correct formation and alignment of multiple maps. Consistent with this work, dark-rearing leads to misalignment of the maps formed by DS and OS RGCs in the zebrafish tectum at 7 dpf [52].
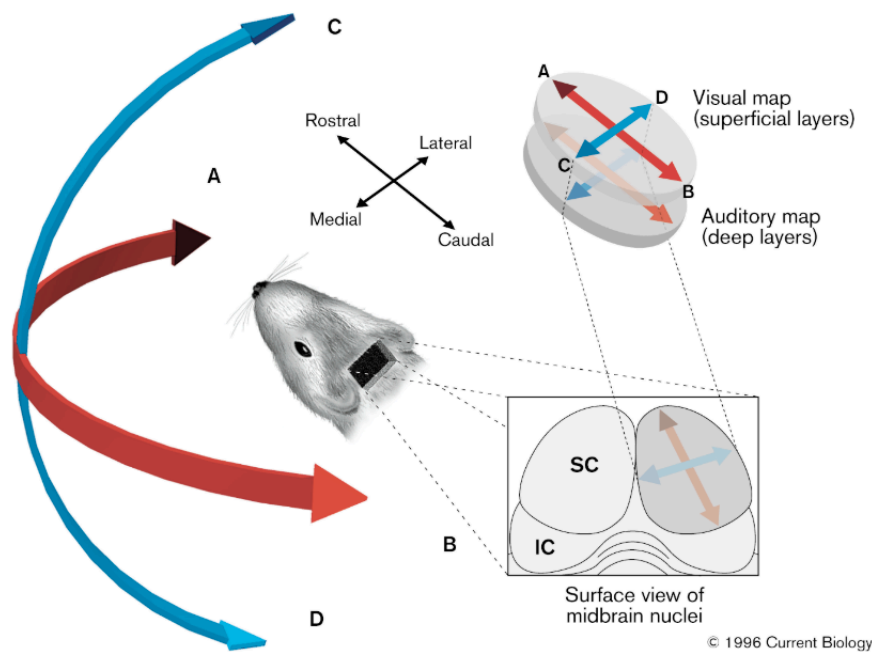
Figure 1.7: Maps representing the visual field and the locations of auditory stimuli are topographically matched in the mammalian SC. Figure from Rees, 1996 [113].

More generally, many maps of visual space must be aligned within the mammalian SC: for example, maps formed by RGCs and maps derived from V1 afferents [109]. Matching between maps formed from retinal and V1 inputs is achieved by activity-dependent plasticity mechanisms: when the retinal map is duplicated by perturbing molecular guidance mechanisms, the V1 map alters to match it. In mammals such alignment precedes eye opening and thus must depend on spontaneous activity. However, the V1 map can still form in a coarsely-ordered fashion with when the eyes are removed, indicating that molecular cues still play a role [110]. After eye opening, map alignment is consolidated by expansion of cortical axonal arbours, in an experience-dependent manner [111]. However, a model for how precisely activity-matching leads to map alignment is still the subject of active research [112].

More intriguing still is the matching of maps derived from different sensory modalities, such as the locations of visual and auditory stimuli (see **fig. 1.7**). The locations of auditory stimuli are not directly encoded by input neurons as they are in the visual system, because they are calculated via comparison of the input from both ears [114–116]. The auditory map is more coarsely-ordered than that of

visual space, based on ensembles rather than simple point-to-point mapping [117]. Matching of the auditory map to the visual one is dependent on sensory experience, mediated specifically via NMDA receptors, in both the owl optic tectum [118] and the ferret SC [119]. More recent experiments in owls indicate that the visual map acts as a template for the auditory one [120].

1.3.4 The retinotectal projection in zebrafish is dynamic

The zebrafish visual system grows throughout life, as with other teleosts. In zebrafish (and goldfish), successive rings of new neurons are added at the outer edge of the retina, while tectal tissue is added in a crescent-shape, with no growth at the rostral edge [121–123]. This asymmetry means that new-born neurons in the temporal retina cannot be matched to new tectal neurons with respect to their topographic location. Thus, the teleost retinotectal projection is not static as with the mammalian retinocollicular one, and RGCs must constantly change the partners with which they make synaptic contacts, moving across the topographic plane of the tectum [124]. As new RGCs axons project from the temporal retina to the rostral tectum, their predecessors must alter their connectivity with tectal neurons in order to move caudally across the tectal surface, as must all neurons.

In order that adult-born RGCs can integrate in the correct topographic locations, ephrin gradients in the tectum persist into adulthood [125]. For correct targeting of new-born RGCs, it is particularly important that guidance by ephrin gradients is ratiometric rather than absolute [53]. In contrast, in the chick and mouse these gradients disappear after retinotectal/retinocollicular connections are established [65, 126]. Activity-dependent mechanisms also persist, as patterned visual input continues.

1.4 Regional specialisation in the retina

The visuotopic cortical representation found in V1, originally discovered in monkeys [127], revealed that the projections corresponding to the central retina, including the fovea, occupied a larger cortical area than their peripheral counterparts. The mammalian fovea, is a specialised retinal region with increased density of both

cone photoreceptors and RGCs, meaning that the corresponding area of the visual field is encoded with far greater acuity [128]. The whole retina has a gradient of neuronal density: the fovea is the centre at which this density is the greatest. In the retinotopic portions of the mammalian visual cortex, this increased retinal neuronal density is reciprocated as a magnification factor [129], such that the downstream representation of each RGC occupies a roughly equivalent area of cortex and that the areas of visual space in which there are more RGCs occupy more cortical area [130]. Magnification factors have been observed earlier in the visual pathway, such as the SC of the cat [131].

Many fish have foveae, which are usually located in the temporal retina, presumably to facilitate forward/binocular vision [132]. Similarly to the "red" area of the pigeon [133], many fish also have areas of increased photoreceptor density that are not marked by characteristic foveal depressions. Generally, these areas of higher visual acuity tend to match the animal's preferred angle of approach during prey capture. For example, in fish which approach their prey from below it is situated ventrotemporally [134, 135], and dorsotemporally in bottom-feeders [136]. Perhaps the most striking example of this is in the archerfish, which hunts by shooting jets of water at insects and knocking them off trees overhanging the water [137], and has a tenfold difference in photoreceptor and RGC density between the densest and sparsest areas. The densest region is in the line of sight for Snell's window, the area in which objects out of the water can be detected effectively, indicating the area's utility for targeting prey [138]. In the tecta of certain teleosts, such areas of increased retinal cell density are reciprocated according to the same rules as primate cortical magnification factors, occupying proportionately more tectal area [139].

The foveae and equivalents are an example of regional specialisation within the retina - areas with higher visual acuity. However, it is additionally possible that there are areas specialised for the detection of specific kinds of visual feature, and this would be evident at the level of differences in density between classes of RGC. For example, the mouse was originally believed, like the zebrafish [140], to have uniform photoreceptor/RGC density. However, a recent study has indicated that at least two molecularly-defined classes of RGC have non-uniform, and non-matching, density across the retina [22]. The bipolar cells presynaptic to these two classes did not have matching density gradients, implying that RGCs in nasal (sparse) regions integrate across more bipolar cells. Conversely, in temporal regions visual space

is sampled with a higher resolution, with RGCs integrating across fewer bipolar cells. However, whether temporal RGCs occupy proportionally more space in retinorecipient areas (as with primate magnification factors) has not been assessed.

Most recently, one study found that the visuotopic map in the mouse SC is biased in terms of the directions of motion encoded, with the region encoding the binocular region of the visual field having a strong bias for the detection of nasal motion, and the monocular region having a strong bias for the detection of temporal motion in the visual field [141]. However, it is not clear how such biases in collicular neurons arise from RGC inputs. Could similar biases be present in the zebrafish?

Zebrafish have asymmetries in their photoreceptor complement across the retina, with opsins detecting longer wavelengths more prevalent, at the expense of opsins detecting shorter wavelengths, in the ventral/temporal retina [142]. Downstream, there are biases in the distributions of bipolar cells [143]. Retinal asymmetries in spectral sensitivity could be explained by an evolutionary process maximising the overlap between the wavelengths of light most likely to fall on a given retinal region and the sensitivity of the photoreceptors in that region. This predicts that such asymmetries will be found if there are stereotyped differences between the spectra of light originating in specific portions of the visual field. Complementarity between stereotypy in the spectra of animals normal visual environments and the spectral sensitivity of retinal regions has been identified in archerfish [138], mice [144] and most recently zebrafish [30]. What might this mean for experimental zebrafish, which are normally stored in clear petri dishes (allowing light from below the animals as well as above) in white-lit incubators (containing very little detail)? Clearly these artificial environments are far less complex and contain none of the consistent biases of the natural environments for which their visual systems have evolved [30].

The first zebrafish RGCs to differentiate are in the ventronasal retina, at around 2 dpf, but has been thought to equilibrate across the retina before the emergence of visual-evoked neuronal responses can be detected at 70 hpf [140]. It is currently not clear whether there is any particular functional significance of the early-emerging RGCs. A mismatch between the density of OS & DS RGCs, as compared to those responsive to looming stimuli, has been observed at 7 dpf [38, 52]. Given that differences in photoreceptor complement affect the functional identity of otherwise equivalent bipolar cells [30], these differences are likely to be passed forward,

affecting functional selectivity in RGCs. This implies that morphologically, and molecularly, indistinguishable RGCs in different parts of the retina might have different functional selectivity. How might such differences impact on downstream topographic maps?

1.5 Importance of topography

As discussed above, neuronal activity during development (either spontaneous or visual-evoked) acts to refine the axonal arbours of RGCs in their targets. It has been widely assumed that this refinement, demonstrated for the most part at the single-neuron level, will additionally refine topographic maps and make them more precise [145]. However, this has never been conclusively demonstrated experimentally.

In fact, the precise purpose of neuronal maps has been suggested as one of the major open questions in systems neuroscience [1]. Recent work seems to suggest that topographic decoding of the visual field is sub-optimal, and that other algorithms would be more efficient [146, 147]. Such work suggests that the topographic map formed by molecular guidance mechanisms might be an early heuristic for creating circuits capable of decoding the visual field, later superseded by more sophisticate decoding methods as activity-dependent refinement becomes relatively more important [58]. Despite the limitations of this work, performed using data from tectal cell bodies which may not be perfectly topographic with respect to their dendrites, it does raise interesting questions regarding the precise function and necessity of retinotopic maps.

1.5.1 Development of topographic precision

The PhD thesis of Aenea Hendry [52] provided the first examples of topographic mappings formed by two populations of feature-selective RGCs (DS and OS) in 7 dpf zebrafish, by means of functional imaging (discussed below). However, her work was limited in that it did not examine how maps change over development. One way to assess the importance of precise topographic mapping is to examine the development of topographic maps; specifically, how their precision changes

as the animal moves towards adulthood. How do the activity-dependent plasticity mechanisms described above actually impact on the precision of the maps of visual space?

Although the precision of topographic maps during development has not been specifically examined before, there is some work that might give us hints about how visual information is organised [148]. The structure of ensembles of tectal neurons, as measured by their spontaneous activity, changes between 4 and 9 dpf such that ensembles become more spatially compact over time, but have a transient peak in size at 5-6 dpf, when ensembles involve more neurons. Dark-reared animals at 6 dpf appear to have less-organised spontaneous activity, as measured by how coherent their ensembles are [148]. Can these properties be directly linked to the precision of the input maps formed by RGCs?

1.6   The study of maps

To answer some of the questions raised above, quantitative descriptions of functionally-selective classes of RGCs forming topographic maps, during development, are necessary. Creation and analysis of such maps entails a number of technical challenges. Firstly, how can we obtain data about both the anatomical locations and functional selectivity of many neurons in single animals? Secondly, how can we maximise the usefulness of incomplete data from multiple experimental subjects? Finally, how can the properties of a topographic map, including its precision, be optimally quantified?

1.6.1   Functional imaging and genetically-encoded calcium indicators

In order to characterise cells according to their functional identity, some measure of their activity in response to presenting stimuli is necessary. This has been widely accomplished in the past using electrophysiological methods. Electrophysiological methods have been used in the past to map receptive field properties of zebrafish tectal neurons [149], and more generally the functional properties of neurons elsewhere in the brain [150].

However, such methods are limited by the number of electrodes that can be

used - although there are computer-assisted systems allowing the simultaneous monitoring of up to 16 neurons [151], this is still a very laborious and unreliable process. Additionally, targeting of specific neuronal subsets requires the use of genetic labelling and imaging to guide the experimenter while selecting neurons to perform experiments on [152]. When attempting to describe topographic maps, it is particularly useful to record from as many neurons as possible in a single animal - it is the relationships between the positions of neurons that are particularly important. Multiple electrode arrays allow for more high-throughput data acquisition, with some probes capable of recording from 960 electrodes simultaneously [153], but completely preclude the use of markers for specific genetically or morphologically defined cell types. They are also constrained to a specific 2/3D arrangement of these electrodes, and interpreting the recorded signals as arising from individual neurons is technically challenging. All electrophysiological techniques are additionally limited by the issues caused by sticking solid objects into soft tissue: distortion of the tissue and damage to its constituent cells. This is more of a problem for larval fish than it is for rodents, simply due to their size.

Optical imaging of intrinsic signals relies on the altered scattering, reflective and absorptive properties of neural tissue in different metabolic states, although the precise metabolic changes underlying the observed signals were a subject of long debate [154]. Noninvasive techniques were used to map cortical activity in the monkey [155] and rat [156]. Retinotopic maps were observed using this technique in owl V1 [154], while modified versions of the method, with periodic stimuli and fourier-based analysis techniques, have been used to examine topographic maps within the mouse SC [90, 157]. However it is limited by spatial and temporal resolution, the inability to target specific cell types, and its indirect relationship to neuronal activity.

Chemical calcium indicators represent one way of optically measuring the activity of many neurons simultaneously, with confocal microscopes allowing the resolution of individual neurons, or even synapses. Oregon Green BAPTA, and various other examples, work by undergoing conformational changes when bound to Ca^{2+} ions, meaning that their level of fluorescence changes according to the concentration of Ca^{2+} ions [158]. As action potentials trigger a large influx of Ca^{2+} [159], the level of fluorescence in any cell loaded with such as dye tracks the level of neuronal activity [160]. Unfortunately, chemical calcium indicators cannot be precisely targeted to one cell type: if injected, they are absorbed by all cells in the vicinity

[161]. Additionally, these chemical dyes can sometimes require difficult surgical preparations, or long incubation times following injection, which can interfere with normal development unless concentrations are carefully titrated, due to chelation of Ca^{2+} ions [162].

Thus, for the study of specific cell types, the use of genetically encoded calcium indicators (GECIs) is preferred. Given the flexibility of modern genetic tools, they can be targeted to specific cell types, and even specific subcellular compartments. The most widely-adopted family of GECIs are the GCaMP proteins, developed by fusing a circularly-permuted version of GFP to calmodulin and a fragment of myosin light chain kinase [163]. When the calmodulin binds calcium, this allows the GFP to undergo conformational change, increasing its level of fluorescence. Since their inception, the GCaMP family has undergone a number of generations, each made via edits of the original sequence [164–168] in order to improve dynamic range, alter affinity for Ca^{2+}, and increase signal-to-noise. For the purposes of imaging in multiple colours, or to avoid spectral overlap with other fluorophores in the same experiment, red versions (RCaMP [169] and R-GECO [170]) and a blue version (B-GECO [170]) have also been developed. The latest generation, the GCaMP6 proteins [168] has three different versions, with fast, medium and slow (suffixed f, m and s) attack and decay kinetics, with signal-to-noise greatest for the slowest version (GCaMP6s). The kinetics of these probes do pose a challenge for data analysis, as the rise and fall times of the probes are rather slower than the timescales of action potentials, with decay times in the hundreds of milliseconds [168]. It should be noted that measurement of $[Ca^{2+}]$ is not a perfect proxy for neuronal activity [168, 171].

As discussed in **section 1.1.1**, in the zebrafish there are no well-defined genetic markers for specific types of RGC (in contrast to the mouse), although Isl2b marks most RGCs [172]. Thus, one approach to characterising the topographic maps formed by different classes of RGC is to express a GECI in all RGCs, and to classify them according to their functional selectivity [37, 38, 52, 173]. Fortunately for this project, a line already exists with pan-RGC expression (driven by the Isl2b promoter) of Synaptophysin-tagged GCaMP6s, meaning that it is preferentially trafficked from the cell body to presynaptic terminals [174].

1.6.2 Standardised anatomical spaces

Standardised spaces allow the analysis and visualisation of data from multiple experimental subjects in a single, three dimensional anatomical space. The data used can be from many levels: single synapses, neurons, or anatomical structures. As often the amount of data that can be extracted from an individual subject is limited, pooling of data across subjects can reveal distributions that would not be visible in individuals.

Imaging approaches to functional characterisation are particularly amenable to such analysis, as imaging almost allows the linkage of functional to anatomical data with a minimum of extra experimental labour, as imaging approaches necessarily capture morphological features. There has been a great increase in the use of standardised spaces, particularly in the zebrafish, over the last few years [175].

One study characterised the axo-dendritic morphology of over 400 RGCs [34], identifying more that 50 possible types according to morphological criteria. Placing individually-labelled neurons into a standardised space allowed the identification of regional biases in the RGC complement innervating AF9: the authors showed that the dorsal and ventral regions received input from different kinds of RGC. Such insight, from singly-labelled neurons, could only be obtained by the pooling of data into a standardised space.

In a series of studies using functional imaging to examine the angle of motion which different voxels within the tectum preferentially responded to, it was only the use of a standardised anatomical model of the tectum which made laminar distribution of the different variants clear, allowing the direct relation of function to anatomical position, validating the different variants [37, 38]. A similar approach was used to characterise the transformation from three variants of DS RGC, each encoding a different direction of motion, to the four directions of motion encoded in tectal neurons [173]. Additionally, standardised spaces were used in the first functional characterisation of zebrafish visuotopic maps [52].

The use of standardised spaces must be approached carefully. Individual experimental subjects often have differences in the size and shape of different anatomical features, as well as carrying variability in the numbers and distributions of specific kinds of cells. Perfect correspondence cannot be assured, particularly between the locations of individual neurons or their neurites. Thus, pooling across

subjects and examining distributions abstracts from exact locations of objects, rather giving probability densities for objects within the anatomical space [175].

1.6.3 Quantifying topographic precision

As discussed before, it would be advantageous to be able to quantify the topographic precision of maps, in order to compare how precise different maps are. In specific terms, this means asking how "correctly" the visual field is reciprocated by the positions of RGC axons in the tectum.

There are many different approaches to quantifying topographic order, and these are non-trivially different in terms of the mappings which they define as optimal: where qualitatively different mappings are assessed and compared according to different metrics, metrics do not agree on which mapping is optimal. Furthermore, when maps are created using different metrics as optimisation objectives, they take on qualitatively different forms [176, 177]. One of the most widely-used frameworks used in derivation of metrics for topography takes pairwise distances in both spaces, and computes a measure of correlation between these pairwise distances [178]. However, their output, and the properties of the map described as optimally ordered still depends heavily on both the methods for calculation of distances, and the precise way that they examine their similarity [176].

Thus, for each application, the metric chosen must be validated on data that mimics the use case as closely as possible. Given the technical constraints of the current project, the metric chosen here should:

- allow comparison of the level of order between multiple maps.

- be suitable for maps derived from multiple experimental subjects.

- be minimally affected by nonlinear mappings.

- require the smallest possible amount of data in order to perform optimally.

The operational parameters of different techniques are difficult to intuit, meaning that they require empirical validation using modelled data. For example, one study examining the mapping of a 1D feature space to a space representing a 2D cortical map revealed that each metric requires a different amount of data in order to

detect topographic order greater than that expected from a random mapping [179]. However, additional modelling work is required in order to find the metric that best satisfies the criteria described above.

1.7 Experimental Aims

Based on the questions raised in this chapter, I performed the following theoretical and experimental work:

In **Chapter 2**, given the need for ways to optimally quantify the precision of topographic maps, I used in-silico modelled data to assess a number of different metrics for topography. I compared them based on suitability for maps derived from multiple experimental subjects, the amount of data they required to perform optimally in this context, how well they detected topography in coarsely-ordered maps, and how they were affected by nonlinear map distortion. A framework for statistically testing for differences between multisubject maps, using a Monte Carlo resampling strategy, is demonstrated. Finally, I examined whether it is possible to interpret deviations from perfect topographic order as arising from a 2D probability distribution in biologically-relevant distance units.

The construction and quality control of a novel visual presentation system to allow functional characterisation of neurons labelled with GECIs in response to visual stimuli is detailed in **Appendix A**. I used this system to examine topographic maps formed by DS and OS RGCs in the zebrafish tectum. These were placed into standardised spaces representing the tectal neuropil.

In **Chapter 3**, characterisation of two maps representing different visual features, at three different developmental timepoints, allowed the exploration of a number of questions discussed in this chapter. Firstly, examining the distribution of synapses over the tectal topographic surface, allowed an exploration of regional specialisation; whether or not specific regions contain more synapses for detection of specific features. Next, it allowed comparison of map precision over time, and between maps representing different visual features (using the framework developed in **Chapter 2**). Additionally, it allowed the assessment of alignment between maps, to examine whether multiple laminar maps emerge in alignment or progressively align as animals age. Within the DS and OS populations of

synapses I then examined what parameters (such as contrast and the preferred angle) contribute to segregation of synapses in both laminar and topographic axes: that is, which features appear to be represented as separate maps in different laminae, and whether regional specialisation exists for such parameters.

Finally, in **Chapter 4**, animals were reared in different visual environments: complete darkness, strobe lights, and an enriched/naturalistic environment. Such experiments were designed to elucidate the effects of visual experience on map precision, the requirement of visual experience for the alignment of alignment, and allowed the examination of whether different types of RGC are differentially affected by visual experience.

Chapter 2

Metrics for Topography

2.1   Introduction

Quantifying the existence and precision of topographic maps is a non-trivial problem. Over the years, many different metrics and methods for quantification have been developed, all relying on different assumptions and ways of quantifying neighbour relations. In one sense, any given metric uses a different mathematical definition of what a perfect topographic mapping would look like [178]. If maps are nonlinear, there is no known exact mathematical solution for perfect order. Thus, any method for quantifying topographic order must be validated empirically [179], particularly as maps in the brain are demonstrably nonlinear (see **Chapter 1**, [52]).

Collecting datasets representing complete topographic maps in a single experimental subject is a technical challenge. Anatomical studies have tended to use sparse or even single-neuron labelling techniques [33, 34], while electrophysiological studies have been limited in the number of electrodes that can be simultaneously implanted. A far more efficient method for quantitative characterisation of maps is to derive incomplete maps in multiple subjects and to pool data together via standardised spaces [175].

However, such pooling can create additional problems regarding the quantification of order in the situation where there is inter-subject variance in map position, size or shape. Intersubject variance could come from a range of sources - it could be due to real biological differences in the size and shape of the individual brain areas,

or the way that such areas are mapped into a single reference space (referred to as the "Lack of Correspondence Problem" [175]). However, it could also be an artefact of how data are acquired: for example, if a visuotopic map is derived using a functional approach, in which receptive field centres for neurons are calculated based on the responses to a defined stimulus [52, 146], receptive field centres are dependent on the precise location of the eye while the stimulus is presented. If data are pooled without regard for the adjustment according to where the animal is looking, topographic order is likely to be underestimated.

Modelled data, incorporating different amounts of topographic disorder, have been used to explore the behaviour of various metrics in both single- and multiple-subject context, such that their utility can be compared quantitatively and the best choice selected. These results facilitate optimisation of both experimental priorities and statistical analyses.

Whenever data sets are subjected to statistical analysis, the amount of data used impacts on the reliability of the statistical description. However, increasing the size of datatsets is subject to diminishing returns. The amount of data required by each metric to provide an optimally reliable description of the level of topographic order has been described. From this description, the relative statistical power for discrimination of different levels of order between different maps has also been compared. These properties have been generalised to the multiple-subjects context, taking account of the amount of data within each experimental subject, and the number of subjects. Work has also performed, using a technique established for single-subject metrics [179], to look at the relative amounts of data required by the multiple-subject metrics for reliable detection of order, examining the effects of both N, the number of subjects, and n, the number of points per subject.

The results of this comparative work have additionally enabled the derivation of a method for testing for differences in topographic order between multiple-subject derived maps, based on the analysis of multiple subsamples of the data obtained. Finally, a framework has been derived which allows the quantification of topographic disorder in the distance units of the original maps. This allows the relation of statistics regarding a topographic map back to the sizes of the biological components that make it up: neurite arbors, or receptive fields.

2.2 Methods

2.2.1 Metrics for topography

Let two spaces be termed T and V, each containing n matched points. Then let $d^V(...,...)$ equal the euclidean distance between any two points in space V, with corresponding notation in space T.

The **topgraphic product** is a metric with its roots in graph theory [177]. Neighbour relations of points in either space are specified as follows: let $f_1^V(j)$ refer to js nearest point, according to the euclidean distance in V. Then, let $f_k^V(j)$ refer to js kth nearest point, according to the distance in V. Using the distance notation defined above, $d^V(j, f_k^T(j))$ is the distance, measured in V, between j and js kth nearest point according to distance in T. Two sets of distance ratios are defined:

$$Q_1(j, k) = \frac{d^V\left(j, f_k^T\right)}{d^V\left(j, f_k^V\right)} \tag{2.1}$$

$$Q_2(j, k) = \frac{d^T\left(j, f_k^T\right)}{d^T\left(j, f_k^V\right)} \tag{2.2}$$

Q_1 is the ratio of distances, measured in V, of j and its kth nearest point in T, and its kth nearest point in V. Q_2 is the ratio of distances, measured in T, of j and its kth nearest point in T, and its kth nearest point in V. These ratios are combined to produce a value P_3, which represents the level of neighbourhood conservation for each point and neighbourhood size (i.e. up-to-the-kth nearest neighbour of each point):

$$P_3(j, k) = \left(\prod_{l=1}^{k} Q_1(j, l) Q_2(j, l)\right)^{\frac{1}{2k}} \tag{2.3}$$

There will be $n(n-1)$ P_3 values. To summarise these numbers, natural logarithms are taken of P_3, and it is made positive to facilitate calculation of p-values [179] and normalisation (see **appendix B**). The mean is taken across all neighbourhood sizes

of all points, to give a final value P_T:

$$P_T = \frac{1}{n(n-1)} \sum_{j=1}^{n} \sum_{k=1}^{n-1} |\ln P_3(j,k)| \qquad (2.4)$$

Normalisation of P_T can be performed via randomly permuting the point-to-point correspondence between spaces V and T, producing a shuffled map. Not all random permutations will be equal: thus normally, a large number N_{shuf} should be performed. Within this report, $N_{shuf} = 100$, but the more general constraint is that $1 \leq N_{shuf} \leq n!$. P_T is calculated for the original map ($P_T(true)$), and for all of the shuffled versions individually. Subtracting the normalised value from 1 means that 1 represents perfect order, while 0 indicates an absence of order.

$$\text{normalised } P_T = 1 - \frac{P_T(true)}{\frac{1}{N_{shuf}} \left(\sum_{shuf=1}^{N_{shuf}} P_T(shuf) \right)} \qquad (2.5)$$

The **euclidean distance correlation** uses the Pearson correlation coefficient between $d^V(i,j)$ and $d^T(i,j)$ in both spaces:

$$C_{EC} = \frac{\sum_{i=2}^{n} \sum_{j=1}^{i-1} \left(d^V(i,j) - \bar{d}^V \right) \left(d^T(i,j) - \bar{d}^T \right)}{\sqrt{\sum_{i=2}^{n} \sum_{j=1}^{i-1} \left(d^V(i,j) - \bar{d}^V \right)^2 \sum_{i=2}^{n} \sum_{j=1}^{i-1} \left(d^T(i,j) - \bar{d}^T \right)^2}} \qquad (2.6)$$

The **topological correlation** C_{TC} [180] uses Delaunay triangulations [181] of the points in V and T. The distances used in the euclidean correlation are then replaced by geodesic distances: $g^V(i,j)$ is the minimum number of edges between i and j in the Delaunay triangulation of V. C_{TC} is then the pearson correlation coefficient of $g^V(i,j)$ and $g^T(i,j)$ for all i,j:

$$C_{TC} = \frac{\sum_{i=2}^{n} \sum_{j=1}^{i-1} \left(g^V(i,j) - \bar{g}^V \right) \left(g^T(i,j) - \bar{g}^T \right)}{\sqrt{\sum_{i=2}^{n} \sum_{j=1}^{i-1} \left(g^V(i,j) - \bar{g}^V \right)^2 \sum_{i=2}^{n} \sum_{j=1}^{i-1} \left(g^T(i,j) - \bar{g}^T \right)^2}} \qquad (2.7)$$

Both of these metrics are theoretically bounded between 1 and -1. However, it seems extremely unlikely that a value much lower than 0 could ever emerge: 0

represents the absence of any order at all, and it is difficult to envisage a scenario in which the pairwise distances are anti-correlated.

The **scaled cosine similarity**, developed by Dr Andrew Lowe, is a rather more involved process. First, T is transformed into a new space U via a series of affine and non-affine transformations, in such a way as to minimise the distances between each point j in U and V, and also minimise the difference in their areas. Then, pairwise comparisons between all point-to-point vectors are used to calculate a statistic c representing the similarity of these aligned maps. With $\alpha(i,j)$ referring to the angle between the vectors ij in V and ij in U, $c(i,j)$ is calculated as follows:

$$c_s(i,j) = \min\left(\frac{d^V(i,j)}{d^U(i,j)}, \frac{d^U(i,j)}{d^V(i,j)}\right) \cos \alpha(i,j) \tag{2.8}$$

c_s is a measure of similarity between each point-to-point vectors in V and U: there will be $n(n-1)$ c values. It is bounded between 1 and -1 due to the properties of the cosine curve, and the minimisation of the ratio of distances. A histogram of the density of $c_s(i,j)$ for all i,j over this interval can be created, and the distribution can be usually approximated by a pair of half gaussians. The final value S is the peak of this distribution, and is bounded between 1 (representing order) and -1. If the fitted curve does not meet the criteria that $R^2 > 0.8$, S is undefined.

For the **multisubject metrics**, let there be N subjects s, each containing n_s points.

P_{Ts} represents a mean-of-means for single subject calculations:

$$P_{Ts} = \frac{1}{N} \sum_{s=1}^{N} \left(\frac{1}{n_s(n_s-1)} \sum_{j=1}^{n_s} \sum_{k=1}^{n_s-1} |\ln P_3(j,k,s)| \right) \tag{2.9}$$

P_{Tdist} is also a mean of means, but in which P_3 values calculated in the individual subjects (see **eq. (2.3)**) are pooled according to distance. For N_d linearly spaced distance bins in space T, $P_T dist$ is the mean of means according to *d*istance. n_d is the number of P_3 values placed in the bin d, so the point identifiers j and k are here replaced by a vector identifier l. For the purposes of this report, $N_d = 25$.

$$P_{Tdist} = \frac{1}{N_d} \sum_{d=1}^{N_d} \left(\frac{1}{n_d} \sum_{l=1}^{n_d} |\ln P_3(l)| \right) \tag{2.10}$$

Normalised versions of P_{Ts} and P_{Tdist} are calculated analogously to normalised P_T. Random point reassignment is performed within each subject, meaning that constraints on the number of shuffles performed are: $1 \leq N_{shuf} \leq \prod_{s=1}^{N} (n_s (n_s - 1))$. Although P_{Tdist} and it's normalised equivalent were were developed for use in multiple-subject context, in **figs. 2.3 and 2.4**, $N = 1$.

Using the following definition of mean distances,

$$\bar{d^V} = \frac{\sum_{s=1}^{N} \sum_{i=2}^{n_s} \sum_{j=1}^{i-1} \left(d^V (i,j,s) \right)}{\sum_{s=1}^{N} (n_s)} \tag{2.11}$$

and corresponding definitions for the other space and distance measure, multisubject correlations are defined as follows:

$$C_{EC} = \frac{\sum_{s=1}^{N} \sum_{i=2}^{n_s} \sum_{j=1}^{i-1} \left(d^V (i,j,s) - \bar{d^V} \right) \left(d^T (i,j,s) - \bar{d^T} \right)}{\sqrt{\sum_{s=1}^{N} \sum_{i=2}^{n_s} \sum_{j=1}^{i-1} \left(d^V (i,j,s) - \bar{d^V} \right)^2 \sum_{s=1}^{N} \sum_{i=2}^{n_s} \sum_{j=1}^{i-1} \left(d^T (i,j,s) - \bar{d^T} \right)^2}} \tag{2.12}$$

$$C_{TC} = \frac{\sum_{s=1}^{N} \sum_{i=2}^{n_s} \sum_{j=1}^{i-1} \left(g^V (i,j,s) - \bar{g^V} \right) \left(g^T (i,j,s) - \bar{g^T} \right)}{\sqrt{\sum_{s=1}^{N} \sum_{i=2}^{n_s} \sum_{j=1}^{i-1} \left(g^V (i,j,s) - \bar{g^V} \right)^2 \sum_{s=1}^{N} \sum_{i=2}^{n_s} \sum_{j=1}^{i-1} \left(g^T (i,j,s) - \bar{g^T} \right)^2}} \tag{2.13}$$

All modelling and analysis was performed using custom MATLAB scripts, developed by the author. All modelling was carried out using the Neuroimaging Analysis Network servers, at the Institute of Psychiatry, Psychology and Neuroscience `https://mri.iop.kcl.ac.uk/index.php/NaN_Servers`.

2.2.2 Modelling of map curvature

In order to simulate map curvature, a transformation was created to emulate the curvature of the tectum, creating "curvy" maps. Based on data from the thesis of Aenea Hendry [52], a bilinear quadratic transform was derived by Dr Andrew Lowe,

mapping points (x, y) in space V to (x', y') in space T as follows:

$$x' = -0.0212\,y^2 + 0.8157\,y + 0.2105 + x \qquad (2.14)$$

$$y' = -0.003x^2 - 0.0448x + 3.6028 + y \qquad (2.15)$$

2.2.3   Calculation of redundancy, coefficient of variation, power and results at redundancy

Single subjects:

For these purposes, maps were generated by selecting random points in a $100 \times 100\mu m$ space. n, the number of points in the maps, was stepped between 10 and 1500 in increments of 10. The area of the convex hull in the "tectal" maps were used to determine the point density. There were 40 maps modelled at each value of n, for a total of 6000 metric values for each metric, at each noise level. "Tectal" space was modelled either by applying gaussian noise (in straight maps), or by applying a number of affine transformations and a bilinear quadratic transform, followed by gaussian noise (in curvy maps).

In order to obtain the redundant density, a sliding-window coefficient of variation (CoV), with a density window of width 0.004 and step size 0.001 was calculated. A curve of the form $CoV = k/d + c$ was fitted via a nonlinear least-squares approach, with d representing the density of points in the tectal space, and constants k and c. The density at which redundancy was reached, R, was found symbolically:

$$\frac{1}{\sqrt{2}} = \frac{\frac{k}{2R} + c}{\frac{k}{R} + c} \qquad (2.16)$$

Which rearranges to:

$$R = \frac{(2 - \sqrt{2})k}{(2\sqrt{2} - 2)c} \qquad (2.17)$$

Statistical power at redundancy was calculated as an arbitrary value of the power of a metric to detect a 10% change in it's value at the redundant density. This is found as follows, with CoV_R representing the coefficient of variation at the redundant density:

$$\text{power} = \frac{0.1}{CoV_R \sqrt{R}} \tag{2.18}$$

Multiple subjects:

Data were modelled, varying both point density and N, in both straight and curvy maps. A 2D sliding window was used to calculate local coefficients of variation. A surface was then fitted to them, of the following form:

$$CoV_{(d,N)} = \frac{k}{d} + \frac{l}{N} + \frac{m}{dN} + c \tag{2.19}$$

For given d, there is a value N_R for which:

$$\frac{1}{\sqrt{(2)}} = \frac{CoV_{(d,2N_R)}}{CoV_{(d,N_R)}} \tag{2.20}$$

Which, substituting in the full equation for the surface, rearranges to:

$$N_R = \frac{m + l d}{\sqrt{2}\,(k + cd)} \tag{2.21}$$

Statistical power is then calculated as in **eq. (2.18)**.

Modelling of multisubject datasets, for assessing resistance to jitter

Multisubject map pairs were created by taking topographic maps of DS RGC axon terminals in the zebrafish tectum from the thesis of Aenea Hendry, and projecting the visual receptive field centres of direction-selective voxels into an imaginary tectal space using a bilinear quadratic transform, before applying gaussian intra-subject noise and inter-subject jitter. Thus, while N was fixed at 28 (the number of fish imaged), n was variable (between 5 and 65). For P_{Tdist},

distances used for pooling of P_3 values were measured in "tectal" space. Each pixel in the heatmaps **fig. 2.2B-D** represents one such daraset.

Detection of significant topographic order

For any given metric, testing the null hypothesis that no topographic order involves comparing the value of a metric with its value calculated from many (N_{shuf}) shuffled versions of the map, in which point correspondences are randomly permuted. The probability that the map exhibits order (i.e. reject the null hypothesis) is calculated from the number of metric values from shuffled maps that exceed the true metric value (N_{better}), adjusted as follows:

$$p = \frac{N_{better} + 1}{N_{shuf} + 1} \qquad (2.22)$$

In the multiple-subject context, random point reassignment is performed within each subject, meaning that constraints on the number of shuffles performed are: $1 \leq N_{shuf} \leq \prod_{s=1}^{N} (n_s (n_s - 1))$.

Determination of N_{80}

N_{80}, defined here as the number of subjects required to detect order in 80% of datasets **fig. 2.8**, was found as follows:

100 multiple-subject curvy maps were created, with N subjects, and drawing the number of points in each individual subject from a Rayleigh distribution, with mean $\bar{n}$. For each value of $\bar{n}$, N was initially set at 20. The percentage of maps that were significantly ordered, F, was determined using **eq. (2.22)**. This procedure was repeated while adjusting N according to bisection search, to find the N for which $F = 80$.

This approach is inherently noisy. Thus, after convergence of bisection search to an integer value, a curve of the form $F = a - be^{-cN}$ was fitted in the least squares sense. The N_{80} is then $-c \ln \frac{(a-80)}{b}$.

Framework for assessing noise in biological units

In order to calculate the amount of noise present in distance units, $d^V(i,j)$ and $d^T(i,j)$ are calculated for all i,j. These are then normalised separately to have zero-mean and unit variance, and a best-fit line minimising orthogonal residuals found using PCA. If topographic order is present, the first principle component will represent the combined map distance, and the second the residuals.

θ represents the arctangent gradient of the best-fit line derived from PCA, after undoing normalisation, while $r(i,j)$ represents the length of an orthogonal residual of this line. For a given dataset, there will be the same number of r values as the number of point-to-point distances incorporated i.e. $n(n-1)$ in single subjects, or, for multiple subjects, $\sum_1^{s=N} n_s(n_s-1)$.

These residuals can be projected into either one of the spaces, or can be expressed as a nonlinear combination of the two, as shown in **fig. 2.11D**. The residuals projected into a combination of either space can be expressed as a function of the angle ϕ, where $0 \leq \phi \leq \frac{\pi}{2}$, where $\phi = 0$ represents projection only into V, and $\phi = \frac{\pi}{2}$ represents projection only into T.

$$r_V = \frac{r \cos\theta \sin\theta \cos\phi}{\sin(\pi - \theta - \phi)} \tag{2.23}$$

$$r_T = \frac{r \cos\theta \sin\theta \sin\phi}{\sin(\pi - \theta - \phi)} \tag{2.24}$$

Gaussian curves are then fitted to these r, allowing the calculation of noise levels in biological units.

2.3 Results

A number of metrics were selected as potentially useful, for varying reasons. The topographic product P_T [177] (**eqs. (2.1) to (2.5)**) has been previously explored in the author's MRes. It has its roots in graph theory, and is based on comparisons of equally-ranked distances between points in both maps. A novel normalisation, utilising multiple versions of the map in which point correspondences are randomly reassigned, was found to improve the metric's resistance to changes in map shape (see **Appendix B**). The euclidean distance correlation [182] (**eq. (2.6)**) and topological correlation [180] (**eq. (2.7)**) are examples of correlation-based metrics. These are based on the calculation of pairwise point-to-point distance measures in both maps, and an estimation of a correlation coefficient that represents how closely these matched distances correspond [178]. Various metrics differ in their method for calculating point-to-point distances, or how they calculate the correlation coefficient. The two metrics chosen, the euclidean distance correlation and the topological correlation, are widely used in the literature [176, 178], and were found to have relatively high statistical power to detect topography [179]. The scaled cosine similarity has been developed by the author's supervisor (Dr Lowe). It requires a pre-processing step in which one map is aligned to the other using a series of transformations. It then examines the angle between matched point-to-point vectors in each map, scaled by the minimum ratio of vector magnitudes (see **eq. (2.8)**). It was chosen as it assesses the angular displacements within the maps rather than absolute distances. The metrics are all bounded between 1 (perfect order) and 0 (complete disorder). While the lattice method [90] was a tempting choice, it was not included as a formulation allowing pooling across multiple subjects could not be easily formulated.

In-silico retinotectal maps were generated to examine metrics for topographic order. Each map consisted of matched-pair points in a "visual" and a "tectal" space. Although a complete exploration of the effects of global map distortion on metrics would be advantageous, it is impossible due to the unbounded space of possible transformations that could be applied. Two types of maps have been used for this study: straight maps, defined here as maps in which no curvature or other global distortion is applied (**fig. 2.1A**), and curvy maps, in which the curvature of the tectal map mimicks that found in real tecta (**fig. 2.1B-C, section 2.2.2**). The dimensions and shape of these curvy maps are based on summaries of those

derived experimentally by Dr Hendry [52]. Varying amounts of Gaussian noise were applied to the points in tectal space to simulate map disorder, although the exact structure underlying disorder in biological topographic maps is unknown.
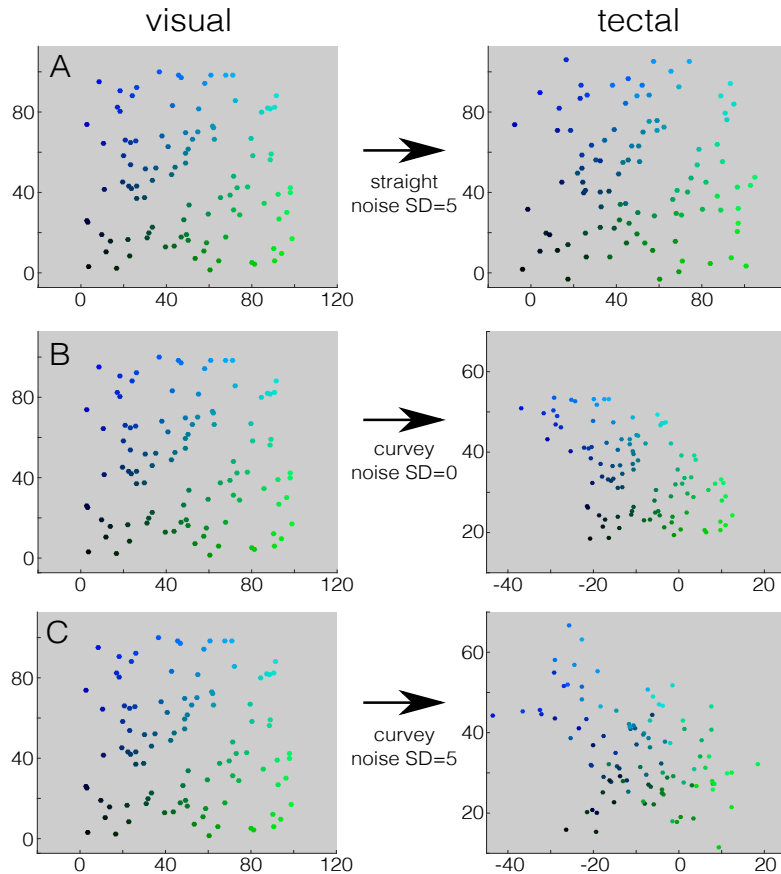
Figure 2.1: **Example map pairs, representing visual space and various tectal spaces**. Like-coloured points indicate matched pairs between spaces. Points in visual space were generated according to a 2D uniform distribution within a 100-by-100 space. **A** is a a straight map with gaussian noise (SD = 5) added. **B** shows a curvy map, in which a bilinear quadratic transformation is applied to the visual space (see **section 2.2.2** for details). **C** is a curvy map which additionally has noise (SD = 5) added.

2.3.1 Metrics must be reformulated for use in multi-subject datasets incorporating jitter

In a real experimental setting, it is not always possible to derive complete topographic maps from each individual experimental subject. A potential solution to this issue is to acquire partial maps from many individuals and pool them

via standardised spaces [175]. However, due to experimental artefacts, or real biological variability, there is a possibility of inter-subject variance in map position (see **fig. 2.2A**), henceforth referred to as jitter.

In order to assess the resistance of a metric to jitter, modelled multisubject datasets were created based on the visual receptive field centres of DS RGC axon terminals [52]: the locations of DS RGC receptive field centres from a multisubject dataset ($N = 28$, $5 \leq n \leq 65$) were used, and transformed into a tectal space prior to the addition of both noise and jitter. Jitter was applied by displacement of all tectal points in each individual subject according to an amount chosen from a 2D gaussian with defined SD. The pooling of multisubject datasets in presence of jitter leads to under-estimations of order due the additive effect of intra- and inter-subject noise (**fig. 2.2B**).

It is however possible to formulate alternative pooling strategies by pooling statistics derived from each subject's individual map for calculation of the final summary statistic, rather than pooling points. One approach would be to analyse each subject separately, and to combine these into a summary statistic. An example is P_{Ts}, a mean-of-means by subject (**eq. (2.9)**). Note that when there is only one experimental subject (as in **figs. 2.3 and 2.4**), this is identical to P_T. Given the formulation of P_T, in which a statistic $P3$ is determined pairwise for each combination of points (**eq. (2.3)**), another alternative presents itself: $P3$ values are calculated for each subject individually and then these intermediate statistics are pooled across subjects to produce a final summary statistic P_{Tdist}, a mean-of-means according to binned distance between points (**eq. (2.10)**). Both approaches have been piloted: both normalised P_{Ts} and normalised P_{Tdist} circumvent problems with jitter, as there is no association between the level of jitter applied and the metric value (**fig. 2.2C,D**). However, normalised P_{Tdist} produces much less variability in the metric values for comparable datasets (**fig. 2.2E**).

Metrics other than the topographic product can also be utilised in this way. For the euclidean and topological correlations, this corresponds to determining pairwise distances within maps, but determining the correlation coefficients of these distances, once pooled, across maps (see **eqs. (2.12) and (2.13)**). For the scaled cosine similarity, the alignment of the two maps must be performed on pooled data; however, the pairwise values c_s (see **eq. (2.8)**) are calculated only between point pairs within the same subject.
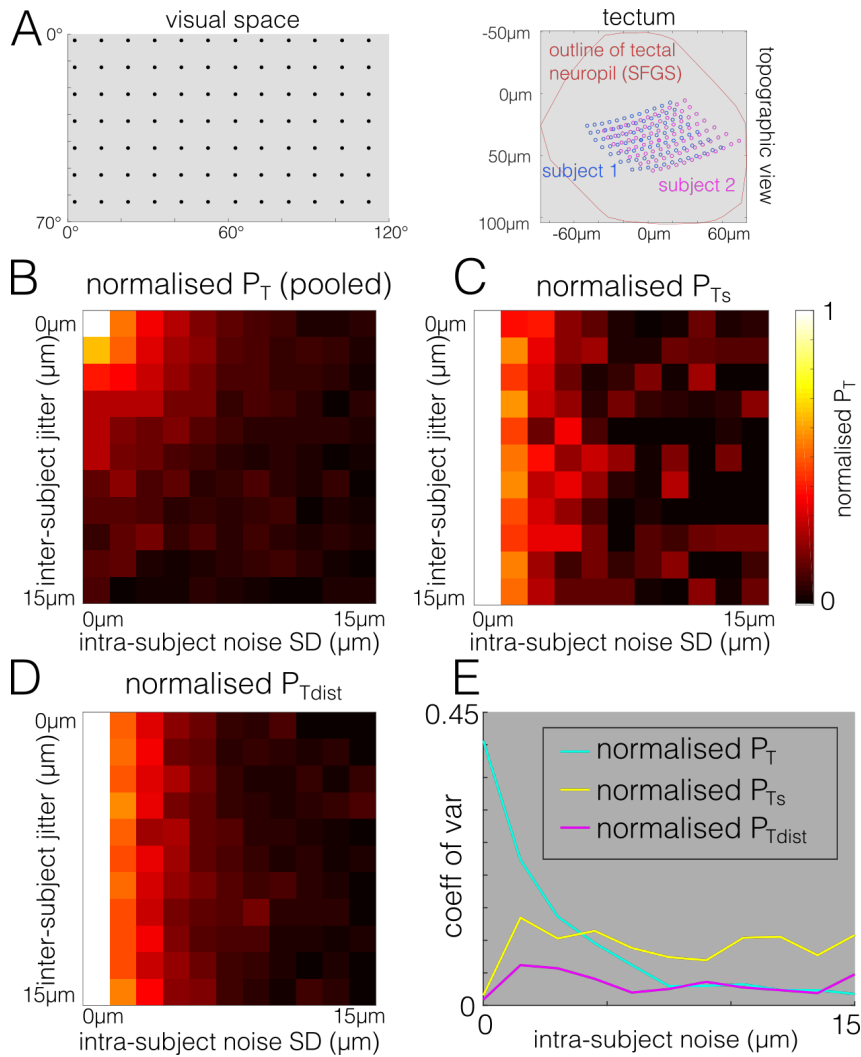
Figure 2.2: **Example modification of metrics for use in multisubject datasets incorporating jitter. A.** Illustration of inter-subject variance in topographic map position - jitter. **B.** Normalised P_T for varying degrees of intra- and inter-subject added disorder. Color scale as in C. **C-D.** Two alternative formulations, P_{Ts} and P_{Tdist}. All normalisations calculated using 100 shuffled versions of maps. **E.** Estimated metric coefficient of variance collapsed across the range of applied inter-subject jitter. Each heatmap pixel represent a single modelled multisubject dataset, N=28 subjects, and $5 \leq n \leq 65$ within each subject.

2.3.2 Redundancy and statistical power in the single-subject context

In general, increasing the sample size of a dataset improves the reliability of any summary statistic, although there is a decreasing return with ever larger sample sizes. There is a point when acquiring more data becomes redundant, with a diminishing return on the metric's reliability. An examination of such a point would reveal how much data each metric requires to reach a given improvement in its reliable estimate of order. This so called redundancy density has been defined here as the density at which doubling the density of points (representing the sampling rate within a single experimental subject) reduces the coefficient of variation of the metric values by a factor of $\leq \sqrt{2}$. The values of the chosen metrics were determined for many maps with varying point density and applied disorder. Although novel datasets were generated for each metric, these used the same underlying parameters (i.e. point densities, number of subjects and noise level.**Figure 2.3A** shows an example of how the variance of the values of a metric (in this case, the euclidean distance correlation) decreases with increasing density of points within the maps at constant noise. Deriving a moving CoV (**fig. 2.3B**), one can more clearly define the relationship as of the form $CoV = k/d + c$, where d is the density of points, and k and c are constants. This fitted curve enables the redundant density to be determined for each metric (**eqs. (2.16) and (2.17)**), with different levels of noise (**fig. 2.3C**).

The scaled cosine similarity has the lowest redundant densities, but this does not necessarily indicate that it produces reliable results with very little data - it could in fact indicate that increases in the amount of data fail to improve highly variable results. Normalised P_T and $P_{T\,dist}$ exhibit an expected relationship between the noise level and redundant densities: more data are required to effectively quantify a higher level of noise. In contrast, the euclidean and topological correlations have redundant densities that appear to be unrelated with the noise level. This suggests that regardless of the level of noise being quantified, for these correlation-based metrics there is a constant amount of data that will provide the optimally consistent quantification of that noise.

The modelled maps allow an estimation of the relative statistical power to detect a 10% change in metric value (**eq. (2.18)**). This is equivalent to comparing the confidence that two maps have different levels of noise, if their metric values differ by 10%. Relative power curves are directly comparable between metrics, and when
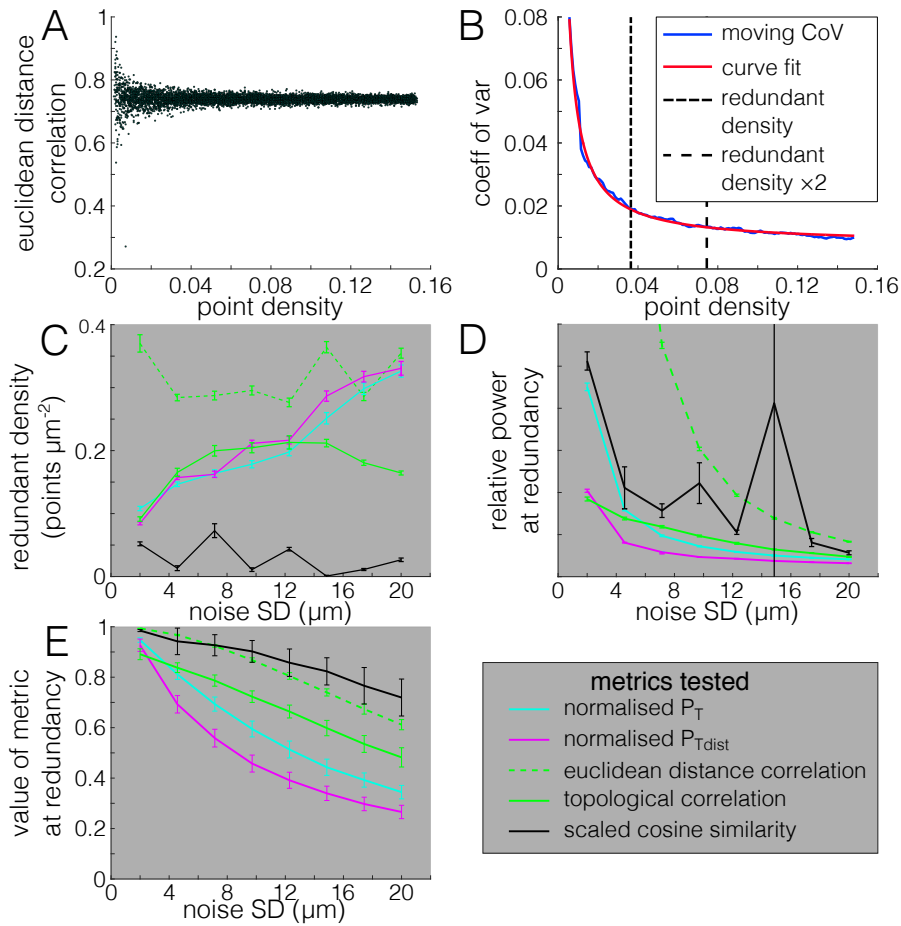
Figure 2.3: **Statistical power of metrics for topography in straight maps**. **A.** Example dataset. Topographic maps are generated with a given level of added disorder and varying density of points enable evaluation of metric (such as the euclidean distance correlation shown here). This highlights decreasing variance with increasing point density. **B.** A sliding window estimate of the coefficient of variance of (A) across varying point densities, with width 0.008. Fitted curve is of the form $CoV = k/d + c$. For this example, $R^2 = 0.988$. **C.** Estimated redundant densities, evaluated for different levels of topographic disorder. **D.** Statistical power to detect a 10% change in metric value, at the redundant density. **E.** Values of the metrics at their redundant density. All plots are mean ±SD.

evaluated at the redundant density, is an estimate of the The inverse relationship between statistical power and applied noise across all metrics tested suggests that the more topographic disorder is present, the less reliably different levels of disorder can be discriminated (**fig. 2.3D**). Normalised P_T and P_{Tdist} have very sharp declines from low to high noise levels, while the topological correlation has a less sharp decline, meaning that for the higher noise levels the topological correlation outperforms the P_T-based metrics. However, the euclidean distance correlation clearly has the highest power to detect changes in noise level across the board. The erratic curve for relative statistical power resulting from the scaled cosine similarity is likely a result of the extremely low redundancy values, leading to unstable results in power calculations as the redundant density is used as a denominator.

In addition to the statistical power of metrics to discern differences in topographic order, it is also important to understand the shape of the relationship between noise levels and metric values. This allows comparisons of metric dynamic ranges. These have been examined at the redundant density for each noise level and metric (**fig. 2.3E**). The topological and euclidean correlations appear to vary approximately linearly across the noise levels tested. In contrast, normalised P_T and P_{Tdist} have a more limited dynamic range, and begin to flatten out at the higher noise levels tested. This potentially makes them less useful than the correlation-based metrics, as if maps are highly-disordered, they are less able to discriminate between different levels of order (borne out additionally by their lower statistical power).

To understand how metrics behave for the complete topographic maps found in vivo, models must incorporate global shape distortions, including shearing and nonlinearities ("curvy" maps, **fig. 2.1B,C**). When redundancy calculations are repeated in curvy maps (**fig. 2.4A**), the redundant density is much higher for all metrics than in the straight maps (compare **fig. 2.3C** with **fig. 2.4A**). This indicates that more data is required to optimally define levels of topographic disorder in situation where maps are distorted - metric values are inherently more unstable in situations of map curvature. Counterintuitively, the redundant density for the scaled cosine similarity goes down with increasing noise, suggesting the metric is failing. the low redundant densities in **fig. 2.4A** are as a result of inherently variable metric values rather than reliable values with small amounts of data. It is potentially due to issues with map alignment.

In terms of the statistical power of metric at redundancy in curvy maps, (**fig. 2.4B**),
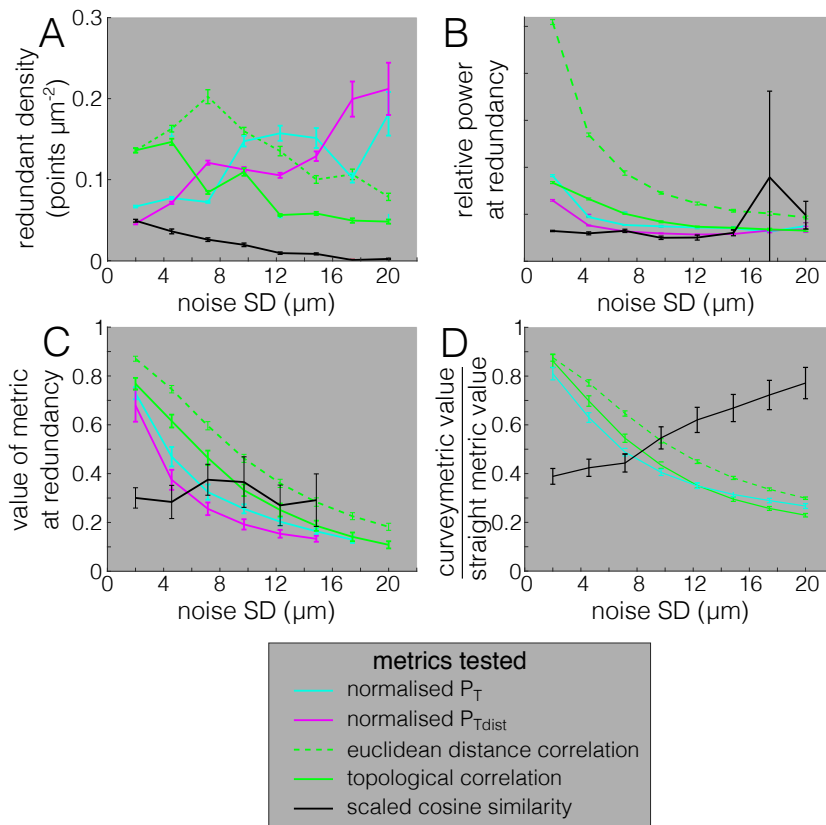
Figure 2.4: **Assessment of metric statistical power in modelled maps mimicking tectal curvature. A.** The density of points at which redundancy is reached for different metrics. **B.** The relative statistical power of these metrics to detect a 10% change in value, at their redundant density. **C-D** Values of the metrics at their redundant density. All plots are mean ±SD. **D** Ratio of curvy result and straight result at the same density (~0.1)

the euclidean distance correlation seems to perform the best, while the scaled cosine similarity performs the worst. This is likely to be due to the problems with the map alignment step of the metric calculation failing to cope well with distortions of map shape: it may also be associated with the surprisingly low redundant densities. The relative power for normalised P_T and P_{Tdist}, and the correlation metrics echo those in the straight maps, and have similar shapes, although the topological correlation seems do better relative to the normalised P_T metrics in presence of map curvature. The scaled cosine similarity has, by a small margin, the lowest relative power.

Plots of the metric values at redundancy (**fig. 2.4C**) show that the euclidean distance correlation and topological correlation seem to have the widest dynamic range. The scaled cosine similarity gives low and very variable results that are not affected by the applied noise level. This is consistent with the interpretation that the low redundant densities in **fig. 2.4A** are as a result of inherently variable metric values rather than reliable values with small amounts of data. It is potentially due to issues with map alignment.

In order to examine how the value of the metric is affected by curvature in the map, the ratio of metric values for curvy and straight maps was examined (**fig. 2.4D**). In presence of map curvature, the metrics all indicate lower levels of order (as the ratios shown are all below 1). This indicates that for all of the metrics tested, the ability of the metrics to reveal true order in presence of global distortion is impaired. The reason that the ratio of metric values for the scaled cosine similarity increases with noise is that the metric value does not appear to decrease with noise in curvy maps (**fig. 2.4C**) - that is, the metric is no longer detecting changes in noise. For the other metrics, the ratio decreases with noise, meaning that an increased noise in these curvy maps has a proportionally bigger effect on detected map disorder than in the straight maps. Although the resulting ratios are very close between metrics (except for the scaled cosine similarity), the euclidean distance correlation is least affected by map curvature as the ratios of metric values in curvy and straight maps are the closest to 1, across all noise levels tested.

2.3.3   Redundancy and statistical power in the multisubject context

In a real experimental setting, the possibility of jitter cannot be excluded [175], and removing it is extremely difficult. Thus, only metric formulations which are invariant to jitter were examined further. Invariance to jitter comes from using only point-to-point distances/vectors between points within each subjects, and pooling summary statistics across the multiple subjects used (see **fig. 2.2**). Using only metrics invariant to jitter means that jitter does not need to be included in model data.

In order to explore the concepts of redundancy and statistical power in a multisubject context, curvy model datasets were generated while varying both the within-subject point $d$ensity, and the Number of subjects. The range of densities measured were chosen to include the redundant densities found previously (**fig. 2.4**). Metrics were evaluated for these datasets, allowing the calculation of a 2D-sliding-window CoV. A surface was then fitted to these values (see **eq. (2.19)**).

The redundant number of subjects, N_R, is here defined as, for given d, the N at which doubling N reduces the coefficient of variation of the metric values by a factor of $< \sqrt{2}$, analogously to in the single-subject context (**eqs. (2.20) and (2.21)**). For simplicity, this is not constrained to integer values. In all datasets, the R^2 value for the surface fits to the scaled cosine similarity were < 0.5, meaning that N_R and relative statistical power could not be calculated.

In terms of N_R , a main feature is that for all noise levels tested in curvy maps, statistical redundancy is found below $N = 30$ for all metrics, densities and noise levels (**fig. 2.5**). This gives an upper limit for how many experimental animals are required to produce optimal comparisons between topographic maps. A surprising feature is that, apart from normalised P_{Tdist}, N_R does not appear to be related to noise level in the same way as the single-subject redundant density. For these multiple subject metrics, increasing the number of sample points per subject has far more impact on the accuracy of map order quantification than does the number of experimental subjects.

It appears that N_R is positively correlated with the single-subject point density with all metrics except, possibly, the euclidean distance correlation, meaning that the more subjects are required to reach redundancy when there is more data per subject. This seems counterintuitive until the relative statistical power is considered:
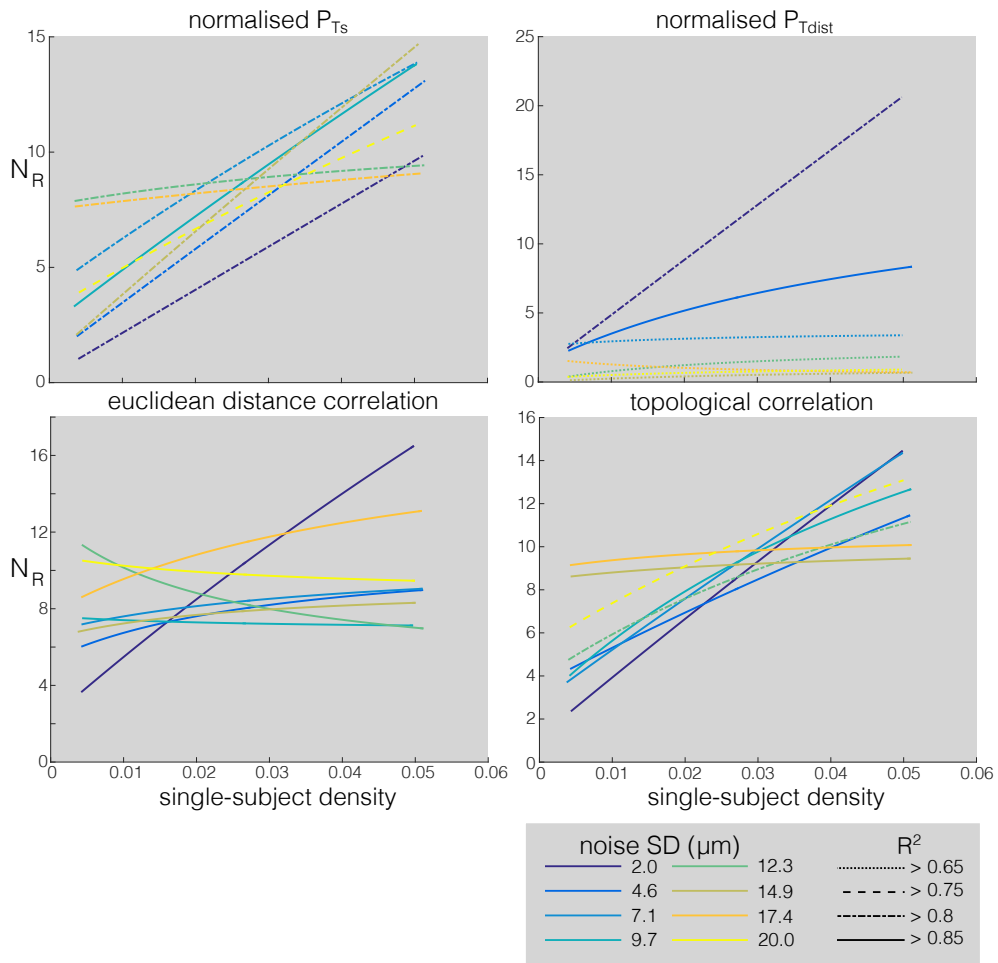
Figure 2.5: **N_R derived from surface fits to local coefficient of variation as a function of d and N.** Multisubject datasets per surface fit = 2475, $1 \leq N \leq 50$ per dataset. Line colours indicate applied noise level, while pattern indicates goodness-of-fit of the surface used to derive it.

with more data per subject, statistical power at redundancy is higher. This implies that N_R is limiting for statistical power rather than providing an optimum tradeoff point. When looking at the results for both redundancy and statistical power together, it appears that metrics/noise levels with a higher N_R also appear to have a higher statistical power at that N. This effect means that redundancy should be thought of as the point at which there is no point adding more data - but not that a low value indicates increased utility.

All metrics give a higher statistical power for lower noise levels, which is expected from previous results. The best statistical power is achieved by the euclidean distance correlation, followed by the topological correlation (**fig. 2.6**), while normalised P_{Ts} appears to have greater power than P_{Tdist} - consistent with the single-subject results. Additionally, the available statistical power is increased by a greater amount of data per subject, which is to be expected.

Examining the metric values as a function of the noise applied to the maps, it is clear that the metric giving the most linear relationship between applied noise and metric value is the euclidean distance correlation, followed closely by the topological correlation. **Figure 2.7B** examines how the gradient of the metric value varies with the value of the metric itself in the multisubject context. This means that for any given metric value, the plot shows the change in the metric value that would result from a noise level increased by 1. The greatest dynamic range is given by the euclidean distance correlation.

2.3.4 Detecting order in the multisubject context

Results so far have focussed on quantifying different levels of topographic order between maps, in order to precisely resolve different levels of order/disorder. However, they tell us little about the power for detecting whether topographic order is present at all. This is particularly important in cases where maps are comparatively disordered. Although the utility of metrics for order detection has been adequately covered in the single-subject context [179], no such work has been performed before for multiple-subject metrics.

A map is defined as ordered if it's true metric value indicates a higher level of order than "shuffled" versions in which point correspondences between spaces have been randomly permuted. Many of these shuffled maps are used to calculate a
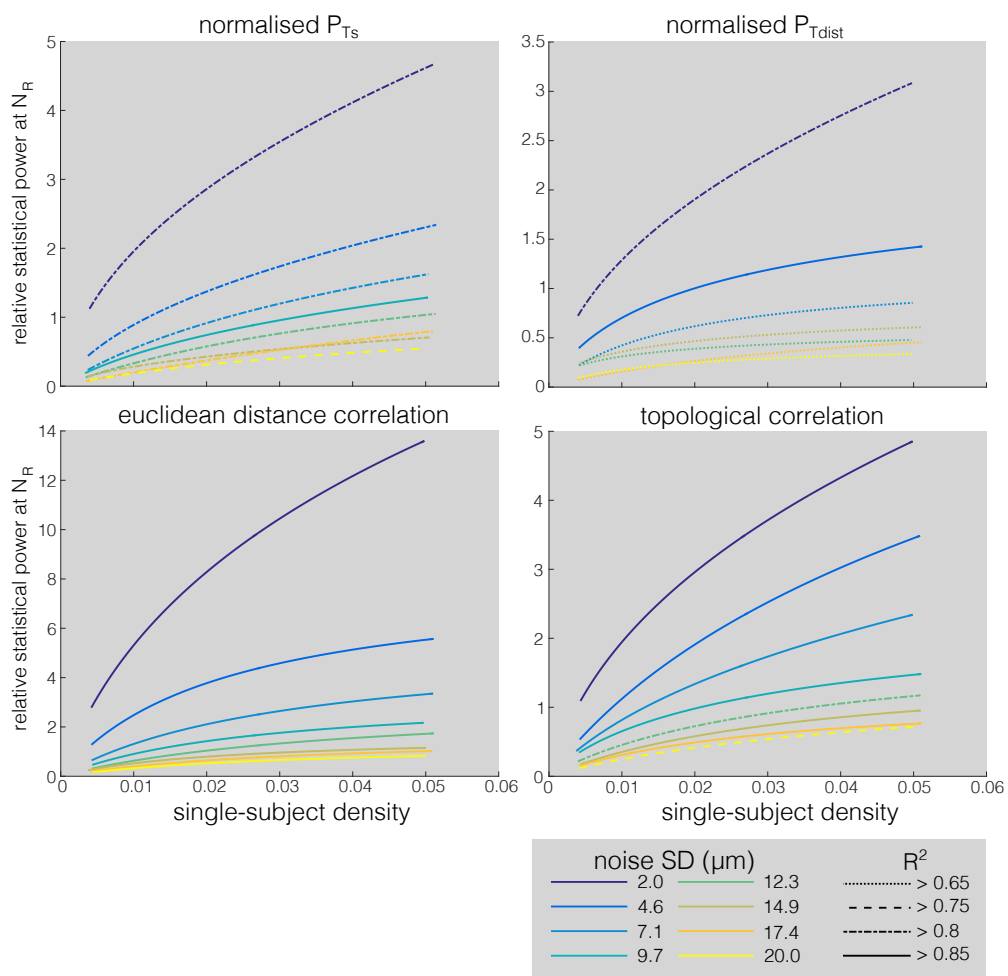
Figure 2.6: **Statistical power for discrimination of map disorder discrimination, evaluated at N_R (see fig. 2.5).** Line colours indicate applied noise level, while pattern indicates goodness-of-fit of the surface used to derive it.
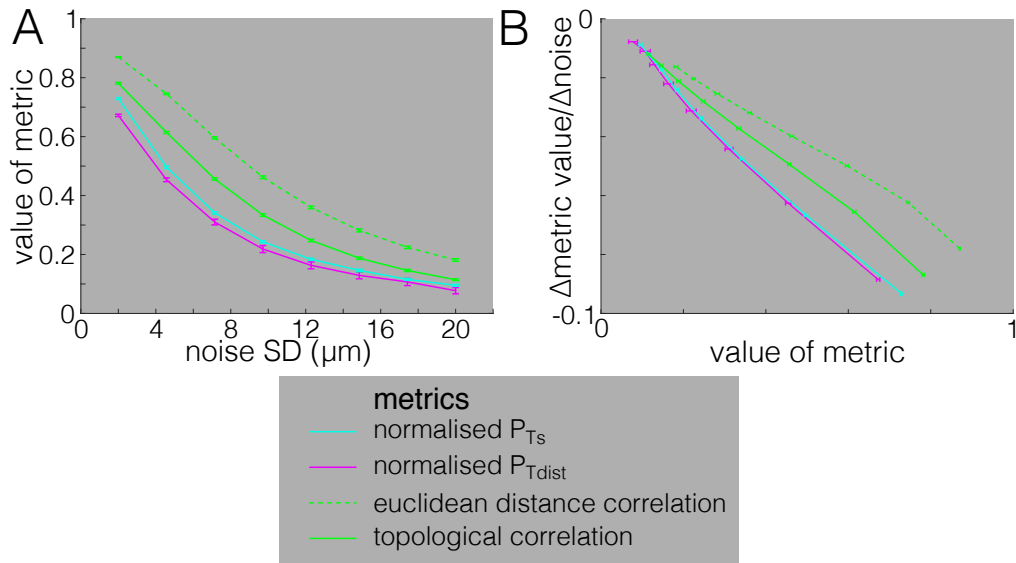
Figure 2.7: **A graph of the metric value as a function of applied noise** at $0.04 \leq d \leq 0.05$, $N = 32$. Error bars calculated from the coefficient of variation surfaces. **B** Plot of metric value against gradient of **A**.

p-value for whether the observed order is greater than that expected by chance, given the distributions of point locations in both spaces (**eq. (2.22)**, [179].

Here, I present an assessment of metrics power to detect order in multiple-subject datasets. This can be achieved by looking at how N_{80}, meaning the number of subjects required for detection of statistically significant topographic order in 80% of datasets [179], varies as a function of the mean n in each subject with constant noise levels. Maps are defined as ordered when the probability that the observed level of order would be observed by chance, given distributions of constituent points, is ≤ 0.05 (see **eq. (2.22)**).

As expected, the number of subjects required for reliable detection of order was inversely correlated with the number of points in each subject (**fig. 2.8**). The metric which reliably detects topographic order with the smallest amount of data is the euclidean distance correlation, closely followed by the topological correlation, followed by normalised P_{Tdist}, and finally P_{Ts}. Using different values of noise gave similar results with respect to ordering of metrics (data not shown).
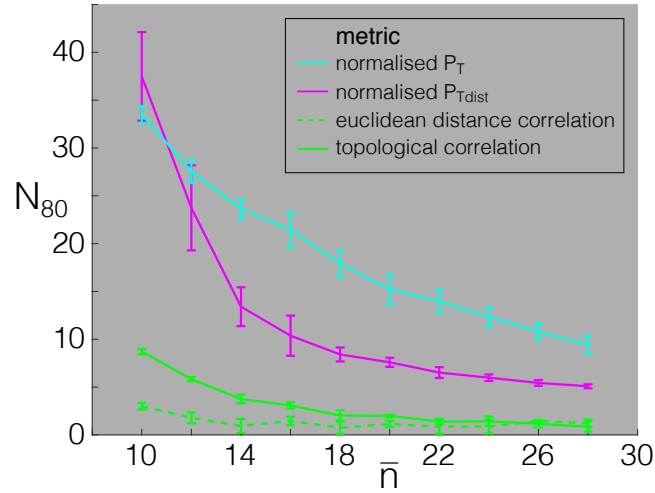
Figure 2.8: **Evaluation of power to detect topographic order for multisubject metrics in curvy maps.** In order to ensure a realistic distribution of n, individual subject ns were drawn from a Rayleigh distribution with defined mean ($\bar{n}$). For each dataset (i.e. a multiple-subject map pair), significant order was said to be detected if $p \leq 0.05$, as determined by eq. (2.22). N_{80} for each $\bar{n}$ was found using bisection search followed by an exponential decay curve fit, starting with $N = 20$, see **section 2.2.3** for further details. All R^2 for curve fits ≥ 0.9. Data shown are mean $\pm$ SD from 5 such fits (all $R^2 > 0.9$ for curve fits). The noise SD used, 18 μm, was selected as being within the dynamic ranges of all metrics tested.
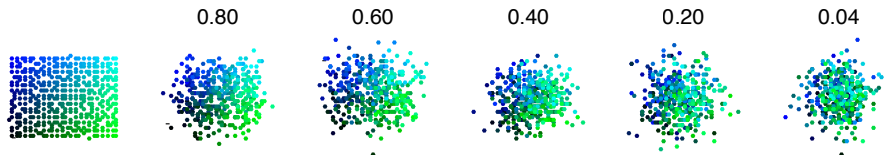
Figure 2.9: Example maps. **Left:** "Visual" map **Right:** Different "tectal" maps, with R^2 values measured by the euclidean distance correlation shown above them.

74

2.3.5   Summary: Euclidean distance correlation is the best metric

One of the problems with the scaled cosine similarity is that it often fails to produce a finite value due to a failure in the map alignment step, particularly in curvy maps.   It should be noted that this failure rate means that for any given experimental dataset, the metric could either be unusable, or require manual curation, rendering comparisons between maps difficult if not impossible. Additionally, it did not function well within the statistical framework used here, particularly in the multisubject context, making it difficult to evaluate critically.

Overall, in the single subject context, the euclidean distance correlation has the highest statistical power at low noise levels, and outperforms the topological correlation and normalised P_T and P_{Tdist}. It additionally has the widest dynamic range.   In the multisubject context, interpretation is more complicated due to the extra dimensionality involved.   Although normalised P_{Tdist} has the steepest gradient in response to noise for the lower levels of noise, this does not make it the optimal choice, as it indicates limited dynamic range. The euclidean distance correlation has high N_R, and the highest relative statistical power. The euclidean distance correlation additionally appears to have N_R uncorrelated with noise levels and density of points - which is advantageous as it means that the number of subjects can be chosen without preliminary data. Overall, the euclidean distance correlation has the highest statistical power for distinguishing different noise levels, requires the least data to detect topography, and has the widest dynamic range. In **fig. 2.9**, there are example maps to show qualitatively what maps with different levels of order look like.

Given these clear results, extensions to the euclidean distance correlation have been formulated and optimised to enable statistical tests for differences in topographic order between multiple-subject topographic maps, and also to allow estimation of levels of disorder in biological distance units:

2.3.6   Statistically testing for differences in order across different maps in the multisubject context

The relative power calculations shown above give an indication of how powerful a metric is for testing for different levels of order. However, the values calculated

are relative, and likely to only be valid for scenarios in which the amount of data (d or n and N) are roughly equal between the maps to be compared. Dr Lowe has derived the following framework for testing for differences in topographic order between maps using different amounts of data - and for testing the significance of a difference found:

Each calculation of the euclidean distance correlation produces a single value of R^2, representing the level of topographic order. However, if maps are subsampled, many R^2 values may be generated from a single map pair. In order to utilise standard statistical tests on these values, the subsampling must produce minimally-dependent submaps. This is illustrated in **fig. 2.10**: as the number of points in each submap is increased, the spread of many R^2 values, calculated from these submaps, decreases according to a characteristic shape on a log-log plot. Where the curve is approximately linear, this is due to the metric gaining precision, similar to **fig. 2.3A-B**. The steep downward curve to the right represents the loss of independence between maps - as the same sets of points are repeatedly used in multiple submaps, their R^2 values become more similar. When all points are used, the spread of R^2 is 0 as all "submaps" are identical. The log-log plot can be used to select a number of points which gives maximal independence in both maps, but still keeps their spread small. Where two maps contain different numbers of points, the minimum selected subsample size should be used for both maps.

This generates two large populations of R^2 values. In order to test for a statistical difference between them, these must be subsampled further as classical statistics do not perform well with overly large sample sizes. Performing many t-tests on small subsamples of the two R^2 populations will produce many p-values. A false-discovery rate (FDR) adjustment [183] is performed as follows: the p-values are ranked in ascending order, and given index i. If we define a threshold q as the fraction of significant p that are allowed to be false, we can then define, for each $p\left(i\right)$, a value $q\left(i\right) = \frac{p(i)N}{i}$. This represents the minimum threshold q at which we would find $p\left(i\right)$ to be significant. These are then re-ranked so as to be monotonically increasing, and the final p for the difference between the two maps is the maximum $p\left(i\right)$ such that $q\left(i\right) \leq q$.

Care must be taken with selection of the number of points used for subsampling. If too large a number is chosen, statistical tests cannot be used properly as the R^2 values generated will not be independent. However, if too few are chosen, their
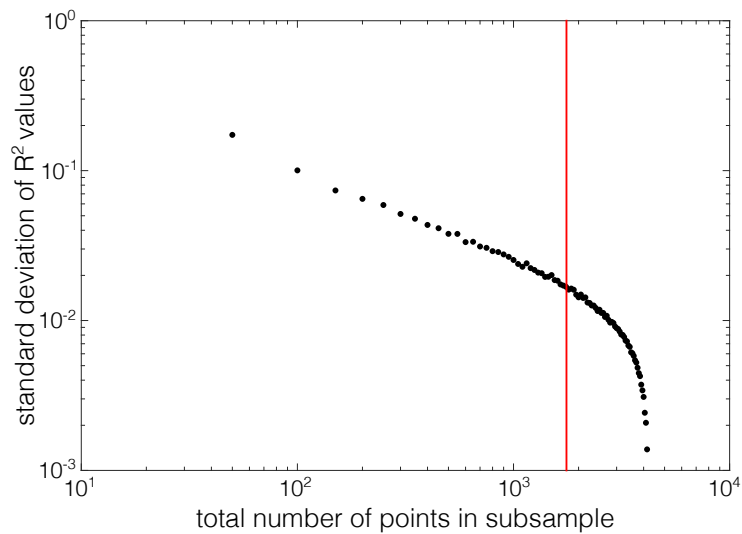
Figure 2.10: **Effect of subsampling different numbers of points on distribution of submap** R^2**.** Data derived from all reactive voxels for which receptive fields could be calculated in the tecta of 32 zebrafish, obtained by Dr Aenea Hendry [52]. Each point represents the SD of 1000 submaps, each containing the same number of points. As the number of points in a submap approaches the total number of available points, the spread approaches zero as submaps progressively have more points in common. The red line indicates a reasonable choice of subsample size.

spread will be too large and statistical power is lost. Thus, the ideal point on this curve will be one as far to the right as possible on the linear portion, as indicating in **fig. 2.10**.

2.3.7 A framework for deriving noise estimates in biological units of distance

Finally, using the euclidean distance correlation as a basis, I have developed a technique to derive estimates of biological noise values in the original biological units of measurement. This represents an estimate of the distribution of point displacements from their "ideal" positions in a perfectly-ordered map. Such an estimate is useful in that it allows us to relate topographic order in the global, abstract sense back to real biological parameters - for example, the sizes of receptive fields, or axonal arbours.

First, pairwise distance measurements are calculated as for the euclidean distance correlation, either in the single- or multiple-subjects sense. A best-fit line is

calculated to minimise least-squared orthogonal residuals (**fig. 2.11A**), achieved using principle component analysis, following normalisation for zero mean and unit variance. A binned histogram of residuals is then examined via a fitted gaussian (**fig. 2.11C**), from which the standard deviation can be extracted, summarising the level of noise in both maps. This technique explicitly assumes that the only source of topographic disorder is gaussian noise.

The orthogonal residuals can be projected back into the units of the original distance axes. The direction in which this projection occurs represents interpreting the topographic disorder as originating in one or the other of the two maps (**section 2.2.3**). However, the level of disorder can be regarded as interchangeable between the scale units of the two maps, in which case they can both be presented as a function of a dummy variable ϕ (see **eq. (2.23)**, **fig. 2.11D**).

Examining the result of this technique over a range of noise levels, in both straight and curvy multisubject maps, shows that in general the estimated noise SD closely matches that used in creating the maps. However, in curvy maps, global map distortion leads to overestimation of noise levels (see **fig. 2.12**).
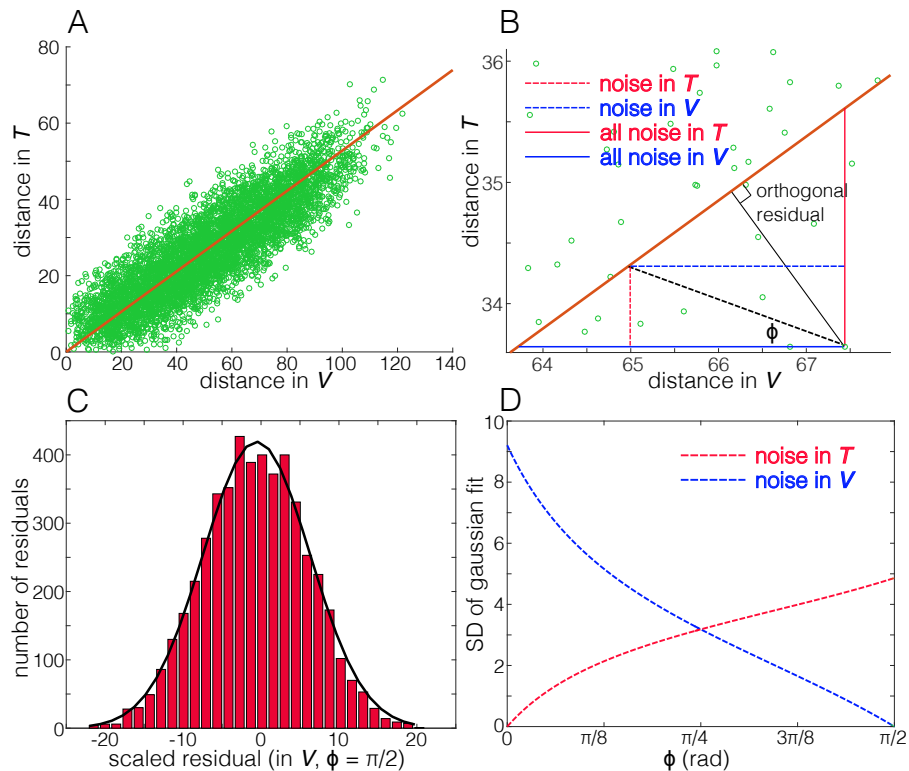
Figure 2.11: **Illustration of procedure for estimating noise in biological distance units, under the assumption that it represents a 2D gaussian distribution. A** Scatter plot of pairwise point-to-point distances in a single-subject straight map pair with line of best fit minimising orthogonal residuals. Map consists of 100 points, with a scaling factor of 0.5 and a noise of 5 applied to space T. **B** Expanded section of **A**, illustrating how the orthogonal residual relates to projections into either axis. **C. Histogram of the residuals projected into the units of space T**, with gaussian fit used to derive biological noise estimates. **D. Noise can be represented as a nonlinear combination of noise in both maps, with the angle ϕ determining which space the noise is projected into.**
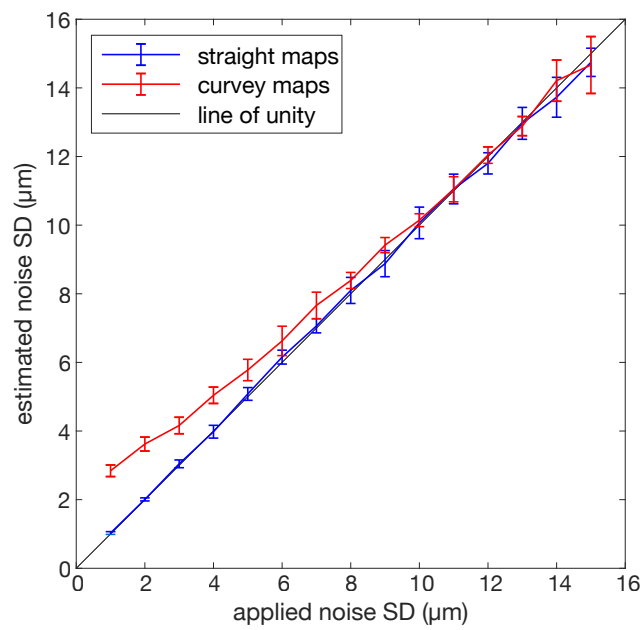
Figure 2.12: **Estimates of biological noise for straight and curvy maps**. Straight and curvy multisubject maps were generated using different noise levels, with $N = 12$ subjects, $d \simeq 0.04$ in each subject. Estimated noise level, in space T (i.e. $\phi = \frac{\pi}{2}$). Error bars show mean $\pm$ SD for 10 such datasets at each noise level.

2.4 Discussion

Overall, this work has introduced two new measures for assessing the utility of metrics for topographic order - those of redundancy and statistical power. These measures were designed to assess how much data a metric required to produce reliable results in multiple datasets with the same underlying parameters, and the power of a metric to discriminate between different levels of topographic order. In addition, I have explored the potential of metrics to detect topographic order in the multisubject context, under noise levels which make maps very disordered. I have concluded that based on these criteria, a single metric, the euclidean distance correlation, is superior to the others. Based on this metric, a method for testing differences in order between maps derived from multiple subjects has been developed, as well as a way of accounting for topographic disorder in biological distance units.

2.4.1 Redundancy represents an upper bound on how much data is useful

Originally, the concept of redundancy was formulated as a method for ascertaining which metrics require the least amount of data to function efficiently. However, given that in general, metrics in particular scenarios having a higher redundancy point (either with respect to point density or number of subjects) also have a higher statistical power at this amount of data, it should best be interpreted as the point at which adding data has no further advantage - but that in general, the more data can be added while still providing gains, the greater the maximum power will be, although not without penalty. Conversely, if a metric has a very low redundancy point (such as the scaled cosine similarity in single-subject context), this likely indicates that it is unreliable no matter how much data is provided, rather than that it is reliable with very little data. This view is also supported by the fact that most of the metrics tested have a higher redundant number of subjects at higher, rather than lower, point density (see **fig. 2.6**).

Simpson's Paradox in testing for differences in order between maps

We know that the variance in euclidean distance correlation result is affected by sampling density and by the number of experimental subjects. However, it remains to be seen how this variance is affected by different distributions of sample densities for comparable maps - although as a result of Simpson's paradox this is highly likely [184]. However, it can be easily circumvented by downsampling one (or both) of the maps such that distributions are matched in real datasets.

2.4.2 Evaluating noise in biological distance units

The technique for estimating the level of noise in biological distance units was developed following the conclusions that the euclidean distance correlation was the most reliable metric, on the basis that a method for noise estimation should be based around a metric which can efficiently quantify overall order. The method described explicitly assumes that sources of topographic disorder are gaussian, and additionally requires knowledge of which space the topographic disorder originates in. Where these assumptions are met, the technique gives good estimations.

Although the technique presented works well in the context of undistorted maps, if distortions are present, noise is overestimated. It might, however, be possible to combine a nonlinear map alignment step in which one map is distorted to match, as closely as possible, the shape of the other prior to noise quantification. Although difficult to evaluate at scale (due to the need for manual curation), a nonlinear alignment approach could well be useful in future. If the goal was to compare levels of topographic order/disorder between two maps, (such as two populations of neurons in the same brain area), one strategy could be to perform the nonlinear alignment step with the two maps pooled (necessitating the assumption that the nonlinear distortion is shared between them). An additional consideration would be that noise cannot be evaluated in biological distance units of the space which has been distorted.

Chapter 3

Development of topographic maps formed by motion-selective RGCs

3.1 Introduction

In this chapter, I set out to characterise the topographic properties of the zebrafish retinotectal projection during development. Specifically, I set out to chart the development of maps formed by two functional types of RGCs: those selective for a specific direction of motion (DS), and those selective for a specific orientation of motion (OS), exhibiting uni- and bimodal responses to circularly-spaced directions of motion respectively [37]. While the emergence of the laminar distributions of DS and OS RGC axons within the tectum over development has been explored previously [38], and the PhD thesis of Dr Aenea Hendry explored the topographic maps formed by them at a single age [52], these two areas of research have not been combined before. Additionally, these previous studies were limited by the extent of the visual field covered by visual presentation systems: only approximately 90° by 60°.

Examining maps formed by two functional types of RGC allows the comparison of map properties: do they develop according to the same rules, and do their properties change in a way that is matched in time? Although this project's main

focus is on topographic maps, the necessary experiments additionally yield a plethora of other parameters, such as selectivity for specific angles of motion and contrast changes, allowing finer-scale classification, and the distributions of the identified functional typess within the tectum.

Three ages were chosen to reflect the development of DS and OS maps. The first RGC axons enter the tectum around 2-3 days-post-fertilisation (dpf) [49, 54]. This coincides with the emergence of tectal laminae [185]. Thus, fish aged 3 dpf were studied in order to characterise maps as early as possible after RGCs enter the tectum and form their axonal arbours. Larvae begin to hunt between 5-6 dpf [186], and there is some evidence for visually-driven preference for conspecifics at 7 dpf [187]. They are capable of responding to objects as small as 1° at 6-8 dpf [188]. Much work has focussed on 7 dpf larvae [37, 38, 52, 173, 188–190], and to allow the greatest possible comparisons with other research 7 dpf was chosen as an additional timepoint. A perspective on changes further into adulthood was provided by the study of 10 dpf animals: despite recent advances in genetic techniques for functional imaging further into adulthood [191], at the time that experiments were performed this was the latest time-point that promised usable functional data from the available transgenic fish.

Using a novel visual presentation system, designed to provide maximal coverage of the visual field at the highest possible resolution (see **Appendix A**), I performed confocal functional imaging experiments on larval zebrafish expressing a synaptophysin-tagged genetically-encoded calcium indicator (which is specifically trafficked to presynaptic axon terminals) in their RGCs, and lacking melanophores [174]. Stimuli were designed to allow measurement of motion and contrast selectivity, and various properties of receptive fields, such as sizes and locations within the visual field.

Although functional imaging experiments were performed on single (2D) slices to maximise temporal resolution (with multiple slices scanned per experimental animal), these were placed into 3D by co-registration with separate structural scans. I then placed regions of interest (ROIs) meeting DS or OS criteria into 3D standardised spaces generated from multiple experimental subjects [175], representing a population tectal neuropil for each age-group. These ROIs, which correspond to punctate areas of high SyGCaMP6s fluorescence (see **section 3.2**) are likely to correspond to presynaptic axon terminals of RGCs [57].

Generating a rich dataset, incorporating both functional properties and anatomical locations of RGC axon terminals, allowed quantitative descriptions of the topographic maps formed by DS and OS RGCs. In addition to quantification of topographic order using the framework developed in **Chapter 2**, the distributions of the axon terminals formed by DS and OS RGCs within the laminar and topographic axes of the tectum, changes in contrast selectivity, receptive field size, and the alignment of the two maps have been explored. Finally, using a wavelet-based clustering method, I have explored how previously-identified putative variants of DS and OS RGC [38] might form their own submaps.

3.2   Methods & Reagents

3.2.1   Experimental animals

Experimental animals were double transgenic Isl2b:Gal4,UAS:SyGCaMP6f, maintained on a *nacre*-/- background [174]. Larvae were reared at 28.5°C, in an incubator with a luminance of ~280 Lux on a 14 hour light/10 hour dark cycle. They were maintained in mains water, run through a reverse osmosis filter, reconstituted to a pH of 7.0 with sodium bicarbonate and a conductivity of 535 µS/m using Tropic Marin salt, with 1.33 mg/l Methylene Blue added. A 50% water change was performed approximately every 2 days after 3 dpf. Fish aged 5 dpf and older (capable of independent feeding [186]) were fed on Gemma Micro 75 dry diet (Skretting) every 24 hours, with a maximum of 20 larvae per petri dish.

Around 60 adults were maintained and bred to produce experimental larvae. They were divided into 4 sets, so that while random adults were selected on any given day from within a set (3-5 breeding pairs per day), each adult was bred a maximum of once every 10 days.

3.2.2   Visual stimuli

Stimuli were presented using a purpose-built system, utilising an array of LCD screens; see **Appendix A** for details of design, construction and quality control. The area viewable by the fish was approximately 180° (azimuth) by 56° (elevation), with a resolution of ~0.07°/px. Stimulus sets were generated using custom MATLAB software, and presented at 30 frames/second.

Moving bars

Twelve second videos of bars, oriented in different ways, were used to assess motion selectivity. The bars faded from mean grey for 1 second at the start, and faded to mean grey for the final second, in a linear fashion to avoid sudden luminance changes. The mean luminance of the screens, 32 cd/m^2, was maintained at all times. There were 2 different sets of bars: "dark", composed of 10° bars of 0.25×mean grey separated by 30° bars of 1.25× mean grey, and "light",

composed of 10° bars of 1.75×mean grey separated by 30° bars of 0.75× mean grey. They moved with a speed of 20°/s orthogonal to their edges (see **fig. 3.1**). The angles referred to in this thesis always refer to the direction of motion. The background also changed luminance over the same period, maintaining constant mean luminance over the whole screen. There were 24 of these movies: Bars moving in 12 directions at 30° intervals, both dark and light. These were presented in a random order, generated at the start of each experiment, with a rest period of 10s between movies.

Sparse noise

Additionally, for estimating the receptive fields of neurons, a sparse noise stimulus was used. Dark (0.25×mean grey luminance) or light (1.75×mean grey luminance) 7.5° squares were presented on a mean grey background to tile visual space with 50% overlap. The squares appeared and disappeared suddenly in order to produce impulse responses. The total number of centres was 658 with the centres distributed 3.25° apart across the screens, and each centre (red dots in right panel of **fig. 3.1**) used exactly once by both dark and light squares. Due to the overlap of squares, screen locations were each covered 9 times, with the exception of edges which were covered 3 times, and corners, covered once. Each epoch consisted of 1 second with squares on-screen, and 0.5 seconds with no squares. Complete coverage of the screens required 400 epochs, with either 3 or 4 squares per epoch. (see **fig. 3.1**). These were randomly selected, with constraints set on the minimum distance between their centres (>20°). Ten different versions of this stimulus were created (in which squares were shown in different combinations), with one selected randomly at the start of each experiment.

3.2.3   Imaging

Fish were immobilised in 2.5% agarose, mounted on custom-built slides for use in the stimulus presentation system (see **Appendix A** for details). All images were acquired using a Nikon A1R confocal microscope, using a resonance scanner in order to record images from single slices at ~15Hz, 512×512 voxels of size 0.39× 0.39 μm. Due to large changes in fluorescence observed at the start of imaging (data not shown), stimulus epochs began a minimum of 30s after the start of

imaging. Imaging was performed at roughly the same time each day (between 1pm and 6pm), in order to minimise effects of circadian rhythms on neuronal activity patterns [192, 193]. On any given day, between 1 and 3 animals were imaged.

Anatomical Imaging

After placing the fish in the imaging chamber, a single structural scan was taken, extending from above the dorsal pole of the neuropil for 80-150 µm ventrally. Slices were 0.725 µm apart, and the final image calculated using the mean of 8 scans per plane to increase signal-to-noise.

Functional imaging

Care was taken to adjust the laser power and gain to obtain maximal dynamic range within images without producing clipping artefacts. All experiments were of a single slice, with a minimum of 3 µm between experimental planes in each subject to minimise duplication of ROIs across multiple scans. In each subject, between 3 and 7 planes were scanned (although not all were included in the final dataset, see **section 3.2.4**). For each plane, the sparse noise stimulus was presented first, followed by the oriented bars.

3.2.4   Analysis

Functional scan pre-processing

Images were converted from the Nikon proprietary .nd2 format to NIfTI format, using in-house MATLAB scripts. Acquired time-series were temporally downsampled by a factor of two (to ~7.5Hz) by taking the mean of each voxel in temporally adjacent frames in a non-overlapping fashion, increasing signal-to-noise. After downsampling, each set of experiments on a slice was spatially realigned to its first frame, then its mean image and resampled using SPM8 [194] to remove motion artefacts in 2D. All alignments were manually checked, and excluded from subsequent analyses if satisfactory motion-correction could not be achieved after 3 separate attempts, or if z-drift was observed (indicated by, for example,

the appearance or disappearance of prominent morphological features or visible changes in the shape of the neuropil).

Each voxel's time-series was independently rescaled to have zero mean and unit variance, taking advantage of the maximum dynamic range available in the NIfTI int16 format. Each voxel was then Savitsky-Golay filtered [195] across time, using the MATLAB *sgolay* function in order to further increase signal-to-noise. In voxels where the time-series is dominated by high-frequency noise, this reduces the dynamic range far more than in those voxels whose intensity varies slowly, with the stimuli.

ROI identification from functional time-series

For each voxel, the entropy of its fluorescence intensity profile over time was calculated. This provided a simple heuristic of whether voxels were of interest, in order to to speed analysis, as voxels with high entropy over time tend to be those fluorescently-labelled within the neuropil. As the tectum typically occupied less than half of the field of view, only the 50% of voxels with the highest entropy in each scan were considered for further analysis. Remaining voxels were sorted by the standard deviation of their intensities over time, meaning that the voxels with the most variable signal were used as seed points first. Using these most variable voxels, pairwise euclidean distances d_r in a response space for which each timepoint in a functional scan is considered a dimension were calculated between the seed and all other voxels. Voxels are binned according to their distance from the seed in anatomical space, d_a, and a curve of the form $d_r = \frac{1}{Ae^{-\lambda d_a}}$ fitted. Voxels are assigned to the same ROI as the seed if their $\frac{1}{d_r}$ exceeds 1.5× full-width half maximum of this curve. After assignment to an ROI, voxels were excluded from this assignment procedure, which repeats, taking the most variable voxel as a seed, until all voxels have been included in an ROI, or excluded due to size constraints. ROIs had a minimum size of 5 voxels, and a maximum size of 200 voxels, corresponding to an area of between 0.76 and 30.4 μm^2 in the imaging plane. These areas were selected as being biologically plausible given the size of presynaptic puncta on RGC axons in a previous study, labelled using a similar transgenic line [57].

Motion selectivity estimation from bar stimuli, and contrast change selectivity

The moving bar stimuli were used to calculate the selectivity of individual ROIs for different directions of motion. Unimodal responses to motion are hereafter referred to as direction-selective (DS), while bimodal are referred to as orientation-selective (OS).

Epoch starts and ends were calculated as described in **Appendix A**. Responses during inter-epoch intervals were assumed to be null. Thus, baseline fluorescence was removed from epochs via linearly interpolating from the mean fluorescence during their adjacent inter-epoch intervals and subtracting the result at each time-point, producing a ΔF value for each ROI at each time-point. The responses to each angle T were calculated as the integral ΔF to their epoch, producing a 12-element response vector. $\Delta F/F$ was not calculated, as comparisons are only ever made within (rather than between) ROIs, and the division adds noise due to errors in estimation of baseline fluorescence.

Preferred angles (Θ_{pref}) were calculated via a von Mises fit to the response vector [196], with a unimodal fit used for DS and a bimodal fit for OS responses. $T_{\Theta_{pref}}$ was the peak height of the von Mises fit. Θ_{null} refers to the opposite angle (i.e. shifted by π radians), while Θ_{orth} is the orthogonal angle (shifted by π radians). Direction selectivity index (DSI) and orientation selectivity index (OSI) calculated as described previously [38, 197]:

$$DSI = \frac{T_{\Theta_{pref}} - T_{\Theta_{null}}}{T_{\Theta_{pref}} + T_{\Theta_{null}}} \tag{3.1}$$

$$OSI = \frac{T_{\Theta_{pref}} - T_{\Theta_{orth}}}{T_{\Theta_{pref}} + T_{\Theta_{orth}}} \tag{3.2}$$

Voxels were classified as DS if their DSI >0.5, OSI <0.5, and goodness-of-fit for the von Mises profile, R^2>0.8, and as OS if their OSI>0.5, DSI<0.5, and goodness-of-fit for the von Mises profile, R^2>0.8. Thus, OS and DS ROIs were mutually exclusive. During this analysis, responses to the 10° bright and dark bars were analysed separately. If an ROI met DS criteria when stimulated with bright bars, but not with dark, in was considered an ON-DS. If the converse was true, it was considered OFF-DS. If responses to both bright and dark bars met DS criteria, it was considered
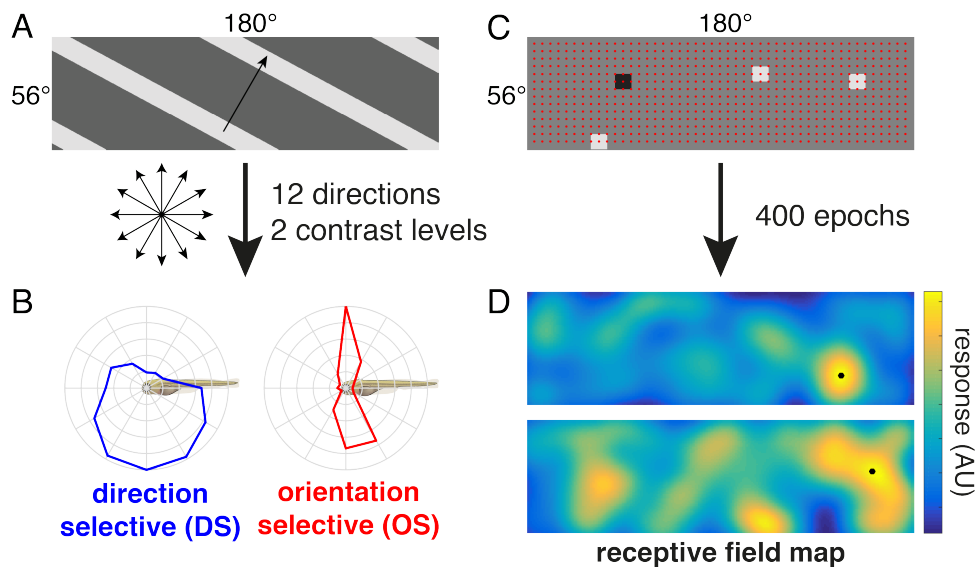
Figure 3.1: **Stimuli and example responses from functional imaging experiments. A** Example light bars. **B** Example responses of DS and OS ROIs. **C** Example epoch from sparse noise stimulus. Red dots represent centres of all presented squares throughout the whole experiment. **D** Representative example receptive field maps from 2 ROIs, after gaussian smoothing. Black dots indicate calculated receptive field centres.

ON-OFF DS. The procedure was identical with respect to the OS ROIs.

Receptive field estimation from sparse noise stimuli

Receptive fields were calculated for ROIs identified using the bar stimuli, via a reverse correlation approach similar to Ramdya et al., 2006 [198]. Responses of each epoch were determined as an integral under the curve of fits to the onset and end of each epoch, using a function allowing both transient and sustained responses. This model was designed by Dr Andrew Lowe. The fitted parameters were as follows:

- t time since epoch start, in seconds

- y_t, the change in fluorescence from baseline at a particular time

- y_{init} value of y from previous epoch, evaluated at $t = 0$. For the first epoch, $y_{init} = 0$.

- x_1 time from epoch onset to beginning of transient response

- x_2 time from epoch onset to end of sustained response

- x_3 time from epoch onset to transient peak

- x_4 time from epoch onset to end of sustained response

- A amplitude of the transient response

- B amplitude of the sustained response

- Bs amplitude of held component of sustained response

- τ_{rise} = 0.083s, defined based on the kinetics of the GCaMP6s probe [168].

- τ_{fall} = 0.60s, defined based on the kinetics of the GCaMP6s probe [168].

$$
y_t = \begin{cases}
y_{init}\, e^{-\frac{t}{\tau_{fall}}} & : t < x_1, \text{ if } y_{init} > 0 \\[2ex]
y_{init}\left(1 - e^{-\frac{t}{\tau_{rise}}}\right) & : t < x_1, \text{ if } y_{init} < 0 \\[2ex]
y_{t=x_1} + (A - y_{t=x_1})\left(1 - e^{-\frac{t-x_1}{\tau_{rise}}}\right) & : x_1 \le t < x_2 \\[2ex]
y_{t=x_2}\, e^{-\frac{t-x_2}{\tau_{fall}}} & : x_2 \le t < x_3 \\[2ex]
\max\left(\begin{array}{c} y_{t=x_3} + (B - y_{t=x_3})\left(1 - e^{-\frac{t-x_3}{\tau_{rise}}}\right) \\[1ex] B_s \end{array}\right) & : x_3 \le t < x_4 \\[3ex]
y_{t=x_4}\, e^{-\frac{t-x_4}{\tau_{fall}}} & : t \ge x_4
\end{cases}
\tag{3.3}
$$

$$
y_t = \begin{cases}
y_{init}\, e^{-\frac{t}{\tau_{fall}}} & : t < x_1, \text{ if } y_{init} > 0 \\[2ex]
y_{init}\left(1 - e^{-\frac{t}{\tau_{rise}}}\right) & : t < x_1, \text{ if } y_{init} < 0 \\[2ex]
A - (A + y_{t=x_1})\, e^{-\frac{t-x_1}{\tau_{fall}}} & : x_1 \le t < x_2 \\[2ex]
y_{t=x_2} - y_{t=x_2}\left(1 - e^{-\frac{t-x_2}{\tau_{rise}}}\right) & : x_2 \le t < x_3 \\[2ex]
\min\left(\begin{array}{c} B - (B + y_{t=x_3})\, e^{-\frac{t-x_3}{\tau_{fall}}} \\[1ex] B_s \end{array}\right) & : x_3 \le t < x_4 \\[3ex]
y_{t=x_4} - y_{t=x_4}\left(1 - e^{-\frac{t-x_4}{\tau_{rise}}}\right) & : t \ge x_4
\end{cases}
\tag{3.4}
$$

Parameters other than τ_{fall} and τ_{fall} were fitted to each epoch using the MATLAB *fminsearchcon* function. The fit was formulated in such a way as to automate
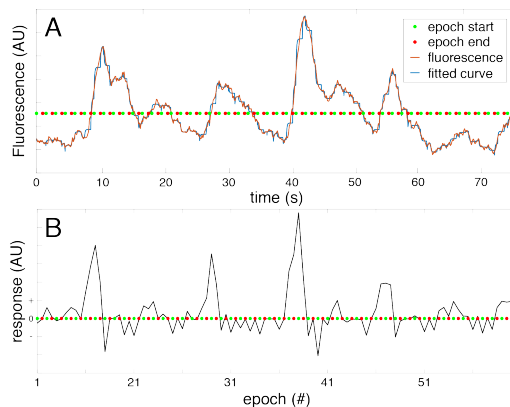
Figure 3.2: **A** Example fluorescence trace, with model fit overlaid and sparse noise epoch start and ends marked. **B** Epoch-wise responses extracted from model fit.

selection of **eq. (3.3)** if the epoch caused an increase in fluorescence or **eq. (3.4)** if the epoch caused a decrease in fluorescence. As some RGCs are tonically active [199], it was important to use this approach, allowing both increases and decreases in fluorescence in response to the stimulus. An example fluorescence trace, and it's fitted model, can be seen in **fig. 3.2**.

As the sparse noise stimuli had multiple squares per epoch, the response to each epoch corresponded to multiple screen locations (either 3 or 4, see **section 3.2.2**). Due to the overlap between the squares used, each location on the screen was covered 9 times by both dark and light squares (with the exception of edges and corners). Maps of responses to positive and negative contrast changes were thus built up by assigning the responses of an ROI at each epoch to the screen locations where luminance changes occurred. Maps of responses to negative contrast changes were built from the appearance of a dark square, or the disappearance of a bright one, while maps of responses to positive contrast changes were built from the appearance of a bright square or the disappearance of a dark one. The final response to either contrast change at a particular point in visual space was calculated as the average of the responses to epochs containing luminance changes covering that point. This gave 2 maps, for positive and negative contrast responses. To find receptive field centres, the mean of the modulus of these two maps was gaussian-filtered (with SD of 7.5°) and thresholded at 2 SD above its mean. If multiple non-contiguous regions were found to be supra-threshold, only the largest was retained. This approach was expected to lead to noisy receptive fields (see lower example in **fig. 3.1D**) but if the receptive field is coherent and larger

than 3.5° in diameter, it should be revealed. The centre of mass of the thresholded map was taken as the receptive field centre. The area of the receptive field was taken as the area of all supra-threshold pixels. Examples of these receptive field weightings prior to thresholding can be see in the lower right panel of **fig. 3.1**.

Clustering of OS & DS variants

Clustering of angle-selective variants of DS and OS ROIs was performed as described in Lowe et al., 2013 [38]: For DS ROIs, the Haar wavelet coefficients were derived from the 12-element response vector from bar experiments. The 5 wavelet coefficients with the highest variance over the ROIs within each age-group were selected and then used as input for *wave_clus*, a semi-supervised clustering toolbox [200]. *Wave_clus* was chosen as it was the method used in previous research [38]. For OS ROIs, which have preferred angles only between 0° and 180°, the 12-element response vector was taken as the mean of equivalent elements (for example, 0° and 180°) and only the 3 most variant wavelet coefficients (of 6 total) were used for clustering. All clustering was performed within age-group. Correspondence between clusters across ages was subjectively assessed based on similarity of angular selectivity and relative abundance. The angle at which the fish views the screen affects how the 12 different directions of motion are projected onto the retina, and thus how they are encoded in the RGCs. Thus, for comparisons of variants between age groups to be valid, it must be assumed that there are no systematic differences between the age groups in the angles that the fish were mounted.

Construction and usage of standardised spaces

All alignments were performed using SPM8 [194].

Z-coordinates for functional scans were checked manually and corrected if necessary, by comparing the mean image of the functional time-series against the planes of the structural image, in case the fish had drifted in z during the experimental session. In order to estimate the 2D rigid-body transformations to bring ROI coordinates into reference with the anatomical image, the mean image from 30 frames of the functional time-series (in order to match signal-to-noise ratio)

was aligned to its corresponding slice from the structural scan, using spm8.

In order to aid alignment despite fine-scale disparities between subjects, a simplified representation of the RGC-recipient neuropil, comprising just the SFGS and optic nerve, was produced for each subject. This simplification was produced by a multi-stage process. First, the image was masked to remove skin autofluorescence, using an in-house MATLAB script produced by Dr Andrew Lowe. The resultant image was then thresholded, setting all but the most brightly-fluorescent of voxels to 0, with the fraction of retained voxels determined by the experimenter on a case-by-case basis. This was followed by median filtering and whitening (using parameters adjusted on a case-by-case basis).

From each age group, 6 subjects were selected by hand as having the closest correspondence between the z-axis of the image and the dorsoventral axis of the fish: the fish was mounted "straight". Five of these 6 masked, filtered and whitened images selected for the template were aligned to the remaining one, then all of them were aligned to their mean, and resliced. The template was created by rescaling all voxel brightnesses to match ranges (so that especially bright images did not dominate) and defining each voxel brightness as the mean of the corresponding non-zero voxels in the individual subjects. Masked/filtered/whitened images from all subjects were then individually aligned to the age-appropriate template. The mean (unprocessed) image of the realigned animals used in the template can be seen in **fig. 3.3** - the gross laminae of the tectal neuropil (the SO, SFGS, SAC and SGC) are clearly visible. There are, however, discrepancies visible at the poles of the neuropil, due to the limitations of the rigid-body approach used here.

In order to assure the quality of the registration procedure, there were stringent manual comparisons made between each subject, and the template image. Various morphological markers were particularly considered: the optic nerve entry point, the rostral and caudal edges of the neuropil across dorso-ventral coordinates, the dorsal border of the neuropil across different rostro-caudal coordinates, and, where visible, laminae and tectal subregions. A subset of pairwise comparisons were additionally made between individual subjects. Finally, the boundaries of the whole tectal neuropil, and boundaries of the the SFGS traced on the mean of all realigned/resampled structural images using an in-house MATLAB script, producing a mesh representation of the neuropil volume into which coordinates of ROIs could be placed (see **fig. 3.5**) [38, 77].
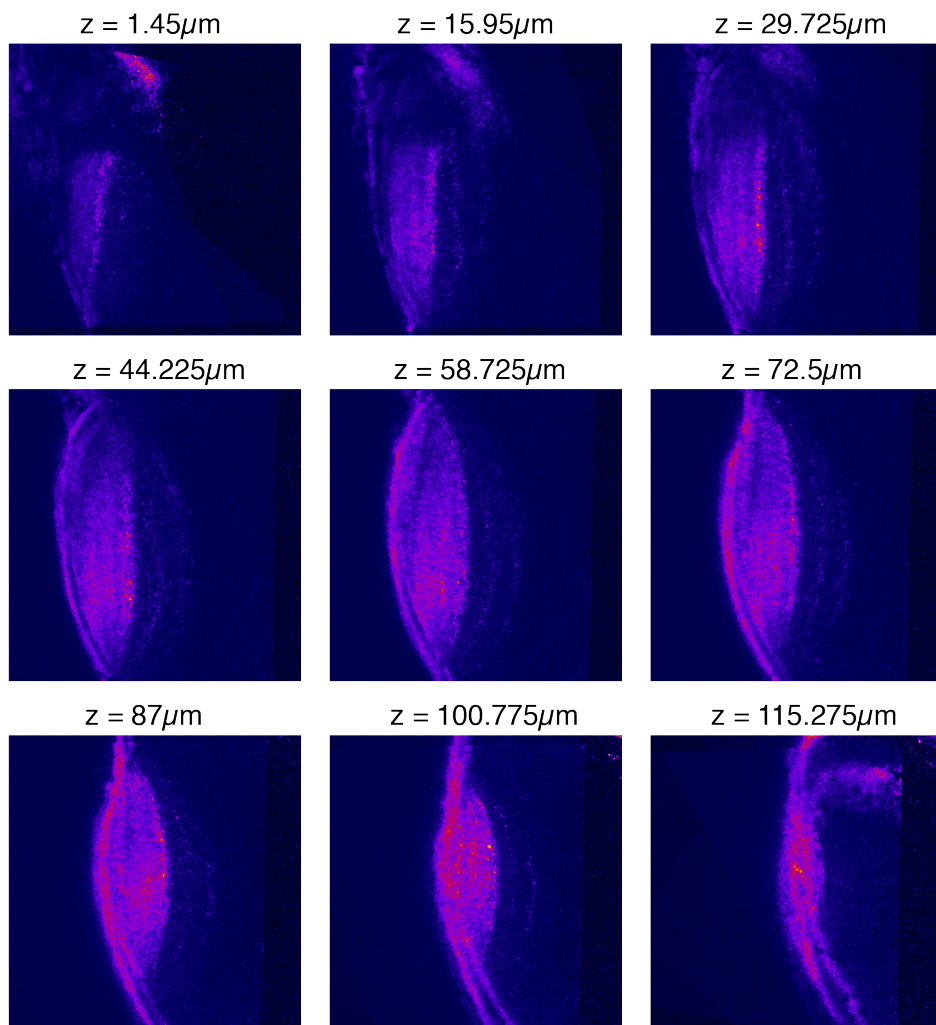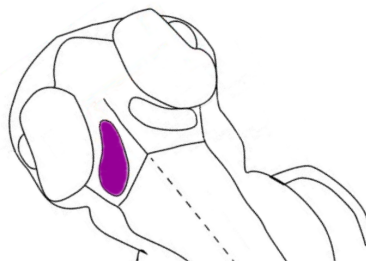
Figure 3.3: **Top:** Mean structural image from 6 7 dpf animals, used as template for other subjects. Laminae of the tectal neuropil are clearly visible. The z-coordinates shown are relative to the ventral-most slice, with more positive meaning more dorsal. Individual slices are approximately linearly spaced in z. This is a top-down view of the left tectum, but as images have been realigned it does not precisely equate to the acquisition view in all subjects. The bright patch at top of the top-left panel is the optic nerve. **Bottom:** Illustration of the approximate orientation of the animal for the above images: the tectum imaged is highlighted in purple. Image adapted from Kita et al., 2014 [50].

Estimation of laminar and topographic axes

Estimates of the topographic plane and laminar axis for each age-group were based on the four "poles" of the tectum [38]. Given that templates were created in alignment with a single subject judged to be upright, the dorsal and ventral poles were judged to be the centres of mass of the uppermost and lowermost layers (respectively) of the manually-segmented template SFGS. The anterior and posterior poles were taken as the two furthest-apart points within any single acquisition plane (i.e. the tectum's longest axis in the horizontal plane). The topographic plane was defined by fitting a plane to these landmarks in the least-squares sense.

Once the topographic plane had been estimated, the coordinates of ROIs could be transformed such that their 3 coordinates now represented the two axes of the topographic plane, and the "laminar" position within the tectum: the normal to the topographic plane was taken to represent the laminar axis. Thus in **fig. 3.7**, the coordinates visualised represent the coordinates of the topographic plane, while **fig. 3.6** represents only the laminar coordinate. The correspondence between these coordinates and the cardinal axes of the fish are clearly visualised in **fig. 3.5**.

If the topographic plane defined here represents functionally-defined retinorecipient laminae, then the coordinates of DS and OS in the topographic plane should be uncorrelated with the laminar coordinate. If the estimated plane was incorrect, then the true plane would be at an angle to it, introducing correlations between the topographic coordinates and the laminar ones. To test this, Pearson's correlation coefficients between the topographic and laminar coordinates were calculated: For all ages and both DS and OS ROIs, the correlation coefficients were <0.03.

Estimation of relative laminar location, and tectal laminar segmentation

For each ROI, its relative position through the laminar coordinate of the SFGS (in **fig. 3.6**) was estimated, allowing the representation of the laminar coordinate of any ROI as being between 0 (most deep) and 1 (most superficial):

- Finding the facets of the SFGS boundary mesh lying directly above and below the ROI in question.

- Linearly interpolating the precise "laminar" coordinate of the mesh above and below the ROI using only these facets.

- Calculating the location of the ROI as a fraction of the distance between the two points directly above and below it.

Laminar boundaries for DS & OS ROIs were defined as lying between the centre of a single fitted gaussian and 1 standard deviation in either direction from it. As these laminae do not have clean morphological boundaries dividing them [38], they were allowed to overlap.

Generation of azimuth and elevation maps, showing visuotopy

In **fig. 3.9**, the topographic plane of the standardised tectum (i.e. ignoring the laminar coordinate of ROIs) was divided into 10 μm^2 bins. Each bin containing 3 or more ROIs was colour-coded according to the mean azimuthal (or elevational) receptive field centre of the ROIs lying within it.

Estimation of tectal azimuth and elevation axes, and magnification factors

Receptive field centres in visual space were collapsed to their azimuthal (or elevational) coordinate. Topography was measured as described in **Chapter 2** between the azimuthal (or elevational) coordinate in visual space, and the tectal coordinate, projected into 1D along an axis rotated by $0 \leq \Theta \leq \pi$ radians. Θ_{az} (or Θ_{el}) was taken as the angle which maximised topographic order between azimuthal (or elevational) screen location and 1D-projected tectal location. The magnification factor was calculated as the gradient of the best-fit line (estimated using the *polyfit* MATLAB function) between the azimuthal (or elevational) coordinate and the 1D-projected tectal location which gave the maximal topographic order.

Testing for differences in topographic order

In order to compare the level of topographic order between two different maps, the framework described in **section 2.3.6** was used. For each map, a Monte Carlo subsample size was selected as described in **section 2.3.6**. For each map being
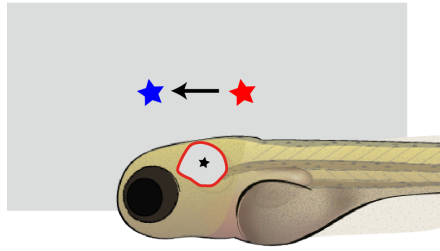
Figure 3.4: Examining the displacement between visual space locations in two maps, for the same tectal location, represents a measure of map alignment. This diagram shows an example tectal location (black star), the mean receptive field locations of DS (blue) and OS (red) ROIs in visual space (grey rectangle), and the displacement vector between them (black arrow).

compared, 1000 subsampled maps were generated using the smaller of the two selected Monte Carlo subsample sizes: this offers a more stringent test than using independently-selected subsample sizes, and ensures a fair comparison where numbers of points in the two maps are uneven. The topographic order of each subsample was quantified using the multisubject euclidean distance correlation described in **eq. (2.12)**, producing two populations of 1000 R^2 (one for each map). In order to calculate whether they are statistically different, t-tests were performed on 10000 random subsamples from the populations of R^2 values, drawing 12 R^2 values randomly from each population, for each test. The final p-value was calculated using the FDR-correction procedure described in **section 2.3.6** [183].

Estimation of displacement between maps

In order to estimate whether or not two maps are aligned with each other in the topographic plane, the displacement between them was estimated in visual space. This process is equivalent to using an electrode stuck down the laminar axis of the tectum and measuring the difference in receptive field centres:

In order to estimate this displacement, the topographic plane of the tectum was divided into 20× 20 μm^2 bins, and for each bin the centres of masses of both DS and OS ROIs was estimated, via a two-step process: Any bin which contained $\geq$ 6 DS and $\geq$ 6 OS ROIs had the centre of mass of each map estimated in visual space. The distribution of distances (x) between all points and the centre of mass in visual space were fitted with Rayleigh distributions, using the MATLAB *fminsearch*

function to minimise squared differences between the predicted abundance, *A* and the actual one.

$$A = \frac{Hx}{\sigma^2} \exp \frac{x^2}{2\sigma^2} \tag{3.5}$$

where σ is the Rayleigh spread parameter and H is the peak height. Fits were performed independently for DS and OS distributions. In order to remove outliers, any points further than $2\sigma°$ from the initial centre of mass were removed, and the centre recalculated. A Rayleigh test for circular uniformity, as implemented in the *circstat* MATLAB toolbox [201], was used to test for systematic differences in visual space position between maps.

3.3 Results

Functional imaging experiments were performed on 3,7 and 10 dpf fish to allow the classification of ROIs into DS and OS, and also to estimate their receptive field centres. Isl2b:Gal4;UAS:SyGCaMP6s;*nacre* −/− fish [174] express synaptophysin-tagged GCaMP6s in their retinal ganglion cells, and this is preferentially trafficked to axon terminals. GCaMP6s provides a proxy for neuronal activity. Visual stimuli were presented using a specially-constructed visual presentation system, which covers 180° (azimuth) by 56° (elevation) of the visual field (see **Appendix A** for details).

These functional imaging experiments, consisting of dark or light square-wave gratings moving in 12 different directions evenly spaced around a circle, and a sparse noise stimulus using 3-4 dark or light 7.5° squares per epoch, distributed on a 2.25° grid. ROIs were automatically defined as groups of voxels with highly-variable and highly-correlated levels of fluorescence over time, sizes expected from an axon terminal (see **section 3.2.4**). The drifting bars allow the calculation of orientation and direction selectivity according to previously-accepted criteria [37, 38, 173]. After classification as DS or OS, the receptive field centre was calculated using reverse-correlation to the sparse noise. The number of ROIs from each age and functional type is shown in **table 3.1**.

Once ROIs had been selected based on their functional properties, they were mapped back into a standardised space. This represents an anatomical average of a subset of fish used within each age group, and means that data can be pooled across fish in order to examine whether distributions of ROIs are biased and/or nonmatching. An example 3D standardised space for the 7 dpf tectal neuropil, showing manually-segmented anatomical boundaries, is shown in **fig. 3.5**. The vast majority of DS and OS ROIs were found within the stratum fibrosum et griseum superficiale (SFGS; 76% of DS/OS ROIs from 3 dpf, 94% from 7 dpf 92% from 10 dpf). Additionally, given that coherent retinotopic maps are found within the SFGS neuropil [52], inclusion of ROIs found elsewhere would represent confounding data. The larger numbers of ROIs outside the SFGS at 3 dpf represent a combination of false positives due to "spiky" responses in neurons projecting to deeper tectal layers [38]. Thus, only data from the SFGS are presented. As RGCs are not bistratified [33], they must originate from different functional types of RGC.

Anatomical landmarks previously used [52] corresponding to the anatomical "poles" were selected based on the shape of the meshes surrounding the neuropil. These poles were used to rotate the neuropil such that the three axes now represented the two axes of the topographic plane (in which azimuthal and elevational representations of visual space should lie) and the laminar axis, along which we expect topographic maps of visual space to be overlaid (see **fig. 1.3**).

Age (dpf)	ROI type	N	# scans	total n	n scan^{-1}
3	DS	14	71	1010	14.2
3	OS	14	71	250	3.5
7	DS	17	70	3385	48.4
7	OS	17	70	1706	24.4
10	DS	16	71	1296	18.3
10	OS	16	71	978	13.8

Table 3.1: Summary of DS and OS ROIs from the SFGS tectal region obtained from functional imaging of Isl2b:Gal4;UAS:SyGCaMP6s zebrafish of different ages. Both OS and DS ROIs were found in all fish imaged, at all ages.

3.3.1   Distributions of DS and OS ROIs within standard tecta

Quantifying the laminar distributions of DS and OS ROIs, **fig. 3.6** shows the probability densities for DS and OS functional units, as determined by counting numbers of ROIs along the laminar axis of the SFGS neuropil. DS and OS lie in clearly-defined laminae, with the DS RGCs more superficial, as previously shown [38]. Laminar boundaries have been defined here using single gaussian fits to these densities, with their boundaries set at one standard deviation from the peak (shown as dotted lines in **fig. 3.6**).

Although there are very few OS RGCs at 3 dpf, they appear to be far more uniformly distributed across the SFGS than the DS, starting with a very diffuse distribution which refines from 3-10 dpf, as previously observed [38]. A secondary OS lamina emerges deeper within the tectum, evident at 7 dpf and becoming more pronounced between 7 and 10 dpf. It appears that the main DS lamina moves from more superficial to deeper within the tectum over development, which has not been previously observed [38]. Could this effect be due to the thickening of the statum opticum (SO), which lies superficial to the SFGS, combined with small errors in alignment and segmentation? Such errors would also tend to make laminae appear
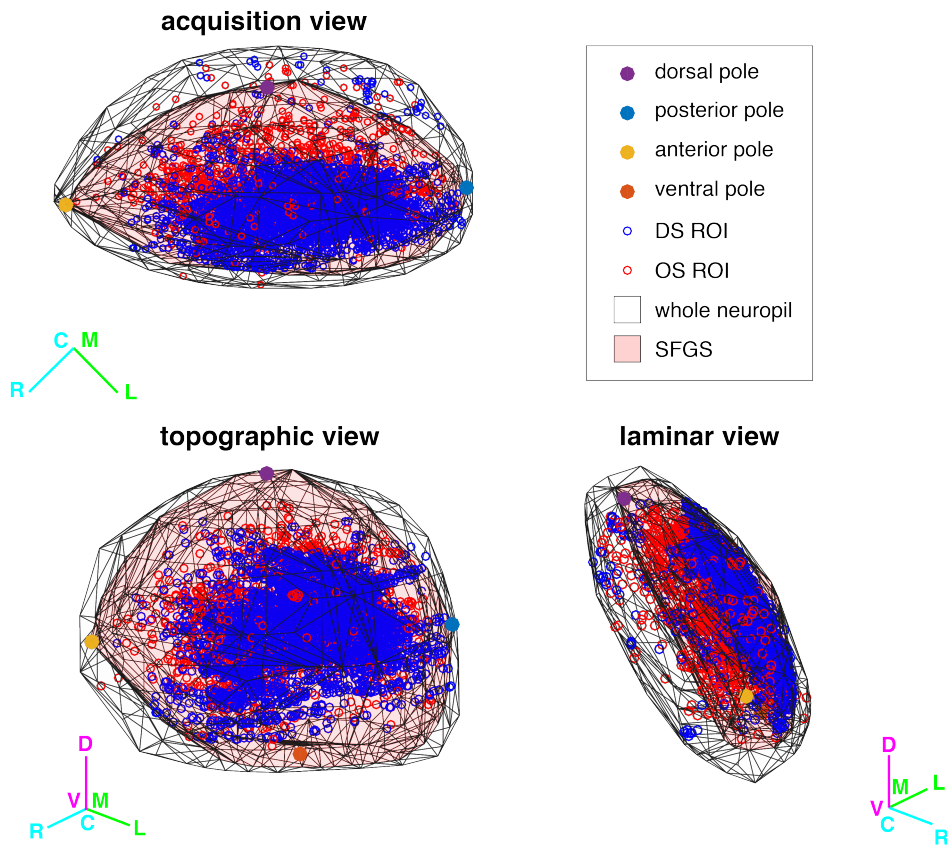
Figure 3.5: **Standardised space for 7 dpf tectal neuropil, with anatomical poles marked**. Scale bars are 30 μm, and show the approximate dorsoventral, rostrocaudal and mediolateral axes of the fish. Axes are centred in the same 3D location for each image. Top left image is roughly equivalent to the acquisition view, although the angle of the acquisition view varied slightly between fish. Other rotations show the topographic view - the plane in which topographic maps lie, and an orthogonal view, revealing the laminae in which DS and OS predominantly lie.
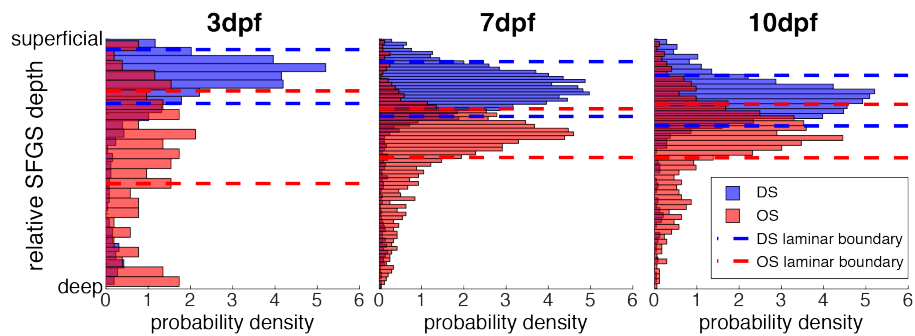
Figure 3.6: **Histograms showing probability density over the laminar axis for DS and OS ROIs, over development.** Dotted lines represent 1 standard deviation from the mean of a single fitted gaussian, the laminar boundaries used to estimate coverage (in **fig. 3.7**). Histogram bin widths were selected to maximise the entropy of the bin height distribution.

more diffuse, and to equally shift the OS lamina - effects which are not seen here, meaning that the change in depth is real.

Examining the distributions of DS and OS ROIs in the topographic plane, corrected for the number of times different regions were imaged (**fig. 3.7B**), certain features are particularly evident. While there are prominent peaks in the density of DS ROIs, the OS ROIs appear to be more uniformly distributed, particularly at 10 dpf. Consistent with previous findings [38, 52], there is an area of tectum which has very sparse DS and OS ROIs in the dorsal/anterior part of the tectum - this becomes more pronounced through development, producing a "hole" at 10 dpf, which corresponds to the anterior/upper region of visual space. This is particularly evident in the density of DS ROIs, and less so with the OS.

The low density of ROIs at the extremities of the tectum could be in part due to the increased likelihood of receptive fields lying outside the area of visual space covered by the visual presentation system: although the screen was designed to cover as much of the field of view as possible (see **Appendix A**), the angle from which the fish viewed the screen could not be perfectly matched every time, meaning that ROIs with receptive fields at the extremities of visual space are more likely to be missed with this experimental setup. However, it is also possible that there are in fact fewer DS and OS ROIs at the very edges of the tectum, although bulk density of RGC axons is not altered in this manner [69], and additionally indicated by constant density of fluorescently-labelled puncta (for example see **fig. 3.3**).
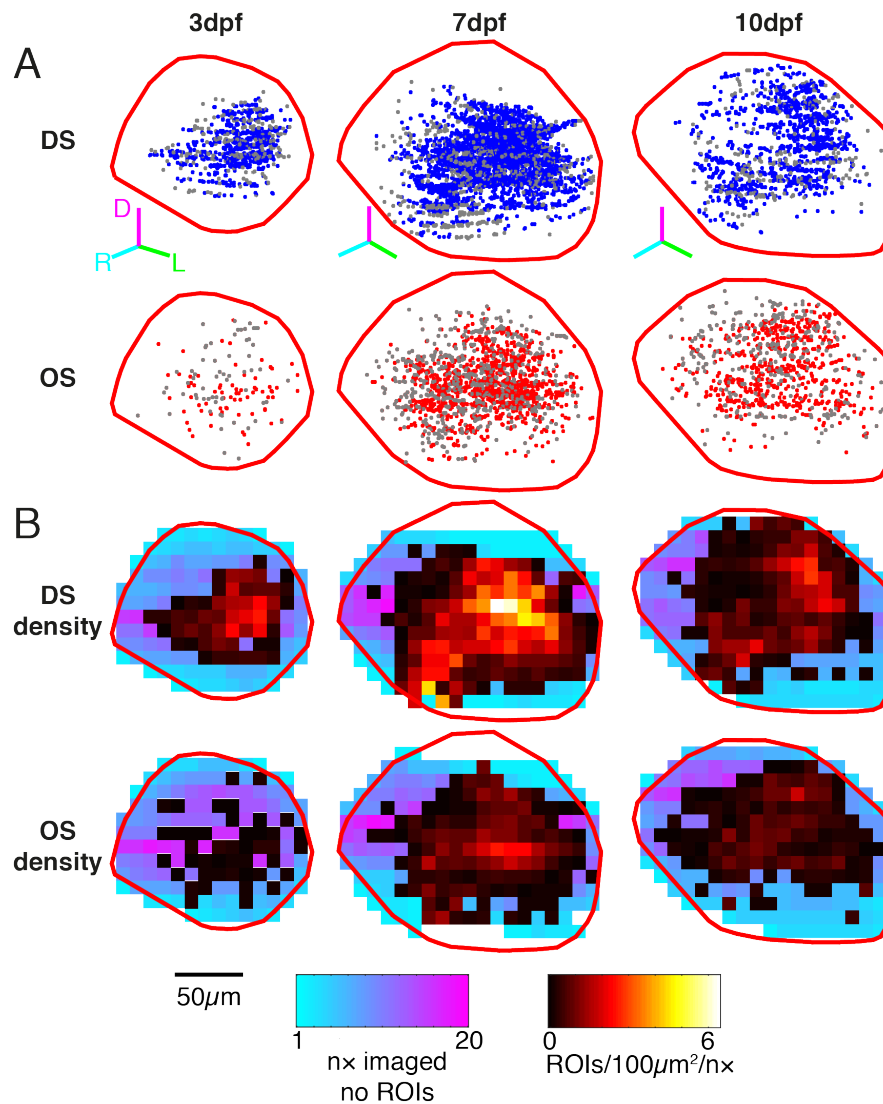
Figure 3.7: **A** Distributions of all DS and OS ROIs in 3,7 and 10 dpf larvae, projected onto the topographic plane of the SFGS standardised space. Grey points indicate ROIs found outside the lamina. Boundaries of dominant laminae were estimated via a gaussian fit to the normalised distance through the SFGS (see **fig. 3.6**). **B** Maps of ROI density within the dominant lamina for each ROI functional type. In laminar pixels where no ROIs were found, the number of times the pixel was imaged is indicated.
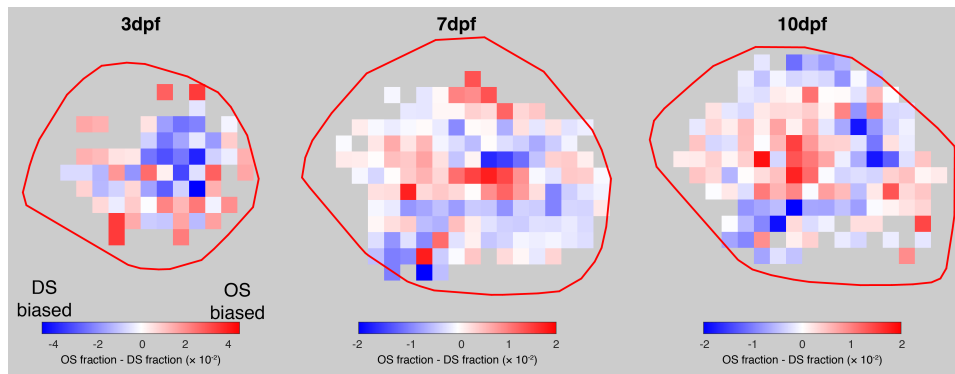
Figure 3.8: **Differential probabilities for OS and DS RGCs.** Densities of ROIs corrected for the number of times pixels were imaged (lower panels of **fig. 3.7**) were rescaled to sum to 1, indicating the fraction of DS (or OS) ROIs found in each pixel. The rescaled DS density was then subtracted from the rescaled OS density, meaning that the integral of each parametric map is 0. Only pixels in which density of either functional type is non-zero are shown.

Additionally, it appears that the areas with the most DS do not correspond with those with the most OS. The peak in DS density appears to be dorsal and caudal of the peak in OS density. This difference is more pronounced at 10 dpf than at 7 dpf, hinting at the possibility of developing regional specialisation: certain areas of the tectum have a denser representation of DS over OS, or vice versa. In order to more explicitly explore this possibility, parametric maps of the difference between the fractions of OS and DS ROIs were generated (**fig. 3.8**). These show an index of bias for one population versus another across the maps, by subtracting the fraction of DS density, corrected for imaging coverage, from the corresponding fraction of OS found in a pixel. By comparing two maps in this way, we can ensure that any regional specialisation observed is not due to sampling biases in visual space.

While at 3 dpf the differential fraction is extremely noisy (in part due to a very low number of OS ROIs), by 7 dpf there appears to be some semblance of structure, and this becomes more pronounced by 10 dpf (**fig. 3.8**). By 10 dpf, there is clear region of OS bias in the central tectum, with a DS bias in peripheral regions: particularly in the ventral/caudal regions. This equates to greater representation by DS in the temporal/ regions of lower areas of visual space, as illustrated in **fig. 3.9**, which visualises how visual space is reciprocated in the tectum.

106

3.3.2 Topographic order

In order to examine the topographic order within DS and OS maps in a qualitative
fashion, parametric maps of the receptive field locations to which ROIs in different
tectal locations responded were produced (**fig. 3.9**). Qualitatively, it appears that
the DS maps more accurately reflect visual space than the OS, showing a cleaner
colour gradient, at all ages. It appears that both maps are only coarsely ordered
at 3 dpf, and are far more ordered at 7 dpf, with a less clean gradient seen at 10
dpf. Comparing with **fig. 3.7**, it becomes apparent that the peak in DS density
corresponds to the anterior/upper region of visual space in both 7 and 10 dpf
animals. However, note that due to pooling of data across subject and the fact
that individual subjects did not necessarily view the screen from the same angle,
order is better judged from descriptive statistics which take this potential issue into
account (see **chapter 2**) than to visually examine maps where this problem cannot
be fixed.

Age (dpf)	ROI type	total n	Monte Carlo n	p (N_{shuf} = 1000)
3	DS	1010	391	0.001
3	OS	250	90	0.001
7	DS	3385	1027	0.001
7	OS	1706	573	0.001
10	DS	1296	449	0.001
10	OS	978	313	0.001

Table 3.2: DS and OS maps are statistically significantly topographically ordered, at all
ages. p-values represent the probability that the level of topographic order observed could
occur by chance given the distributions of points in both visual and tectal spaces, tested
via randomly permuting point correspondences in the tectum (see **eq. (2.22)**). Monte Carlo
subsample sizes were chosen as described in **section 2.3.6**.

These qualitative trends were then examined quantitatively, using the multisubject
euclidean distance correlation described in **Chapter 2**. As expected, DS and OS
maps are statistically significantly topographically ordered at all ages, relative to
chance (**table 3.2**). Comparing between maps, at all ages the DS map is statistically
significantly more ordered than the OS (**fig. 3.10 and table 3.3**). Examining the
topographic order of the DS and OS maps at 3,7 and 10 dpf shows that DS and
OS follow the same trend: maps are very poorly ordered at 3 dpf (although they are
all significantly ordered relative to randomly-permuted versions), becoming more
ordered at 7 dpf. However, the map order then decreases from 7 to 10 dpf. This is
consistent with the qualitative properties of **fig. 3.9**.
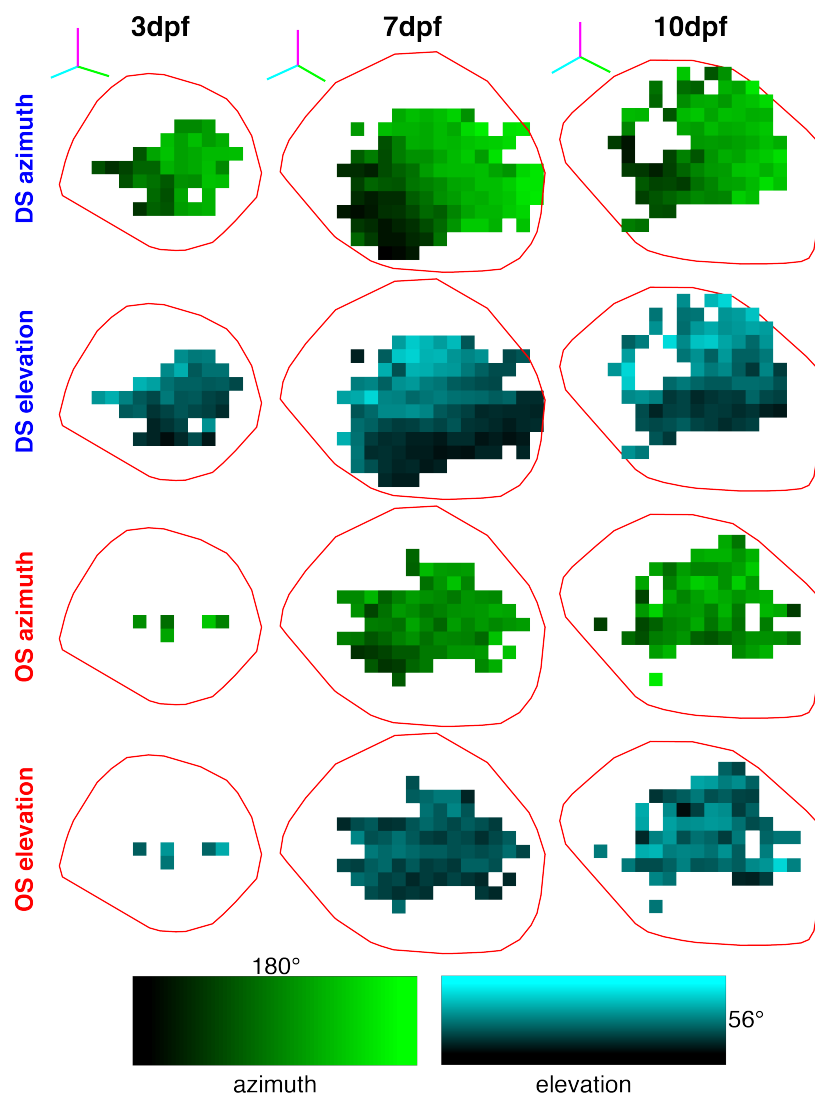
Figure 3.9: **Maps of azimuth and elevation for DS and OS ROIs**. Each pixel with >3 ROIs of the relevant functional type is coloured according to the mean azimuthal/elevational coordinate of the receptive field centres of the ROIs within it, as described in section 3.2.4.
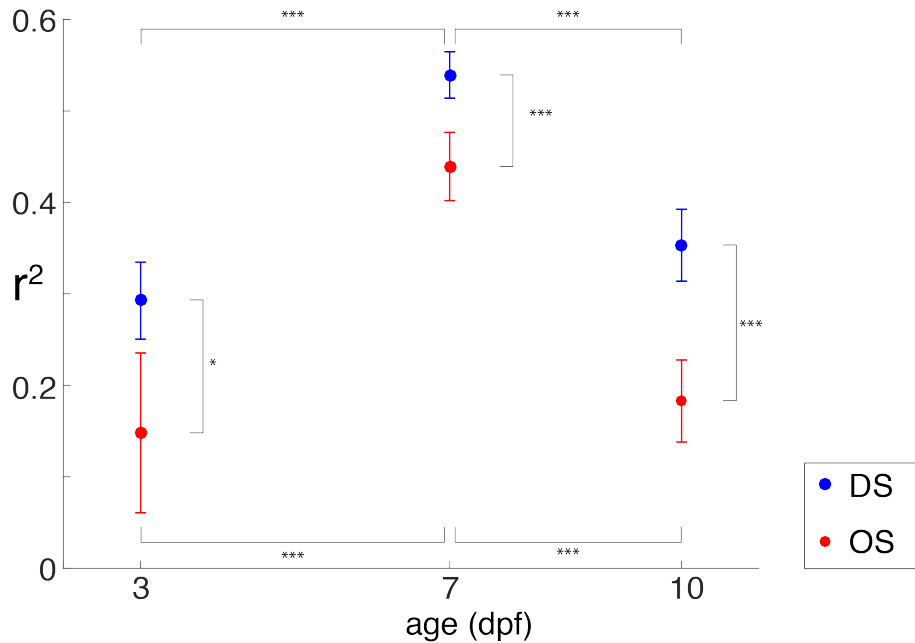
Figure 3.10: **Topographic order for DS and OS maps in the tectum from 3-10 dpf**, calculated using the multiple-subject modified euclidean distance correlation metric described in **chapter 2 and eq. (2.12)**. Error bars represent standard deviation of 1000 monte-carlo resampled maps (**section 2.3.6**), using all data, subsampled according to the sizes in **table 3.2**. Significance: * indicates p<0.05, * indicates p<0.01, ***indicates p<0.001. Precise p-values shown in **table 3.3**.

Group 1	Group 2	p (q=0.2)
3 dpf - DS	3 dpf - OS	0.0089
7 dpf - DS	7 dpf - OS	0
10 dpf - DS	10 dpf - OS	0
3 dpf - DS	7 dpf - DS	0
7 dpf - DS	10 dpf - DS	0
3 dpf - OS	7 dpf - OS	0
7 dpf - OS	10 dpf - OS	0

Table 3.3: **Statistics for pairwise comparisons of topographic order in DS and OS maps.** FDR-corrected p-values calculated as described in **section 2.3.6**, with $q = 0.2$, using Monte Carlo subsample sizes listed in **table 3.2**. Tests were performed with matched subsample sizes, in order to ensure fair comparisons where numbers of points were mismatched.

Further examination of **fig. 3.9** suggests that the azimuthal and elevational axes of visual space are not orthogonally represented in the tectum; the colour gradients do not appear to be in orthogonal directions. In order to examine quantitatively how the cardinal axes of visual space are reciprocated in the tectum, an heuristic approach based on topographic order was developed. Receptive field centres were projected on to only azimuth or elevational axes. Correspondingly, the locations of ROIs in the tectal topographic plane was collapsed into a 1D representation, following a rotation of the 2D tectal coordinates in the topographic plane. Calculation of the topographic order between these 1D projected maps allowed the generation of curves, shown in **fig. 3.11**, which show the measured 1D topographic order as a function of rotation angle. As the euclidean distance correlation examines pairwise distances and thus produces the same result if a map is inverted, these curves are periodic about 180°. The angle producing the peak topographic order represents the axis in which the corresponding visual axis is optimally represented.

For azimuthal and elevational axes, the phase difference of these curves gives the angle between the azimuthal and elevational axes within the tectum. If axes are truly orthogonal, this phase difference is precisely 90°, while deviations from 90° indicate that axes are non-orthogonal. None of these axes are orthogonal, as previously indicated at 7 dpf [52], indicating that the tectal map is nonlinear. At 3 dpf, the DS azimuth and elevation are separated by approximately 80°, while due to low numbers of OS ROIs there is a very large spread in the possible values of the phase difference. At 7 dpf and 10 dpf the maps are highly sheared, with approximately 60° between azimuth and elevation. The angles that optimally represent the cardinal axes of visual space can be seen overlaid onto the tectum in **fig. 3.12**.

Using the projection angles giving maximum topographic order with respect to azimuth/elevation, magnification factors [129] can be calculated for the cardinal axes of visual space. Magnification factors represent the distance in visual space that is travelled for a given distance across the tectal surface: in this case, measured in° μm^{-1}. Examining these magnification factors, shown in **fig. 3.13**, it appears that the elevational map is compressed relative to the azimuthal one, which can be seen qualitatively in the range of **fig. 3.9**. Is this a biological effect, or simply an artefact of the experimental setup? Clearly receptive fields (or parts thereof) which lie outside the screen cannot be recovered fully. Assuming that receptive field sizes for a single functional type are uniform across the visual field, those ROIs with receptive fields close to the edge of the screen will exhibit compressed receptive fields. Thus, the
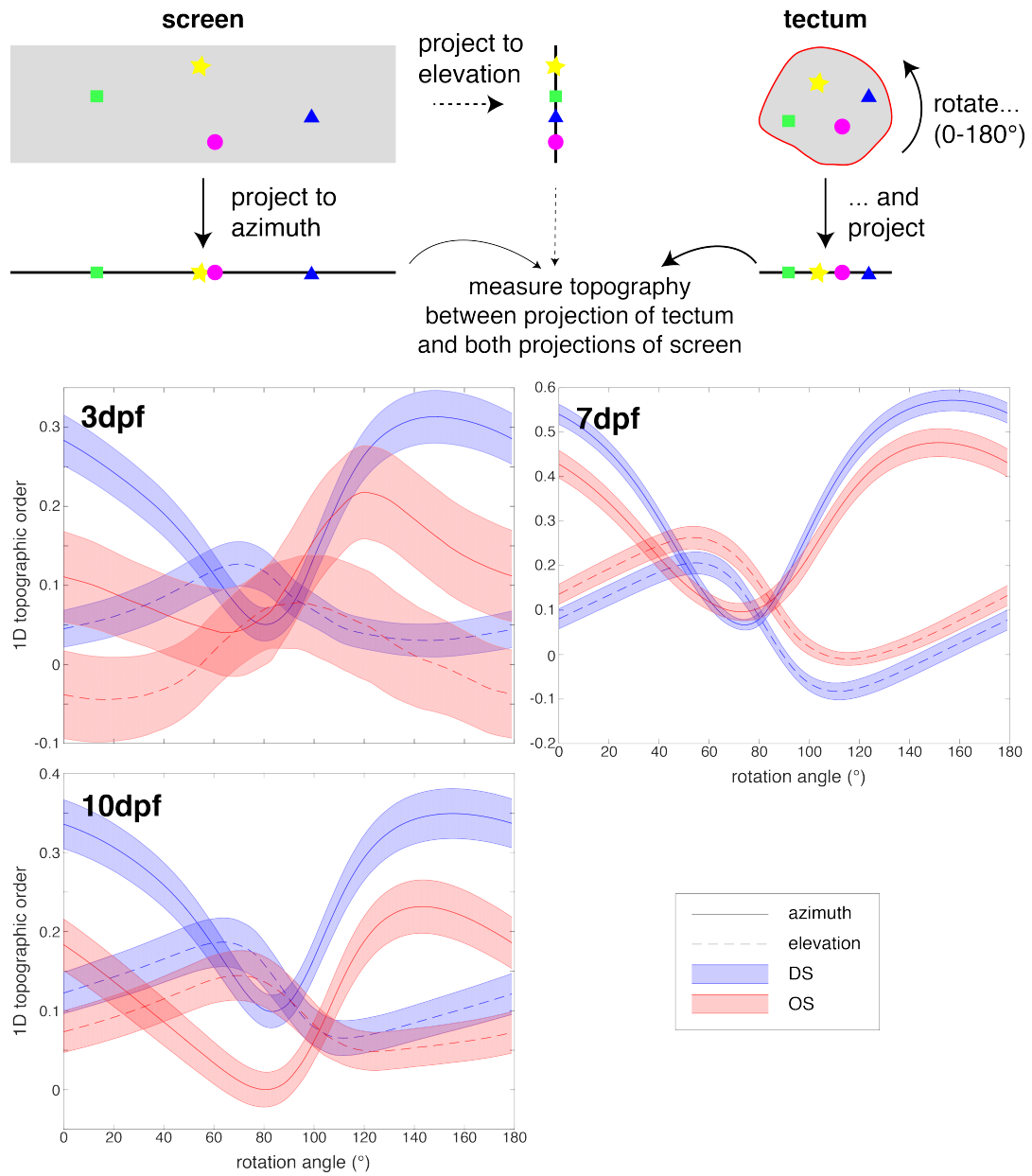
Figure 3.11: **Topographic order for rotated, 1D-projected OS and DS maps.** Error bars calculated using 1000 monte-carlo subsamples, with each subsample used for a full 180° rotation.
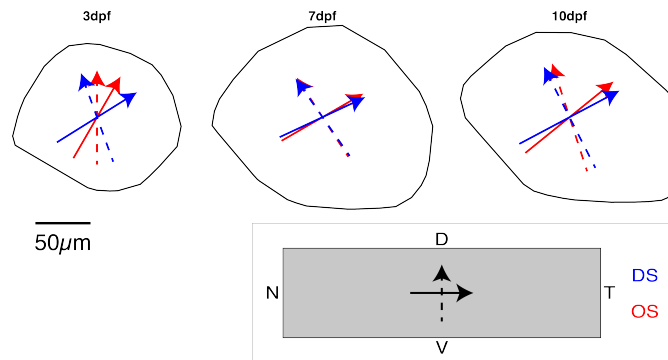
Figure 3.12: **Top:** The angles giving peak 1D topographic order and representing the azimuthal and elevational axes of visual space, determined from the maximum of the curves in **fig. 3.11** and indicated below. **Bottom:** The visual field as viewed by experimental animals, to indicate azimuthal and elevational axes.
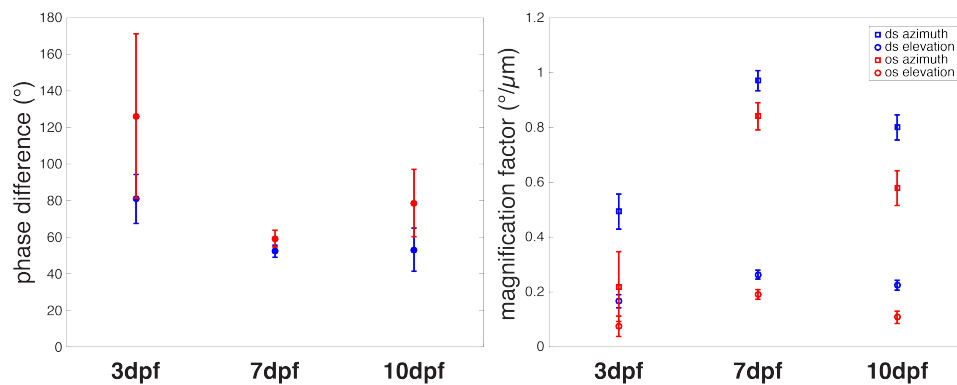
Figure 3.13: **Phase difference and magnification factors, as indicated by 1D topographic order in fig. 3.11**. Error bars are mean ± SD from 1000 resampled datasets. Phase differences were calculated within each subsample, as the angular shift of elevational topographic order giving the maximum circular cross-correlation with the azimuthal topographic order across rotation angles. Magnification factors were calculated as the gradient of a linear fit bmetween visual and tectal distances after the rotation/projection giving maximum topographic order (see **fig. 3.12**), as decribed in **section 3.2.4**.
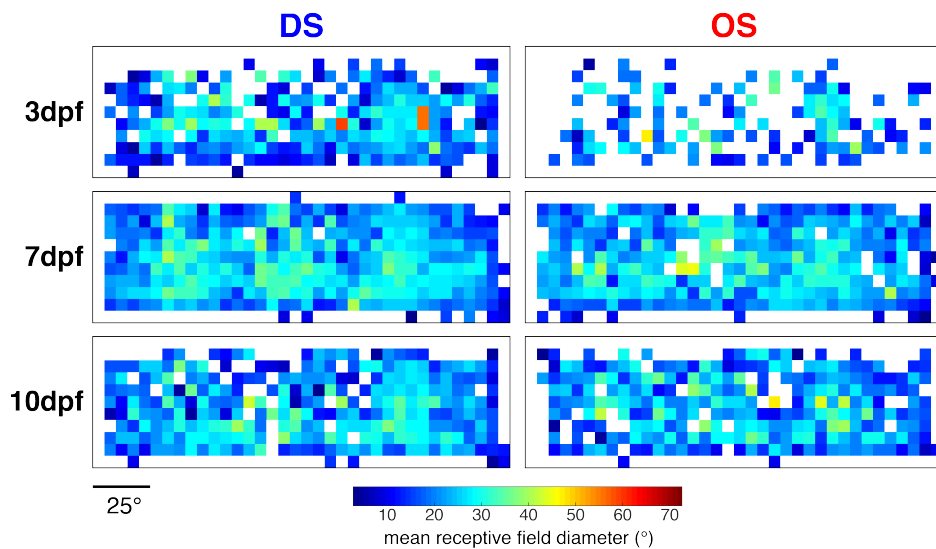
Figure 3.14: **Parametric maps of receptive field size, for DS and OS ROIs, projected onto the screen area used to present visual stimuli.** Receptive fields tend to be smaller at the borders of the screens, and this differentially affects azimuth and elevation due to the aspect ratio of the screen.

aspect ratio of the screens (see **Appendix A**) means that the elevational axis could be artificially compressed more than the azimuthal one. To examine whether such an effect exists, parametric maps of receptive field size in different screen locations were produced. As expected, receptive fields at the borders of the screens are smaller, and this compression affects proportionally more of the elevational axis than the azimuthal one (**fig. 3.14**), consistent with the hypothesis that elevational magnification factors are being underestimated more than azimuthal ones.

Finally, an attempt was made to quantify topographic order in units of biologically-relevant distance: that is, the distribution of how far each ROI is from where it might be situated if the visuotopic map were perfect. The deviations from perfect topographic order observed in DS and OS maps were interpreted as arising from the standard deviation (SD) of a symmetric 2D gaussian, using the technique described in **section 2.3.7**. This represents the distribution of how far each ROI in the tectum is from the position that would give perfect topographic order ($R^2 = 1$). The SD of the DS map reduces between 3 and 7 dpf, although the change is very small. It remains approximately constant at ~14 µm between 7 and 10 dpf. However, the OS distribution of distances is more dynamic: it is at its highest at 3 dpf, before decreasing to a distribution more similar to the DS at 7 dpf, and
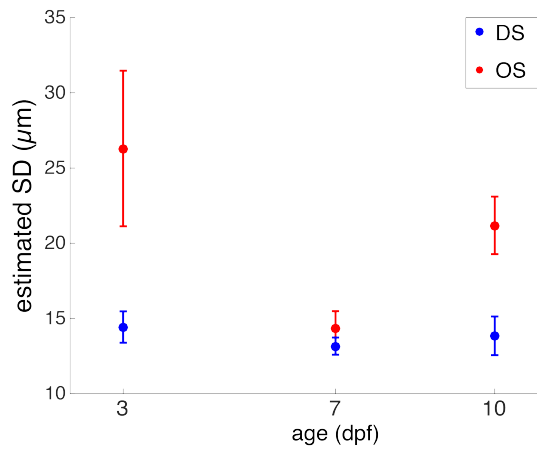
Figure 3.15: **2D standard deviation giving rise to deviations from perfect topographic order for DS and OS maps in the tectum from 3-10 dpf**, calculated using the multiple-subject modified euclidean distance correlation metric described in **eq. (2.12)**, with the SD estimated as described in **section 2.3.7**. Error bars represent standard deviation of 1000 monte-carlo resampled maps, using the subsample sizes described in **table 3.2**.

Age (dpf)	Type	Age (dpf)	Type	p (q=0.2)
3	**DS**	3	**OS**	0
7	**DS**	7	**OS**	0.0098
10	**DS**	10	**OS**	0
3	**DS**	7	**DS**	0.0051
7	**DS**	10	**DS**	0.23
3	**OS**	7	**OS**	0
7	**OS**	10	**OS**	0

Table 3.4: **Pairwise comparisons of 2D standard deviation giving rise to deviations from perfect topographic order in DS and OS maps.** FDR-corrected p-values calculated as described in **section 2.3.6**, with $q = 0.2$.

increasing again at 10 dpf to around 22 µm (see **fig. 3.15 and table 3.4**). However, given that axes are non-orthogonal, and that it appears that the angle between them changes over development (**fig. 3.13**), these estimates are an unreliable metric. However, they are consistent with diameters of axonal arbours described by sparse labelling of RGCs [33].

3.3.3 Receptive field sizes

An additional parameter to consider is the receptive field sizes of the two populations. Do receptive field sizes change over development? Do DS and
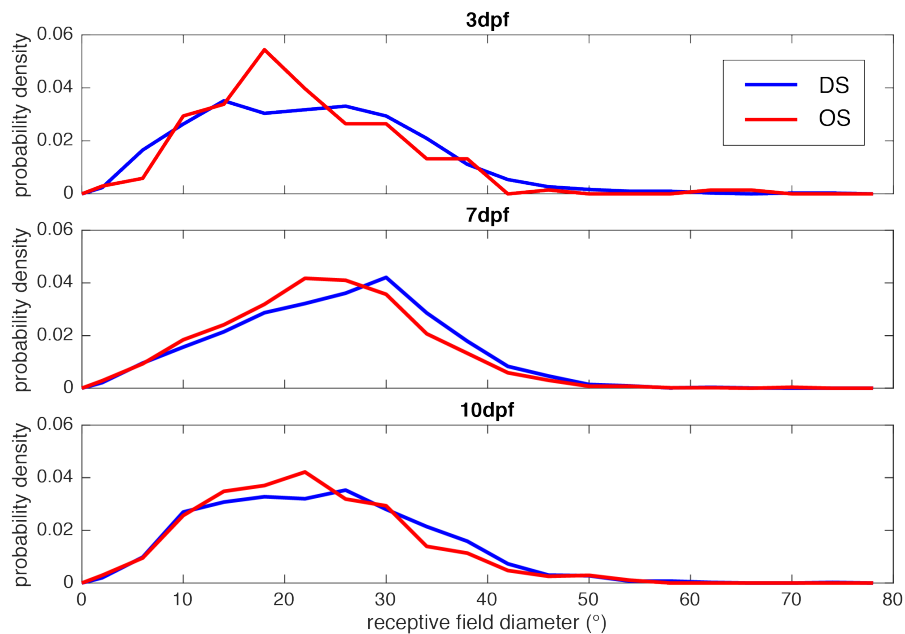
Figure 3.16: **Probability density disttributions for receptive field diameters of DS and OS ROIs across ages.**

OS populations have different sizes, and how might this relate to the topographic precision described earlier?

Overall, the receptive fields measured have a very wide spread, with a peak at ~20° (**fig. 3.16**). This is roughly consistent with a previous finding that both DS and OS RGCs have a mean receptive field size of ~24° at 7 dpf [52]. However, DS receptive fields are bigger than OS at 7 dpf, but the difference is small and is not present at either 3 dpf or 10 dpf (**fig. 3.16 and table 3.5**). Over development, DS receptive field sizes get bigger from 3 dpf to 7 dpf, but then shrink from 7 dpf to 10 dpf. However, no such changes can be seen in the OS population, which appear to have constant receptive field size (**fig. 3.16 and table 3.5**).

3.3.4 Map alignment

As demonstrated, previously, the tectum contains overlaid topographic maps of the visual field representing both direction and orientation of motion. These maps are expected to be in alignment: that is, points matched in the topographic plane are expected to represent the same location in visual space. In practical terms, if

	DF	F	p
Age	3	43.22	0
Type	1	44.86	0
Age*Type	3	3.41	0.0169

Age (dpf)	Type	Age (dpf)	Type	p	Significant?
3	**DS**	3	**OS**	0.8792	**NO**
7	**DS**	7	**OS**	0.001	**YES**
10	**DS**	10	**OS**	0.2328	**NO**
3	**DS**	7	**DS**	0	**YES**
7	**DS**	10	**DS**	0	**YES**
3	**OS**	7	**OS**	0.0566	**NO**
7	**OS**	10	**OS**	0.0214	**NO**

Table 3.5: **2-way ANOVA testing the effects of group and functional type on receptive field size,** performed using the *anovan* MATLAB function. Significance for pairwise comparisons is calculated using a Bonferroni correction (i.e. significant if $p < 0.0071$.)

a single electrode were stuck orthogonal to the topographic plane, it should hit the equivalent point in visual space. Do the maps appear in alignment, or do they emerge and then align progressively? To answer this question, the vector between visual space locations corresponding to the same tectal location in OS and DS maps, which represents the displacement between maps, was analysed (**section 3.2.4**). Such a measure is subject to a number of sources of noise: any eccentricities in the angle of the different fish relative to the screen; compression artefacts which affect magnification factor as above; and real topographic disorder in the maps being compared. Thus, for any single tectal location, it is unlikely that the displacement will be exactly zero. Maps are, as a result, said to be in alignment here if the distribution of displacements derived from multiple tectal locations is circular. Conversely, if there is a systematic displacement in a particular direction (meaning that the distribution is not circular), then maps are misaligned.

Age (dpf)	d.f.	z	p
3	6	1.378	0.26
7	14	1.524	0.221
10	14	0.736	0.486

Table 3.6: Rayleigh circularity test statistics for displacements between DS and OS maps.

As expected, none of the calculated displacements in visual space are precisely zero (**fig. 3.17**). However, the spread in displacements is small, representing less
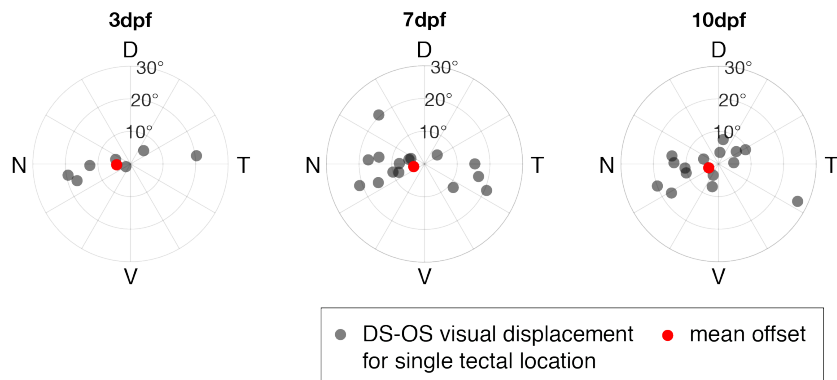
Figure 3.17: **Displacements between DS and OS maps in the tectum** for different ages of fish. Polar plots show such displacements for many tectal locations (see **section 3.2.4**), and mean displacement for each age group

than one receptive field width (**fig. 3.16**), and with mean displacements less than 5° at all ages. However, displacements in visual space appear to be uniform at all ages, given that distributions of displacements in each age group are circular (**table 3.6**). That is, maps are on average aligned in DS and OS laminae, at all ages. The increased spread in azimuth relative to elevation is likely to be due to the elevational compression artefact demonstrated in **fig. 3.14**.

3.3.5   Topography of angular selective variants of DS and OS RGCs

Having established global properties for DS and OS maps, I set out to examine the topographic properties of previously-identified angular selective putative variants of DS and OS RGC [38]. Do the RGCs selective for specific angles of motion have equivalent topographic order? Is there any evidence for regional specialisation at the level of OS and DS RGCs selective for different angles?

Using a wavelet-based clustering approach to classify variants of DS ROIs yields 3 variants, as previously shown [38]. The most abundant variant is selective for approximately horizontal nasal motion, while the remaining 2 are temporal/dorsal and temporal/ventral (**fig. 3.18A**). They exhibit qualitatively similar laminar distributions to previous work, found in adjacent but overlapping laminae (see **fig. 3.18C**), with the nasal/horizontal variant found most superficially, then the ventral/temporal variant, and the dorsal/temporal variant found deepest.

All variants are significantly ordered at all ages, with the exception of the 166°
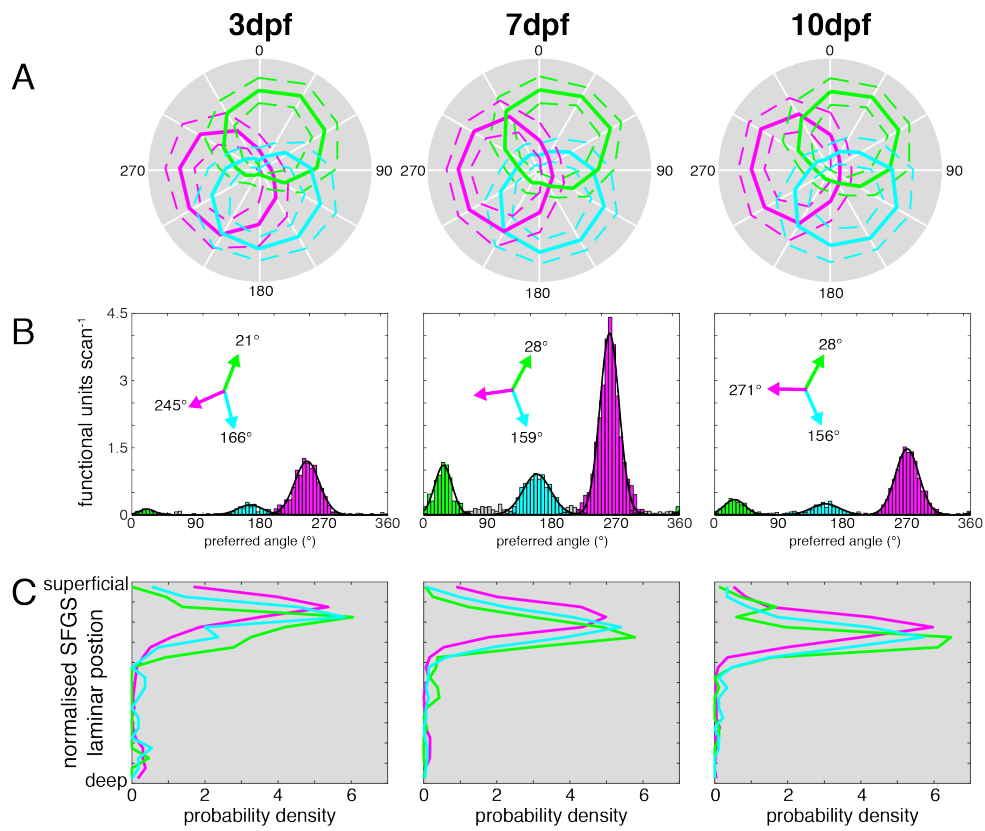
Figure 3.18: **Clustering of DS ROIs yields 3 variants. A** Mean normalised responses of variants to bar motion, ± SD, for each variant. The response vector for each ROI was normalised to its maximum prior to calculation of mean and SD. **B** Distributions of preferred angles, coloured by variant. Bin width is 5°. Inset represents peak preferred angles of variants, calculated from von Mises fit to each variant (shown in black). Bins are 5°. **C** Laminar distributions of variants, using normalised distance within SFGS as in **fig. 3.6**.

Age	DS variant	N fish	total n	p (N_{shuf} = 1000)	Monte Carlo n
3	245	10	754	0.001	183
3	21	7	49	0.001	25
3	166	7	136	0.263	n/a
7	261	16	2026	0.001	549
7	28	12	492	0.001	175
7	159	11	606	0.001	209
10	271	12	887	0.001	220
10	28	10	176	0.001	66
10	156	11	180	0.001	70

Table 3.7: **Descriptive statistics for angular-selective DS variants.** *N* represents the number of fish in which variant members were observed. *p* represents the proability that the observed level of topographic order could occur by chance, see **eq. (2.22)**. The subsample size used in significance testing was selected as described in **section 2.3.6**.

118

(ventral/temporal motion) variant at 3 dpf (see **table 3.7**). Its is possible, particularly with low numbers of ROIs, to fail to detect topography where sampling is sparse (see **fig. 2.8**). An additional consideration not accounted for in **Chapter 2** was the area covered by the sampled points: intuitively, if a map is ordered but contains noise, and the points sampled are all close together compared to the spatial scale of the noise, then topography would not be detected. The vast majority of ROIs found within this map were found within a small region of the tectum: ~40× 40 μm^2, (see bottom left panel of **fig. 3.19**), and the SD of gaussian noise accounting for deviations from perfect topographic order is 15 μm (see **fig. 3.15**), so it is quite possible that this failure to detect order is an artefact due to limitations within the dataset.

Map 1 age (dpf)	DS variant	Map 2 age (dpf)	DS variant	Monte carlo p (q=0.2)
3	245	7	261	0
7	261	10	271	0
3	21	7	28	0.872
7	28	10	28	0
3	166	7	159	n/a
7	159	10	156	0
3	245	3	21	0.0006
3	245	3	166	n/a
3	21	3	166	n/a
7	261	7	28	0
7	261	7	159	1
7	28	7	159	0
10	271	10	28	0.223
10	271	10	156	0.967
10	28	10	156	0.802

Table 3.8: **Pairwise tests for differences in topographic order between angular-selective DS variant maps.** Tests were only performed between maps found to have significant order.

In terms of their distribution across the topographic plane of the tectum, variants appear to be roughly equivalent, all showing a peak density in the posterior/dorsal area, and very few ROIs in the anterior/dorsal area (**fig. 3.19**, consistent with the pooled density, **fig. 3.7**). However, when examining topographic order, the variants are very different - topographic order cannot be detected in the temporal/ventral direction at 3 dpf (**table 3.7**), while the nasal-directed variant is as highly ordered as it is at 7 dpf. It is additionally more highly ordered than either other variant. By 10 dpf, all variants have equivalent topographic order (**fig. 3.20 and table 3.8**).
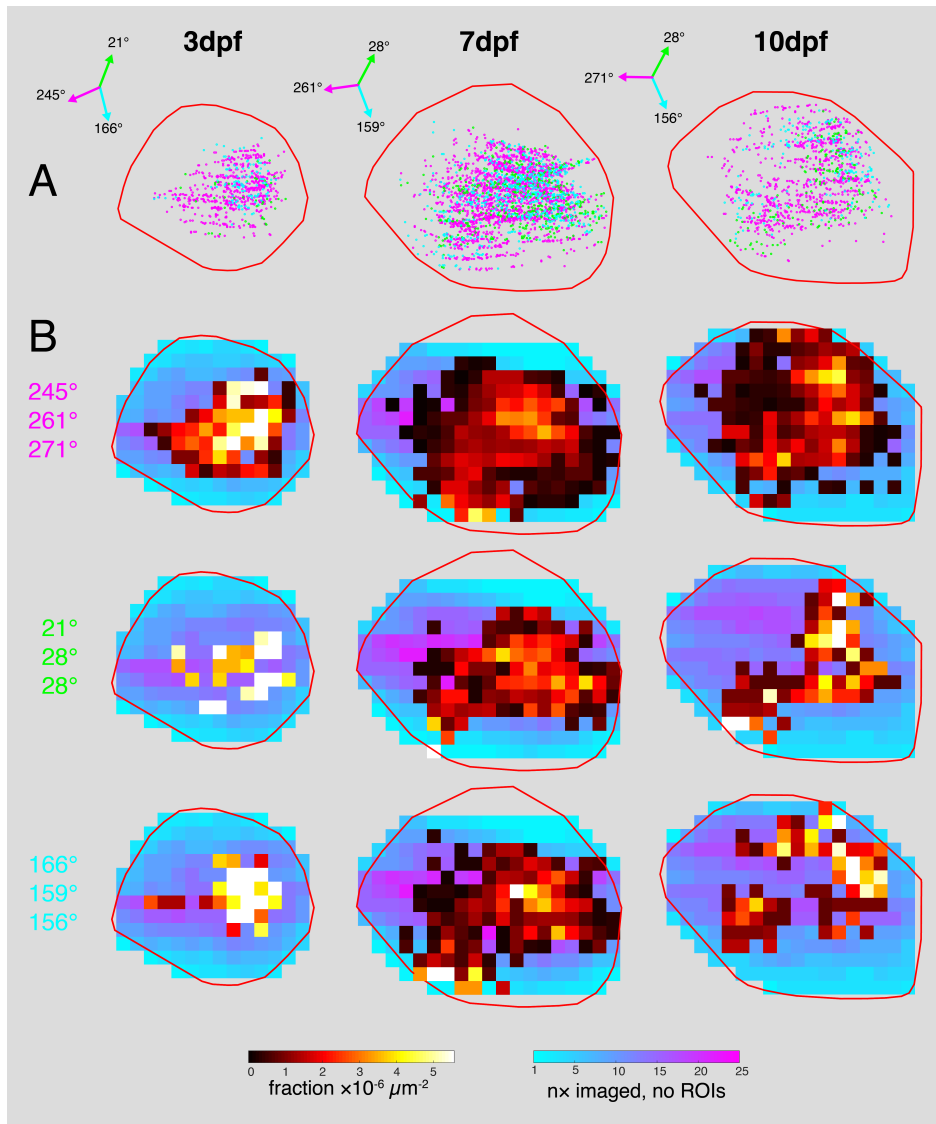
Figure 3.19: **Density of DS variants from topographic view. A** Raw locations of DS RGCs within the main lamina, coloured by variant identity. **B** Normalised densities calculated dividing the tectal surface in to 10 μm^2 bins, and dividing the number of ROIs within each bin by the number of times an imaging plane intersected the main DS lamina, as defined in **fig. 3.6**
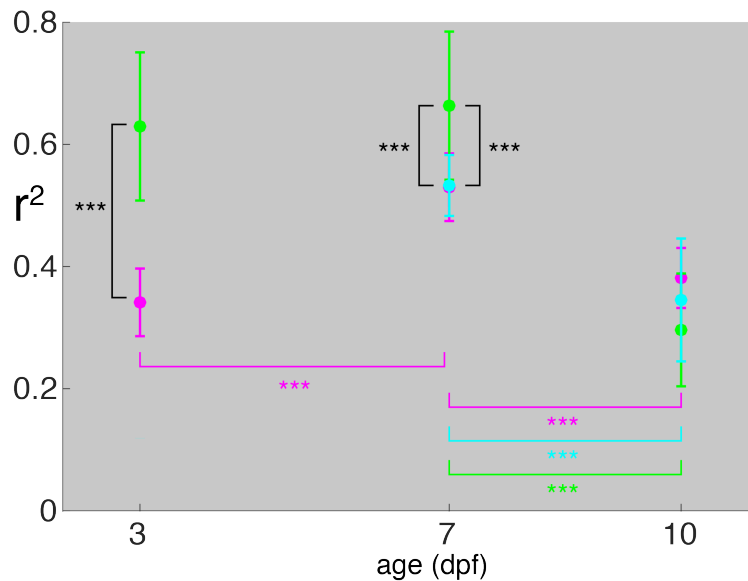
Figure 3.20: **Topographic order of DS variants over development** Error bars represent ± SD calculated from 1000 resampled datasets, using the sample sizes from **table 3.7**. Significance: * indicates p<0.05, * indicates p<0.01, ***indicates p<0.001. Precise p-values shown in **table 3.8**.

Similar clustering of OS ROIs yields 4 variants, spaced roughly equally within 180° (**fig. 3.21**). OS laminae are very ill-defined at 3 dpf: although there are few ROIs, the variants do not appear to segregate at all in the laminar axis (**fig. 3.21**). This is consistent with previously reported findings, that OS laminae emerge later than DS [38]. At 10 dpf, the secondary lamina of OS appears to be comprised almost solely of the horizontal OS RGCs, although there is a small contribution from the vertical variant. This is in contrast to previous findings [38], which found the secondary lamina to be composed of vertical OS.

Previous literature has found only one OS variant at 3 dpf [38]. It is possible that this discrepancy is due to the topographically restricted visual presentation, and tectal imaging, used in [38], combined with a biased representation in the topographic plane at 3 dpf. That is, within the region in which OS voxels could be discovered, there were very few OS ROIs from other variants. Lowe et al., 2013 [38] found most OS ROIs in the caudo-ventral region of 3 dpf animals (lower right in this thesis). However, my data does not indicate a particular bias for OS selective for 135-180° in this area at 3 dpf (**fig. 3.22**). At 7 dpf and 10 dpf, densities in the topographic plane are still noisy due to the low number of ROIs within each variant, making them
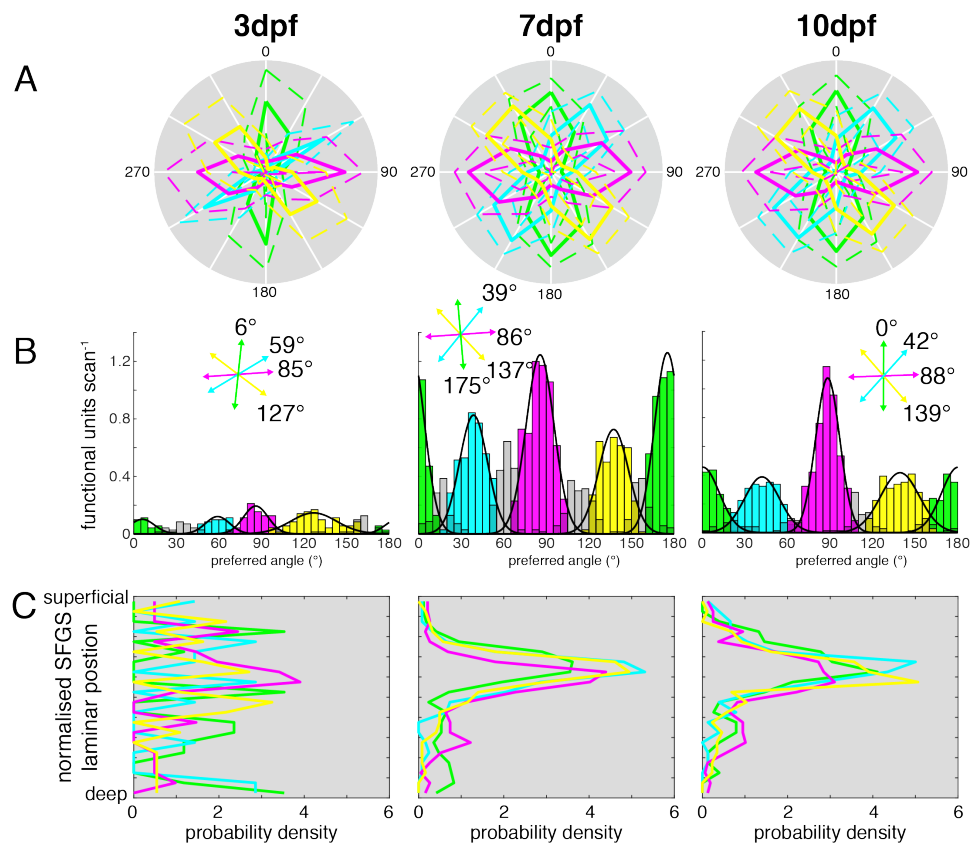
Figure 3.21: **Clustering of OS ROIs yields 4 variants. A** Normalised mean responses of OS variants to bar motion, ± SD. The response vector for each ROI was normalised to its maximum prior to calculation of mean and SD. **B** Distributions of preferred angles, coloured by variant. Bin width is 5°. Inset represents peak preferred angles of variants, calculated from von Mises fit to each variant (shown in black). **C** Laminar distributions of variants, using normalised distance within SFGS as in **fig. 3.6**. Abundance normalised to maximum within age group.

hard to interpret (**fig. 3.22**). However, at 7 dpf it still appears that the peak in density lies in the same tectal location for all variants, with the possible exception of the horizontal-selective variant which might have its peak more dorsally.

At 3 dpf, only the horizontal-selective variant was found to be topographically ordered **table 3.9**. However, with very sparse data (as in this case, see false negatives are possible as demonstrated in **fig. 2.8** - there could be coarse topography not detected in this dataset given the low number of ROIs in each of the variants **table 3.9**). Given that when the variants are pooled, topography is seen, this seems particularly likely. In additional support of this view, the horizontal-selective variant shows a similar level of order to the pooled dataset (~0.3, see **fig. 3.10**); the addition of the variants in which order cannot be detected does not lower the overall level of topography. By 7 dpf, all variants are ordered.

OS variant	N fish	total n	p (N_{shuf} = 1000)	Monte Carlo n
6	3	30	0.479	n/a
59	6	33	0.0701	n/a
85	5	57	0.001	20
127	7	79	0.0949	n/a
175	15	378	0.001	137
39	11	274	0.001	99
86	15	416	0.001	143
137	10	250	0.001	87
0	11	180	0.001	61
42	10	163	0.002	66
88	11	334	0.001	122
139	10	189	0.001	66

Table 3.9: **Descriptive statistics for angular-selective OS variants.** *N* represents the number of fish in which variant members were observed. *p* represents the proability that the observed level of topographic order could occur by chance, see **eq. (2.22)**. The subsample size used in significance testing was selected as described in **section 2.3.6**.

How do the relative abundances of the DS and OS variants change over development? The fractions do not remain constant, for either DS or OS (**table 3.11**). The fractions of each variant for DS and OS can be seen in **fig. 3.24**. As seen before [37, 38], the most abundant DS variant is that selective for motion in the nasal direction of the visual field. At 7 dpf, the other variants become more abundant, and by 10 dpf the fraction of nasal DS increases again, although the two other variants are then roughly equally-represented, in contrast to 3 dpf. The most abundant OS variant throughout is selective for approximately horizontal motion.
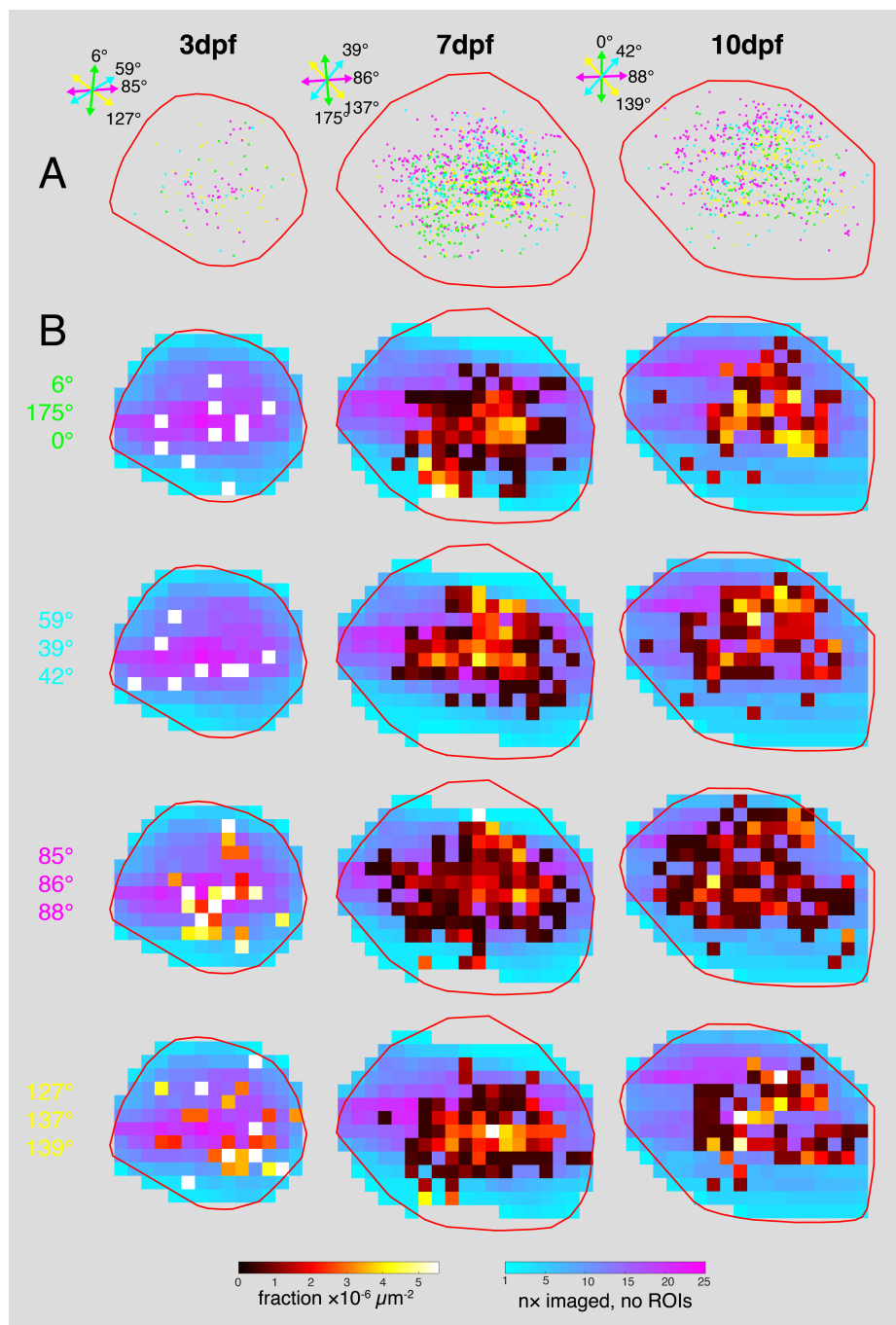
Figure 3.22: Density of OS variants, from topographic view. **A** Raw locations of OS RGCs within the main lamina, as shown, coloured by variant identity. **B** Normalised densities calculated dividing the tectal surface in to 10 µm^2 bins, and dividing the number of ROIs within each bin by the number of times an imaging plane intersected the main OS lamina, as defined in **fig. 3.6**. Colour scale where no ROIs were found represent the number of times a voxel was imaged.

Map 1 age (dpf)	OS variant	Map 2 age (dpf)	OS variant	Monte carlo p (q=0.2)
3	6	7	175	n/a
7	175	10	0	0
3	59	7	39	n/a
7	39	10	42	0.5325
3	85	7	86	0.1113
7	86	10	88	0
3	127	7	137	n/a
7	137	10	139	0.0473
3	6	3	59	n/a
3	6	3	85	n/a
3	6	3	59	n/a
3	2	3	85	n/a
3	2	3	127	n/a
3	85	3	127	n/a
7	175	7	39	0
7	175	7	86	0.0014
7	175	7	137	0.2181
7	39	7	86	0.2512
7	39	7	137	0.0209
7	3	7	137	0.9595
10	0	10	42	1
10	0	10	88	0.0892
10	0	10	139	0.9159
10	42	10	88	0.088
10	42	10	139	0.4093
10	88	10	139	0.0046

Table 3.10: Pairwise comparisons of topographic order between OS variants. Tests were only performed between pairs of maps found to have significant topographic order.
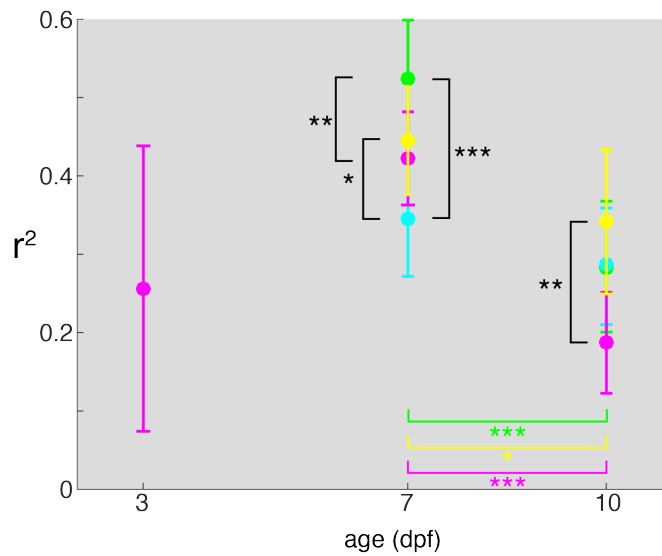
Figure 3.23: **Topographic order of OS variants over development.** Error bars represent ± SD calculated from 1000 resampled datasets, using the sample sizes from **table 3.7**. Significance: * indicates p<0.05, * indicates p<0.01, ***indicates p<0.001. Precise p-values shown in **table 3.10**. Only variants with significant order are shown.

As with the DS variants, 7 dpf is the age at which the variants are most equally represented.

	Comparison	d.f	X^2	p	Significant?
DS	**Global**	6	100.47	2.05E-19	**YES**
DS	3 dpf/7 dpf	3	73.8	6.45E-16	**YES**
DS	7 dpf/10 dpf	3	38.03	2.79E-08	**YES**
OS	**Global**	8	108	9.77E-20	**YES**
OS	3 dpf/7 dpf	4	21.5	2.50E-04	**YES**
OS	7 dpf/10 dpf	4	93.6	2.23E-19	**YES**

Table 3.11: X^2 **statistics for comparisons of abundance of DS and OS variants over development.** All p-values calculated using the MATLAB *crosstab* function. Significance levels are Bonferroni adjusted.

3.3.6   DS and OS RGCs selective for different contrast changes

Finally, I analysed the distribution and proportions of DS- and OS-RGCs selective for different contrast changes: the ON, OFF and ON-OFF populations. All combinations of DS angular-selective variants and contrast-selectivity were seen, at all ages. A similar result was seen for OS, with the exception of the

126
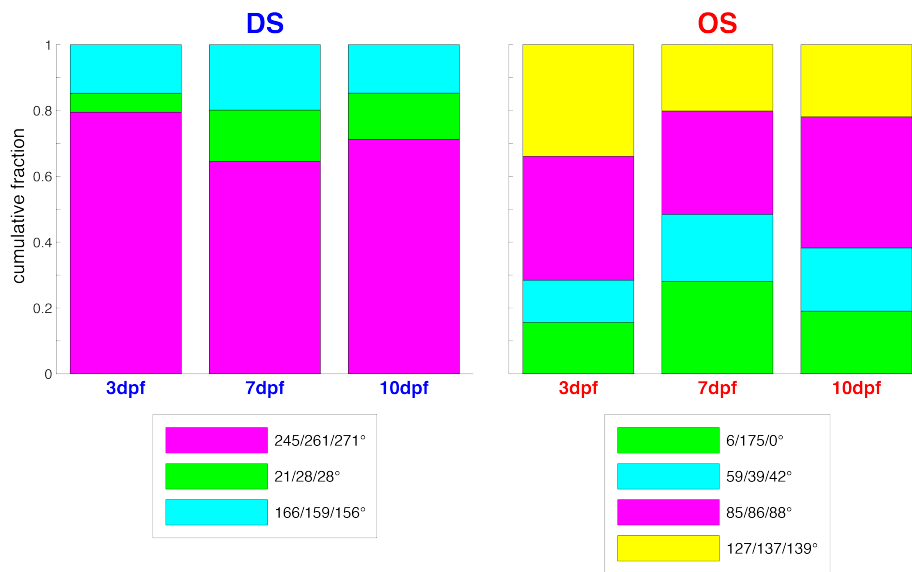
Figure 3.24: **Fractions of DS and OS ROIs, by angle-selective variant**, over development.

ON-OFF population at 3 dpf, which consists of only 3 ROIs. Examining the fractions of DS and OS ROIs specific for different contrast changes, there are statistically significant changes over development (**table 3.12**). While the DS-RGCs change from an OFF-dominant representation, to having many more ON-OFF, before returning to an OFF-dominant state, the OS maps remain OFF-dominant throughout (**fig. 3.25**). There are very few ON-OFF OS-RGCs, consistent with findings from the mouse retina [32].

	Comparison	d.f	X^2	p	Significant?
DS	**Global**	4	247.6	2.11E-52	**YES**
DS	3 dpf/7 dpf	2	168.8	2.22E-37	**YES**
DS	7 dpf/10 dpf	2	135	4.89E-30	**YES**
OS	**Global**	4	33.2	1.08E-06	**YES**
OS	3 dpf/7 dpf	2	16.7	2.33E-04	**YES**
OS	7 dpf/10 dpf	2	16.6	2.44E-04	**YES**

Table 3.12: X^2 **statistics for changes in contrast selectivity over development.** All p-values calculated using the MATLAB *crosstab* function. Significance levels are Bonferroni adjusted.

In order to investigate how RGCs selective for different contrast changes are organised within the tectum, their distributions within the standard tecta were examined. For both DS and OS populations, ON, OFF and ON-OFF populations do not appear to form separate laminae (**fig. 3.26**). That is, the probability densities
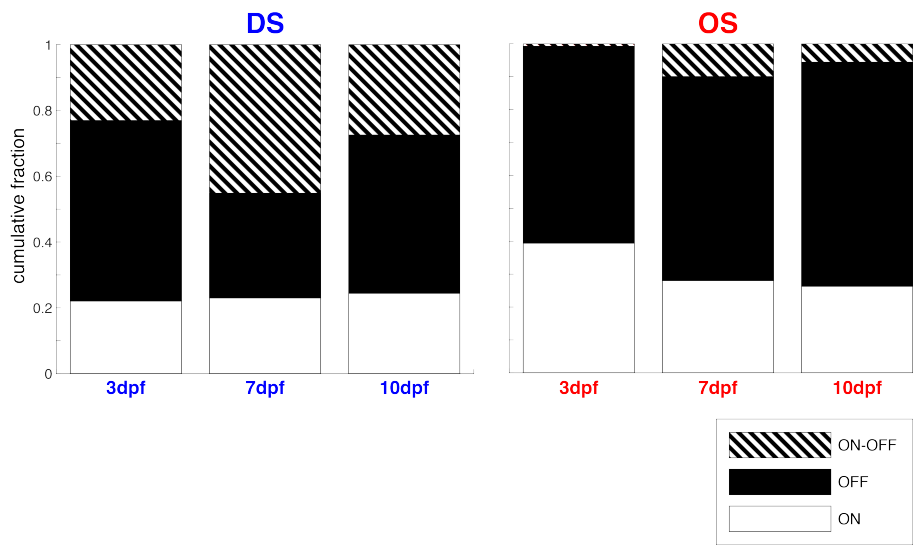
Figure 3.25: **Fractions of DS and OS ROIs selective for different contrast changes**, over development

across the laminar axes appear very similar to the pooled OS and DS distributions in **fig. 3.6**.

However, an additional hypothesis was that contrast-selective maps were overlaid within the laminae selective for each direction/orientation of motion. Representative example laminar distributions of ON, OFF and ON-OFF DS and OS ROIs for angular-selective variants are shown in **fig. 3.27**. There is no evidence for laminar segregation of contrast selectivity within angular variants. Overall, my data suggest that in fact there is no laminar separation of contrast-selective DS or OS ROIs within the tectal neuropil.

Similarly, examinations of densities in the topographic plane (**figs. 3.28 and 3.29**) show no regions that appear to have particular biases for ON, OFF, or ON-OFF selective DS or OS ROIs; the peaks and troughs in density appear to match almost perfectly between contrast-selective variants, in both DS (**fig. 3.28**) and OS (**fig. 3.29**) maps, aside from the fact that the more abundant contrast-selective types (for example ON-OFF DS at 7 dpf) cover more of the tectal surface, and the less abundant classes have noisier distributions (for example, ON-OFF OS at 10 dpf); effects which are to be expected.
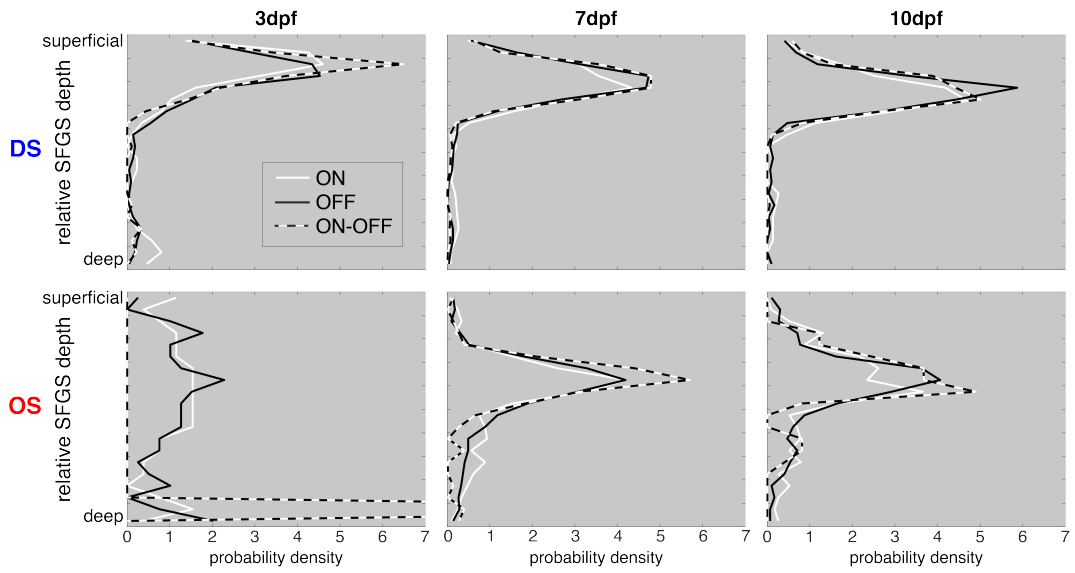
Figure 3.26: **Laminar distribution of DS and OS ROIs selective for different contrast changes.**
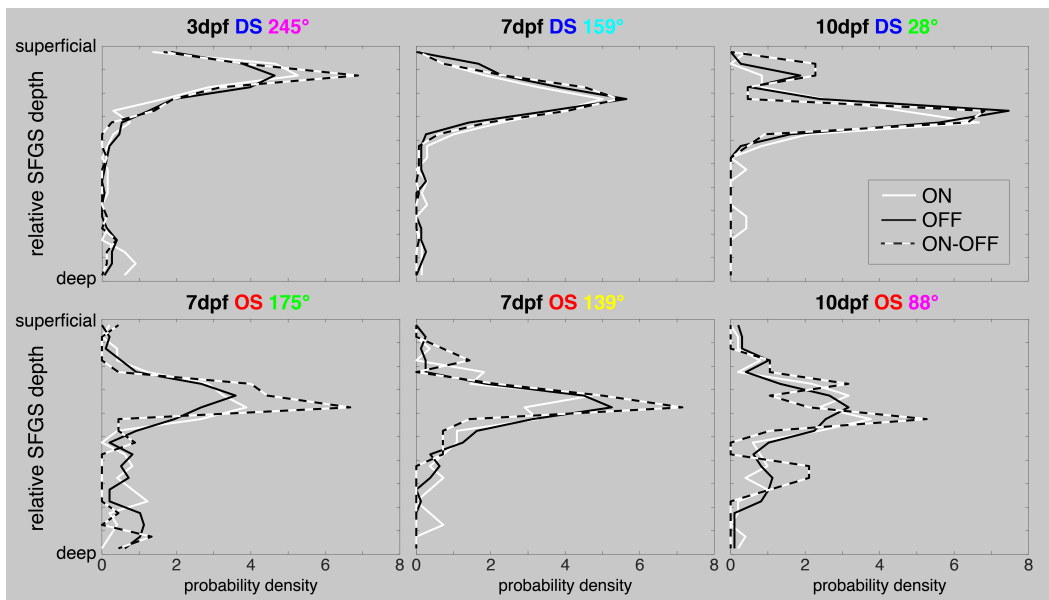
Figure 3.27: **Representative examples of laminar distributions of DS and OS ROI variants selective for different kinds of contrast changes.**

129
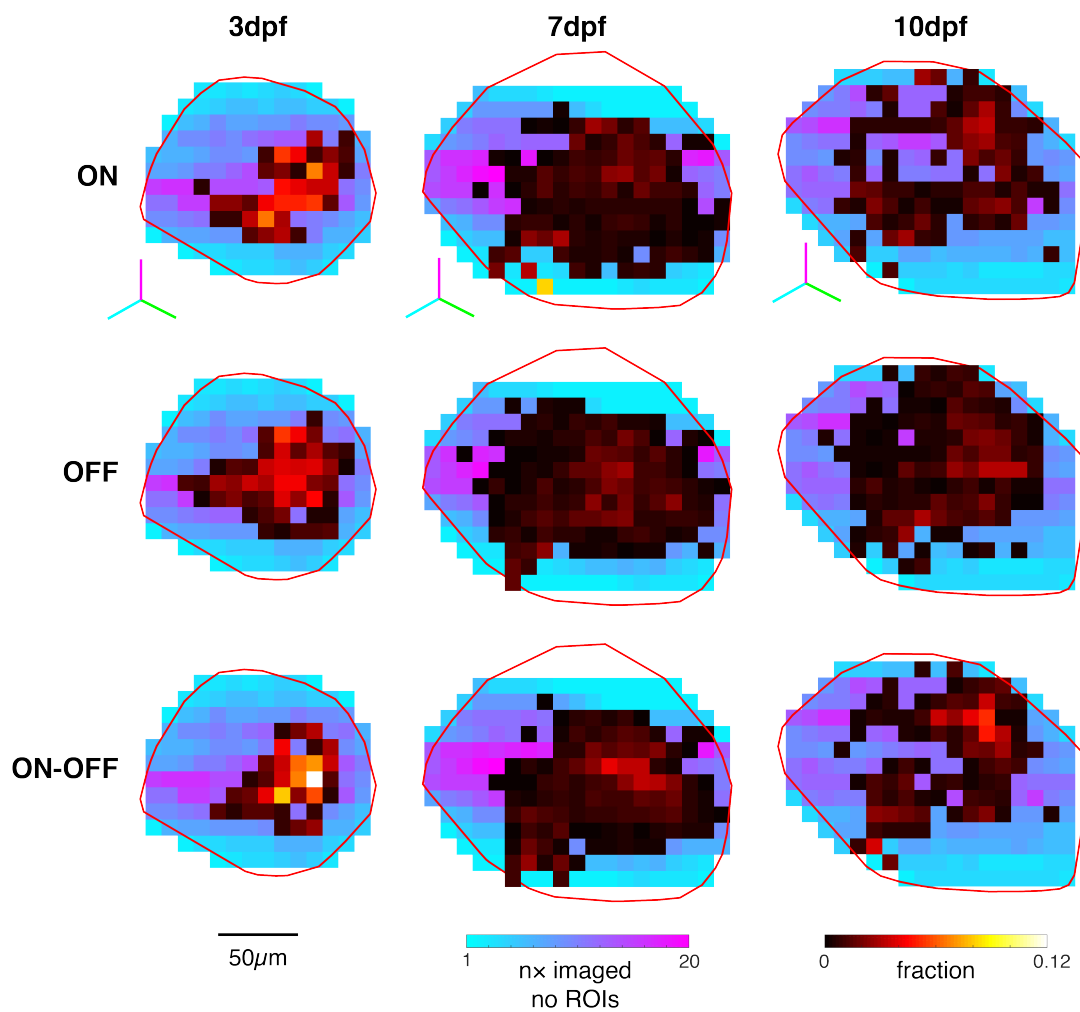
Figure 3.28: **Distribution of contrast-selective DS ROIs in the topographic plane,** corrected for imaging coverage.
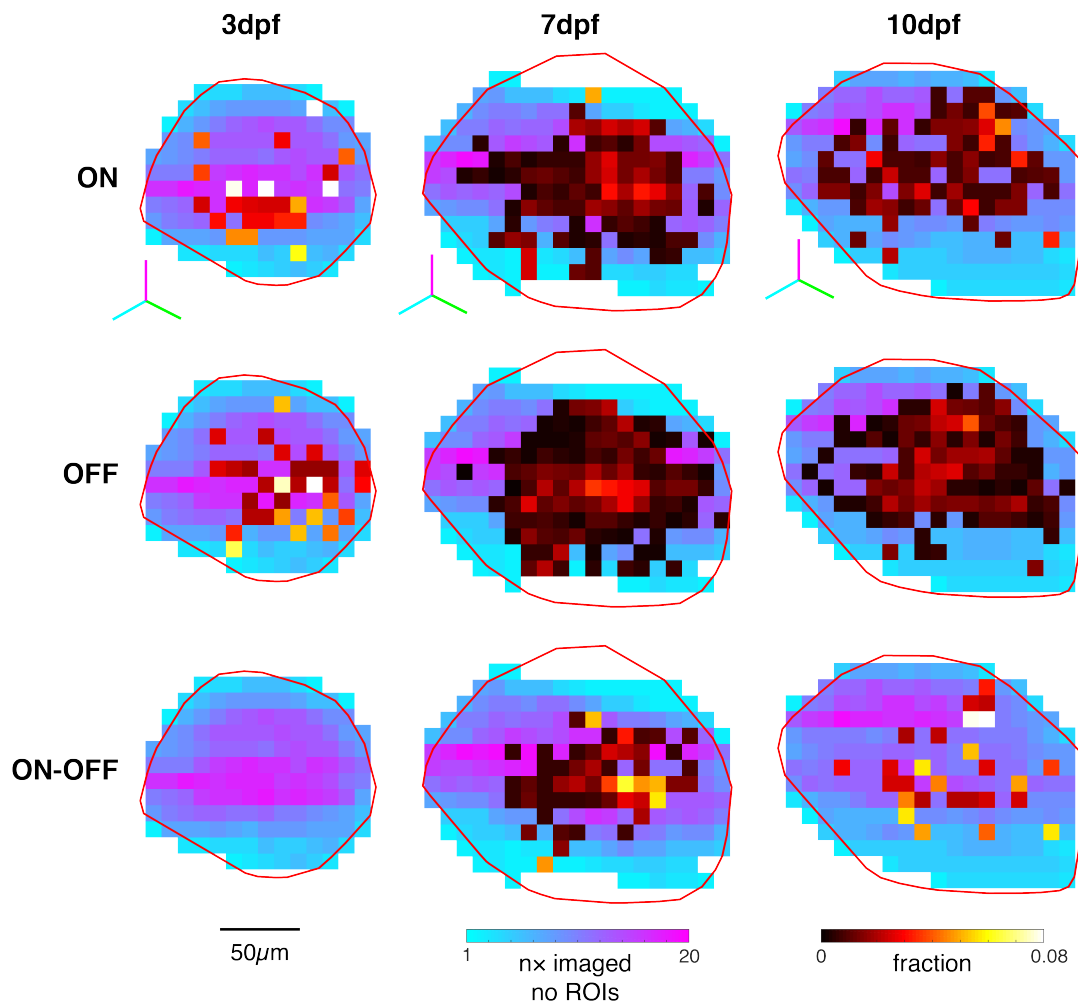
Figure 3.29: **Distribution of contrast-selective OS ROIs in the topographic plane,** corrected for imaging coverage.

3.4 Discussion

In this chapter, I used synchronised visual stimulus presentation and imaging of a genetically-encoded calcium indicator, combined with standardised spaces representing the tectum, to characterise the topographic maps formed by the axons of two functional types of feature-selective RGCs, at 3 developmental timepoints. I examined the distributions of DS and OS ROIs (representing the presynaptic axon terminals of RGCs) within standard tecta, revealing that the axon terminals of these two functional types of RGC are distributed in a manner that strongly suggests regional specialisation for detection of the different features represented by these RGCs.

I quantified the levels of topographic order within the DS and OS maps, showing that the the maps representing visual space become more ordered from 3 dpf to 7 dpf, but less ordered from 7 dpf to 10 dpf. Additionally, DS maps are more ordered than OS at all ages. I additionally demonstrated that the cardinal axes of visual space are represented non-orthogonally in the tectum, and that the angle of this non-orthogonality changes during development. No misalignment could be detected between maps formed by DS and OS ROIs at any of the ages tested.

When split into their angular-selective variants, it does not appear that there is regional specialisation with respect to different directions or orientations, although the maps formed by the angular-specific variants do change differentially across ages. Examining the distributions of DS and OS ROIs selective for positive or negative contrast changes, reveals no organisation of RGC inputs into contrast-specific laminae, or bias with respect to regions of the topographic plane.

3.4.1 Reduction in number of ROIs from 7 dpf to 10 dpf

It is striking that far fewer DS and OS RGCs are identified in 10 dpf fish than 7 dpf fish, even when corrected for imaging coverage (**table 3.1 and fig. 3.7**), as seen before [38]. Could the reduction in ROI number represent a reduction in RGC numbers? Apoptosis in the visual system is a well-documented part of normal development, in a number of species [202]. Although apoptosis does occur in zebrafish RGCs during normal development, this peaks at around 3 dpf, with only around 1% of neurons affected [203], meaning that it is extremely unlikely to

account for the reduction in numbers observed here.

The reduction in numbers could be a consequence of lowering expression levels of the fluorescent label, which has been observed repeatedly in similar transgenic lines [191]. Such reduction is likely to lead to reduced signal-to-noise and a higher false negative rate during ROI selection. If this were the case, it is unlikely to bias the analyses presented here: qualitatively, the OS and DS laminae did not exhibit different levels of fluorescence, meaning that artefactual reductions in ROI number are unlikely to be biased towards OS or DS. Additionally, quantifying the level of order (as described in **Chapter 2**) should not be affected by the number of ROIs present, beyond the uncertainty with which it can be quantified.

An additional possibility is that functional selectivity might change over same period: that is, stimuli used might less closely match the selectivity of the neurons being measured, according to their size, spatiotemporal frequencies or luminance increment/decrement. This possibility will be discussed further in **section 3.4.5**.

Given that each ROI most likely represents a synapse, rather than the axonal arbour of an entire RGC, could the reduction be as a result of synaptic pruning? Previous literature is contradictory: one study examined the number of synaptophysin-labelled puncta in single RGC axons, finding that the number of such puncta remains constant over between 7 and 10 dpf period [57]. However, the receptive fields of tectal neurons get larger from 4-6 dpf, and shrink from 6-8 dpf, as a consequence of changing retinotectal connectivity over that time frame [204]. Such a finding is consistent with the change in ROI numbers observed here; a greater number of synapses from RGCs could mean that tectal neurons integrate over a larger area of visual field. However, the increase and subsequent decrease of tectal receptive fields [204] could also be interpreted as being a downstream of the changes in receptive field sizes of RGCs shown here.

What could be the ethological significance of a reduction in RGC-tectal synapse number from 7 dpf to 10 dpf? It could be specifically to drive sharpening of receptive fields [204], or it could potentially be interpreted as being due to maturation of tectal circuits [148], meaning that less input is required for efficient decoding of the visual field [147].

3.4.2 Development of topographic order

The axes of visual space are represented non-orthogonally in the tectum, at all ages tested (**fig. 3.13**). This is consistent with previous findings at 7 dpf [52]. Of particular interest is the rotation of the cardinal axes of visual space over development: changes from 3-7 dpf are far greater than from 7-10 dpf, when the axes are approximately 70° apart.

My data could be interpreted as indicating that the elevational magnification factor is smaller than that of the azimuthal (**fig. 3.13**) - however, this is likely an artefact of the visual presentation system used (**fig. 3.14**). Measuring magnification factors is additionally vulnerable to topographic disorder, meaning that the measurements made here are likely underestimates.

Overall, both DS and OS maps are least ordered at 3 dpf, becoming more ordered at 7 dpf, and then less ordered at 10 dpf. At all ages tested, the DS topographic map is more ordered than the OS indicating that different features are encoded with different precision (**fig. 3.10**). Interestingly, while the degree to which maps are ordered follows the same trend for DS and OS, quantifying the noise leading to deviations from perfect order in biological distance units showed a disparity between DS and OS: the SD of the DS ROIs stays constant at roughly 15 µm, while the SD of the OS ROIs starts very high (at around 25 µm), then decreases to be similar to the DS at 7 dpf and increases back up to around 20 µm at 10 dpf (**fig. 3.15**). Due to the presence of nonlinearity in the maps, these rough estimations are prone to error. Such estimates of biological distances are, however, consistent with anatomical studies which find axonal arbours to have diameters mostly between 25 µm and 50 µm [33]. An important next step would be to examine whether the axonal arbours of DS and OS RGCs differ in size - however, as discussed in **section 1.1.1**, it is both labour-intensive and technically challenging to examine both functional selectivity and morphology without genetic markers for the functional types.

The finding that both DS and OS maps have less order at 10 dpf than at 7 dpf is surprising, in that it has been widely assumed that refinement of neuronal connectivity during development would lead to increased topographic order [145]. Under this model the maps would become more ordered from 7 dpf to 10 dpf, as well as from 3 dpf to 7 dpf.

My data provides empirical support for the theoretical view, found in [146, 147],

that topographic maps are in fact limited in their potential for encoding information and that the underlying algorithm used by the tectum to decode the visual scene might be based around an alternative, at least at later developmental timepoints. This view suggests that molecular mechanisms for generating topographic order early on are an useful heuristic for generating rough connectivity, but that as the balance of forces controlling connectivity shifts from molecular pre-specification toward activity-dependent plasticity [58], the map is superseded by some more sophisticated decoding model. One way of asking whether this is the case is to alter the visual experience of the fish during development, and to ask how topographic order is affected, an idea which will be explored in **Chapter 4**.

3.4.3   Directions/orientations of motion obey different developmental rules with respect to topographic order

We have seen that with DS RGCs, there are 3 easily-identifiable variants which respond to different angles, and 4 similar variants of OS RGC (**figs. 3.18 and 3.21**). Qualitatively, these variants appear to develop in similar ways with respect to their tectal distributions (**figs. 3.19 and 3.22**), although their abundances differ (**fig. 3.24**). Differences in the progression of topographic order are evident for both DS or OS variants, with maps encoding specific directions/orientations of motion more ordered at different ages: at 3 dpf and 7 dpf, the most ordered DS map is that encoding dorsal/temporal motion, while the most ordered OS map is that encoding vertical motion. However, by 10 dpf those differences disappear for DS maps, and are far smaller for OS, making statements about their potential ethological significance difficult. Regarding the distributions of the variants within the tectum, laminae containing RGCs selective for the different angles have been seen previously [38], and were recapitulated here. As expected, DS laminae were already present at 3 dpf, while OS laminae appeared progressively from 3-10 dpf. With regard to distribution across the topographic plane, it is difficult to make statements regarding the distributions at 3 dpf given the low numbers of ROIs from each variant, but at 7 dpf and 10 dpf, they appear to be roughly equally distributed over the topographic plane in both DS and OS.

Recent work in the adult mouse superior colliculus has revealed strong topographic biases for nasal or temporal motion in collicular neurons [141]. However, it is not clear whether, or how, this bias relates to the organisation of RGC inputs, for which

no known similar bias exists [141]. It will be interesting to examine whether such a bias also exists in zebrafish tectal neurons, and how this relates to both RGC inputs and intertectal projections, which have been unexplored so far at the functional level.

3.4.4   Organisation of contrast-change selective RGCs

While the DS-RGCs change from an OFF-dominant representation, to having many more ON-OFF, before returning to an OFF-dominant state, the OS maps remain OFF-dominant throughout (**fig. 3.25**). ON-OFF OS RGCs, entirely absent in the mouse [32], appear to be present at very low abundance - it is possible that these are false-positives. There were no particular combinations of angular- and contrast-selective variants that were absent - in contrast to the mouse, in which the only ON DS population is upward-motion selective. Generally, OFF-dominance is to be expected from studies of visual areas in many other vertebrates, mice [32], cats [205, 206], and macaques [207], and from psychophysical measurements in humans [208, 209]. This OFF-dominant representation has been demonstrated to be optimal for the statistics of natural images [210].

Are the DS and OS laminae composed of specific angular-selective variants subdivided further into ON, OFF, ON-OFF sublaminae? The data presented here suggest this is not the case (**fig. 3.27**), in contrast with the mouse superior colliculus, where direction- and contrast-selective RGCs occupy distinct laminae [28, 211, 212]. However, it is possible that the standardised spaces used here do not have sufficient resolution with respect to biological variability; although angular-selective sublaminae can be visualised, contrast-selective sublaminae could be even smaller. In the zebrafish, RGCs selective for different contrast changes may not require "separate" maps, unlike in the retina, in which the ganglion cells take their contrast selectivity from the laminar position of their dendrites within the inner plexiform layer, across vertebrates [29]. However, lack of laminar segregation does not preclude the separate usage of contrast channels in downstream processing: the formation of clear laminae are in fact not required for the emergence of functional properties in downstream tectal neurons, at least in the case of orientation selectivity [81], meaning that alternative mechanisms for synaptic specificity operate.

3.4.5   Development of regional specialisation

I explored the distribution of DS and OS ROIs within standardised tecta, in part to examine whether both functional types of ROI are distributed uniformly, and to examine the possibillity of regional specialisation for the detection of particular visual features.   Qualitatively, the "hole" in the anterior/dorsal region of the topographic plane for OS and DS maps is more prominent at 10 dpf than at 7 dpf (**fig. 3.7**). Additionally, over the course of development, is appears that certain areas have a bias towards OS/DS representation, with central areas of the tectum biased toward OS, and peripheral areas biased towards DS (**fig. 3.8**). This indicates that either OS and DS axonal arbours develop differentially, adding/removing more or less synapses within different regions of the tectum, or that their functional selectivity changes differentially across the retina. However, definitively disambiguating these two possibilities is hard to test without examining a larger stimulus space, given that the angular-selective and contrast-selective variants of DS and OS do not appear to be differentially spread over the tectum. It is entirely possible that the areas in which both DS and OS appear sparser, corresponding to the anterior/dorsal visual field, still contains both OS and DS but that their spatiotemporal tuning is different to that tested. For example, if such an area were specialised to detect the presence and position of prey, then we might easily expect to find smaller DS and OS sensitive to faster movement and smaller objects (i.e. faster temporal and smaller spatial frequencies). A next step in this direction would be to look for regional biases in RGC dendritic morphology within the retina within specific types of RGC. In absence of genetically-defined RGC types, a sparse-labelling approach allowing both functional identification and neurite tracing of RGCs would certainly be an option. An alternative might be a high throughput approach to functional characterisation of flat-mounted retinae, similar to that of Baden et al., 2016 [32], which could give insight into regional biases.

Recent findings from the larval zebrafish retina indicate that the visual field is not uniformly represented at the level of photoreceptors, and of bipolar cells [30]. These findings have been linked to the spectral properties of the zebrafish natural environment.   My data suggest that at the level of RGC inputs to the tectum, the visual scene is not uniformly represented with respect to motion direction and orientation. Can the natural statistics of visual features like motion be similarly linked to ethologically significant biases in what the fish has around them?

Alternatively, are certain visual features more likely to be ethologically significant if they are present in certain parts of the visual field, requiring denser representation? Certainly, the probability of initiation of prey capture behaviour depends on the location of prey within the visual field [213]. Does this dependence exist as a result of regional specialisation within the retina and tectum? This is a hard question to answer, and would likely require a larger stimulus set to more precisely characterise the differences in functional selectivity found over different parts of the visual field.

3.4.6   Development of visual topography is not monotonic

A number of measured parameters including topographic order (**fig. 3.10**), the relative numbers of ROIs selective for particular contrast changes (**fig. 3.25**), DS receptive field sizes (**fig. 3.16**), and the abundances of angular-selective DS variants (**fig. 3.24**) change in one direction from 3 dpf to 7 dpf, but then change in the opposite direction from 7 dpf to 10 dpf. Such opposing changes in organisation suggest that visual development proceeds in stages rather than being a continuous, monotonic change from an immature to mature state.

Although it seems likely that the changes in map properties from 7 dpf to 10 dpf are a shift from an intermediate to a more adult-like organisation (particularly as they are roughly concurrent with huge behavioural change), the possibility cannot be excluded that there are additional stages in development of the visual system. There are later behavioural alterations, which also might coincide with alterations in visual drive, such as the development of social behaviour which is absent at 7 dpf, but develops between 10 and 21 dpf [214, 215].

The idea that the development of the visual system proceeds in stages is consistent with work on zebrafish tectal receptive fields, which found that tectal receptive fields grow from 4-6 dpf and shrink from 6-8 dpf, as a result of changes in retinotectal connectivity [204]. Spontaneous activity in the tectum is similarly affected, with assemblies of frequently-coactive neurons becoming more compact from 4-6 dpf, but then increasing in size later on [148]. What could the ethological relevance of these changes in retinotectal connectivity, and connectivity within the tectum, be? It is tempting to ascribe them to behavioural changes such as the emergence of hunting behaviour at around 5 dpf [186], or the recognition of conspecifics, which could emerge as early as 7 dpf [187, 214].

Alterations in the visual system that occur around the same time as the emergence of specific behaviours could be a consequence of alterations in the statistics of the visual environment as a result of changes in the motion of the fish. For example, as the fish begins to hunt (perhaps due to changes in connectivity elsewhere), the statistics of its visual input will be changed, meaning that activity-dependent plasticity mechanisms will change retinotectal wiring accordingly. Alternatively, such changes could be genetically hardwired but temporally coincidental, perhaps even permissive for, such behavioural shifts. The most obvious example of such a permissive change would be something akin to the emergence of "bug detector" neurons in the frog retina [216]. One way of disambiguating whether changes to visual topography are up- or downstream of behavioural changes is to examine how the maps respond to alterations in visual environment, which will be the focus of **Chapter 4**. If map properties are severely affected by visual drive, this is evidence in favour of the hypothesis that changes in visual physiology are downstream of behavioural changes; if not, then the changes are are more likely to be hardwired and permissive for hunting.

Chapter 4

Effects of altered visual experience on visual topography

4.1 Introduction

Having characterised how the topographic maps formed by DS- and OS-RGCs change over development, I next sought to examine how these properties were affected by visual experience. This is particularly interesting given the changes from 7 dpf to 10 dpf, with maps becoming less precise. What is the role of visual experience in creating this change; are the effects of plasticity dependent on visual experience actively disordering the maps? How does visual experience feed into other parameters, like contrast selectivity, and the different angles of motion that are encoded? Is the maintenance of alignment between maps an experience-dependent process?

Previous work indicates that silencing RGC axons increases the dynamicity and size of their arbours during development, altering how neurons compete for space within the tectum [217]. This raises a key question: when the statistics of visual experience are altered during development, presumably changing the relative activities of the different types of RGC, are the relative domains of those RGC types altered? Unfortunately, the original study did not make any distinction between axonal arbour shapes in the topographic and laminar axes, roughly corresponding to alterations in domain within- or between-type respectively. However, more recent

work indicates that dark-reared animals do not have deficits in the structure of tectal laminae when examined in totality [76].

In dark-reared fish, the functional properties of OS and DS RGCs were not altered at 7 dpf, with the same balance of angular-selective variants [38]. Likewise, the overall distributions in both laminar and topographic axes were unchanged in the dark-reared fish. However, more recent data indicates that there is no displacement in visual space between OS and DS maps on WT 7 dpf fish, but there is in dark-reared fish [52]. In light of the continual movement of RGC axons across the tectal surface due to mismatched growth of retina and tectum [124], this displacement can be interpreted as arising due altered migration, meaning that movement of OS maps across the tectum is retarded by visual experience, while the DS map is similarly affected but to a lesser extent [52].

In order to further explore whether the effects of visual experience on the developmental alterations in map properties, I performed experiments to examine the effects of visual experience on map properties at 10 dpf. Wild-type (WT) data within this chapter are the same as that used in **Chapter 3**, and three additional conditions were considered, with animals reared as far as possible in their altered environments up until the point of imaging.

Fish were reared as far as possible in environments where no light is present at all, in order to completely remove visual experience (Dark reared, DR). Based on the data in **Chapter 3**, if modifications of retinotectal connectivity due to visual experience were leading to the decrease in topographic order seen between 7 dpf and 10 dpf, then both DS and OS maps should have greater topographic order at 10 dpf in DR animals. Such an effect has been seen at 7 dpf, but only in DS maps [52].

Fish were reared in an "enriched" visual environment (enriched reared, ER), which should closer match the natural statistics of a real zebrafish habitat, containing relatively close-up 3-dimensional objects (gravel). The hypothesis being tested was that the statistics of visual information experienced impact on the organisation of visual information during larval development, rather than just any visual experience. Providing a richer visual environment, with more varied visual statistics, gives a contrasting experiment to the DR, and was expected to also give opposite effects on the properties of the maps formed, making DS maps less precise than their WT counterparts.

Strobe rearing (SR) was chosen as a way to isolate the effects of motion on how maps are organised. The hypothesis being tested was that maps encoding different features should be differentially affected by this manipulation. In direct support of this hypothesis, strobe rearing has been previously shown to impact on the morphology of RGCs in the goldfish [104], apparently having differential effects on morphologically-defined types of axonal arbours (although no functional characterisation was attempted). Parameters were selected based on findings across many species, in an attempt to create a visual experience in which images could be discerned by RGCs and their tectal postsynaptic partners, but the movement of the bars used as stimuli across a typical RGC receptive field could not.

Animals were reared to 10 dpf under these different conditions, and the same experiments as in **Chapter 3** performed, allowing the characterisation of the distributions, functional properties and map organisation of DS and OS RGCs axon terminals in the tectum.

4.2 Methods & Reagents

4.2.1 Animals

As in **Chapter 3**, all animals were of genotype Isl2b:Gal4;UAS:SyGCaMP6s, reared in the same incubator and under all the same conditions as the WT fish in **Chapter 3**. Functional imaging was performed at 10 dpf according to the same protocol as in **Chapter 3**, using the same pool of adult animals to breed experimental larvae.

DR and SR fish were health-checked, fed and had their water changed under red light (625nm) to minimise visual experience, as zebrafish pigments are blue-shifted relative to humans [218]. Although they would still see images under these conditions, the total time they would be exposed was $\leq$ 15 minutes in total. Prior to imaging, the fish were removed from their altered environment for ~2 hours - a period which should allow their retinae to adapt to ambient light conditions (behaviourally, larvae habituate to changes in ambient light in under an hour [219]), but minimise developmental changes in retinotectal connectivity.

Experiments on the three altered-rearing conditions were performed contemporaneously, although all data from WT (10 dpf) experiments were acquired for **Chapter 3** had been previously acquired (~2 months previously). On any given day, only 2 animals were imaged, and parents used for generation of larvae were randomised throughout the period when experiments were being performed.

4.2.2 Dark rearing

Dark-rearing chambers (see **fig. 4.1**) were designed (using **https://www.tinkercad.com**) to completely isolate the fish from light while providing adequate ventilation. All components were printed using a Makerbot Replicator 2X (Makerbot). They were built such that interior surfaces of the ventilation tunnel could be painted with matt black paint (**https://culturehustle.com**) to avoid light reflecting in via the shiny black plastic.
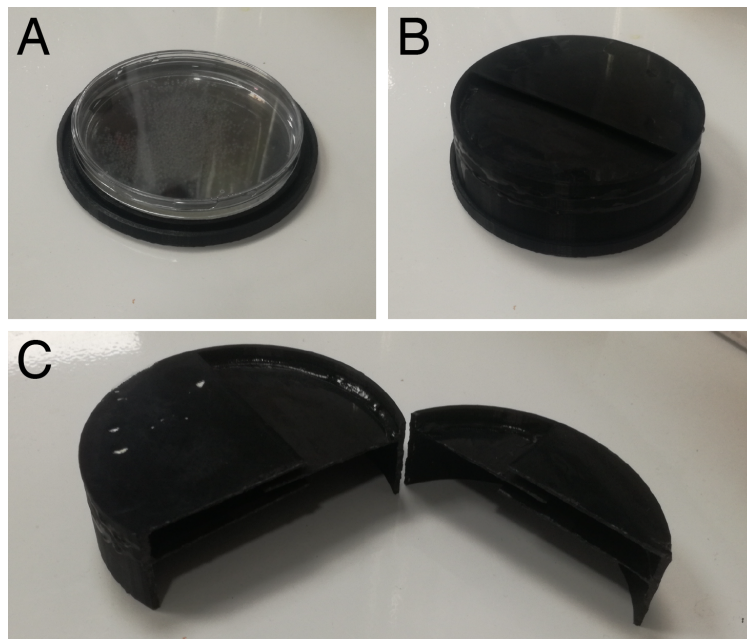
Figure 4.1: **Dark-rearing chambers. A** Base, with zebrafish embryos. **B** Complete dark rearing chamber. **C** Lid in cross-section, showing ventilation channel.

4.2.3 Enriched rearing

Fish were raised in petri dishes supported over a bed of gravel (**fig. 4.2**), with the same lighting conditions as the WT fish (see **section 3.2**). This should provide a more naturalistic environment, with closer 3 dimensional objects, shadows and sources of contrast compared to the sparse visual details in the incubator. Note that at no point did the fish have direct contact with the gravel, which was placed in a petri dish underneath that containing the fish, and sealed using a hot glue gun. Gravel was obtained from Branscombe Beach, South Devon, UK.

4.2.4 Strobe rearing

Using strobe rearing was designed to affect specifically neurons encoding motion - parameters were chosen to make sure that image-forming vision was possible (although this was not tested), but so that there was a reduced likelihood that motion could be encoded.

Figure 4.2: **Enriched-reared zebrafish embryos** on a bed of gravel in order to ensure a visual environment closer to that found in nature.

Rationale

The period with the light on must be smaller than the time over which RGCs integrate motion. In the Reichardt detector model, in which motion is detected via a coincidence detector with two inputs spatially separated in the direction of the motion to be detected and with one of them subject to a delay [220], this would correspond to the delay time, τ. No direct observations have been made of this parameter. Furthermore, the off period must be greater than the time over which these same RGCs integrate. These two conditions ensure that a single RGC has a reduced likelihood of encoding the motion during a single flash, and additionally will have reduced likelihood of creating motion-like artefacts by integrating over multiple flashes, as in the flicker-fusion effect.

Data on such parameters are difficult to measure for the zebrafish, due in large part to their reliance on psychophysical experiments. Behavioural experiments using the opotokinetic response have shown that sensitivity to moving gratings drops off sharply over 2-7Hz [221]. However, the cutoff of a behavioural response represents a lower bound on the highest temporal frequency of motion that can be encoded in RGCs. Thus, they must be inferred and data must be carefully interpreted in context of other organisms. Psychophysical measurements are also limited in their usefulness for inferring the properties of sensory neurons due to the many

nonlinearities present throughout the nervous system, meaning that behavioural output can be divorced from the properties of sensory input neurons. However, psychophysical thresholds for flicker fusion frequency (in humans) are recapitulated at the neuronal level in the visual thalamus of the macaque monkey, measured electrophysiologically [222]. Ideally, the ON-period of the strobe must exceed the time necessary for image-forming vision. This has not been measured in the zebrafish, but in humans and macaques, the minimal time for image-forming vision is 13ms [223, 224]. The ON-period was selected as 20ms. Tectal neurons have been shown to integrate over as long as 300ms [149]. This represents an upper bound on the integration period of RGCs, but due to retrograde signalling by tectal neurons onto RGCs, and the effects of this signalling on RGC axonal connectivity, this must be upheld within our study, and was set as the OFF-period.

One final question of design is the brightness of the strobe light during its ON period. In order to ensure that data obtained from SR fish are most comparable with those from WT and ER conditions, there are 2 alternatives for how to set the brightness. Either the peak brightness of the strobe should match the luminance inside the WT incubator (ensuring that the images the animals see have the same brightness), or the mean brightness over time should be maintained, meaning that the ON period is lighter than the WT incubator. Few studies have directly compared these alternatives. In hamsters, adjusting the peak luminance such that the mean luminance remained constant caused worse visual deficits than using the normal mean luminance as the peak of the strobe [225], albeit at the level of gross eye morphology rather than any functional properties. Brightness was adjusted so that the peak brightness of the strobe was matched to the luminance in the incubator for fish reared in WT/ER conditions.

Construction

Components were designed using **https://www.tinkercad.com**, and printed using a Makerbot Replicator 2X (Makerbot) and black ABS plastic (Makerbot). The lid used on the strobe chambers was the same as that for the DR chambers, allowing no light in while providing ventilation (see **fig. 4.1B, fig. 4.3B,C**). Light was provided by Rebel Star CW100 LEDs (Opulent), and their brightness was controlled using a RCD-24-0.70/W/X3 LED driver (RECOM). They were mounted to heat-sinks (MQ75-1, Aavid Thermalloy). Power was supplied using a dual 12V/5V DC PSU,

cannibalised from a laptop power supply.

Timings were programmed via a Teensy 3.2 (**https://www.pjrc.com**). The analog dimmer for the LED driver received input from a 5V PSU, via a 200KΩ trimmer potentiometer (3362P-1-203LF, Bourns) allowing the brightness of the LEDs to be altered after multiple chambers were connected. Multiple connectors were wired in parallel to allow >1 chamber to be connected simultaneously. The digital (PWM) input of the LED driver took its input from one of the binary (5V) outputs of the Teensy, which was programmed to cycle 20ms LOW (corresponding to light on), 300ms HIGH (corresponding to light off). All wiring was done on a Raspberry Pi Perma-proto soldered breadboard (Adafruit Industries). Wired connectors (129-6460, Binder) ensured that no chamber became disconnected from this board by accident during operation.

On top of the LED was mounted a white weighing-boat (611-0094, VWR), in order to diffuse the light and make it as uniform as possible over the dish. The petri dish containing fish rested on two petri dish lids, both covered in diffusing plastic sheeting to further equalise the luminance. For interior structure, see **fig. 4.3C**. The ambient luminance in the normal incubator was ~280 Lux, measured using an ILM1335 Light Meter (Iso-Tech), and the luminance of the strobe chambers was altered to match this during the on-period. The strobe light was powered according to the same 14 hour on/10 hours off cycle as the lights of the normal incubator.

4.2.5 Imaging and analysis

All imaging and analysis was conducted using the same parameters, protocols and pipeline as the WT animals, described **section 3.2**. Separate standardised spaces were made for each rearing condition. Subjects chosen for inclusion in the template for each group were first aligned to the WT 10 dpf template, prior to alignment with each other, maximising overlap with the WT template as far as possible in order to aid in gross morphological comparisons.
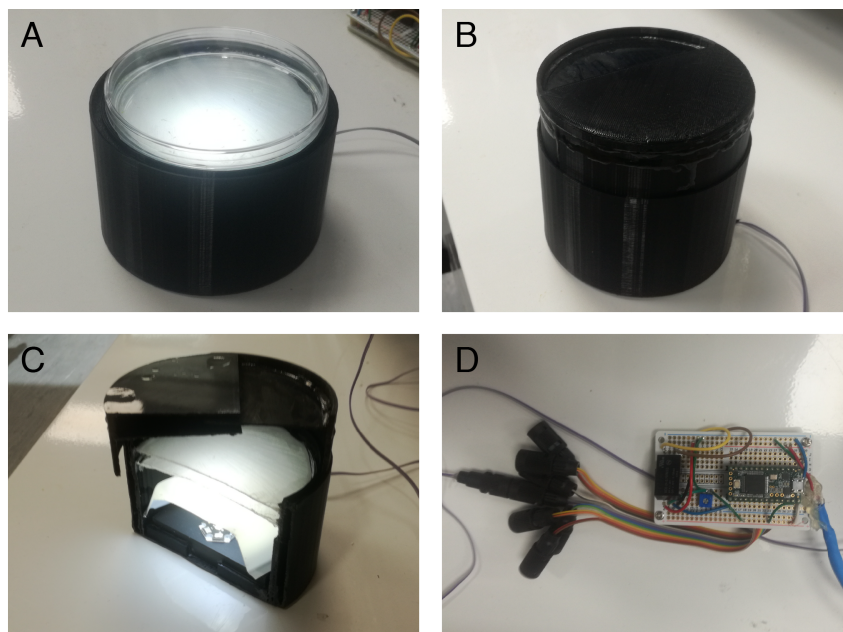
Figure 4.3: **Custom-built strobe-rearing chamber. A** View of fish living in interior, with LED on. **B** Complete chamber, with lid on. **C** Cross-section of a strobe-rearing base, showing LED with heat-sink, and multiple layers of optical-diffusing plastic. Cut using a Versatile Muti Tool with reciprocating saw attachment (Wickes). **D** the wired components.

4.3 Results

The same functional imaging and analysis pipeline as in **Chapter 3** was used, but on fish reared to 10 dpf in altered visual environments (N = 12 animals per condition). Three different environments were selected. DR: fish reared in complete darkness, ER: reared in a more naturalistic environment and SR: reared in custom-built strobe chambers. These environments were engineered as far as possible to ensure that no parameters other than the visual environment were affected (such as temperature and airflow). WT data shown here are the 10 dpf dataset presented in **Chapter 3**. Compared to the WT animals, there are changes in the numbers of ROIs found in these animals, with fewer of both DS and OS in the DR, and more in the ER condition. In the SR condition, there are fewer DS ROIs, but the number of OS ROIs is unaffected (**table 4.1**).

Rearing	ROI type	N	# scans	total n	n scan^{-1}	p
WT	DS	16	71	1296	18.3	N/A
WT	OS	16	71	978	13.8	N/A
DR	DS	12	52	562	10.8	0.0007
DR	OS	12	52	436	8.4	0.0133
ER	DS	12	49	2381	48.6	0.0258
ER	OS	12	49	1579	32.2	0.0038
SR	DS	12	51	759	14.9	0.0086
SR	OS	12	51	578	11.3	0.1401

Table 4.1: Summary of DS and OS ROIs in the SFGS tectal region, obtained from the functional imaging of lsl2b:Gal4; UAS:SyGCaMP6s zebrafish, reared in different visual environments. p-values shown are from the Wilcoxon rank sum test, calculated using the MATLAB *ranksum* function, comparing the number of ROIs per scan in each functional type to the WT equivalent.

4.3.1 Distributions of DS & OS ROIs in standard tecta

Separate standardised spaces were generated for each rearing condition (for volumes, see **table 4.2**). Examining the laminar distributions of DS and OS ROIs (**fig. 4.4**) showed that there are small differences in the positions of DS and OS laminae, potentially due to small inconsistencies in the shapes of the standard tecta, they are very similar in terms of extent and position of the dominant laminae. In one previous study, dark-reared animals did not appear to exhibit altered laminar structure when RGCs are pooled [76]. However, more recent work examining

functionally-defined RGC inputs to the tectum has given contrasting results, with small alterations in the laminar distribution of OS RGCs [38]. One observation is that the peak-to-peak distance between DS and OS laminae appears greatest for the ER condition, while it appears reduced in the DR and SR conditions relative to the WT - additionally, the widths of the laminae appear to follow the same trend (**fig. 4.4**).

Condition	SFGS volume ($\times 10^5$ μm^3)
DR	5.67
SR	6.32
WT	7.51
ER	7.76

Table 4.2: **Volumes of SFGS neuropil in standard tecta**, calculated as the convex hull volume of the manually-segmented mesh.
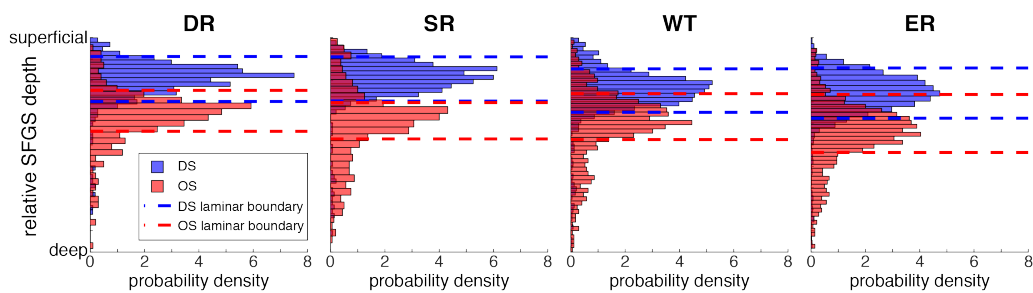
Figure 4.4: Probability densities in the laminar axis, by RGC functional type, from 10 dpf fish reared in different visual environments. Dotted lines represent 1 standard deviation from the mean of a single fitted gaussian, the laminar boundaries used to estimate coverage (in **fig. 4.5**).

In the DR and SR conditions, the distribution of ROIs appear to be more topographically restricted (**fig. 4.5**). There is an area of of increased DS density in the ventral/anterior quadrant, close to the point of optic nerve entry. All conditions appear to exhibit a similar "hole" in the density of DS and OS ROIs in the dorsal/anterior quadrant. Additionally, there is an apparent ventral (high) to dorsal (low) gradient in the density of both OS, and to a lesser extent DS, ROIs in the ER condition, which cannot be seen in any of the other conditions. The area of high DS density close to the optic nerve entry point in DR animals is particularly interesting: previous work has indicated that some axons terminate prematurely when silenced [69, 95].

The difference of OS and DS density appears to exhibit roughly the same structure
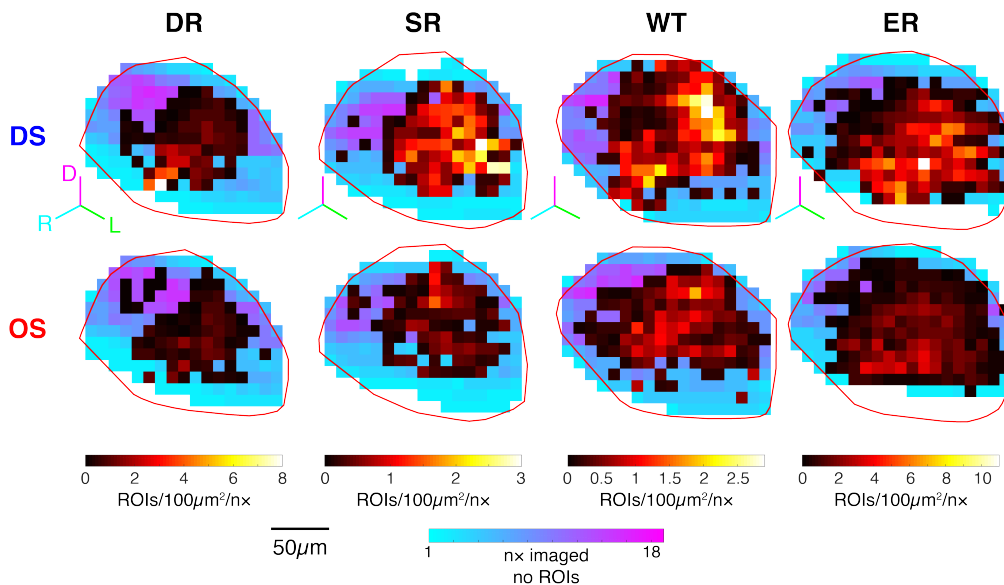
Figure 4.5: **Maps of DS & OS ROI density, corrected for imaging coverage, within the dominant lamina.** In laminar pixels where no ROIs were found, the number of times the pixel was imaged is indicated.

in the WT and ER animals, with a central bias for OS and a posterior/ventral DS bias (**fig. 4.6**). However, it appears that the magnitude of the differences, and the smoothness of the gradients, is reduced in the ER condition. This suggests that the regional specialisation observed in the WT might in fact be due to an environment that does not contain enough detail for correct visual development. In support of this point of view, the differences of densities of DR and SR maps have areas with higher levels of bias than the WT and ER conditions. However, one open question is whether skewed visual statistics are impairing normal development, or driving a specific different solution to tectal topography which can be related to the statistics present.

4.3.2 Topographic order and map curvature

The levels of topographic order in DS & OS maps were assessed using the multisubject euclidean distance correlation developed in **Chapter 2**. As expected, both DS and OS maps, in all conditions, were statistically significantly topographically ordered (**table 4.3**). As with the WT animals, and at earlier ages, in all cases the DS map is statistically significantly more ordered than the OS.
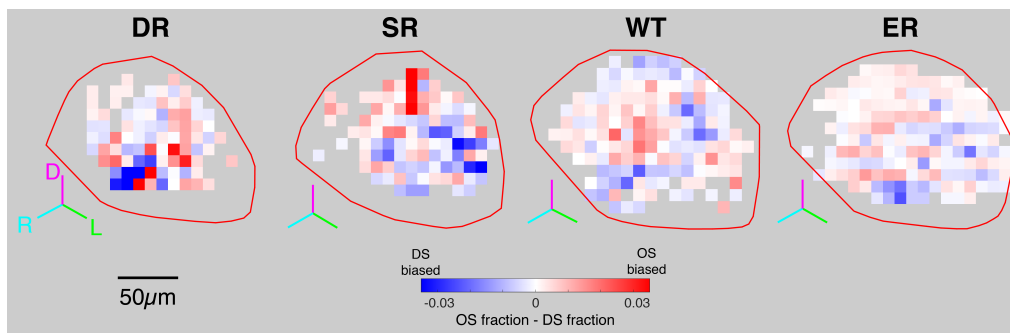
Figure 4.6: **Differential probabilities for OS and DS RGCs.** Densities of ROIs corrected for the number of times pixels were imaged (**fig. 4.5**) were rescaled to sum to 1, indicating the fraction of DS (or OS) ROIs found in each pixel. The rescaled DS density was then subtracted from the rescaled OS density, meaning that the integral of each parametric map is 0. Only pixels in which density of either functional type is non-zero are shown.

Surprisingly, it appears that in all three altered rearing conditions, topographic order is increased in both DS and OS maps relative to the WT animals (**fig. 4.7 and table 4.4**), with the exception of the OS map in the SR animals. As experiments for wild-type animals and other conditions were not performed contemporaneously, there is a remote possibility that this is an artefact of different parental health or imaging technique; discussed at greater length later.

Rearing	ROI type	total n	Monte Carlo n	p (N_{shuf} = 1000)
WT	DS	1296	449	0.001
WT	OS	978	313	0.001
DR	DS	562	126	0.001
DR	OS	436	132	0.001
ER	DS	2381	887	0.001
ER	OS	1579	550	0.001
SR	DS	759	279	0.001
SR	OS	578	188	0.001

Table 4.3: DS and OS maps, in all conditions, are statistically significantly topographically ordered. p-values represent the probability that the level of topographic order observed could occur by chance given distributions of points, see **Chapter 2** for details. Monte Carlo subsample sizes were chosen as described in **section 2.3.6**

The topographic order of 1D-projected tectal coordinates against azimuthal and elevational axes of visual space were calculated (**fig. 4.8**), using the framework established in **Chapter 3**. This process involved collapsing visual space coordinates of receptive fields to their azimuthal or elevational coordinate, and measuring the level of topographic order between the azimuth and elevational, and
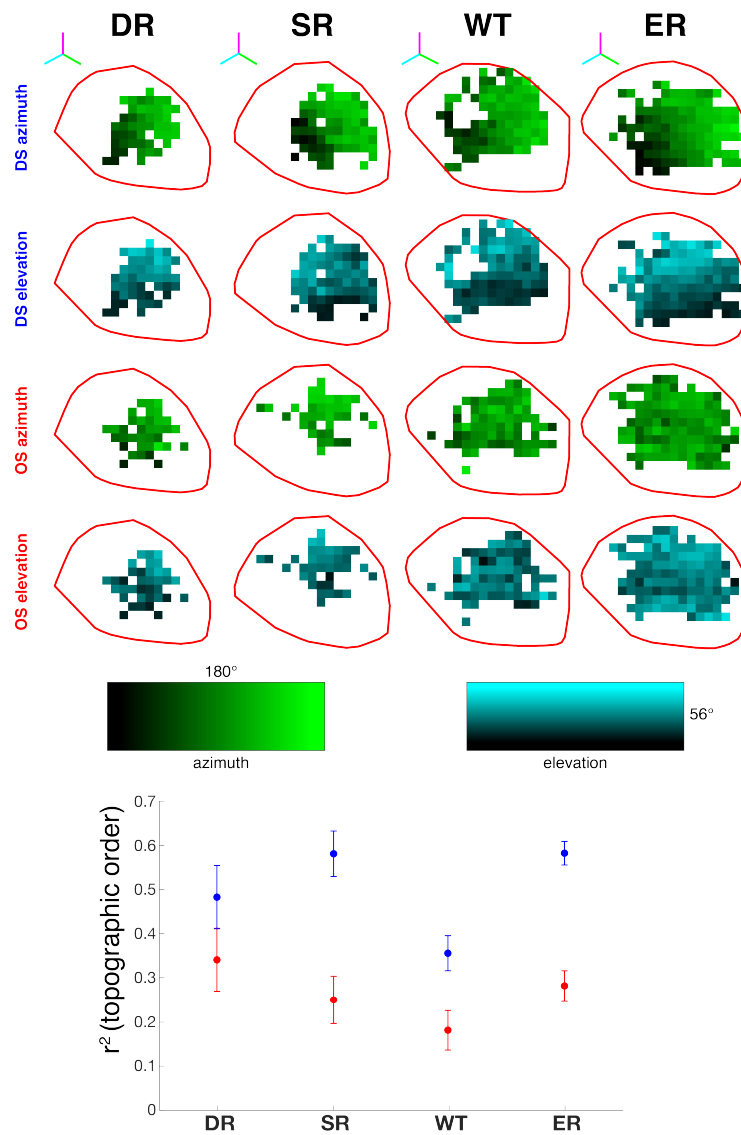
Figure 4.7: **Top:** DS and OS topographic maps formed in the tecta of 10 dpf fish reared in different visual environments. **Bottom:** Topographic order, calculated using the multiple-subject modified euclidean distance correlation metric described in chapter 2 and eq. (2.12). Error bars represent standard deviation of 1000 monte-carlo resampled maps (see **section 2.3.6**), using all ROIs resampled according to subsample sizes described in **table 4.3**. p-values shown in **table 3.3**.

Group 1	Group 2	p (q=0.2)
WT - DS	WT - OS	0
DR - DS	DR - OS	0.0013
ER - DS	ER - OS	0
SR - DS	SR - OS	0
WT - DS	DR - DS	0.004
WT - DS	ER - DS	0
WT - DS	SR - DS	0
DR - DS	ER - DS	0.0186
DR - DS	SR - DS	0.0071
ER - DS	SR - DS	0.9993
WT - OS	DR - OS	0.0002
WT - OS	ER - OS	0
WT - OS	SR - OS	0.0657
DR - OS	ER - OS	0.312
DR - OS	SR - OS	0.0058
ER - OS	SR - OS	0.824

Table 4.4: **Pairwise tests for differences in topographic order** between DS and OS maps in animals reared in different conditions. FDR-corrected p-values calculated as described in **section 2.3.6**, with $q = 0.2$, using Monte Carlo subsample sizes listed in **table 4.3**. Tests were performed with matched subsample sizes, in order to ensure fair comparisons where numbers of points were mismatched.
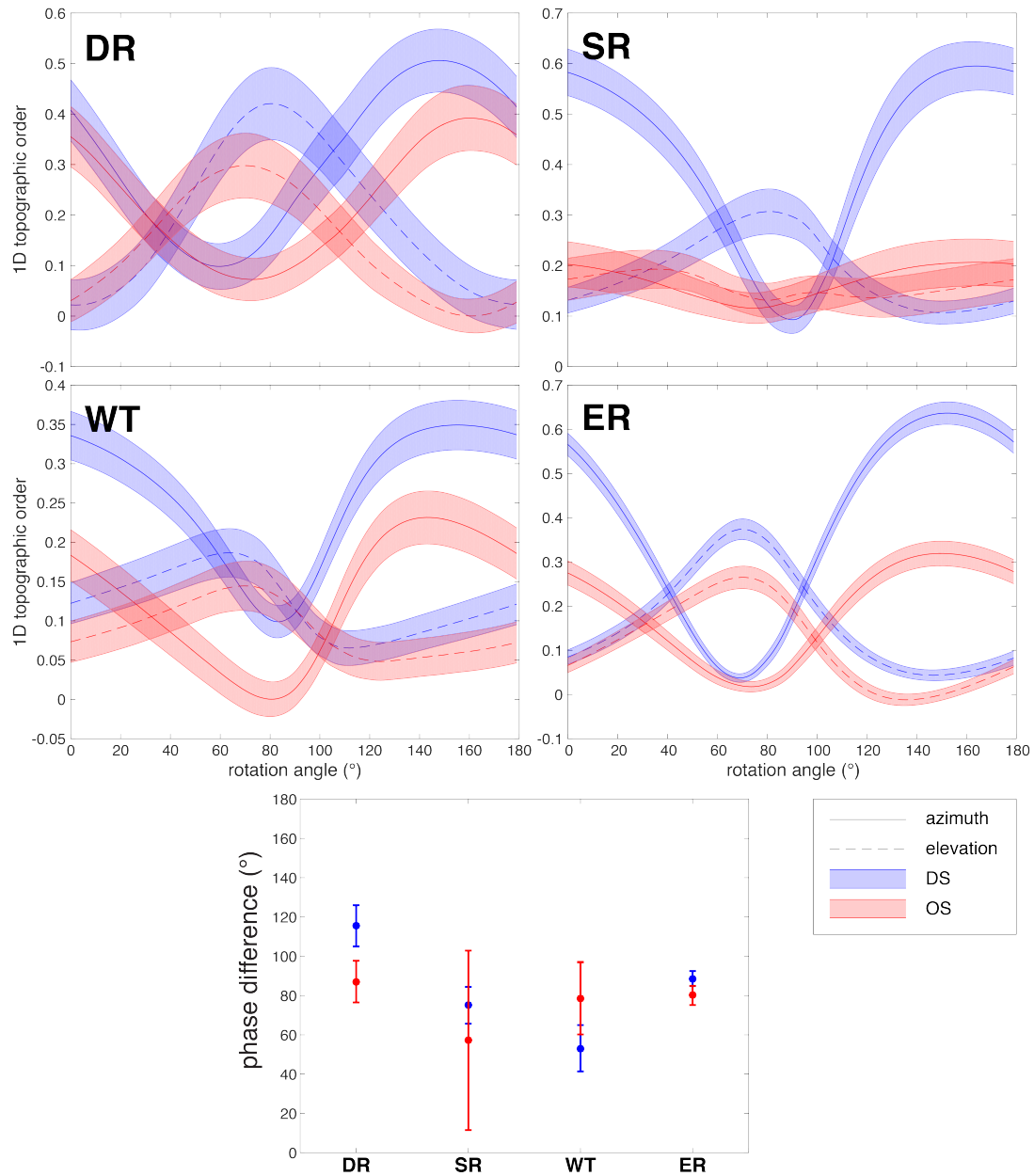
Figure 4.8: **Quantification of azimuth and elevation axes in the tectum. Top:** Topographic order for rotated, 1D-projected OS and DS maps. Error bars calculated using 1000 monte-carlo subsamples, with each subsample used for a full 180° rotation. **Bottom:** Phase difference, as indicated by maximal circular cross-correlation of 1D topographic order for azimuth and elevational axes. Error bars are mean ± SD from 1000 resampled datasets.
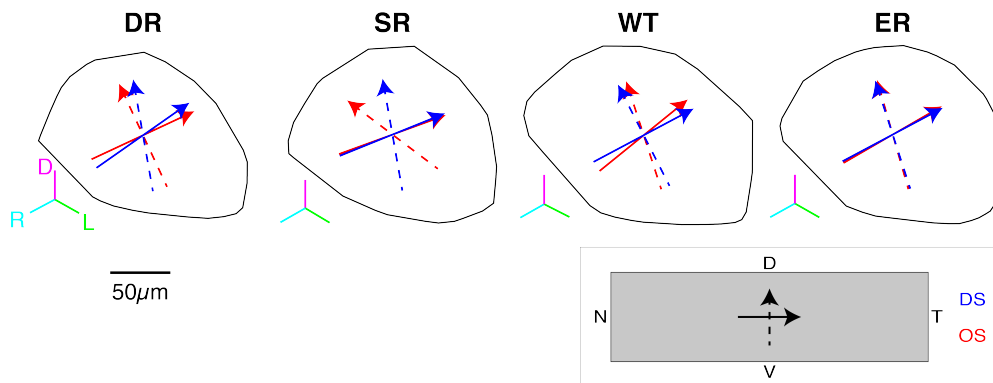
Figure 4.9: The angles giving peak 1D topographic order and representing the cardinal axes of visual space, as determined from the maximum of the curves shown in **fig. 4.8**.

the 1D-projected tectal coordinate after 0-180° rotations in the topographic plane. The angles that optimally represent the cardinal axes of visual space can be seen overlaid onto the tectum in **fig. 4.9**. Interestingly, the curves for the ER and DR datasets resemble sinusoids far closer than that of the other datasets. Why could this be? Intuitively, the deviation of these curves from a sinusoid could result from nonlinear curvature of the maps. Such an effect is confirmed in modelled data: using the modelling framework from **Chapter 2**, it becomes clear that deviation from a sinusoidal curve of topographic order against projection angle can arise as a result of map curvature (**fig. 4.10**). Thus, it appears that the ER maps, aside from having the phase difference closest to 90° (which would indicate orthogonal representations of azimuth and elevational axes, see bottom panel of **fig. 4.8**), and which has the axes of the DS and OS maps in closest agreement (**fig. 4.9**), is also the map whose plots of 1D topographic order against projection angle closest resemble sinusoids, implying that they are least likely to be subject to nonlinear distortion. A similar finding applies to the DR maps relative to the WT and SR maps.

In the SR OS map, topographic order in the elevational axis seems to be specifically disrupted. Although the curve of topographic order against rotation angle for the azimuth is shallow relative to the DS map, or the maps in other conditions, in contrast there is no single peak or trough in the curve for the elevation. This suggests that the elevational axis of the OS map is specifically vulnerable to the SR condition - although the reasons for this would require further exploration.

156
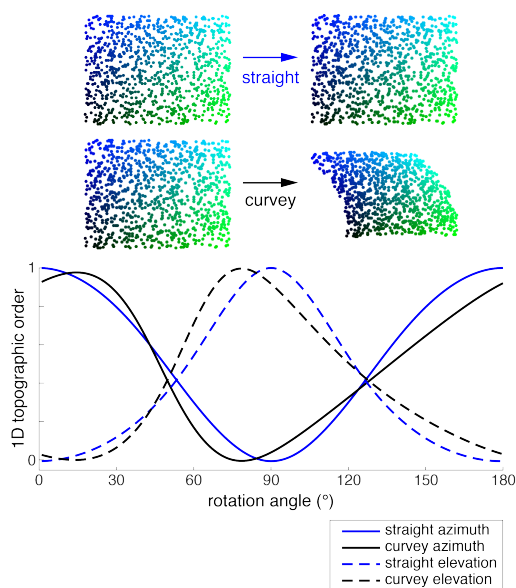
Figure 4.10: **Modelled data suggest that deviations from a sinusoidal topographic order curve arise as a result of map curvature.** Matched colours indicates point correspondence on top panels.

4.3.3 Angular-selective variants of DS & OS ROIs

I set out to analyse whether the angular-specific variants of DS and OS were affected by rearing in altered visual conditions. Applying the wavelet-based clustering technique used previously [38] to the data reveals that overall, the same variants are present in both DS and OS populations (**figs. 4.11 and 4.12**). In the DS populations, there are 3 variants, selective for nasal, dorsal/temporal and ventral/temporal motion. In the OS populations, there are 4 variants, roughly evenly spaced. Although there are small differences in preferred angle, these are small, and could be a result of small biases in the way the different animals were mounted/viewed the screen. As with the pooled DS and OS data, examining the laminar distributions of the DS and OS variants (bottom panels of **figs. 4.11 and 4.12**) shows that the laminar coordinates are largely unaffected: in the DS variants, the ordering of the angular-selective laminae remains. In the OS, the laminar distributions appear noisier in the DR and SR conditions (potentially due to low number of ROIs) but generally the same, with an overlapping primary lamina and the secondary, deeper lamina largely consisting of the horizontal-selective variant.

Although the functional identities and laminar distributions of the angular-selective

157
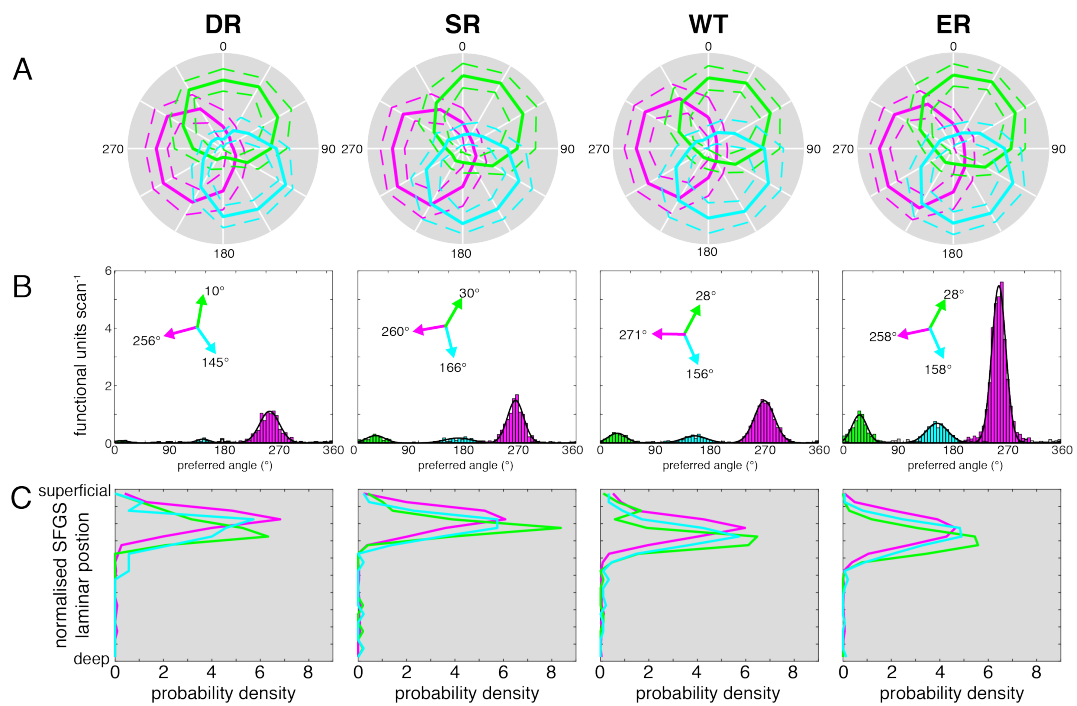
Figure 4.11: **DS variants are largely unchanged by altered rearing. A** Normalised mean responses of OS clusters to directions of motion, ± SD. The response vector for each ROI was normalised to its maximum prior to calculation of mean and SD from all members of each variant. **B** Distributions of preferred angles, coloured by cluster. Bin width is 5°. Inset represents peak preferred angles of clusters, calculated from von Mises fit to each cluster (shown in black). **C** Laminar distributions of clusters, using normalised distance within SFGS as in fig. 3.6.
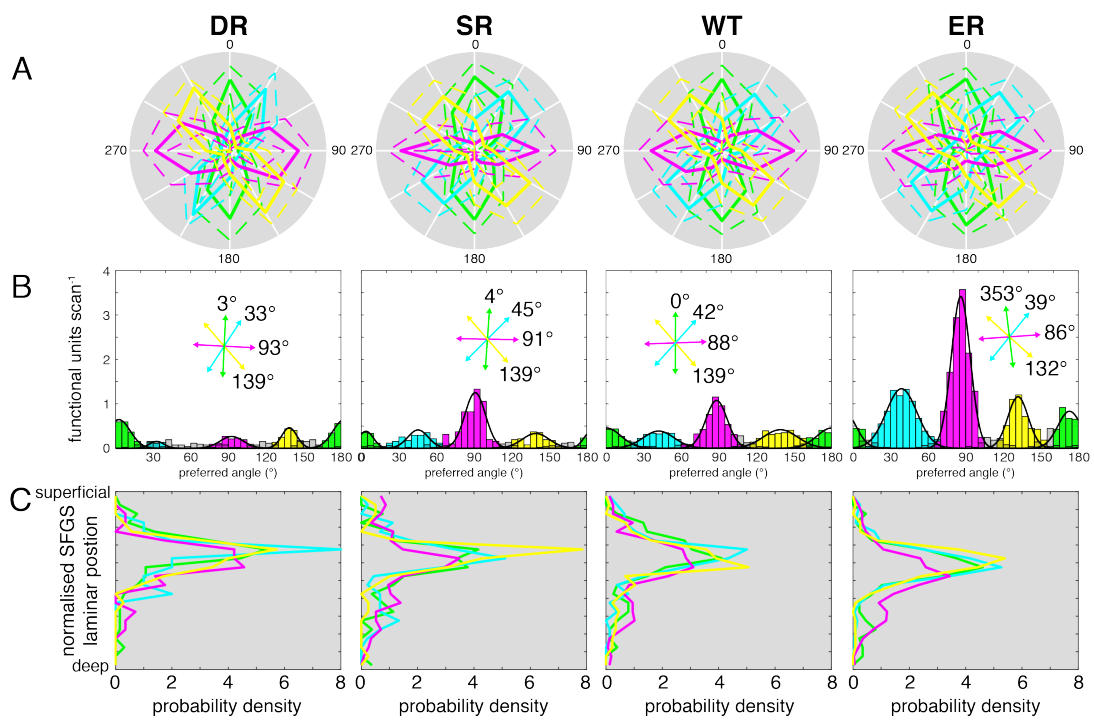
Figure 4.12: **OS variants are largely unchanged by altered rearing. A** Normalised mean responses of OS clusters to bar motion, ± SD. The response vector for each ROI was normalised to its maximum prior to calculation of mean and SD from all members of each variant. **B** Distributions of preferred angles, coloured by cluster. Bin width is 5°. Inset represents peak preferred angles of clusters, calculated from von Mises fit to each cluster (shown in black). **C** Laminar distributions of clusters, using normalised distance with in SFGS as in fig. 3.6.

variants do not appear to be affected by visual experience (**figs. 4.11 and 4.12**), their relative abundances are (see **fig. 4.13**). In the DS populations, fractions of the different variants are unchanged except in the DR condition, in which there is a disproportionate reduction in the dorsal/temporal and ventral/temporal variants, making the nasal-selective variant even more dominant. In the OS populations, there are differences between abundances of all different rearing conditions, but by far the most profound effect is in the DR animals, in which all populations are expanded at the expense of the horizontal motion variant, creating a strong bias towards the vertical variant. Additionally, the vertical-selective variant is reduced, and the horizontal variant expanded, in the SR condition. This observation could complement the finding that the SR OS map is specifically disrupted in the elevational axis (**fig. 4.8**) - although exactly how these findings are directly related remains to be seen.
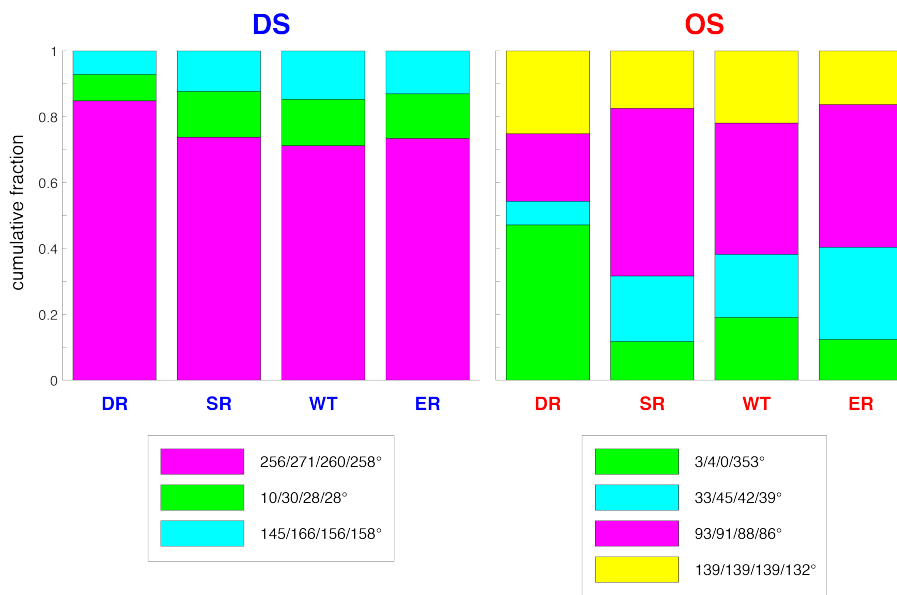
Figure 4.13: **Fractions of DS and OS ROIs, by angle-selective variant**, in animals reared in different visual environments.

4.3.4   Altered rearing and contrast selectivity

Next, the effects of altered visual environments on the selectivity for different contrast changes of DS and OS ROIs were examined (**fig. 4.14**). In the DS maps, it is apparent that there is a massive enlargement of the ON-OFF population in the ER

	Comparison	d.f.	X^2	p	Significant?
DS	**Global**	9	90.88	1.08E-15	**YES**
DS	WT/DR	3	75.51	2.82E-16	**YES**
DS	WT/ER	3	3.753	0.2894	NO
DS	WT/SR	3	2.708	0.439	NO
DS	DR/ER	3	67.67	1.35E-14	**YES**
DS	DR/SR	3	45.5	7.23E-10	**YES**
DS	ER/SR	3	0.355	9.49E-01	NO
OS	**Global**	12	349.4	1.85E-67	**YES**
OS	WT/DR	4	150.2	1.82E-31	**YES**
OS	WT/ER	4	43.18	9.48E-09	**YES**
OS	WT/SR	4	20.57	3.88E-04	**YES**
OS	DR/ER	4	300.1	1.02E-63	**YES**
OS	DR/SR	4	179.5	9.78E-38	**YES**
OS	ER/SR	4	16.15	2.80E-03	**YES**

Table 4.5: X^2 **statistics for comparisons of abundance of DS and OS angular-selective variants for animals reared in different visual environments.** All p-values calculated using the MATLAB *crosstab* function. Significance levels are Bonferroni adjusted, i.e. significant if p<0.0083.

animals relative to all other conditions (**table 4.6**). This potentially means that the ON-OFF population of DS-RGCs has a particular requirement for visual stimulation in order to elaborate or maintain axonal arbours. Meanwhile, the ON population is reduced more than the others in the SR condition. In the OS maps, the fraction of ON-ROIs remains roughly constant. Like the DS population, the most ON-OFF are found in the ER animals, while there appear to be a reduced number in the SR animals.

4.3.5 Displacement in visual space between DS and OS maps

In order to assess the role of visual experience in the alignment of DS and OS maps, the displacements between them were calculated as in **section 3.2.4**. Within different rearing conditions, no misalignment could be detected, with the exception of the dark-reared animals (**fig. 4.15 and table 4.7**). As the mismatched growth of retina and tectum, with retinal neurons added in concentric rings and tectal neurons added at the posterior, anterior and ventral borders necessitates the movement of RGC synapses in order to maintain topography as the animal grows [124]. Maps formed by RGC axons must migrate from the dorsal edge downwards.
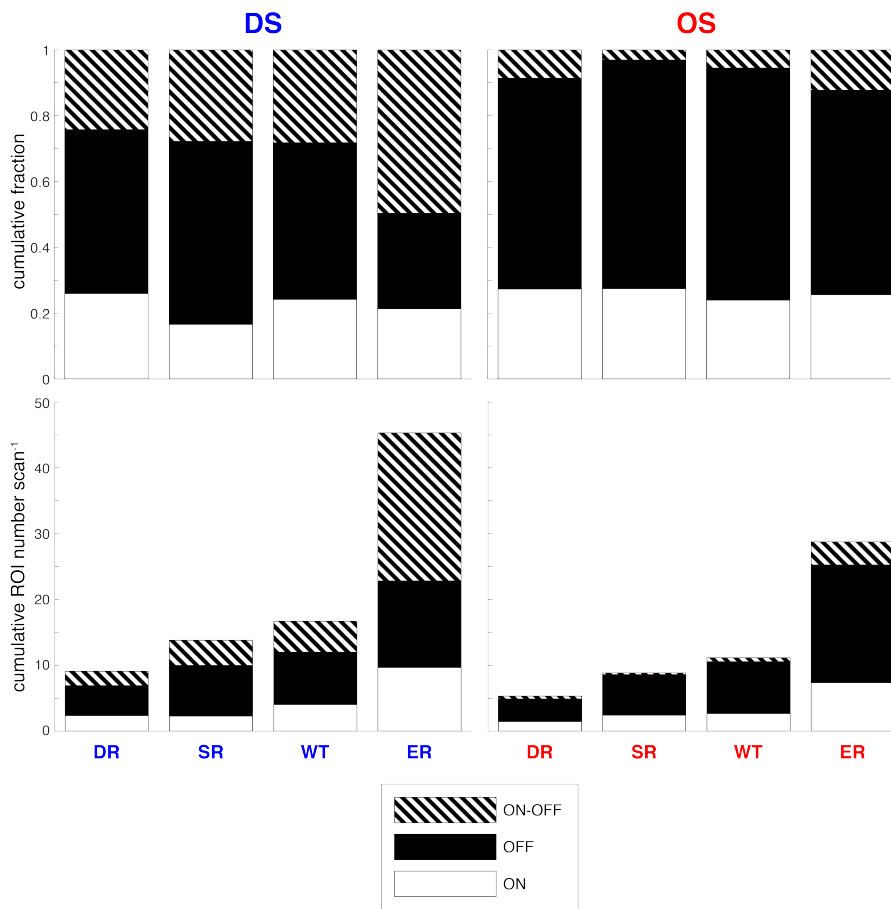
Figure 4.14: **DS and OS ROIs selective for different contrast changes**, for animals reared in different visual environments conditions. **Top:** Cumulative fractions. **Bottom:** Cumulative number of ROIs, per scan.

Thus, the ventral/nasal displacement of the DR OS map relative to the DS OS one corresponds to a faster movement of the OS map than the DS, consistent with previous data from 7 dpf animals [52].
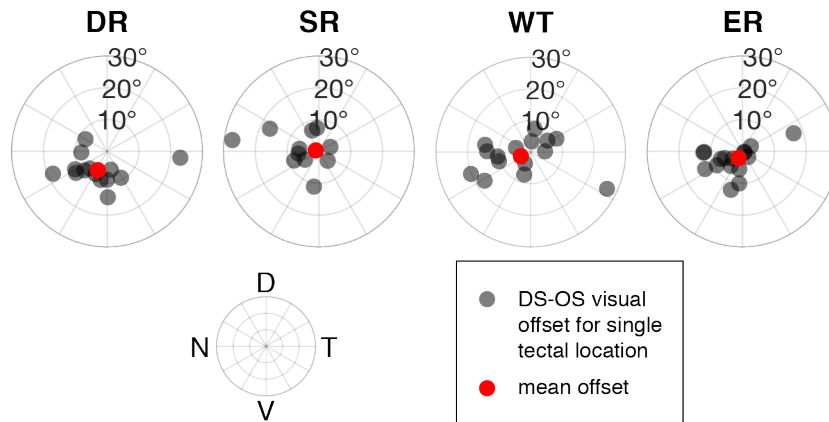
Figure 4.15: Displacements between DS and OS maps at different tectal locations, calculated in the same way as in **section 3.2.4**.

	Comparison	d.f	X^2	p	Significant?
DS	**Global**	6	313.8	9.03E-65	**YES**
DS	WT/DR	2	3.886	1.43E-01	NO
DS	WT/ER	2	161.11	1.04E-35	**YES**
DS	WT/SR	2	17.58	1.51E-04	**YES**
DS	DR/ER	2	123.24	1.73E-27	**YES**
DS	DR/SR	2	17.87	2.16E-04	**YES**
DS	ER/SR	2	173.27	2.38E-38	**YES**
OS	**Global**	6	50.3266	4.04E-09	**YES**
OS	WT/DR	2	5.19	7.46E-02	NO
OS	WT/ER	2	27	1.37E-06	**YES**
OS	WT/SR	2	4.3	1.16E-01	NO
OS	DR/ER	2	2.69	2.60E-01	NO
OS	DR/SR	2	11.9	2.50E-03	**YES**
OS	ER/SR	2	30.9	1.94E-07	**YES**

Table 4.6: X^2 **statistics for fractions of contrast-selective DS and OS ROIs by rearing condition** All p-values calculated using the MATLAB *crosstab* function. Significance levels are Bonferroni adjusted i.e. considered significant if p<0.0083.

Condition	d.f.	z	p
WT	14	0.7363	0.4863
DR	13	6.04	0.00138
ER	16	1.51	0.223
SR	11	0.9835	0.382

Table 4.7: Rayleigh test statistics for circularity of DS-OS displacements in visual space.

4.4 Discussion

In this chapter, I developed bespoke experimental apparatus to allow manipulation of visual experience in larval zebrafish during development. I then characterised the topographic maps formed by direction- and orientation-selective RGCs in the tecta of larval zebrafish reared using such apparatus, in an attempt to elucidate the contributions of visual experience to the properties of maps formed in WT animals (**Chapter 3**). My data indicate that providing a naturalistic visual experience leads to greater numbers of DS and OS ROIs, while restricting visual experience by dark- or strobe-rearing has the opposite effect. Visual experience appears to have differential effects on the balance of contrast- and angular-selective variants of DS and OS RGC axons. My data also suggests that visual experience is necessary, but that motion is not required, for the maintenance of alignment between DS and OS maps. Finally, my work reveals a complex and non-intuitive relationship between visual experience and the precision of topographic maps.

4.4.1 Effects of altered rearing on ROI number, and density

Of particular note is the massively-increased number of ROIs in the enriched-reared fish (**table 4.1**). Additionally, the size of the tectal neuropil does appear to be correlated with the level of visual experience (**table 4.2**). An interesting point is whether such alterations represent a different number of neurons, more developed axonal arbours on each neuron, or an alteration in the functional selectivity of neurons rather than a change in number, meaning that more ROIs meet the stringent criteria set for OS and DS. A change in the number of RGCs is unlikely, as examination of the RGC cell bodies and dendrites of dark-reared animals did not reveal gross morphological defects [76]. However, it should be noted that the DR animals in this previous study were compared with "WT" animals (which could be visually deprived, see **section 4.4.6**), and there could be an increase in RGC number in the ER condition.

In zebrafish, the effects of visual experience on RGC selectivity are unknown although the laminar distributions of their dendrites within the retina (which are major determinants of functional identity) are unaffected by dark-rearing [76]. This finding suggest that changes in ROI number are not necessarily a result of altered

RGC selectivity, and are more likely to result from changes in axonal arbourisation. Similarly, in the rabbit visual experience does not impact on the development of DS-RGC dendritic morphology [226]. In direct contrast to this view, recordings of the electroretinogram are altered by rearing in constant light [227], meaning that retinal circuitry can be altered by experience. Such an effect has also been demonstrated in the mouse [228–230], with visual experience directly affecting retinal circuitry, and other studies have found experience-dependent remodelling of upstream retinal circuitry in mice [231], and rats [232].

It is interesting that alterations in the density of ROIs in the ER condition occur over the whole tectum, with increased density everywhere **fig. 4.5**, even though after the time at which larvae start to swim upright (by 3 dpf [233]), visual experience was altered far more in the ventral portion of the visual field. Reflections of the gravel from the lid of the petri dish containing the experimental animals, which would result in changes in visual statistics over the whole visual field, will be extremely faint as lighting intensity is far higher from above the dishes than below them - due to the gravel. As the time of upright swimming is very nearly concurrent with the arrival of the first RGC axons into the tectum [54, 233], the alterations in topography are extremely unlikely to result from developmental changes preceding the period when fish swim upright. Potentially linked to this is the ventral-dorsal gradient of DS and OS density seen in the ER condition, meaning that the ventral visual field specifically contains more ROIs (**fig. 4.9**).

Additionally interesting are the alterations in the bias for DS vs OS ROIs seen in the DR and SR maps (**fig. 4.6**). In the DR animals, there are many more DS ROIs than OS found in the area close to the point of optic nerve entry, while in the SR there is massive OS bias in the dorsal area. How and why these specific biases emerge is an open question. However, the different biases present in all conditions here indicate that skewed visual statistics can drive different specific solutions for visual topography.

4.4.2 Dark-reared animals do not simply exhibit delayed development

In DR animals at 10 dpf, levels of topographic order in DS and OS maps are intermediate between that found in the WT dataset at 7 dpf and 10 dpf (**figs. 3.10 and 4.7**). It could be supposed, based only on this observation, that the DR animals

are subject to delayed development due to poor nutrition, as animals could be less able to find food after their yolk sac is depleted around 6 dpf [234]. However, in a number of other parameters (for example, the balance of contrast-selective ROIs, the abundance of DS variants, and the number of ROIs), they far more closely resemble the WT 10 dpf animals than the 7 dpf. Additionally in support of this, zebrafish larvae can forage almost as efficiently in the dark as in light up to 10 dpf [235]. Thus, although the progression of topographic order in DR animals may be delayed as a result of loss of visual experience, this is not simply a knock-on effect of a broader delay in development of the whole animal, and represents a specific effect of visual experience on topographic precision.

4.4.3 Visual experience is necessary for map alignment

It is very interesting that maps require visual experience to remain in alignment (**fig. 4.15 and table 4.7**), even though they emerge in alignment at 3 dpf (see **Chapter 3**). RGC axons are organised chronotopically within the optic nerve, with the most recently-added RGCs at its outer circumference [236]. As the retina grows at its circumference, it is presumed that this corresponds to a retinotopic mapping. Similar organisation has also been identified in other teleosts [237]. Given that RGC axons only enter the tectum between 2.5-3 dpf [54], it remains to be seen whether visual experience has major effects on map alignment (or topographic order) at such an early stage.

The fact that visual experience is necessary for map alignment at 10 dpf, as well as at 7 dpf [52], supports the idea that as animals move toward adulthood, the balance of forces maintaining and creating neuronal connectivity shifts away from molecular pre-specification and towards activity-dependent refinement [58]. In this scenario, and in light of the coarse topographic order found at 3 dpf, maps are created in alignment by molecular mechanisms, but maintenance of this alignment requires visual input. A particularly interesting question, if this were the case, is at what point in the life of DR fish the maps are first misaligned? An additional question is whether there are specific mechanisms that maintain the alignment of multiple maps (and which require visual experience), or whether the mechanisms for specifying topographic map position (for example, axonal competition for tectal space [69, 95, 96]) operate independently across multiple maps, maintaining their alignment passively.

4.4.4 DS and OS RGCs are differentially affected by visual experience

As discussed in **Chapter 1**, in fish the mismatched growth of the retina and tectum necessitates the movement of maps across the tectum [124]. Given that visual experience is necessary for map alignment, the synaptic remodelling which comprises this movement could operate under different parameters in DS and OS maps if there are no specific mechanisms maintaining alignment via visual experience. If there is no specific mechanism of keeping maps aligned, then the maps must move independently of each other but still maintain internal order. Under this model, the misalignment observed in the DR condition would be due to differences in how the maps migrate across the tectum, potentially due different rates of synaptic turnover.

Clearly, the effects of visual experience are different in the two functional types of RGC studied here. The balance of contrast selectivity (**fig. 4.14**), and angular-selective variant (**fig. 4.13**), is far more fluid in the OS than the DS maps. Previous work has suggested that the DS retinotectal projection is more "hardwired", while the OS is more plastic [37, 38, 52]. However, the differences in topographic order are far more pronounced in the DS maps than in the OS, somewhat tempering this view. The results here additionally demonstrate that the laminar and topographic locations of RGCs are differentially affected by visual experience: only very small changes occured in laminar distributions (consistent with previous work [38, 76]), while the distributions in the topographic plane, and levels of topographic order are affected more profoundly, meaning that the maps themselves are more affected by visual experience than their laminar locations.

In my data, strobe-rearing produced an increase in topographic order of DS but not OS maps, a reduction in the number of both DS and OS ROIs, and alterations of the balance of angular-selective variants of OS but not DS RGCs. Strobe-rearing has previously been shown to impact on RGC axonal arbourisation in the developing goldfish, specifically affecting some RGC axons more than others [104], although these findings cannot be directly related to the present study as functional characterisation was not attempted. However, it is consistent with the general finding here that RGC functional types are differentially affected by visual experience.

4.4.5 Visual experience affects map curvature and axis orthogonality

Examination of the topographic order of 1D-projected azimuthal and elevational maps allowed the extraction of information about how the cardinal axes of visual space are represented in the tectum (**fig. 4.8**). As demonstrated in **fig. 4.10**, deviations from sinusoidal relationships are likely to represent axis curvature.

One interesting question which remains unanswered is the precise link between the SR condition and the complete lack of a defined elevational axis in the OS map (**fig. 4.8**). Potentially linked to this is the expansion of the vertical-selective OS variant in the SR condition. However, whether these two observations can be explicitly linked remains to be seen.

Interestingly, both the ER and DR animals appear to have maps in which axes are closer to orthogonal, and which appear to have less curvature in that their plots of projection angle against 1D topographic order are closer to being sinusoidal. The DR DS map appears to have very sinusoidal relationships between projection angle and 1D topographic order, yet also to have non-orthogonal axes. Intuitively, this could correspond to a linearly sheared map of visual space.

4.4.6 Most experimental zebrafish are visually deprived

The result that map properties in enriched-reared animals are vastly altered relative to their wild-type counterparts was unexpected. However, this finding carries with it certain caveats. Data from 10 dpf WT fish in this chapter was recycled from **Chapter 3**, and was not acquired concurrently with that from fish reared in the altered visual environments, meaning that differences could be due to small changes in acquisition technique or the health of the parents. An extra, desirable, control would be to darken the area directly below the fish similarly to the ER condition) but without adding extra detail, as the levels of light experienced by ER animals will have been lower than that of the WT.

That such a small environmental perturbation as the ER condition had such large effects on the functional selectivity and map properties of RGC axons is surprising. Perhaps the "normal" environment most experimental animals develop in, incubators lacking in visual detail, might be negatively impacting their visual

development. It is almost certain that alterations in RGC functional properties impact on those of tectal neurons, and given the reliance of the zebrafish on vision, the whole brain. Given that the tectum is a major site of multimodal sensory integration [238], questions arise regarding all research into zebrafish visual representation, and as a result, their behaviour. One example of such a potential mistake can be found in **fig. 3.8**, which appears to show the emergence of regional specialisation from 3-10 dpf, with areas of the tectum in which DS and OS are unbalanced in terms of their density. However, in the ER fish, it appears that the magnitude of these differences is smaller (**fig. 4.6**), suggesting that the regional specialisation observed in the WT might be a by-product of a visually-deprived environment.

Perhaps the WT visual environment is specifically detrimental to map development, given the sparse incubator environment, lacking in detail. Certainly, exposure to constant illumination has negative effects on the visual system, both at the level of photoreceptors [227] and in terms of behaviour [239]. In this thesis, the ER animals experienced less light than the WT due to the opaque dish beneath them and unfortunately, the differences cannot be definitively attributed to changes in detail versus changes in light levels. The WT incubator environment could be producing a less pronounced version of the condition produced by exposure to constant light. In contrast, the DR animals have no visual experience, and the organisation of their neurons must then rely entirely on molecular processes and spontaneous activity rather than visual-evoked activity. Perhaps a complete lack of input leads to more healthy map development than the visually-impoverished, or potentially overly-lit "WT" input, in which plasticity mechanisms disorder the maps.

One hypothesis is that as the balance of factors affecting neuronal connectivity shifts from being dominated by molecular factors, to activity-dependent plasticity [58], the "WT" animals visual systems may be deleteriously affected by the poorly-structured input, similarly to animals reared in constant light [227, 239]. The important question is then, at what point do the topographic maps of animals reared in different visual environments diverge? Potentially, it might correspond to the onset of hunting behaviour at 5-6 dpf [186], which will hugely impact on the statistics of the visual environment and perhaps increase the effects of activity-dependent plasticity on retinotectal connectivity, as discussed in **Chapter 3**. The most important experiment to test this hypothesis would be to produce developmental profiles for the ER and DR animals, similar to that in

4.4.7 The effects of altered visual environments on topographic order are complex

The topographic order seen in altered visual environments is certainly not as expected. All animals reared in altered environments exhibit increased topographic order in both DS and OS maps relative to the WT animals (**fig. 4.7**). I originally hypothesised that DR animals should have increased topographic order, while ER animals should have reduced topographic order. While my data is consistent with the former hypothesis, in fact the topographic order in the ER animals was increased. This is unexpected, as reducing visual experience (as in DR animals) and increasing its complexity (as in ER) were predicted to have opposite effects on topographic order. How can these findings be reconciled? How do they relate to the finding that WT animals maps become less precise from 7 dpf to 10 dpf?

Examination of map curvature using 1D projections shows that ER and DR maps have more orthogonal axes and are likely to have less curvature than the WT condition (**fig. 4.8**). A potential confounding factor here is that maps with more curvature will have their level of topographic order underestimated to a greater extent (despite efforts to mitigate this effect, see **Chapter 2**). Thus, it is perhaps unsurprising that the ER maps appear to be the most ordered given that they also appear to have axes closest-to-orthogonal.

As mentioned earlier, it is possible that in fact the WT fish are not directly comparable to the other conditions due to non-concurrent data acquisition. Under this assumption, the Wt data should be disregarded and comparisons should be drawn only from comparisons of the remaining datasets. The data presented here would conclude that visual experience is necessary to refine DS maps, making them more precise. It would appear that, as the ER and SR maps have equivalent levels of order, the exact statistics of the visual experience provided do not affect DS map precision. Meanwhile, the precision of OS maps is once again complex as highest topographic order is seen for the DR condition, while the lowest is for SR. These findings imply that movement is not specifically necessary for DS maps to form precisely, but that it is for OS.

However, if there is no artefact due to poor experimental technique, an alternative

view can be presented: Given the fact that ER maps are the most highly ordered, it certainly appears that increasing the complexity of visual experience acts to make the map more precise, in line with the expectations of Kutsarova et al., 2017 [145], and disagree with the view that maps are a non-optimal way of encoding the visual field [146, 147]. An important next step in exploring the influence of visual experience would be to produce developmental profiles for all the altered visual environments used here - particularly the ER condition. An extra control would be to darken the area directly below the fish (in a similar way to the ER condition) but without adding extra detail.

Chapter 5

Conclusions & Further Work

In this thesis, I have examined the development of visuotopic maps in the zebrafish tectum, and the contribution of visual experience to these maps.

In **Chapter 2**, using in-silico modelled data, I selected one metric, the euclidean distance correlation, for topographic precision which was optimally suited for quantifying maps derived from multiple experimental subjects. This metric was expanded to allow statistical testing of differences between subjects using a Monte Carlo resampling strategy, and to allow the quantification of deviations from perfect topographic order in biological distance units. The major findings are as follows:

- Four metrics for topographic order were assessed based on the amount of data required for, and the precision with which they could resolve it, topographic order, using in-silico modelled data

- Selected metrics were reformulated to allow quantification of maps derived from multiple experimental subjects, and the above analysis repeated in that context.

- The euclidean distance correlation was selected as the metric allowing best quantification.

- A framework for testing of statistical differences between maps derived from multiple experimental subjects was demonstrated

- A technique for estimating sources of topographic disorder in biological distance units was developed and validated.

In **Chapter 3**, I examined the development of tectal visuotopic maps formed by synapses from two populations of motion-selective RGC. I used synchronised visual stimuli (presented with a custom built system, described in **Appendix A**) with confocal imaging, in conjunction with standardised spaces representing the tectum, to examine the development of visuotopic maps formed by direction-selective and orientation-selective RGCs of larval zebrafish of three different ages (3, 7 and 10 dpf). These experiments suggested development of regional specialisation, with certain regions of the tectum containing a biased representation of DS relative to OS. DS and OS maps appear in alignment with respect to the visual field from 3 dpf onwards. Examining the contrast-selective DS and OS RGCs, no contrast-change-specific sublaminae were observed, either within DS and OS, or within the angular-selective variants of DS and OS identified. Unexpectedly, topographic order did not increase monotonically with age; while it increased from 3 dpf to 7 dpf, it reduced from 7 dpf to 10 dpf.

- Using a custom-built experimental setup, topographic maps formed by DS and OS RGCs in the tectum were derived from zebrafish at 3, 7 and 10 dpf.

- DS maps are more ordered than OS at all ages

- Topographic order increases from 3-7dpf, but decreases from 7-10dpf, in both DS and OS maps

- Differential densities of DS and OS suggest regional specialisation within the tectum

- No misalignment between DS and OS maps could be detected at any age

- Variants selective for different angles were identified, consistent with previous literature

In **Chapter 4**, animals reared in the dark, an enriched/naturalistic environment and strobe lights were examined at 10 dpf using the same experimental and analytical framework as **Chapter 3**. Such experiments revealed complex relationships between visual experience and topographic order: order was increased in all altered

visual environments relative to the "WT" animals. One interpretation is that in fact the WT fish are visually deprived. Additionally, a more uniform distribution in enriched-reared (ER) fish suggested that the regional specialisation revealed in **Chapter 3** could be an artefact of the WT rearing condition. Finally, the alignment of DS and OS maps appeared to be dependent on visual experience.

- Topographic maps formed by DS and OS RGCs in the tectum were derived at 10 dpf after rearing in altered visual environments: dark-reared animals, strobe-reared animals and animals reared in an enriched visual environment

- Strangely, topographic order was increased in all altered conditions

- Enriched rearing massively increased the number of DS and OS ROIs detected, and reduces the degree to which regional specialisation could be seen

- Reduced numbers of ROIs were seen in dark- and strobe-reared animals

- Angular-selective variants were identified, and while their selectivity and relative distribution across the tectum was unchanged, their relative abundances were changed within the dark-reared condition

- Misalignment of DS and OS maps could be detected in the dark-reared condition, but no others.

Here, the major findings of this work will be discussed at greater length, and the next steps that could be taken will be considered.

5.1   Quantifying topographic precision

First, in **Chapter 2**, I developed a framework for assessing which of a number of metrics for topographic precision were best-suited to quantifying and comparing the precision of multiple maps, derived from multiple experimental subjects. Using this framework, based on the amount of data required to reliably quantify defined levels of topographic order, I selected one particular metric, a multisubject version of the euclidean distance correlation, for further development. I demonstrated that it can be used to estimate deviations from perfect topographic order in biological

distance units, as long as the mapping did not contain nonlinear distortion. Additionally, using a Monte Carlo resampling strategy and a false discovery rate correction (developed by Dr Andrew Lowe), it can be used to test for statistical differences between maps derived from multiple experimental subjects.

This work was further extended in **Chapter 3**, by using 1D projections following a rotation to estimate how the cardinal axes of visual space are represented in the tectum. Intuitively, if the cardinal axes of visual space are reciprocated orthogonally in the tectum, the curves relating 1D topographic order to the angle of 1D projection should resemble sinusoidal curves offset by 90°. In **Chapter 4**, a cursory model dataset illustrated that increasing map curvature also increased the deviation of the curve from a sinusoid. One possibility for extending modelling work would be to examine how the spectral content (that is, the fourier transform [240]) of the curves used to estimate cardinal axes relate to map curvature in a quantitative manner. If such an endeavour succeeded, one additional possibility might be to attempt to use the relationship between spectral content and map curvature to unwarp curved axes and so produce estimates of map disorder in biological distance units, independently of nonlinearities.

In sparse and coarsely-ordered datasets, false negatives are common [179], and this observation was taken account of within the selection of my optimal metric. However, some considerations were unfortunately not taken into account - for example, the case where sample points are close together as compared to the level of noise that explains map imperfections. This became apparent when assessing the levels of order in the angular-selective variants of DS RGC; in some of the variants, topographic order could not be detected.

5.1.1 What do nonmatching axes really mean?

If multiple overlaid maps have different cardinal axes (as demonstrated in vivo across **Chapters 3 and 4**), it follows that at certain points within the maps they should be misaligned. How can a situation arise where maps are aligned, but their cardinal axes are not - which is the case for many experimental conditions?

Firstly, if maps are not perfectly ordered (as is the case for all the maps in this thesis), the displacement of each point in the map relative to the location it would occupy if the map were perfectly ordered could eclipse the level of misalignment

caused by axis disagreement. That is, the displacement between maps with different axes might be below the level of noise within each of the individual maps, making it undetectable. However, examining whether this is the case cannot be determined using techniques established in this thesis, as measurement of sources of map disorder depends on the level of distortion of the map, as demonstrated in **Chapter 2** and the maps have different levels of distortion.

Secondly, the tests for alignment used in this thesis are performed across the whole map, and do not take into account local distortions. Thus, if maps are aligned at their centres, then it is possible that the displacements due to differences in their cardinal axes at their edges cancel out; at one extreme of the tectal surface, the displacement could be precisely the inverse of that at the other.

Finally, throughout this thesis, topographic maps have been examined after projection into a 2D plane. However, tectal laminae are not planar, but rather lie on a curved manifold; with the caveat that even this is an approximation due to the partially-overlapping nature of the laminae. Given that the DS and OS maps will have different topology, their common projection into 2D will introduce different distortions, potentially leading to the discrepancies in axis alignment shown here.

5.2   Limitations of the experimental setup

As demonstrated in **Chapter 3**, there are issues surrounding compression of the receptive fields due to to the aspect ratio of the screen. This could hopefully be circumvented in future iterations by using screens covering more elevational area. As flexible screens become more widely available, the ideal screen configuration would be hemispherical, or even spherical. Although such a configuration has been developed using a spherical array of LEDs, it currently has very limited resolution and has only been used for behavioural work so far [Arrenberg AB, personal communication].

Recent work indicates that UV-detecting cones dominate the photoreceptor complement in the nasal/upper visual field [30], corresponding precisely with the area of the tectum where a particularly low density of DS and OS ROIs were seen (**Chapters 3 and 4**, an effect also remarked upon in the thesis of Aenea Hendry [52]). As the screens used in my system are optimised for viewing by humans,

one possibility that could explain the low density of DS and OS in that tectal area is that the screens do not present their patterns in the UV range detected by the zebrafish photoreceptors. Thus, a useful control would be to examine the output of the screens with an optical spectrometer, to see whether the contrast patterns presented in the human-visible range are also detected in the UV range of the cones which dominate the zebrafish retina in the area corresponding to nasal/upper visual field.

Finally, in future iterations it would be preferable if there were a method for fixing the position of the screens relative to the microscope objective. This would allow differences in fish mounting position to be recorded and taken into account in analysis: for example, to allow compensation of bar motion angles, and locations of receptive fields in visual space for animals viewing the screens from different angles. Such corrections, when correctly applied, would allow exploration of biases in feature detection in visual as well as tectal space.

5.3   Development is not monotonic

One of the key findings, gleaned from a number of parameters, in **Chapter 3**, was that many changes from 7 dpf to 10 dpf are in the opposite direction as from 3 dpf to 7 dpf, suggesting that during development there is a transient state. Similar findings have emerged from studies of tectal activity: spontaneously active ensembles of tectal neurons become more compact from 4-6 dpf, but then increase in size later on [148].

One interpretation of the results in **Chapter 4** was that in "WT" animals, poorly structured visual input actively degrades the maps formed by RGCs in the tectum. In particular, over a number of different parameters the ER maps resemble the 7 dpf WT condition more than the 10 dpf WT condition. This raises the question of when precisely the animals in altered environments actually diverge from the WT ones, and in what manner.

Previous experiments with dark-reared (DR) animals show that topographic maps formed by DS RGCs in the tectum already diverge from WT at 7 dpf [52], and properties of tectal activity diverge at 6 dpf [148]. Additionally, the massive reduction in number of OS and DS ROIs seen in **Chapter 4** has been seen at 7 dpf

[38]. Such findings raise the question of when, precisely, the differences between animals reared in different visual environments become apparent. Extra work is needed to see whether changes from 7 to 10 dpf in the WT are recapitulated in the ER condition, and thus whether the WT condition is specifically deleterious after a certain timepoint, due to alterations in the balance of molecular and synaptic plasticity related forces determining neuronal connectivity [58]. The best experiment would be to produce full developmental profiles for the DR and ER conditions, and to examine more time-points between 3 and 10 dpf, in order to find the first point at which divergence occurs between the different conditions. This would establish at which point loss of DS and OS synapses in the tectum occurs (and whether it occurs in ER animals as well as in WT), reveal whether a reduction in topographic order is present in all rearing conditions, and establish whether poorly-structured visual input in WT animals is damaging the visual system, and at what point this becomes important.

5.4 Development of regional specialisation

Results in **Chapter 3** suggested that over time, regions of the tectum have a biased representation of DS against OS input. This is interesting, as the pooled density of RGC axons within the tectum is broadly uniform [69]. Thus, presumably, the density gradients of all types of RGC must sum to uniformity. As the areas of DS and OS bias shown here are not reciprocal, there must be further regional specialisation in other, as-yet unidentified, types of RGC. However, at 10 dpf, such regional specialisation appears to be much reduced in the ER animals (**Chapter 4**). As discussed before, the regional specialisation hinted at earlier may then be an artefact of poorly-structured visual input, in a similar manner to the effects of visual environment on topographic order.

At 7 dpf there is a region of very sparse DS and OS corresponding to the upper/nasal visual field [52] and this is additionally present at 10 dpf in all conditions examined here. One option, discussed earlier, is that the spectral properties of the current visual presentation system are not compatible with the dominant photoreceptor complement elsewhere. However, this area could have altered functional selectivity in some other domain, and examining either whether regional differences in the functional selectivity of the DS and OS RGCs innervating this area, or discovering

178

which different RGCs are dominant, would require a larger stimulus set.

5.5   Most experimental zebrafish are visually deprived

ER animals have profoundly different organisation of RGC inputs to the tectum than their WT counterparts, across many different measured parameters - most notably their topographic precision (**Chapter 4**). Given the large effects of visual enrichment on topographic properties from such a small manipulation as introducing gravel in the lower portion of the visual field, it seems clear that not only are most experimental zebrafish visually deprived relative to their counterparts in the real world, but also that the organisation of their visual system is impacted as a result.

Recent, unpublished data indicate that the structure of spontaneous tectal activity in ER animals also appears changed, with both individual neurons appearing more active, and larger ensembles of coactive neurons at 7 dpf [Thomas Sainsbury, personal communication/unpublished data]. Such changes in tectal neurons must be a knock-on effect of altered retinal input, and mean that downstream connectivity cannot compensate for the poorly-structured input provided by the WT environment.

The ER manipulation presented herein almost certainly does not completely mimic the rich visual environment which zebrafish in the wild likely experience, and thus the map properties may well be further affected by an even more naturalistic environment, including other fauna and flora.

5.6   What features do RGCs really encode?

One issue with the approach of this project is the simple stimulus set used. Using only simple stimuli means that the functional identities assigned to the RGCs examined might in fact be epiphenomena. In the real world, they might respond to something entirely different, with the responses to grey, straight edges in fact being an epiphenomenon. In fact, this is likely given that receptive fields could be mapped using static sparse noise stimuli, while the criteria used to define the functional types are based on motion.

Secondly, the notion of using motion-encoding RGCs to study topographic maps could be problematic due to their temporally-variant receptive fields [32]. Whether the temporal components of their receptive fields might affect the location of their centres is an open question, given that they encode motion - meaning that the precise parameters of the stimuli used might bias results to some extent.

It is not currently known whether the OS RGCs identified previously [17, 37, 38, 52, 81, 108] and further explored here even encode motion - that is, whether they respond similarly to static bars or gratings as they do to moving ones. There is an obvious experiment to test this: to present both static and moving bars and examine whether or not responses are equivalent, or whether it leads to further subdivision of OS RGCs. This has not been performed. Additionally, further characterisation of the spatiotemporal frequencies driving responses in both DS and OS RGCs is required, particularly in light of the potential regional specialisation observed.

Additionally, to date no study has attempted an unbiased clustering approach similar to those used in the mouse retina [32]. It would be extremely interesting to discover whether the 50+ types of RGC identified according to axo-dendritic morphology [33] can be related to function.

An alternative step towards characterising the features that different RGCs encode in the real world would be to use naturalistic stimuli. Such an approach has been used extensively to recover receptive fields in the mammalian cortex (for example, see Willmore et al., 2010 [36]). However, there are problems with using naturalistic stimuli in conjunction with calcium imaging, given that the dynamics of calcium indicators are much slower than the speeds at which movies of the natural world vary, in conjunction with spatial and temporal correlations within the natural images. Similar problems have been overcome in the past: presented natural movies have been recovered from blood oxygen level-dependent (BOLD) fMRI signals in the human brain [241], which are extremely limited in both spatial and temporal resolution.

180

5.7   The importance of topographic maps for vision

Overall, data are inconclusive about whether topographic maps are actually refined or made more disordered by visual experience. There are two possible interpretations of the data at 10 dpf, as discussed in **Chapter 4**. Either the WT condition is specifically deleterious for map precision, and either removal of visual input or addition of more complexity in the visual input leads to more precise maps, or the presence of visual input increases the precision of DS maps, and reduces it in OS. Vital for disambiguating these possibilities would be full developmental profiles of animals reared in both DR and ER conditions. Generally, the view that improved visual input leads to improved map precision [145] appears to be validated either way, and this weighs in favour of the hypothesis that maps could be used directly in decoding the visual field. Additionally, it appears that the topographic precision of the DS map is more affected than the OS by visual experience; an interesting finding in its own right.

Nikolaou et al., 2015 [81] suggested that correct retinotectal connectivity can be established without correct laminar targeting - could the same be true of the topographic map? Such questions could easily be asked using a similar strategy to that of Avitan et al., 2016 [146]: to ask whether non-topographic encoding strategies such as linear decoders, and maximum likelihood estimation, function as well in animals with altered topographic mapping (including comparisons with the altered visual environments used herein).

The next step would be to use a behavioural paradigm that requires high visual acuity, and to ask which decoding method best correlates with behavioural performance across multiple experimental manipulations. How might this be achieved? One option might be measurement of prey capture efficiency [213]. Rearing animals in altered visual environments and examining behavioural parameters is fraught with difficulties in interpretation (particularly setting lighting levels during the experiments), so these should be complemented with experiments in which genetic manipulations directly affect the organisation of the tectal topographic map [69].

To conclude, this thesis has made some progress in deciphering how topographic maps representing different visual features form and align, and the contribution of visual experience to these processes. However, there are still open questions

regarding the precise function of visual topography [1].

References

1. Hemmen, J. L. in *23 Problems in Systems Neuroscience* 83–102 (2005).

2. Joselevitch, C. & Kamermans, M. Retinal parallel pathways: Seeing with our inner fish. *Vision Research* **49,** 943–959 (2009).

3. Wilkinson-Berka, J. L. Diabetes and retinal vascular disorders: role of the renin–angiotensin system. *Expert Reviews in Molecular Medicine* **6,** 1–18 (2004).

4. Palczewski, K. G protein-coupled receptor rhodopsin. *Annual review of biochemistry* **75,** 743–67 (2006).

5. Branchek, T. & Bremiller, R. The development of photoreceptors in the zebrafish,Brachydanio rerio. I. Structure. *The Journal of Comparative Neurology* **224,** 107–115 (1984).

6. Branchek, T. The development of photoreceptors in the zebrafish,Brachydanio rerio. II. Function. *The Journal of Comparative Neurology* **224,** 116–122 (1984).

7. Endeman, D., Klaassen, L. J. & Kamermans, M. Action spectra of zebrafish cone photoreceptors. *PloS one* **8,** e68540 (2013).

8. Müller, B & Peichl, L. Horizontal cells in the cone-dominated tree shrew retina: morphology, photoreceptor contacts, and topographical distribution. *Journal of Neuroscience* **13,** 3628–46 (1993).

9. Packer, O. S. & Dacey, D. M. Synergistic center-surround receptive field model of monkey H1 horizontal cells. *Journal of vision* **5,** 1038–54 (2005).

10. Hombach, S. *et al.* Functional expression of connexin57 in horizontal cells of the mouse retina. *The European journal of neuroscience* **19,** 2633–40 (2004).

11. Connaughton, V. P., Graham, D & Nelson, R. Identification and morphological classification of horizontal, bipolar, and amacrine cells within the zebrafish retina. *The Journal of comparative neurology* **477,** 371–85 (2004).

12. Song, P. I., Matsui, J. I. & Dowling, J. E. Morphological types and connectivity of horizontal cells found in the adult zebrafish (Danio rerio) retina. *The Journal of comparative neurology* **506,** 328–38 (2008).

13. Baylor, D. A., Lamb, T. D. & Yau, K. W. Responses of retinal rods to single photons. *The Journal of physiology* **288,** 613–34 (1979).

14. Connaughton, V. P. Bipolar cells in the zebrafish retina. English. *Visual neuroscience* **28,** 77–93 (2011).

15. Jusuf, P. R. & Harris, W. A. Ptf1a is expressed transiently in all types of amacrine cells in the embryonic zebrafish retina. *Neural Development* **4,** 34 (2009).

16. Yoshida, K. *et al.* A Key Role of Starburst Amacrine Cells in Originating Retinal Directional Selectivity and Optokinetic Eye Movement. *Neuron* **30,** 771–780 (2001).

17. Antinucci, P., Suleyman, O., Monfries, C. & Hindges, R. Neural Mechanisms Generating Orientation Selectivity in the Retina. *Current Biology* **26,** 1802–1815 (2016).

18. Coombs, J. L., Van Der List, D. & Chalupa, L. M. Morphological properties of mouse retinal ganglion cells during postnatal development. *The Journal of comparative neurology* **503,** 803–14 (2007).

19. Mumm, J. S. *et al.* In vivo imaging reveals dendritic targeting of laminated afferents by zebrafish retinal ganglion cells. *Neuron* **52,** 609–21 (2006).

20. Sanes, J. R. & Masland, R. H. The Types of Retinal Ganglion Cells: Current Status and Implications for Neuronal Classification. *Annual Review of Neuroscience* **38,** 221–246 (2015).

21. Cook, J. E. in *Development and Organization of the Retina* (eds Chaulpa, L. & Finlay, B.) 91–120 (Springer, US, 1998). ISBN: 9781461553335.

22. Bleckert, A., Schwartz, G. W., Turner, M. H., Rieke, F. & Wong, R. O. L. Visual space is represented by nonmatching topographies of distinct mouse retinal ganglion cell types. *Current biology : CB* **24,** 310–5 (2014).

23. Wässle, H & Riemann, H. J. The mosaic of nerve cells in the mammalian retina. *Proceedings of the Royal Society of London. Series B, Biological sciences* **200,** 441–61 (1978).

24. Eglen, S. J. Development of regular cellular spacing in the retina: theoretical models. *Mathematical Medicine and Biology: A Journal of the IMA* **23,** 79–99 (2006).

25. Sterling, P. Microcircuitry of the Cat Retina. *Annual Review of Neuroscience* **6,** 149–185 (1983).

26. Rheaume, B. A. *et al.* Single cell transcriptome profiling of retinal ganglion cells identifies cellular subtypes. *Nature Communications* **9,** 2759 (2018).

27. Kim, I.-J., Zhang, Y., Yamagata, M., Meister, M. & Sanes, J. R. Molecular identification of a retinal cell type that responds to upward motion. *Nature* **452,** 478–482 (2008).

28. Huberman, A. D. *et al.* Genetic Identification of an On-Off Direction- Selective Retinal Ganglion Cell Subtype Reveals a Layer-Specific Subcortical Map of Posterior Motion. *Neuron* **62,** 327–334 (2009).

29. Vaney, D. I., Sivyer, B. & Taylor, W. R. Direction selectivity in the retina: symmetry and asymmetry in structure and function. *Nature Reviews Neuroscience* **13,** 194–208 (2012).

30. Zimmermann, M. J. *et al.* Zebrafish Differentially Process Color across Visual Space to Match Natural Scenes. *Current Biology* **28,** 2018–2032.e5 (2018).

31. Völgyi, B., Chheda, S. & Bloomfield, S. A. Tracer coupling patterns of the ganglion cell subtypes in the mouse retina. *The Journal of comparative neurology* **512,** 664–87 (2009).

32. Baden, T. *et al.* The functional diversity of retinal ganglion cells in the mouse. *Nature* (2016).

33. Robles, E., Filosa, A. & Baier, H. Precise lamination of retinal axons generates multiple parallel input pathways in the tectum. *Journal of Neuroscience* **33,** 5027–39 (2013).

34. Robles, E., Laurell, E. & Baier, H. The Retinal Projectome Reveals Brain-Area-Specific Visual Representations Generated by Ganglion Cell Diversity. *Current Biology* **24,** 2085–2096 (2014).

35. Emran, F. *et al.* OFF ganglion cells cannot drive the optokinetic reflex in zebrafish. *Proceedings of the National Academy of Sciences* **104,** 19126–19131 (2007).

36. Willmore, B. D. B., Prenger, R. J. & Gallant, J. L. Neural Representation of Natural Images in Visual Area V2. *Journal of Neuroscience* **30,** 2102–2114 (2010).

37. Nikolaou, N. *et al.* Parametric functional maps of visual inputs to the tectum. *Neuron* **76,** 317–24 (2012).

38. Lowe, A. S., Nikolaou, N., Hunter, P. R., Thompson, I. D. & Meyer, M. P. A systems-based dissection of retinal inputs to the zebrafish tectum reveals different rules for different functional classes during development. *Journal of Neuroscience* **33,** 13946–56 (2013).

39. Maximov, V., Maximova, E. & Maximov, P. Direction Selectivity in the Goldfish Tectum Revisited. *Annals of the New York Academy of Sciences* **1048,** 198–205 (2005).

40. Trenholm, S., Johnson, K., Li, X., Smith, R. & Awatramani, G. Parallel Mechanisms Encode Direction in the Retina. *Neuron* **71,** 683–694 (2011).

41. Kay, J. N. *et al.* Retinal Ganglion Cells with Distinct Directional Preferences Differ in Molecular Identity, Structure, and Central Projections. *Journal of Neuroscience* **31,** 7753–7762 (2011).

42. Simpson, J. I. The Accessory Optic System. *Annual Review of Neuroscience* **7,** 13–41 (1984).

43. Zhao, X., Chen, H., Liu, X. & Cang, J. Orientation-selective responses in the mouse lateral geniculate nucleus. *Journal of Neuroscience* **33,** 12751–63 (2013).

44. Chen, H., Liu, X. & Tian, N. Subtype-dependent postnatal development of direction- and orientation-selective retinal ganglion cells in mice. *Journal of Neurophysiology* **112,** 2092–2101 (2014).

45. Levick, W. R. & Thibos, L. N. Analysis of orientation bias in cat retina. *The Journal of physiology* **329,** 243–61 (1982).

46. Venkataramani, S. & Taylor, W. R. Orientation Selectivity in Rabbit Retinal Ganglion Cells Is Mediated by Presynaptic Inhibition. *Journal of Neuroscience* **30,** 15664–15676 (2010).

47. Passaglia, C. L., Troy, J. B., Rüttiger, L. & Lee, B. B. Orientation sensitivity of ganglion cells in primate retina. *Vision Research* **42,** 683–694 (2002).

48. Schiller, P. H. Parallel information processing channels created in the retina. *Proceedings of the National Academy of Sciences of the United States of America* **107,** 17087–94 (2010).

49. Burrill, J. D. & Easter, S. S. Development of the retinofugal projections in the embryonic and larval zebrafish (Brachydanio rerio). *The Journal of comparative neurology* **346,** 583–600 (1994).

50. Kita, E. M., Scott, E. K. & Goodhill, G. J. Topographic wiring of the retinotectal connection in zebrafish. *Developmental neurobiology* (2014).

51. Nevin, L. M., Robles, E., Baier, H. & Scott, E. K. Focusing on optic tectum circuitry through the lens of genetics. *BMC biology* **8,** 126 (2010).

52. Hendry, A. C. *Mapping the Functional Visual Topography of the Zebrafish Tectum* PhD Thesis (King's College London, 2016).

53. Stuermer, C. Retinotopic organization of the developing retinotectal projection in the zebrafish embryo. *Journal of Neuroscience* **8,** 4513–4530 (1988).

54. Moorman, S. J. Development of sensory systems in zebrafish (Danio rerio). *ILAR journal* **42,** 292–8 (2001).

55. Simpson, H. D., Kita, E. M., Scott, E. K. & Goodhill, G. J. A quantitative analysis of branching, growth cone turning, and directed growth in zebrafish retinotectal axon guidance. *Journal of Comparative Neurology* **521,** 1409–1429 (2013).

56. Kita, E. M., Scott, E. K. & Goodhill, G. J. The influence of activity on axon pathfinding in the optic tectum. *Developmental Neurobiology* **75,** 608–620 (2015).

57. Meyer, M. P. & Smith, S. J. Evidence from in vivo imaging that synaptogenesis guides the growth and branching of axonal arbors by two distinct mechanisms. *Journal of Neuroscience* **26,** 3604–14 (2006).

58. Kolodkin, A. L. & Hiesinger, P. R. Wiring visual systems: common and divergent mechanisms and principles. *Current Opinion in Neurobiology* **42,** 128–135 (2017).

59. Ashley, J. & Katz, F. Competition and position-dependent targeting in the development of the Drosophila R7 visual projections. *Development* **120,** 1537–1547 (1994).

60. Millard, S. S., Flanagan, J. J., Pappu, K. S., Wu, W. & Zipursky, S. L. Dscam2 mediates axonal tiling in the Drosophila visual system. *Nature* **447,** 720–724 (2007).

61. Sperry, R. W. Effect of 180 degree rotation of the retinal field on visuomotor coordination. *Journal of Experimental Zoology* **92,** 263–279 (1943).

62. Sperry, R. W. Chemoaffinity in the orderly growth of nerve fiber patterns and connections. *Proceedings of the National Academy of Sciences* **50,** 703–710 (1963).

63. Erskine, L. & Herrera, E. The retinal ganglion cell axon's journey: Insights into molecular mechanisms of axon guidance. *Developmental Biology* **308,** 1–14 (2007).

64. Walter, J, Kern-Veits, B, Huf, J, Stolze, B & Bonhoeffer, F. Recognition of position-specific properties of tectal cell membranes by retinal axons in vitro. *Development* **101,** 685–96 (1987).

65. Cheng, H. J., Nakamoto, M, Bergemann, A. D. & Flanagan, J. G. Complementary gradients in expression and binding of ELF-1 and Mek4 in development of the topographic retinotectal projection map. *Cell* **82,** 371–81 (1995).

66. Schmidt, J. T. Regeneration of the retinotectal projection following compression onto a half tectum in goldfish. *Journal of embryology and experimental morphology* **77,** 39–51 (1983).

67. Baier, H *et al.* Genetic dissection of the retinotectal projection. *Development* **123,** 415–25 (1996).

68. Karlstrom, R. O. *et al.* Zebrafish mutations affecting retinotectal axon pathfinding. *Development* **123,** 427–38 (1996).

69. Trowe, T *et al.* Mutations disrupting the ordering and topographic mapping of axons in the retinotectal projection of the zebrafish, Danio rerio. *Development* **123,** 439–50 (1996).

70. Sweeney, N. T., James, K. N., Sales, E. C. & Feldheim, D. A. Ephrin-As are required for the topographic mapping but not laminar choice of physiologically distinct RGC types. *Developmental neurobiology* **75,** 584–93 (2015).

71. Picker, A *et al.* Requirement for the zebrafish mid-hindbrain boundary in midbrain polarisation, mapping and confinement of the retinotectal projection. *Development* **126,** 2967–78 (1999).

72. Woo, S., Rowan, D. J. & Gomez, T. M. Retinotopic mapping requires focal adhesion kinase-mediated regulation of growth cone adhesion. *Journal of Neuroscience* **29,** 13981–91 (2009).

73. Gosse, N. J. & Baier, H. An essential role for Radar (Gdf6a) in inducing dorsal fate in the zebrafish retina. *Proceedings of the National Academy of Sciences of the United States of America* **106,** 2236–41 (2009).

74. Liu, Y. *et al.* Semaphorin3D guides retinal axons along the dorsoventral axis of the tectum. *Journal of Neuroscience* **24,** 310–8 (2004).

75. Yamagata, M & Sanes, J. R. Lamina-specific cues guide outgrowth and arborization of retinal axons in the optic tectum. *Development* **121,** 189–200 (1995).

76. Nevin, L. M., Taylor, M. R. & Baier, H. Hardwiring of fine synaptic layers in the zebrafish visual pathway. *Neural development* **3,** 36 (2008).

77. Martin, R. If you checked this reference, the brandy miniature is yours. *J. Premium Spirits* **1** (2018).

78. Xiao, T. *et al.* Assembly of Lamina-Specific Neuronal Connections by Slit Bound to Type IV Collagen. *Cell* **146,** 164–176 (2011).

79. Campbell, D. S. *et al.* Slit1a inhibits retinal ganglion cell arborization and synaptogenesis via Robo2-dependent and -independent pathways. *Neuron* **55,** 231–45 (2007).

80. Jiang, Y. *et al.* In vitro guidance of retinal axons by a tectal lamina-specific glycoprotein Nel. *Molecular and cellular neurosciences* **41,** 113–9 (2009).

81. Nikolaou, N. & Meyer, M. P. Lamination Speeds the Functional Development of Visual Circuits. *Neuron* **88,** 999–1013 (2015).

82. Constantine-Paton, M & Law, M. I. Eye-specific termination bands in tecta of three-eyed frogs. *Science (New York, N.Y.)* **202,** 639–41 (1978).

83. Boss, V. C. & Schmidt, J. T. Activity and the formation of ocular dominance patches in dually innervated tectum of goldfish. *Journal of Neuroscience* **4,** 2891–905 (1984).

84. Mooney, R, Penn, A. A., Gallego, R & Shatz, C. J. Thalamic relay of spontaneous retinal activity prior to vision. *Neuron* **17,** 863–74 (1996).

85. Galli, L & Maffei, L. Spontaneous impulse activity of rat retinal ganglion cells in prenatal life. *Science (New York, N.Y.)* **242,** 90–1 (1988).

86. Cook, P. M., Prusky, G & Ramoa, A. S. The role of spontaneous retinal activity before eye opening in the maturation of form and function in the retinogeniculate pathway of the ferret. *Visual neuroscience* **16,** 491–501 (1999).

87. Sernagor, E & Grzywacz, N. M. Influence of spontaneous activity and visual experience on developing retinal receptive fields. *Current biology : CB* **6,** 1503–8 (1996).

88. Wong, W. T., Sanes, J. R. & Wong, R. O. L. Developmentally Regulated Spontaneous Activity in the Embryonic Chick Retina. *Journal of Neuroscience* **18,** 8839–8852 (1998).

89. Albert, M. V., Schnabel, A. & Field, D. J. Innate Visual Learning through Spontaneous Activity Patterns. *PLoS Computational Biology* **4** (ed Sporns, O.) (2008).

90. Willshaw, D. J., Sterratt, D. C. & Teriakidis, A. Analysis of local and global topographic order in mouse retinocollicular maps. *Journal of Neuroscience* **34,** 1791–805 (2014).

91. Leiwe, M. N. *et al.* Geniculo-Cortical Projection Diversity Revealed within the Mouse Visual Thalamus. *PLOS ONE* **11** (ed Badea, T. C.) e0144846 (2016).

92. Demas, J. A., Payne, H. & Cline, H. T. Vision drives correlated activity without patterned spontaneous activity in developing Xenopus retina. *Developmental neurobiology* **72,** 537–46 (2012).

93. Kolls, B. J. & Meyer, R. L. Spontaneous Retinal Activity Is Tonic and Does Not Drive Tectal Activity during Activity-Dependent Refinement in Regeneration. *Journal of Neuroscience* **22,** 2626–2636 (2002).

94. Zhang, R.-w., Li, X.-q., Kawakami, K. & Du, J.-l. Stereotyped initiation of retinal waves by bipolar cells via presynaptic NMDA autoreceptors. *Nature Communications* **7,** 12650 (2016).

95. Gnuegge, L, Schmid, S & Neuhauss, S. C. Analysis of the activity-deprived zebrafish mutant macho reveals an essential requirement of neuronal activity for the development of a fine-grained visuotopic map. *Journal of Neuroscience* **21,** 3542–8 (2001).

96. Hua, J. Y., Smear, M. C., Baier, H. & Smith, S. J. Regulation of axon growth in vivo by activity-based competition. *Nature* **434,** 1022–6 (2005).

97. Cline, H. T. & Constantine-Paton, M. NMDA receptor antagonists disrupt the retinotectal topographic map. English. *Neuron* **3,** 413–426 (1989).

98. Schmidt, J. T., Buzzard, M, Borress, R & Dhillon, S. MK801 increases retinotectal arbor size in developing zebrafish without affecting kinetics of branch elimination and addition. *Journal of neurobiology* **42,** 303–14 (2000).

99. Leu, B. H. & Schmidt, J. T. Arachidonic acid as a retrograde signal controlling growth and dynamics of retinotectal arbors. *Developmental neurobiology* **68,** 18–30 (2008).

100. Du, J.-L. & Poo, M.-M. Rapid BDNF-induced retrograde synaptic modification in a developing retinotectal system. *Nature* **429,** 878–83 (2004).

101. Hall, Z. J. & Tropepe, V. Visual Experience Facilitates BDNF-Dependent Adaptive Recruitment of New Neurons in the Postembryonic Optic Tectum. *Journal of Neuroscience* **38,** 2000–2014 (2018).

102. Wiesel, T. N. & Hubel, D. H. Ordered arrangement of orientation columns in monkeys lacking visual experience. *The Journal of comparative neurology* **158,** 307–18 (1974).

103. Schmidt, J. & Eisele, L. Stroboscopic illumination and dark rearing block the sharpening of the regenerated retinotectal map in goldfish. *Neuroscience* **14,** 535–546 (1985).

104. Schmidt, J. T. & Buzzard, M. Activity-driven sharpening of the retinotectal projection in goldfish: Development under stroboscopic illumination prevents sharpening. *Journal of Neurobiology* **24,** 384–399 (1993).

105. Huberman, A. D., Murray, K. D., Warland, D. K., Feldheim, D. A. & Chapman, B. Ephrin-As mediate targeting of eye-specific projections to the lateral geniculate nucleus. *Nature Neuroscience* **8,** 1013–1021 (2005).

106. Lambot, M.-A. Mapping Labels in the Human Developing Visual System and the Evolution of Binocular Vision. *Journal of Neuroscience* **25,** 7232–7237 (2005).

107. Leamey, C. A. *et al.* Ten_m3 Regulates Eye-Specific Patterning in the Mammalian Visual Pathway and Is Required for Binocular Vision. *PLoS Biology* **5** (ed Harris, W. A.) e241 (2007).

108. Antinucci, P., Nikolaou, N., Meyer, M. P. & Hindges, R. Teneurin-3 specifies morphological and functional connectivity of retinal ganglion cells in the vertebrate visual system. *Cell reports* **5,** 582–92 (2013).

109. Rhoades, R. W. & Chalupa, L. M. Functional properties of the corticotectal projection in the golden hamster. *The Journal of Comparative Neurology* **180,** 617–633 (1978).

110. Triplett, J. W. *et al.* Retinal Input Instructs Alignment of Visual Topographic Maps. *Cell* **139,** 175–185 (2009).

111. Phillips, M. *et al.* A Synaptic Strategy for Consolidation of Convergent Visuotopic Maps. *Neuron* **71,** 710–724 (2011).

112. Tikidji-Hamburyan, R. A., El-Ghazawi, T. A. & Triplett, J. W. Novel Models of Visual Topographic Map Alignment in the Superior Colliculus. *PLOS Computational Biology* **12** (ed Blohm, G.) e1005315 (2016).

113. Rees, A. Sensory maps: Aligning maps of visual and auditory space. *Current Biology* **6,** 955–958 (1996).

114. Palmer, A. R. & King, A. J. The representation of auditory space in the mammalian superior colliculus. *Nature* **299,** 248–249 (1982).

115. King, A. J. The Wellcome Prize Lecture. A map of auditory space in the mammalian brain: neural computation and development. *Experimental physiology* **78,** 559–90 (1993).

116. Middlebrooks, J. C. & Knudsen, E. I. A neural code for auditory space in the cat's superior colliculus. *Journal of Neuroscience* **4,** 2621–34 (1984).

117. Wise, L. Z. & Irvine, D. R. Topographic organization of interaural intensity difference sensitivity in deep layers of cat superior colliculus: implications for auditory spatial representation. *Journal of Neurophysiology* **54,** 185–211 (1985).

118. Feldman, D. E., Brainard, M. S. & Knudsen, E. I. Newly learned auditory responses mediated by NMDA receptors in the owl inferior colliculus. *Science (New York, N.Y.)* **271,** 525–8 (1996).

119. Schnupp, J. W., King, A. J., Smith, A. L. & Thompson, I. D. NMDA-receptor antagonists disrupt the formation of the auditory space map in the mammalian superior colliculus. *Journal of Neuroscience* **15,** 1516–31 (1995).

120. Gutfreund, Y., Zheng, W. & Knudsen, E. I. Gated Visual Input to the Central Auditory System. *Science* **297,** 1556–1559 (2002).

121. Raymond, P. A. Movement of retinal terminals in goldfish optic tectum predicted by analysis of neuronal proliferation. *Journal of Neuroscience* **6,** 2479–88 (1986).

122. Marcus, R. C., L., D. C. & Easter, S. S. Neurogenesis in the visual system of embryonic and adult zebrafish (Danio rerio). English. *Visual Neuroscience* **16,** 417–424 (1999).

123. Ito, Y., Tanaka, H., Okamoto, H. & Ohshima, T. Characterization of neural stem cells and their progeny in the adult zebrafish optic tectum. *Developmental biology* **342,** 26–38 (2010).

124. Easter, S. S. & Stuermer, C. A. An evaluation of the hypothesis of shifting terminals in goldfish optic tectum. *Journal of Neuroscience* **4,** 1052–63 (1984).

125. Becker, C. G., Meyer, R. L. & Becker, T. Gradients of ephrin-A2 and ephrin-A5b mRNA during retinotopic regeneration of the optic projection in adult zebrafish. *The Journal of comparative neurology* **427,** 469–83 (2000).

126. Cheng, H. J. & Flanagan, J. G. Identification and cloning of ELF-1, a developmentally expressed ligand for the Mek4 and Sek receptor tyrosine kinases. *Cell* **79,** 157–68 (1994).

127. Talbot, S. A. & Marshall, W. H. Physiological studies on neural mechanisms of visual localization and discrimination. **24** (1941).

128. Walls, G. L. Significance of the foveal depression. *Archives of Ophthalmology* **18,** 912–919 (1937).

129. Daniel, P. M. & Whitteridge, D. The representation of the visual field on the cerebral cortex in monkeys. *The Journal of physiology* **159,** 203–21 (1961).

130. Schwartz, E. L. Analytic structure of the retinotopic mapping and relevance to perception. *6th AnnualMeeting of the Society for Neuroscience Abstracts,* 1636 (1976).

131. Feldon, S., Feldon, P. & Kruger, L. Topography of the retinal projection upon the superior colliculus of the cat. *Vision Research* **10,** 135–143 (1970).

132. Wagner, H.-J. Vergleichende Untersuchungen Uber das Muster der Sehzellen und Horizontalen in der Teleostier-Retina (Pisces). *Zeitschrift fur Morphologie der Tiere* **72** (1972).

133. Clarke, P. G. H. & Whitteridge, D. The projection of the retina, including the 'red area', on to the optic tectum of the pigeon. *Quarterly Journal of Experimental Physiology and Cognate Medical Sciences* **61,** 351–358 (1976).

134. Ahlbert, I. The organisation of the cone cells in the retinae of four teleosts with different feeding habits (Perca fluviatilis L., Lucioperca lucioperca L., Acerina cernua L.and Coregonus albula L). *Arkiv. Zool.* **22,** 445–481 (1969).

135. Ahlbert, I.-B. Organization of the Cone Cells in the Retinae of Salmon (Salmo salar) and Trout (Salmo trutta trutta) in Relation to Their Feeding Habits. *Acta Zoologica* **57,** 13–35 (1976).

136. Engstrom, K & Ahlbert, I. Cone Types and Cone Arrangement in the Retina of some Flatfishes. *Acta Zoologica* **44,** 119–129 (1963).

137. Schuster, S., Wöhl, S., Griebsch, M. & Klostermeier, I. Animal cognition: how archer fish learn to down rapidly moving targets. *Current biology : CB* **16,** 378–83 (2006).

138. Temple, S., Hart, N. S., Marshall, N. J. & Collin, S. P. A spitting image: specializations in archerfish eyes for vision at the interface between air and water. *Proceedings. Biological sciences / The Royal Society* **277,** 2607–15 (2010).

139. Schwassmann, H. O. Visual projection upon the optic tectum in foveate marine teleosts. *Vision research* **8,** 1337–48 (1968).

140. Schmitt, E. A. & Dowling, J. E. Early retinal development in the zebrafish, Danio rerio: light and electron microscopic analyses. *The Journal of comparative neurology* **404,** 515–36 (1999).

141. De Malmazet, D., Kühn, N. K. & Farrow, K. Retinotopic Separation of Nasal and Temporal Motion Selectivity in the Mouse Superior Colliculus. *Current Biology* **28,** 2961–2969.e4 (2018).

142. Takechi, M. & Kawamura, S. Temporal and spatial changes in the expression pattern of multiple red and green subtype opsin genes during zebrafish development. *The Journal of experimental biology* **208,** 1337–45 (2005).

143. Zhao, X.-F., Ellingsen, S. & Fjose, A. Labelling and targeted ablation of specific bipolar cell types in the zebrafish retina. *BMC neuroscience* **10,** 107 (2009).

144. Szél, A *et al.* Unique topographic separation of two spectral classes of cones in the mouse retina. *The Journal of comparative neurology* **325,** 327–42 (1992).

145. Kutsarova, E., Munz, M. & Ruthazer, E. S. Rules for Shaping Neural Connections in the Developing Brain. *Frontiers in Neural Circuits* **10,** 111 (2017).

146. Avitan, L., Pujic, Z., Hughes, N. J., Scott, E. K. & Goodhill, G. J. Limitations of Neural Map Topography for Decoding Spatial Information. *Journal of Neuroscience* **36,** 5385–96 (2016).

147. Avitan, L. & Goodhill, G. J. Code Under Construction: Neural Coding Over Development. *Trends in Neurosciences* **41** (2018).

148. Avitan, L. *et al.* Spontaneous Activity in the Zebrafish Tectum Reorganizes over Development and Is Influenced by Visual Experience. *Current Biology* **27,** 2407–2419.e4 (2017).

149. Reiter, B. *Temporal and spatial receptive field characteristics of tectal neurons in zebrafish larvae* PhD thesis (2006), 1–93.

150. Zhang, R.-w. & Du, J.-l. In Vivo Whole-Cell Patch-Clamp Recording in the Zebrafish Brain. *Methods in molecular biology* **1451,** 281–291 (2016).

151. Perin, R. & Markram, H. A computer-assisted multi-electrode patch-clamp system. *Journal of visualized experiments : JoVE,* e50630 (2013).

152. Wu, Q. & Chubykin, A. A. Application of Automated Image-guided Patch Clamp for the Study of Neurons in Brain Slices. *Journal of Visualized Experiments,* e56010–e56010 (2017).

153. Jun, J. J. *et al.* Fully integrated silicon probes for high-density recording of neural activity. *Nature* **551,** 232–236 (2017).

154. Bonhoeffer, T & Grinvald, A. in *Brain mapping: the methods.* 55–97 (1996).

155. Blasdel, G. G. & Salama, G. Voltage-sensitive dyes reveal a modular organization in monkey striate cortex. *Nature* **321,** 579–585 (1986).

156. Grinvald, A., Lieke, E., Frostig, R. D., Gilbert, C. D. & Wiesel, T. N. Functional architecture of cortex revealed by optical imaging of intrinsic signals. *Nature* **324,** 361–364 (1986).

157. Kalatsky, V. A. & Stryker, M. P. New Paradigm for Optical Imaging: Temporally Encoded Maps of Intrinsic Signal. *Neuron* **38,** 529–545 (2003).

158. Tsien, R. Y. New calcium indicators and buffers with high selectivity against magnesium and protons: design, synthesis, and properties of prototype structures. *Biochemistry* **19,** 2396–2404 (1980).

159. Jaffe, D. B. *et al.* The spread of Na+ spikes determines the pattern of dendritic Ca2+ entry into hippocampal neurons. *Nature* **357,** 244–246 (1992).

160. Denk, W, Yuste, R, Svoboda, K & Tank, D. W. Imaging calcium dynamics in dendritic spines. *Current opinion in neurobiology* **6,** 372–8 (1996).

161. Takahashi, A., Camacho, P., Lechleiter, J. D. & Herman, B. Measurement of Intracellular Calcium. *Physiological Reviews* **79,** 1089–1125 (1999).

162. Ashworth, R., Zimprich, F. & Bolsover, S. R. Buffering intracellular calcium disrupts motoneuron development in intact zebrafish embryos. *Developmental Brain Research* **129,** 169–179 (2001).

163. Nakai, J., Ohkura, M. & Imoto, K. A high signal-to-noise Ca2+ probe composed of a single green fluorescent protein. *Nature Biotechnology* **19,** 137–141 (2001).

164. Tallini, Y. N. *et al.* Imaging cellular signals in the heart in vivo: Cardiac expression of the high-signal Ca2+ indicator GCaMP2. *Proceedings of the National Academy of Sciences* **103,** 4753–4758 (2006).

165. Tian, L. *et al.* Imaging neural activity in worms, flies and mice with improved GCaMP calcium indicators. *Nature Methods* **6,** 875–881 (2009).

166. Akerboom, J. *et al.* Optimization of a GCaMP calcium indicator for neural activity imaging. *Journal of Neuroscience* **32,** 13819–40 (2012).

167. Ohkura, M. *et al.* Genetically Encoded Green Fluorescent Ca2+ Indicators with Improved Detectability for Neuronal Ca2+ Signals. *PLoS ONE* **7** (ed Baudry, M.) e51286 (2012).

168. Chen, T.-W. *et al.* Ultrasensitive fluorescent proteins for imaging neuronal activity. *Nature* **499,** 295–300 (2013).

169. Akerboom, J. *et al.* Genetically encoded calcium indicators for multi-color neural activity imaging and combination with optogenetics. *Frontiers in Molecular Neuroscience* **6,** 2 (2013).

170. Zhao, Y. *et al.* An Expanded Palette of Genetically Encoded Ca2+ Indicators. *Science* **333,** 1888–1891 (2011).

171. Pachitariu, M., Stringer, C. & Harris, K. D. Robustness of Spike Deconvolution for Neuronal Calcium Imaging. *Journal of Neuroscience* **38,** 7976–7985 (2018).

172. Pittman, A. J., Law, M.-Y. & Chien, C.-B. Pathfinding in a large vertebrate axon tract: isotypic interactions guide retinotectal axons at multiple choice points. *Development* **135,** 2865–71 (2008).

173. Hunter, P. R., Lowe, A. S., Thompson, I. D. & Meyer, M. P. Emergent properties of the optic tectum revealed by population analysis of direction and orientation selectivity. *Journal of Neuroscience* **33,** 13940–5 (2013).

174. Dunn, T. W. *et al.* Neural Circuits Underlying Visually Evoked Escapes in Larval Zebrafish. *Neuron* (2016).

175. Hunter, P. R., Hendry, A. C. & Lowe, A. S. Zebrafish brain mapping–standardized spaces, length scales, and the power of N and n. *Developmental neurobiology* **75,** 557–68 (2015).

176. Goodhill, G. J. & Sejnowski, T. J. Quantifying neighbourhood preservation in topographic mappings. *Proceedings of the 3rd Joint Symposium on Neural Computation, La Jolla, CA,* 61–82 (1996).

177. Bauer, H.-U. & Pawelzik, K. Quantifying the neighborhood preservation of self-organizing feature maps. *IEEE Transactions on Neural Networks* **3,** 570–579 (1992).

178. Goodhill, G. J. & Sejnowski, T. J. A Unifying Objective Function for Topographic Mappings. *Neural Computation* **9,** 1291–1303 (1997).

179. Yarrow, S., Razak, K. A., Seitz, A. R. & Seriès, P. Detecting and quantifying topography in neural maps. *PloS one* **9,** e87178 (2014).

180. Doherty, K. A. J., Adams, R. G. & Davey, N. Topological Correlation. *European Symposium on Artificial Neural Networks Bruges (Belgium)* (2006).

181. Delaunay, B. Sur la sphère vide. A la mémoire de Georges Voronoï. *Bulletin de l'Académie des Sciences de l'URSS. Classe des sciences mathématiques et naturelles.* **6,** 793–800 (1934).

182. Bezdek, J. C. & R. Pal, N. An index of topological preservation for feature extraction. *Pattern Recognition* **28,** 381–391 (1995).

183. Yekutieli, D. & Benjamini, Y. The control of the false discovery rate in multiple testing under dependency. *The Annals of Statistics* **29,** 1165–1188 (2001).

184. Wagner, C. H. Simpson's Paradox in Real Life. *The American Statistician* **36,** 46 (1982).

185. Naumann, E. A., Engert, F. A. & Stürmer, C. A. O. *Using G-CaMP 1.6 to Monitor Visually-Evoked Synaptic Activity in Tectal Neurons in vivo* PhD thesis (2005).

186. Strähle, U. *et al.* Zebrafish embryos as an alternative to animal experiments—A commentary on the definition of the onset of protected life stages in animal welfare regulations. *Reproductive Toxicology* **33,** 128–132 (2012).

187. Hinz, F. I., Aizenberg, M., Tushev, G. & Schuman, E. M. Protein synthesis-dependent associative long-term memory in larval zebrafish. *Journal of Neuroscience* **33,** 15382–7 (2013).

188. Bianco, I. H., Kampff, A. R. & Engert, F. Prey Capture Behavior Evoked by Simple Visual Stimuli in Larval Zebrafish. *Frontiers in Systems Neuroscience* **5,** 101 (2011).

189. Barker, A. J. & Baier, H. Sensorimotor Decision Making in the Zebrafish Tectum. *Current Biology* **25,** 2804–2814 (2015).

190. Naumann, E. A. *et al.* From Whole-Brain Data to Functional Circuit Models: The Zebrafish Optomotor Response. *Cell* **167,** 947–960.e20 (2016).

191. Bergmann, K. *et al.* Imaging Neuronal Activity in the Optic Tectum of Late Stage Larval Zebrafish. *Journal of Developmental Biology* **6,** 6 (2018).

192. Li, L & Dowling, J. E. Zebrafish visual sensitivity is regulated by a circadian clock. *Visual neuroscience* **15,** 851–7 (1998).

193. Li, P. *et al.* Circadian rhythms of behavioral cone sensitivity and long wavelength opsin mRNA expression: a correlation study in zebrafish. *Journal of Experimental Biology* **208,** 497–504 (2005).

194. Friston, K. J., Ashburner, J., Kiebel, S., Nichols, T. & Penny, W. D. *Statistical parametric mapping : the analysis of funtional brain images* 647. ISBN: 9780123725608 (Elsevier/Academic Press, 2007).

195. Savitzky, A. & Golay, M. J. E. Smoothing and Differentiation of Data by Simplified Least Squares Procedures. *Z. Physiol. Chem. Chem. & Ind* **40,** 1627–1639 (1964).

196. Swindale, N. Orientation tuning curves: empirical description and estimation of parameters. *Biological Cybernetics* **78,** 45–56 (1998).

197. Niell, C. M. & Stryker, M. P. Highly Selective Receptive Fields in Mouse Visual Cortex. *Journal of Neuroscience* **28,** 7520–7536 (2008).

198. Ramdya, P., Reiter, B. & Engert, F. Reverse correlation of rapid calcium signals in the zebrafish optic tectum in vivo. *Journal of Neuroscience Methods* **157,** 230–237 (2006).

199. Tabata, T. & Kano, M. Heterogeneous Intrinsic Firing Properties of Vertebrate Retinal Ganglion Cells. *Journal of Neurophysiology* **87,** 30–41 (2002).

200. Quiroga, R. Q., Nadasdy, Z. & Ben-Shaul, Y. Unsupervised Spike Detection and Sorting with Wavelets and Superparamagnetic Clustering. *Neural Computation* **16,** 1661–1687 (2004).

201. Berens, P. CircStat: A MATLAB Toolbox for Circular Statistics. *Journal of Statistical Software* **31,** 1–21 (2009).

202. Cellerino, A, Bähr, M & Isenmann, S. Apoptosis in the developing visual system. *Cell and tissue research* **301,** 53–69 (2000).

203. Biehlmaier, O., Neuhauss, S. & Kohler, K. Onset and time course of apoptosis in the developing zebrafish retina. *Cell and Tissue Research* **306,** 199–207 (2001).

204. Zhang, M. *et al.* Functional elimination of excitatory feedforward inputs underlies developmental refinement of visual receptive fields in zebrafish. *Journal of Neuroscience* **31,** 5460–9 (2011).

205. Jin, J. Z. *et al.* On and off domains of geniculate afferents in cat primary visual cortex. *Nature Neuroscience* **11,** 88–94 (2008).

206. Kremkow, J., Jin, J., Wang, Y. & Alonso, J. M. Principles underlying sensory map topography in primary visual cortex. *Nature* **533,** 52–57 (2016).

207. Yeh, C.-I, Xing, D. & Shapley, R. M. "Black" Responses Dominate Macaque Primary Visual Cortex V1. *Journal of Neuroscience* **29,** 11753–11760 (2009).

208. Blackwell, H. R. Contrast thresholds of the human eye. *Journal of the Optical Society of America* **36,** 624–43 (1946).

209. Bowen, R. W., Pokorny, J & Smith, V. C. Sawtooth contrast sensitivity: decrements have the edge. *Vision research* **29,** 1501–9 (1989).

210. Liu, K. & Yao, H. Contrast-dependent OFF-dominance in cat primary visual cortex facilitates discrimination of stimuli with natural contrast statistics. *European Journal of Neuroscience* **39,** 2060–2070 (2014).

211. Huberman, A. D. *et al.* Architecture and Activity-Mediated Refinement of Axonal Projections from a Mosaic of Genetically Identified Retinal Ganglion Cells. *Neuron* **59,** 425–438 (2008).

212. Hong, Y. K., Kim, I.-J. & Sanes, J. R. Stereotyped axonal arbors of retinal ganglion cell subsets in the mouse superior colliculus. *The Journal of comparative neurology* **519,** 1691–711 (2011).

213. Patterson, B. W., Abraham, A. O., MacIver, M. A. & McLean, D. L. Visually guided gradation of prey capture movements in larval zebrafish. *Journal of Experimental Biology* **216** (2013).

214. Engeszer, R. E., Barbiano, L. A. D., Ryan, M. J. & Parichy, D. M. Timing and plasticity of shoaling behaviour in the zebrafish, Danio rerio. *Animal behaviour* **74,** 1269–1275 (2007).

215. Dreosti, E., Lopes, G., Kampff, A. R. & Wilson, S. W. Development of social behavior in young zebrafish. English. *Frontiers in neural circuits* **9,** 39 (2015).

216. Lettvin, J., Maturana, H., McCulloch, W. & Pitts, W. What the Frog's Eye Tells the Frog's Brain. *Proceedings of the IRE* **47,** 1940–1951 (1959).

217. Kaethner, R. J. & Stuermer, C. A. Dynamics of terminal arbor formation and target approach of retinotectal axons in living zebrafish embryos: a time-lapse study of single axons. *Journal of Neuroscience* **12,** 3257–71 (1992).

218. Allison, W. T., Haimberger, T. J., Hawryshyn, C. W. & Temple, S. E. Visual pigment composition in zebrafish: Evidence for a rhodopsin-porphyropsin interchange system. English. *Visual neuroscience* **21,** 945–52 (2004).

219. Burton, C. E., Zhou, Y., Bai, Q. & Burton, E. A. Spectral properties of the zebrafish visual motor response. *Neuroscience letters* **646,** 62–67 (2017).

220. Reichardt, W. Autokorrelationsauswertung als Funktionsprinzip des Zentralnervensystems. *Zeitschrift für Naturforschung* **12b,** 447–457 (1957).

221. Rinner, O., Rick, J. M. & Neuhauss, S. C. F. Contrast Sensitivity, Spatial and Temporal Tuning of the Larval Zebrafish Optokinetic Response. *Investigative Opthalmology & Visual Science* **46,** 137 (2005).

222. Spekreijse, H, Van Norren, D & Van Den Berg, T. J.T. P. Flicker Responses in Monkey Lateral Geniculate Nucleus and Human Perception of Flicker (de Lange characteristics/microelectrodes/macaques/single cells/critical flicker frequency). *Proceedings of the National Academy of Sciences* **68,** 2802–2805 (1971).

223. Hung, C. P., Kreiman, G., Poggio, T. & DiCarlo, J. J. Fast Readout of Object Identity from Macaque Inferior Temporal Cortex. *Science* **310,** 863–866 (2005).

224. Potter, M. C., Wyble, B., Hagmann, C. E. & McCourt, E. S. Detecting meaning in RSVP at 13 ms per picture. *Attention, Perception, & Psychophysics* **76,** 270–279 (2014).

225. Di, Y. *et al.* The effect of various levels of stroboscopic illumination on the growth of guinea pig eyes. *Clinical and Experimental Optometry* **97,** 55–61 (2014).

226. Chan, Y.-C. & Chiao, C.-C. Effect of visual experience on the maturation of ON–OFF direction selective ganglion cells in the rabbit retina. *Vision Research* **48,** 2466–2475 (2008).

227. Saszik, S & Bilotta, J. Effects of abnormal light-rearing conditions on retinal physiology in larvae zebrafish. *Investigative ophthalmology & visual science* **40,** 3026–31 (1999).

228. Tian, N & Copenhagen, D. R. Visual deprivation alters development of synaptic function in inner retina after eye opening. *Neuron* **32,** 439–49 (2001).

229. Tian, N. Visual experience and maturation of retinal synaptic pathways. *Vision Research* **44,** 3307–3316 (2004).

230. Di Marco, S., Nguyen, V. A., Bisti, S. & Protti, D. A. Permanent Functional Reorganization of Retinal Circuits Induced by Early Long-Term Visual Deprivation. *Journal of Neuroscience* **29,** 13691–13701 (2009).

231. Dunn, F. A., Della Santina, L., Parker, E. D. & Wong, R. O. L. Sensory experience shapes the development of the visual system's first synapse. *Neuron* **80,** 1159–66 (2013).

232. Giovannelli, A., Di Marco, S., Maccarone, R. & Bisti, S. Long-term dark rearing induces permanent reorganization in retinal circuitry. *Biochemical and Biophysical Research Communications* **365,** 349–354 (2008).

233. Robertson, G. N., Mcgee, C. A. S., Dumbarton, T. C., Croll, R. P. & Smith, F. M. *Development of the Swimbladder and Its Innervation in the Zebrafish, Danio rerio* tech. rep. (2007), 967–985.

234. Jardine, D. & Litvak, M. K. Direct yolk sac volume manipulation of zebrafish embryos and the relationship between offspring size and yolk sac volume. *Journal of Fish Biology* **63,** 388–397 (2003).

235. Carrillo, A. & McHenry, M. J. Zebrafish learn to forage in the dark. *The Journal of experimental biology* **219,** 582–9 (2016).

236. Diekmann, H., Kalbhen, P. & Fischer, D. Characterization of optic nerve regeneration using transgenic zebrafish. *Frontiers in Cellular Neuroscience* **9,** 118 (2015).

237. Scholes, J. H. Nerve fibre topography in the retinal projection to the tectum. *Nature* **278,** 620–624 (1979).

238. Thompson, A. W. *et al.* Functional Profiles of Visual-, Auditory-, and Water Flow-Responsive Neurons in the Zebrafish Tectum. *Current biology : CB* **26,** 743–54 (2016).

239. Bilotta, J. Effects of abnormal lighting on the development of zebrafish visual behavior. *Behavioural Brain Research* **116,** 81–87 (2000).

240. Conte, S. D. & De Boor, C. *Elementary numerical analysis : an algorithmic approach* 432. ISBN: 0070124477 (McGraw-Hill, 1980).

241. Nishimoto, S. *et al.* Reconstructing visual experiences from brain activity evoked by natural movies. *Current biology : CB* **21,** 1641–6 (2011).

242. Temizer, I., Donovan, J. C., Baier, H. & Semmelhack, J. L. A Visual Pathway for Looming-Evoked Escape in Larval Zebrafish. *Current biology : CB* **25,** 1823–34 (2015).

243. Postel, J. User Datagram Protocol, RFC768. *ISI* (1980).

Appendix A

A high-resolution, high-coverage visual presentation system

A.1 Rationale

Many different systems have been used to present static images and/or videos to zebrafish [37, 52, 174, 242]. The goals of such systems are to allow reproducible, tightly-controlled stimuli to experimental animals, while recordings are made of the neural activity of the animal. This places a number of constraints on such a system, in that it must be robust, have minimal variation in its performance, and have a certain degree of interaction with whatever recording technology is used so that analysis can be automated as far as possible.

In order to maximise the amount of data obtained in each experiment, the maximum possible amount of visual field should be covered during a presentation, as functional properties can only be obtained for neurons whose receptive field contains the screen. The most efficient way to cover maximal visual area would be with a spherical screen. Although options using curved screens were examined, current technology for this proved unworkable for the desired size and level of curvature. An additional concern in this case was that the system must be easily assembled and disassembled, given that the available microscope was shared between many users. This microscope also had severe constraints on space, limiting the size of the system that could be placed inside it.

Projectors, which have been used extensively in previous systems, are not ideal for a number of reasons. Their luminance is not uniform across the surface they project onto. If they are used on curved surfaces, this creates additional nonuniformity in their luminance, and their resolution is also nonuniform. A significant distance is required between the projector and the screen. Finally, they take time to set up and align with their screen, which would limit experimental time on a shared microscope.

Based on these constraints, the chosen solution was a video wall, in which multiple LCD screens facing the experimental subject approximate a curved surface while providing as large as possible a viewing area. Here I show the development process for a novel system, to present videos at high resolution, as well as demonstrating the quality assurance processes during its design.

A.2   Overview & Software

Fortunately, an open source software library designed specifically for low-cost video walls was already in existence (**www.piwall.co.uk**), allowing streaming of movies via UDP [243] from a single "master" computer to multiple screens, each driven by a single Rasperry Pi (RPi). This master/slave type design is well suited to functional imaging experiments as it allows a single point of control for experiments, and generation of metadata files. The data flow in this system can be seen in **fig. A.1A**.

In addition to the 5 RPis driving screens, a sixth was used to generate Transistor-Transistor Logic (TTL) pulses synchronised with movie presentation. This utilised a custom Python script, outputting TTLs according to when data comprising streamed movie is received. Two channels of TTLs are sent from RPi6. On one channel, an analog pin is set to ON at the beginning of the movie, switching OFF after it has finished. The second channel switches its state when every 500th UDP packet is received by RPi6, starting from the first packet. The microscope is set up to record the timing of all rising and falling edges on voltages sent to a TTL interface (in the case a NI-DAQ (Nikon)) directly into the acquired images as metadata, allowing automated analysis when combined with metadata files created by the "master" laptop when movies are streamed.
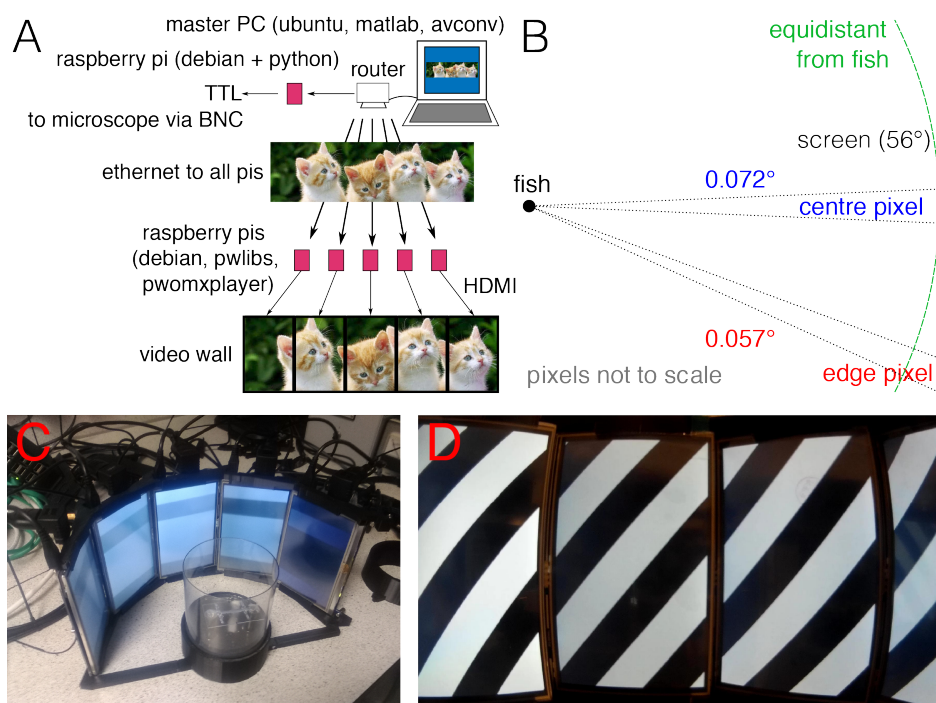
Figure A.1: **A** Data flow in the visual presentation system. **B** Visual distortion resulting from straight screens at a fixed distance from the fish, as pixels cannot be equidistant. **C** The finished system in all its glory. **D** A movie of dark and light bars, corrected for geometric distortions, and with bezel compensation in order to minimise discontinuities across screens. Imaged using a "fisheye" lens under imperfect conditions.

A.2.1   Interface

Given that most analysis would subsequently be performed using MATLAB, the whole system was ultimately driven by MATLAB, for easy compatibility of metadata files. A single function was constructed which reads from lists of movies (for example, "sparsenoise"), randomises their order and streams them to the RPis with a specified inter-epoch interval. It additionally took as input details about the fish - a unique identifier, the fish age, rearing conditions, with certain checks to ensure validity of input information. All this information was then written into a metadata file (named automatically based on the fish identifier and the number of experiments already performed on that fish) which could be used in conjunction with the microscope data for automated analysis. The timing of the movie starts and ends can be calculated from TTL locations within the microscope output (see **appendix A.4.2**), while the metadata specifies which movie is which, and the names of the movies thus connected to changes in fluorescence occurring while they were played.

A.2.2   Correcting for geometric distortion

The different points on a flat screen can never be equidistant from the viewing eye, in either azimuth or elevation. Thus, each pixel on the screen occupies a slightly different visual angle. The visual presentation system was designed such that the vertical axis of the screen was ~110mm, while the horizontal radius of the ring was ~120mm. The whole screen occupies ~56° of visual space vertically. This means that while a 1cm bar at the vertical centre of the screen would appear as 4.8°, the same bar placed at the upper or lower extreme of the screen would occupy only 3.9° (see **fig. A.1B**). The resolution of the screen is then between 0.057 and 0.072°/px at the horizontal screen centres.

There is additional distortion along the horizontal axis, due to the imperfect dovetailing of the screens - one side of each screen was further than the other from the fish (see **fig. A.1C**). In order to remove the effects of the vertical and horizontal distortion, visual presentations were transformed in order to retain constant apparent sizes of the relevant features regardless of their location on the screen and, where appropriate, continuity across screen boundaries (**fig. A.5G**).

Figure A.2: The tank, showing pillars used to hold slides and fish in the centre

A.3   Design and construction of physical components

A.3.1   Tank

The tank in which the fish is mounted was constructed using a thin-walled, cylindrical glass (Riedel H2O), chosen for minimal visual distortion of transmitted light. 10mm×100mm glass test tubes (Kimble Chase) were cut to a length of 50mm, and filled with epoxy resin (Scotch Weld), with the same magnet as on the slides (Eclipse Magnetics N850S) inside one end.

In order to mount these pillars inside the tank, a retort stand held a prebuilt microscope slide (see **fig. A.3B**) inside the tank, with the epoxy-filled test tubes suspended via their magnets. The precise postion of the slide was measured and corrected using callipers, to a precision of ~1mm. Premixed epoxy resin was then poured into the surrounding space to a depth of ~ 5mm and left to set for 24 hours.
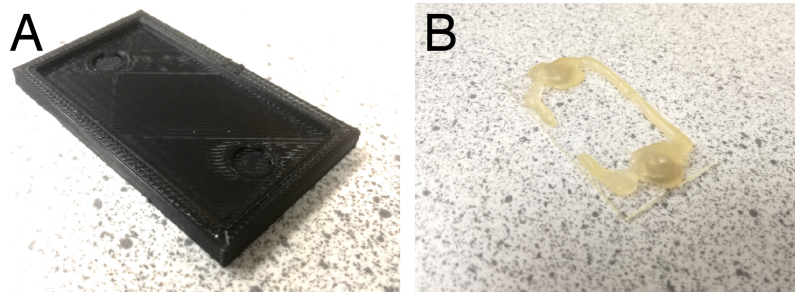
Figure A.3: **A** Jig used for construction of slides. The magnets are placed into the circular recesses, with adhesive surface facing upwards, and a pre-cut glass slide is placed on top. **B** The magnets remain in place, and a border is added using a hot-glue gun.

A.3.2 Microscope slides

Slides for mounting immobilised fish were constructed from glass microscope slides (Thermo Scientific BS7011/2). These were trimmed to a length of 50mm using a tungsten-carbide blade (Stanley), and 6mm self-adhesive magnets (Eclipse Magnetics N850S) were mounted using a jig (see **fig. A.3A**) with a width of 38mm between their centres. The slide was then removed from jig and a border added using a hot-glue-gun, providing a rough surface for setting agarose to adhere to, as well as ensuring the magnets do not fall off when their self-adhesive coating is immersed in water. The magnets facilitate placing the fish in precisely the same location within the system using complementary magnets in the tank itself. Removing and replacing fish within the tank is a difficult task, particularly within the confined environs of a microscope interior, and this magnetic system makes changing experimental animals far easier than the removal and replacement of the tank between animals.

A.3.3 Housing for screens and tank

In order to ensure correct placement of screens relative to the fish, a housing was built to both elevate the tank holding the fish, and to hold all screens in place. Components were designed using **www.tinkercad.com** and printed using a Makerbot Replicator 2X (Makerbot) in black ABS (Makerbot). The enclosure was designed such that the system (**fig. A.1C**) is easily disassembled into a group of 2
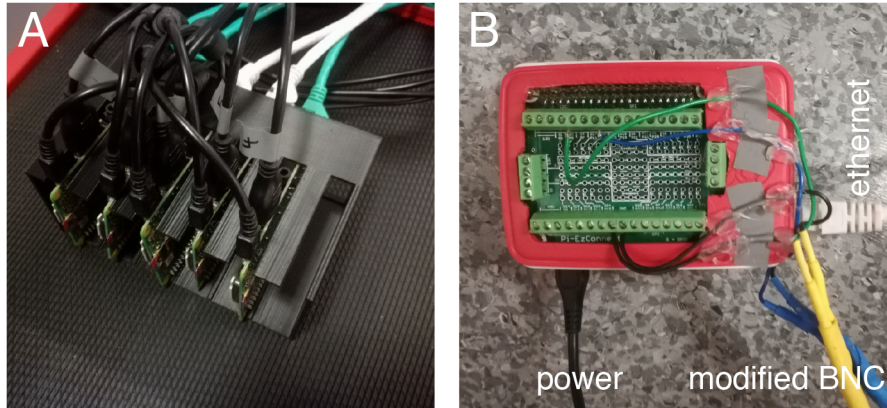
Figure A.4: **A** The 5 RPis which drive video wall screens, in housing and with all cables connected. **B** RPi6, with modified housing, and BNC cables connected.

screens, a group of 3 screens, and the holder for the tank.

A.3.4 Housing for Raspberry Pis

The 5 RPis which drove screens were mounted in a custom "stack" enclosure, printed using a Makerbot Replicator 2X (Makerbot) in black ABS (Makerbot), see (**fig. A.4A**). This facilitates debugging, during experimental setup as it provides easy access to the largest number of fallible cable connections in one location. The design was stolen, shamelessly, from **https://www.thingiverse.com/thing:664343**.

The RPi used for TTL transmission was mounted in a Rasperry Pi Official Case, modified to accommodate the Pi-EzConnect hat (Adafruit) which allows solder-free wire access to the analog output pins (**fig. A.4B**).

A.3.5 Electrical components

RPis were the Raspberry Pi 2 Model B (Raspberry Pi). Screens were Makibes 5" Touch Screen HDMI Monitor Model B, which are 480×800px.

Power was provided to the screens and RPis separately via 2×PowerPort 10 (Anker),

with a micro-usb cable powering each unit.

The router for data streaming was a DSR-250N (D-Link). All streaming was via wired ethernet (rather than wireless) ports to minimise dropouts.

A.4   Quality control and assurance

Such a system inevitably has undesirable characteristics, particularly given the low-cost nature of the components used. Here the exact procedures used to quantify and correct for such issues are documented:

A.4.1   Compensation for differences in screen brightness

Early on, it was noticed that the 5 screens being used were of different luminance, despite their uniform provenance. It was decided that the best way to account for this eccentricity was via lookup tables (LUTs) applied to movies when they were generated, and to always use the same screens.

As LCD screens effectively have separate coloured pixels for each whole pixel, the brightnesses in the colour channels of each pixel sum linearly. This means that matching the brightnesses of each colour channel across all screens also entails matching of grey-tones and brightnesses of these greys. Movies were created to step the brightness of the colour at 1AU/s on an 8bit scale. The luminance emitted from the screen was recorded using an Opti-CAL OP200E (Camrbidge Research Systems). The luminance resulting from linear increase in defined brightness was asymmetrically sigmoidal across all screens and colours (see **fig. A.5A-E**).

LUTs were created such that an 8bit input would produce linearly variable luminance, peaking at the maximum brightness of the dimmest screen (the central one, **fig. A.5C**) . Although this results in a loss of dynamic range across the other screens, it ensures uniform luminance while removing the potential for clipping artefacts.
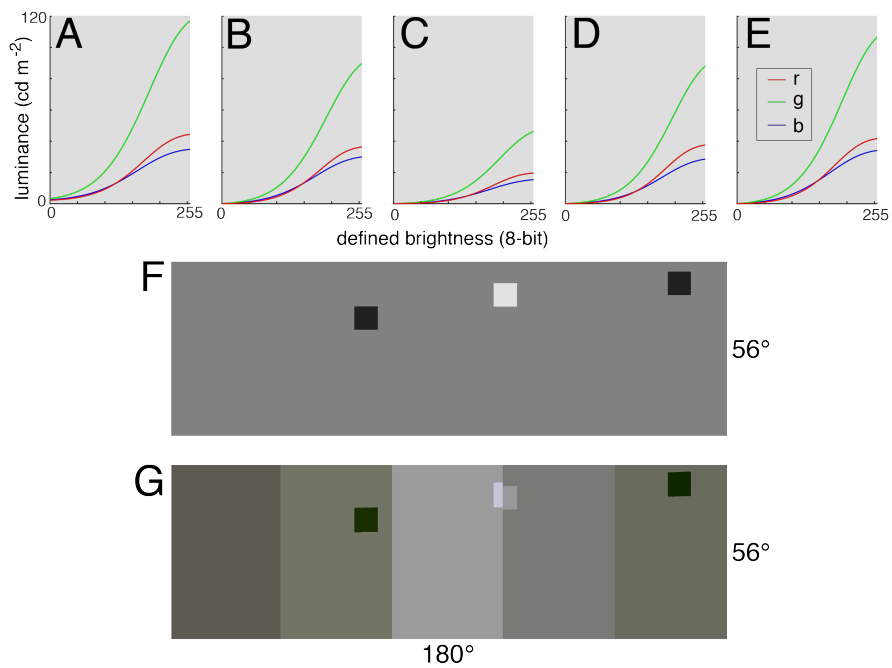
Figure A.5: **A-E** Sigmoidal curves of brightness against luminance for the R, G and B channels of the five screens used in the final system, used to correct movies. **F** Desired appearance of a frame from a sparse noise movie (see **section 3.2.2**). **G** Rendered version of the same frame, after applying compensation for geometric distortion and luminance eccentricity. This will appear similar to **F** when presented on the system.

A.4.2 Movie start and end timings

In order to allow the storage of movie timing information into the images on the microscope, RPi6 was used to convert information about movie streaming into Transistor-Transistor Logic pulses (TTLs). This was achieved using a custom Python script, which monitors the data being streamed through the router and, depending on the amount and nature of such data, turns the RPi analog outputs on or off. Two channels of TTLs are sent from RPi6. On one channel, one analog pin is set to ON at the beginning of the movie, switching OFF after it has finished. The second channel switches its state when every 500th UDP packet is received by RPi6, starting from the first.

There could be a number of sources of timing differences between microscope receiving/recording TTLs, and the actual luminance changes on the screens. For example, although all Raspberry Pis receive video data simultaneously, the latency of the video player software on RPis 1-5 is likely to be different from that of the Python script driving the TTL output on RPi6. Additionally there could be a systematic difference introduced by the Nikon Elements software recording imaging data and the TTLs.

The differential latency was calculated by using a sequence of movies with first frames of radically different brightness than the last frame of the previous one, driving sharp transitions in brightness at each movie start. One of the screens was placed directly under the microscope objective, and scanned with no laser power at $\sim$ 31Hz, while recording TTLs. This approach does not allow separation of the different sources of temporal error: it only facilitates calculation of the overall error introduced over the whole signal path.

For each frame (examples in **fig. A.6A**), the mean luminance was calculated. Calculating the pseudo-derivative of the mean recorded brightness allowed the extraction of peaks representing the actual start times of the movies (**fig. A.6B**). Other peaks represent changes of luminance for the scanned area during the movie - the movement of bars past the area being scanned (see **section 3.2.2**). The latency for movie starts (**fig. A.6C**) was calculated from the difference between the recorded TTL time and the next frame with a change in luminance above the threshold. The overall mean latency for movie start was found to be 22ms, with no association found between the movie shown and the latency (data not shown). Although this

value is arguably negligible given that recording a frame on the microscope takes ~32ms, this quality control step was vital: latency could easily have been on the order of seconds.

In order to calculate movie endpoints, the second channel of TTLs was used. The UDP streaming protocol[243] sends data packets of a uniform size (1433 bytes measured, data not shown). This information, in conjunction with the sizes of the streamed movie files, was used to calculate the endpoints of movies, as there were possibilities of drift in streaming speed. The upper bound for the movie end is set by the "end" movie TTL, but the true endpoint is better estimated via linear interpolation of the "packet" UDP TTLs to find the time at which the presentation ended **fig. A.6D**. This procedure was applied after correction of all TTL timings by the 22ms described above.
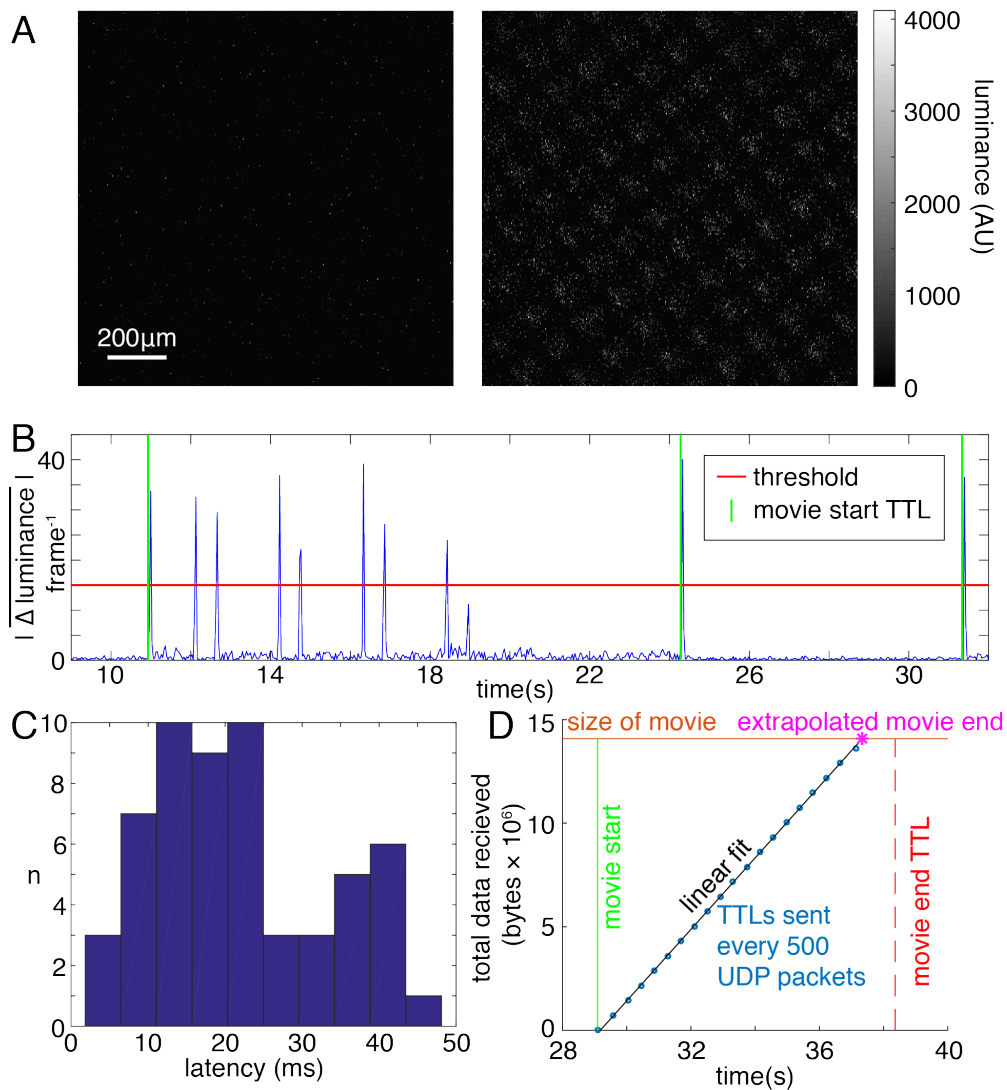
Figure A.6: **A** Example images of low (left) and high (right) luminance frames on a screen, recorded using the same microscope used for functional imaging. **B.**Example trace of the pseudo-derivative from mean luminance traces over images such as in **A**, with the threshold for "large" change in luminance (representing movie starts) and TTLs marked. **C.** Histogram of calculated latencies between TTL and movie start. $\mu = 20$ms **D.** An example plot from a real experiment, demonstrating how end-point is determined automatically from the TTL timestamps, in conjunction with metadata about the size of the presented movie.

A.5 Discussion

Here the design and construction of a new visual presentation, built at extremely low cost, has been described. Although every project has specific needs and considerations, they often persist, making such a procedure worth examination. For example, the TTL latency is microscope-specific, but the method used to calculate and compensate for it is general. In summary, I built a thing. It does stuff, and after a substantial amount of work, I'm pretty sure it is the right stuff. Basically I'm no stupider than anyone else who shows movies to fish, as I often worry.

Appendix B

Topographic maps: conceptually easy, practically hard

Topographic maps: conceptually easy, practically hard

Andrew Bard Rotation 3
Supervised by Andrew Lowe

Abstract

The neurons in sensory epithelia (such as the retina) project to brain areas in such a way that neighbouring cell bodies within the epithelium produce neighbouring axonal arbours within retinorecipient brain areas. Such organisation is an example of topography: two spaces with neighbouring points in one space project to neighbours in the other. Such maps are widespread in nervous systems.

There are two problems concerning the detection and quantification of these maps. Firstly, the maps measured in vivo are often too complex to visualise, making qualitative judgments impossible. Secondly, brain areas usually have distortions at the meso/macro scales relative to the sensory epithelia so quantifying topography is difficult. Thus, the aim of the project was to develop a generalisable metric that could (a) detect the presence of topographic order, with statistical confidence (b) estimate the precision of that order.

Here I explore the topographic product, a graph-theory based metric for topography, and apply it to model data based on visual-to-tectal maps. I have shown that this metric is resistant but not impervious to map shape, and that via a novel normalisation treatment the output is improved. Finally I show that when applied to data modelling multiple independent experimental subjects, it can recover true map precision unless maps across subjects are shifted relative to each other. Under such conditions I have developed a means of quantifying such inter-subject jitter.

Using a dataset derived from functional imaging of zebrafish retinal ganglion cells, I have demonstrated the utility of the topographic product in detecting topographic maps with statistical confidence; the precision of the tectal map; and inter-subject variability.

Introduction

Topographic maps are present throughout the brains of many species. For example, neurons that are adjacent in the retina project their axons to adjacent spaces in retinorecipient brain areas such as the tectum in zebrafish. This means that these areas of the brain have topographic maps of retinal space.

While there has been much research into the processes by which these maps form (for example, molecular guidance cues and neuronal activity patterns required[1]), their actual purpose is far harder to examine. Given that topographic maps are a recurrent feature of visual processing, if we are to understand this system we must also have an appreciation of the extent that topography contributes to it.

This necessitates a robust and quantitative metric for topography. The aim of this project was to research, develop and test a generalisable metric, capable of detecting topographic order with an estimate of statistical confidence. Additionally, this metric should provide estimates of map precision.

The Lowe lab currently uses an in-house metric for topographic order, the scaled cosine of similarity (CoS). This metric scales the cosine of the angle between paired points by the ratio of their lengths such that a value of 1 represents perfect order; zero is orthogonal and -1 the points are inverted. Using all pair-wise comparisons, a distribution of scaled CoS against the distance between each pair of points is derived. Binning this data and finding the maximum value toward which it tends provides an estimate of order.

Using very simple maps I have produced an example of the scaled CoS - when the maps are identical grids, with noise applied independently (**fig. 1A**), the maximum order approaches 1 (**fig. 1B**). However, when a simple 45° rotation is applied to one of the maps (**fig. 1C**), the maximum detected order drops sharply (**fig. 1D**), even though all nearest-neighbour relations are obviously conserved. Although this can be overcome by using a series of transformations to align the maps, this is computationally intensive and not trivial when distorted maps are compared.

This problem illustrates one of the difficulties in quantifying topography: any metric must simultaneously take account of global order and be resistant to differences in shape, size or orientation. These global shape differences, found in vivo, alter neighbour relations at the macroscopic scale.

Figure 1. Scaled cosine of similarity cannot reliably detect the degree of topographic order in maps of altered orientation. (A) A pair of maps generated by adding noise independently to two grids. Same-coloured points across maps represent matched pairs (B) the scaled cosine of similarity reaches a maximum of almost 1 (almost perfect order). (C) A similar pair of maps, but with one rotated 45°. (D) In this case, the scaled cosine of similarity gives a much lower value of maximum order, despite neighbour relations being conserved analogously to (A).

The topographic product (TP) was originally developed to analyse chaotic attractors in nonlinear dynamics[2], but was later implemented for assessing dimensionality mismatches in feature maps[3], like orientation pinwheels found in the mammalian cortex and bat tonotopic maps[4]. It was more recently used in a study which assessed the statistical power of a number of metrics for detecting (but not quantifying) topography, at which it was found to be successful[5]. Although complex and non-intuitive, it is based on principles of graph theory, and is concerned with comparing neighbour identities of each point between the maps, on microscopic and macroscopic scales. I chose to investigate it for this reason.

Topography can be modelled with sets of coordinates in two spaces. Here I exploit this approach to create maps inspired by zebrafish visuotectal maps. The model maps have defined topographic properties and known levels of disorder, and thus have been used to assess empirically the behaviour of the topographic product. Finally, I apply it to a real dataset derived from functional imaging of zebrafish tecta.

Methods

All modelling and analysis performed using Matlab.

The topographic product in theory

The formulae for the topographic product attempts to provide an estimate of order across all scales of the map. It achieves this by examining the ratio of distances in each space (visual or tectal) for all pairs of points representing the map. In contrast to similar metrics, pairs of points are ordered by ranked distance rather than absolute distance. It is the ranking of relative distance that confers its purported resistance to map shape and has its roots in graph theory[3].

Given visual and tectal spaces V and T, with N matched-points sampling both spaces. There is notation for specifying neighbourhood relations, where $n_1^V(j)$ represents the point j's nearest other point, in space V. Then, let $n_k^V(j)$ refer to j's kth nearest point in V. Corresponding notation applies to space T.

Let $d^V(\ldots,\ldots)$ equal the distance between any two points in space V, with corresponding notation in space T. Then, $d^V(j, n_k^T(j))$ refers to the distance, measured in V space, between j and its kth nearest neighbour in T space. Two sets of distance ratios are defined:

$$Q_1(j,k) = \frac{d^V(j, n_k^T(j))}{d^V(j, n_k^V(j))} \tag{1}$$

$$Q_2(j,k) = \frac{d^T(j, n_k^T(j))}{d^T(j, n_k^V(j))} \tag{2}$$

Q_1 represents the ratio of distances in visual space of j and its kth nearest point in T relative to its kth nearest point in visual space. Q_2 represents the ratio of the distances between the same pair of points, but measured in T space. These two ratios are combined to produce a value, P_3, which defines the level of neighbour conservation for each point and neighbourhood size (up-to-the kth nearest neighbour of each point):

$$P_3(j,k) = \left[\prod_{l=1}^{k} Q_1(j,l) Q_2(j,l) \right]^{\frac{1}{2k}} \tag{3}$$

Finally, the natural logarithm is taken of P_3, then it is made positive as in [4] (facilitating calculation of p-values). The mean is taken across all points and neighbourhood sizes to give the final output, P_T:

$$P_T = \frac{1}{N(N-1)} \sum_{j=1}^{N} \sum_{k=1}^{N-1} |\ln P_3(j,k)| \qquad \textbf{(4)}$$

The minimum value this can take is 0, representing perfect order across all scales.

Computational models of visual-to-tectal maps

Visual space was modelled using 120-by-90° spaces, with 5° between points. The tectum was modelled using a biaxial quadratic transformation of the grid (**fig. 2B**), derived from estimates of tectal map curvature by the Lowe lab. Points were randomly displaced in both dimensions according to a normal distribution with mean = 0 and a defined SD. In visual space, the SD was 0.83° in all cases (**fig. 2A**), whilst tectal maps had varying degrees of noise added(for example, **fig. 2C**). These maps were used to examine the relationship between varying degrees of map disorder and the TP.

Figure 2. The topographic product exhibits a linear relationship with added map noise. (A) Visual space (B) Tectal space with no noise. Colours represent matched-pairs with those in visual space. (C) Tectal space with noise added (D) Shuffled version of (C). (E) P_T estimated for each map pair and the shuffled pair for increasing degrees of added noise (F) Normalising the noise applied to the square root of the map area simplifies the curve, and compresses maximum disorder into a cloud. Shuffled P_Ts are the mean of N_{shuf} = 1000.

We can create random permutations of these maps, in which each point in the tectum is randomly reassigned a matched-point in visual space (**fig. 2D**). There are $N!$ different shuffled versions of a map, of which only very few will have order – meaning that if a map is ordered, any individual shuffled version is likely

to be less ordered. N_{shuf} refers to the number of shuffles performed for each "true" map.

Relationship between topographic product and map disorder

To understand how the TP operates for different map conditions it was first necessary to examine the relationship between the TP and map disorder. An initial experiment kept noise in the artificial visual scene constant, while varying the amount of noise in the artificial tectum. The true and shuffled P_Ts were then calculated and reported as a function of the noise introduced (**fig. 2E**). This shows that as the noise within tectal maps increases, so does P_T. However, the curve is complex. Additionally, the P_T of shuffled maps increases with noise, implying that the shape of the map does contribute to P_T, as applying noise progressively degrades whatever shape the map starts with, turning it into a circle.

The point at which true P_T reaches a plateau can be regarded as the point at which all order has been destroyed by noise (maximum disorder), although this plateau itself has a high variance. A corollary of this is that as the plateau is reached, the true P_Ts and shuffled P_Ts converge: the true map is as disordered as the average of many random permutations.

However, the application of noise alters the size of the map; in **fig. 2F**, the standard deviation was normalised to the square root area of the artificial tectum (calculated by Delaunay triangulation[6]):

$$Area\text{-}normalised\ SD = \frac{SD}{\sqrt{Area}} \qquad (5)$$

This has two main effects. Firstly, it simplifies the relationship between noise and P_T. Secondly, the plateau of maximum disorder is converted to a cloud. At the point of maximum disorder, increasing the SD of the noise linearly increases the square root of the area, so the area-normalised standard deviation (ANSD) stays the same.

In terms of fitting curves to these data so that the P_T of a real map pair can be converted into an estimate of disorder, the points appear to approximate a linear relationship, with a levelling-off near zero noise. This can be approximated with the sum of a linear fit and an exponential decay, of the form:

$$y = Ae^{-rx} + bx \qquad (6)$$

The precision of a map can be defined as the smallest distance at which topographic order can be observed, which will be proportional to the noise in the map.

Calculating p-values

To estimate whether any given map pair have topographic order, p-values can be computed using many shuffled maps[4] (see **fig. 2D**). P_T is calculated for a large number of shuffles (N_{shuf}), and the number of these for which shuffled P_T < true P_T is calculated (the number of shuffles for which the shuffled map appears more ordered than the real one, N_{better}).

$$p = \frac{N_{better} + 1}{N_{shuf} + 1} \tag{7}$$

This gives us the probability that the true map is more ordered than would be expected by chance.

Multi-subject analysis

For analyses involving multiple subjects, points from all subjects were combined into a single map. These maps were then subsampled, taking 432 randomly selected points (to produce a "composite"). The normP_T (see **Results**) was calculated for each composite, with N_{shuf}=1. P-values calculated using combined data from many subjects in the manner described above find N_{better} by comparing the shuffled P_Ts compared to the mean P_T from all composites.

Results

The topographic product is resistant to differences in map shape

To verify whether the topographic product is sensitive to transformations of one of the maps, the artificial tectum was transformed in 7 different ways. 4 shape-preserving: a translation, rotation, reflection, expansion (**fig. 3C,E,G,I**), and 3 shape-altering: unidirectional stretch, altering the amount of curvature, and all of the above applied simultaneously. (**fig. 3K,M,O**). The shape-preserving transformations have no noticeable effect on P_T or shuffled P_T (**fig. 3B,D,F,H,J,Q**), meaning that it is instantly an improvement on the scaled CoS.

Normalising P_T improves shape resistance

Differences to true P_T and shuffled P_T appear to be somewhat correlated (**fig. 3Q**): a transformation increasing true P_T appears to at least affect shuffled P_T in the same direction. Thus, I hypothesised that taking the ratio of P_Ts between real and shuffled maps would give a more uniform measure of map disorder. As both P_T and shuffled P_T vary with the shape of the map and the ratio then removes the effect of map shape – within and across transformations.

Indeed, normalising true P_T to shuffled P_T appears to reduce the variance of P_Ts across maps of different shapes (**fig. 4A**). This is validated in that the coefficient of variance is smaller at all values of ANSD (**fig. 4B**). Indeed, curve fits using this data (**equation 6**) produce smaller confidence intervals for their parameters,

giving better predictions of map disorder from the normalised P_T (normP_T) (**fig. 4C-D**).

Figure 3. **The topographic product is resistant to differences in shape.** (A,C,E,G,I,K,M,O) Example transformations applied to artificial tecta prior to the addition of noise. (B,D,F,H,J,L,N,P) Profiles of true and shuffled P_T with variable amounts of noise applied to artificial tecta transformed like the corresponding image, and constant noise in grid (as in **fig. 2A**). (Q) Overlay of previous graphs. The true and shuffled P_T have roughly the same profiles when transformations are applied prior to noise. N_{shuf} = 1000 in all cases.

Figure 4. Normalising P_T to shuffled P_T improves resistance to shape change. (A) overlaid curves for normP_T, using the same data as **figure 3**, appear closer together. (B) The coefficient of variation is lower for normP_T at all values of noise added (calculated separately for each of 50 bins). (C-D) Curve fits for both P_T and normP_T, with confidence intervals. These are much smaller in (D).

Topographic product applied to maps from many artificial map pairs

The models examined so far are somewhat artificial in that they give even coverage of the two spaces and have large numbers of points. For real datasets, a single experimental subject might only yield a few points, which can then be combined into a single map pair.

This means that it is worthwhile to model how normP_T is affected by the pooling of data from multiple map pairs, each with few points.

Multi-subject analysis of sparsely-sampled data can improve resolving power

Fig. 5A demonstrates the strategy used to test multisubject analysis. Artificial maps were generated as before, and 12 evenly spaced points were selected from visual space, along with their tectal partners.

Calculating normP_T for sparsely sampled maps individually and taking the mean gives a higher value of normP_T than when densely sampled maps are used, meaning that the ability of the metric to resolve precision is impaired (**fig. 5B**).

However, recombining the points of these sparsely sampled maps for multisubject analysis allows us to regain the same resolving power, lowering the normP_T values to those of the densely-sampled maps (**fig. 5B**).

Figure 5. NormP_T applied to data from multiple artificial maps with few points each. (A) sampling strategy for choosing 12 points from each original artificial map (B) Red: mean normP_T from 50 artificial map pairs with 432 points, N_{shuf} = 1000. Green: mean normP_T from 50 artificial maps, each with 12 points, N_{shuf} = 1000. Black: multi-subject mean normP_T from the same 50 12-point artificial map pairs for each noise value. New composites were generated for each value of noise until the mean changed by <0.1%. N_{shuf} = 1 per composite. (C) As (B), but with a random offset in x and y of SD 2.5 applied to all artificial tecta.

Multi-subject analysis is vulnerable to jitter

Randomly displacing all of the points in a tectal map by a randomly determined small amount ("jittering" the maps) models inter-subject variation in the position of the maps. **Fig. 5C** was generated by generating jitter with an SD of 2.5. This has no effect on the data from single subjects (to be expected, **fig. 3C-D**).

However, with multisubject analysis, the estimate of precision is poor at low levels of disorder (**fig. 5C**). This can be explained by the process of recombining points; as points are randomly selected, the displacement of each point by jitter ceases to be uniform across the map and instead is interpreted as "extra" random movement. This gives a lower limit of the amount of intra-subject noise that can be resolved.

The ANSD value at which single- and multi-subject curves converge is approximately equal to the ANSD given by using the SD of the jitter as the intra-subject noise. This is true for all values of jitter SD tested (data not shown). In the case shown, this value is ~0.06, as indicated on the graph. Henceforth I refer to this point as the Variability Equals Noise (VEN) limit. This is useful, as it allows us to resolve the relative contributions of intra-subject noise and inter-subject jitter, qualitatively and quantitatively:

If single-subject normP_T is equal to multi-subject normP_T, then inter-subject jitter is less than or equal to intra-subject noise, and there is a good estimate of noise, but not jitter. If the single-subject normP_T is less than the multi-subject normP_T, the inter-subject jitter exceeds the intra-subject noise. In this situation, the single-subject value will be an over-estimate of the disorder present.

Application to functional imaging in the zebrafish tectum

Aenea Hendry has obtained a large dataset from imaging the tecta of zebrafish expressing GCaMP in the axon terminals of their retinal ganglion cells (RGCs)[7]. Reactive clusters of voxels are referred to as points, which, due to the nature of the GCaMP labelling, are putatively synapses. Using a sparse noise visual presentation paradigm, the centre of mass of responsive points receptive fields was determined. Scanning bars were used to determine whether tectal areas were selective for directed (DS) or orientated (OS) motion[8,7]. All points have been placed in a standardised model tectum[7] (**fig. 6A**) which should remove differences in tectal shape between fishes.

To test the hypothesis that these populations of DS and OS points are topographically ordered, and to attempt to estimate map precision, the points in visual and tectal space were analysed using the TP.

Multisubject p-values (see **Methods/equation 7**) are p<0.001 for both DS and OS maps. This is as expected: retinotopy is well established, and there is no reason to expect these classes of neurons to violate it.

The fact that multi-subject P_T appears larger than single-subject indicates that the data lie to the left of the VEN limit: there is more jitter between subjects than there is noise within subjects (**fig. 6B**). In order to control for the effect of the greater number of points in the OS maps, the analysis was repeated after deleting points at random from the OS maps until there were the same number. This produces minimal effects on normP_T, precision and jitter (**fig. 6B-C**).

The amount of jitter and point noise can be estimated (**fig. 6B**): this is achieved by using the normP_T and a curve fitted to multisubject analysis (black points **fig. 5B,** taking the form of **equation 6** with A=0.0464, r=4.94, b=2.66). Because these are rough estimates, error bars have not been presented. Due to the low statistical power of single-subject analysis and the roughness of these estimates, precision between DS/OS populations cannot be compared in a quantitative fashion.

Figure 6. Topography of reactive points in the zebrafish tectum. (A) All reactive points identified using sparse noise, shown within the standardised tectum. The blue and red lamina are those that contain DS and OS points respectively. (B) NormP_T for direction- and orientation-selective points within the tectum. Error bars are 95% confidence intervals. Differences between OS and DS populations are not due to numbers of points. (C) NormP_T converted to estimates of actual precision and jitter, in distance units. Estimates of noise are likely to be overestimates, while estimates of jitter are underestimates.

n=32 fishes
Single-subject analysis uses N_{shuf} = 1000, or the number of unique shuffles (whichever was the smaller number). Fish with fewer than 5 points in a given population of points were excluded.
Multisubject analysis uses 1000 composites, N_{shuf} = 1 per composite.

Discussion

Overall, I have demonstrated that the topographic product, in a normalised form, is a metric capable of both detecting topographic order and quantifying map precision. Further, it appears resistant to map shape and thus a robust option for studying biological topographic maps. Indeed, it has been applied to an experimental dataset derived from functional imaging of zebrafish RGCs, detecting visuotopic order in both populations considered. With the caveats that these are overestimates, the precision is 7.5μm for OS points and 10μm for DS.

The metric could be of great use in studying the development and refinement of circuits within the developing nervous system. One example might be to resolve the relative contributions of visual-evoked activity and intrinsic factors to map refinement at different time points by dark-rearing.

Improving estimates of noise in presence of jitter

The Lowe lab are particularly interested in quantifying topographic map precision in the zebrafish tectum by pooling experimental data from multiple sparsely sampled maps. From my analysis of previously obtained data, it appears that it is affected by jitter. In this situation, intra-subject disorder is overestimated whether we consider single- or multi-subject data. This is probably due to the process of recombining points in the multi-subject analysis; the uniform translation of jitter is converted to noise once it is no longer uniform over the points considered. In future, the formulation of P_T could be remodelled to minimise effects of jitter on pooled data.

Improving estimates of jitter

Additionally, in modelling, there is an upward trend in normP_T for the jittered multisubject data to the left of the VEN limit (**fig. 5B**). It is possible that in directly converting the multisubject normP_T to jitter, this value is underestimated. In future, adding noise to maps to reach the VEN limit could improve the accuracy of this measure.

Parametric maps of precision

One of the inherent limitations of this method is that compressing map disorder into a single number is potentially an oversimplification. In a growing number of systems, non-uniform topographies have been identified, with variable density of constituent neurons and relative expansions of specific parts of feature space[9,10]. Presumably there will be altered precision in expanded regions. This situation is also likely to give us an overestimation of disorder overall, in manner similar to how independent contributions of noise and jitter appear to be or-ed rather than summed (**fig. 5C**). I believe it would be possible to examine how order varies across a map by calculating scores a P_T for each point, allowing the creation of illustrative parametric maps of disorder in both spaces.

References

1.   Cang, J. & Feldheim, D. A. Developmental mechanisms of topographic map formation and alignment. *Annu. Rev. Neurosci.* **36,** 51–77 (2013).

2.   Liebert, W., Pawelzik, K. & Schuster, H. G. Optimal Embeddings of Chaotic Attractors from Topological Considerations. *Europhys. Lett.* **14,** 521–526 (1991).

3.   Bauer, H.-U. & Pawelzik, K. R. Quantifying the neighborhood preservation of self-organizing feature maps. *IEEE Trans. Neural Networks* **3,** 570–579 (1992).

4.   Yarrow, S., Razak, K. A., Seitz, A. R. & Seriès, P. Detecting and quantifying topography in neural maps. *PLoS One* **9,** e87178 (2014).

5.   Yarrow, S., Razak, K. A., Seitz, A. R. & Seriès, P. Detecting and quantifying topography in neural maps. *PLoS One* **9,** e87178 (2014).

6.   Delaunay, B. Sur la sphère vide. A la mémoire de Georges Voronoï. *Bull. l'Académie des Sci. l'URSS. Cl. des Sci. mathématiques na* **6,** 793–800 (1934).

7.   Lowe, A. S., Nikolaou, N., Hunter, P. R., Thompson, I. D. & Meyer, M. P. A systems-based dissection of retinal inputs to the zebrafish tectum reveals different rules for different functional classes during development. *J. Neurosci.* **33,** 13946–56 (2013).

8.   Nikolaou, N. *et al.* Parametric functional maps of visual inputs to the tectum. *Neuron* **76,** 317–24 (2012).

9.   Azzopardi, P. & Cowey, A. The overrepresentation of the fovea and adjacent retina in the striate cortex and dorsal lateral geniculate nucleus of the macaque monkey. *Neuroscience* **72,** 627–39 (1996).

10.   Bleckert, A., Schwartz, G. W., Turner, M. H., Rieke, F. & Wong, R. O. L. Visual space is represented by nonmatching topographies of distinct mouse retinal ganglion cell types. *Curr. Biol.* **24,** 310–5 (2014).